Behavior of thermoset composites during the cure : measurement of process-induced Strains, characterization and modeling of the rheological behavior

Rima Sfar Zbed

DOCTORAT BRETAGNE SCIENCES LOIRE POUR L'INGENIEUR

Nantes Université

THESE DE DOCTORAT DE

NANTES UNIVERSITE

ECOLE DOCTORALE N° 602
Sciences pour l'Ingénieur
Spécialité : *Energétique-Thermique-Combustion*

Par
Rima SFAR ZBED

Behavior of Thermoset Composites during the Cure:
Measurement of Process-Induced Strains, Characterization and Modeling of the Rheological Behavior

Thèse présentée et soutenue à l'université de Nantes, le 07 Novembre 2022
Unité de recherche : Laboratoire de Thermique et Energie de Nantes (LTeN), UMR 6607

Rapporteurs avant soutenance :

Laurent Orgéas	Directeur de Recherche, HDR, CNRS
Pascal Hubert	Professeur, Université McGill, Montréal, Québec, Canada

Composition du Jury :

Présidente :	Véronique Michaud	Professeure associée, EPFL, Lausanne, Suisse
Examinateurs :	Pierre Dumont	Professeur des universités, LaMCoS, INSA Lyon
	Mael Peron	Maitre de conférences, GeM, Nantes Université
Directeur de thèse :	Steven Le Corre	Professeur, LTEN, Nantes Université
Co-directeur de thèse :	Vincent Sobotka	Professeur, LTEN, Nantes Université

ACKNOWLEDGMENTS

This time has finally come and my PhD journey has arrived to an end despite all the ups and downs brought especially by the pandemic period.
I would like to take this opportunity to acknowledge everyone who has helped in every stage of this project.

To start, I would like to express my gratitude to the jury members who carefully read the manuscript. In particular, I would like to thank Mr. Pascal Hubert, Professor at the McGill University of Montréal, and Mr. Laurent Orgéas, Research Director at French National Centre for Scientific Research, for having evaluated my thesis work in a relevant way. I would like to thank them very much for their feedback, evaluation and the reports they provided. I would also like to thank Mrs. Véronique Michaud, Associate Professor at the EPFL of Lausanne, for having done me the honor of chairing the jury. I wish also to thank Mr. Pierre Dumont, Professor at the INSA Lyon and Mr. Mael Peron, Lecturer at Nantes University, for accepting the role of reviewers. I enjoyed the scientific discussion we had during the defense.

I am deeply indebted to my thesis director, Steven Le Corre, and my thesis co-director, Vincent Sobotka, for all their help. Steven, you were an integral part of me being able to make it to the end! Your passion for the field has taught me so much. Thank you for your availability despite the enormous responsibilities. I would also like to thank you for all the guidance, support, understanding, kindness, as well as the many long discussions we had. Vincent, I wish to thank for your scientific support, encouragement and your valuable help throughout these last years.

Additionally, I would like to gratefully thank all the SEF members of the LTEN for their great help, Julien, Arnaud, Christophe and Gwen. Nico, thank you for all the shared moments around the PvT-Haddoc and the many enjoyable conversations. Nathalie, thank you for your IT help, Michèle-Anne and Amandine, for the administrative help, but not just that! Thank you for always being there to listen and to support.

My special thanks also go to the researchers, post-docs and all PhD students. Juliana, Théo, Julien, Rita, and (even just recently, yes!), Sourrour, for being all ears to my problems no matter how silly they were. Rita and Sourrour: thank you girls for the last few days before the defense, you both were more friends than just colleagues! Mehdi, I would like to thank you for being my favorite running buddy along this period. Thank you for all the joyful nighttime running. I would especially like to thank you for your generosity and for your help whenever I need it.

I want to thank the friends that I am grateful to have, the ones who are so far in distance but never in heart, the ones who always show incredible support! Chayma (Canada), Nourchene (Rennes), Abir J (Paris) and Abir S (La Roche-sur-Yon), Hana, Moez, Amal and Youssef (Tunisia) and Ali (Czech): I am lucky to have a trustworthy friends like you guys.

And finally I wish to thank my family who contently inspire me, and who have always supported my desire to learn. I would especially like to thank my parents. You are my heroes. I want to thank my sister and my brother who always know how to make me smile even in the hardest moments. My special thanks go to my husband Anas for accompanying me through this adventure. You are responsible for a large part of the success of this work. Thank you for your patience and endless support.

I just wanted to finish with Hawking's words here to remind every PhD student that it really matters to don't just give up !

"*Remember to look up at the stars and not down at your feet. Try to make sense of what you see and wonder about what makes the universe exist. Be curious. And however difficult life may seem, there is always something you can do and succeed at.*
It matters that you don't just give up. "

– *Stephen Hawking*

Contents

Acknowledgments i

Contents iii

List of Figures vii

List of Tables xv

General Introduction 1

1 Literature review and objectives 5

1.1 General presentation of thermosetting composites . . . 7
1.1.1 Reinforcements . . . 7
1.1.2 Matrix . . . 8
1.1.3 Prepregs . . . 10
1.1.4 Autoclave processing of thermosetting prepregs . . . 13
1.1.5 Physical and chemical properties of thermoset polymers . . . 15
1.1.5.1 Gelation . . . 15
1.1.5.2 Vitrification . . . 15
1.2 Issues statement and scope of study . . . 16
1.2.1 Curing issues of thermoset composites . . . 16
1.2.2 Multi - physical phenomena generating residual stresses and responsible of geometrical variation during composite processing . . . 18
1.2.2.1 Differential thermal expansion . . . 18
1.2.2.2 Chemical shrinkage . . . 20
1.2.2.3 Tool - Part interaction . . . 20
1.2.2.4 Resin flow . . . 22
1.2.3 Synthesis and scope of study . . . 23
1.3 Description of thermo-chemical strains measurement methods . . . 24
1.3.1 Volumetric measurements . . . 24
1.3.2 Directional measurements . . . 26
1.3.2.1 Dynamic Mechanical Analysis (DMA) . . . 26
1.3.2.2 Thermomechanical Analysis (TMA) . . . 27
1.3.2.3 Fiber Bragg Grating (FBG) sensors (optical fiber sensors) . . . 29
1.3.2.4 Digital Image Correlation (DIC) . . . 31
1.4 Consolidation phenomenon of thermosetting prepregs in the uncured state . . . 33

1.5 Measurement techniques and modeling approaches of rheological properties during the cure of thermosetting systems . . . 39
1.5.1 Experimental methods of rheological properties characterization . . . 40
1.5.1.1 Classical detection criteria of gel point . . . 40
1.5.1.2 Yield stress based-approach to investigate the gelation in thermoset resins . . . 43
1.5.1.3 Employed techniques to investigate thermoset composites rheological behavior during the cure . . . 46
1.5.2 Modeling approaches of rheological behavior during the cure . . . 49
1.5.2.1 Rheo-kinetic models for thermosetting resins . . . 49
1.5.2.2 Developed rheological models for thermoset composites . . . 51
1.6 Outlines of this literature review and Objectives . . . 53

2 Materials and methods **55**
2.1 Introduction . . . 56
2.2 Studied material: IMA/M21 toughened prepreg . . . 56
2.2.1 IMA carbon fibers . . . 57
2.2.2 M21-Epoxy resin: Composition and Curing reaction mechanism . . . 58
2.3 Literature review: Reminders on cure kinetics models of Epoxy/Amine systems 59
2.4 Thermo-chemical characterization and model validation of the M21 resin cure kinetics . . . 62
2.4.1 Model validation of the curing kinetics . . . 62
2.4.1.1 Dynamical Scanning Calorimetry (DSC) characterization . . . 62
2.4.1.2 Characterization using the PvT-α mold . . . 65
2.4.2 Characterization of the volumetric behavior of the M21 resin during the cure by using the PvT-α mold . . . 69
2.5 Rheological characterization of the M21 resin: Gel point determination . . . 71
2.6 Presentation of the PvT-HADDOC set-up and the imported improvements . 74
2.6.1 Design and global working principle . . . 74
2.6.2 Thermal control . . . 75
2.6.3 Mechanical state . . . 78
2.6.4 Displacement measurements . . . 81
2.7 Partial conclusion . . . 83

3 Measurements of the anisotropic thermo-chemical strains of the IMA/M21 prepreg during the cure **85**
3.1 Introduction . . . 86
3.2 Sample preparation and set up . . . 86
3.3 Analyses of preliminary tests and definition of new adjusted cure cycles . . . 89
3.3.1 Preliminary test analysis . . . 89
3.3.2 Separation of coupled phenomena . . . 93
3.3.3 Definition of new curing cycles . . . 96
3.4 Analyses of cure-induced strains along the three directions . . . 98
3.4.1 Through-thickness displacement measurements and strains calculation 98
3.4.2 In-plane displacement measurements and strains calculation . . . 100

3.4.3 Comparison between the deformations along the three directions . . . 102
3.5 Compaction behavior in the uncured state through the thickness direction . 104
3.5.1 Compaction behavior analysis . . . 104
3.5.2 Compaction kinetics . . . 107
3.6 Anisotropic thermal expansion and shrinkage measurements results . . . 110
3.6.1 Thermal expansion behavior and CTE measurements . . . 110
3.6.2 Chemical shrinkage behavior and CCS measurements . . . 114
3.7 Partial conclusion ans perspectives . . . 117

4 Multi-layer model considering the presence of resin interleaf layers 119
4.1 Introduction . . . 120
4.2 Brief review on homogenization models employed for composite materials . . 120
4.3 Multi-layer model and laminate constitutive equations . . . 122
4.3.1 Formulation of the multi-layered structure and model description . . 122
4.3.2 Application to thermo-chemo-elasticity . . . 124
4.3.3 Volume fraction of each lamina . . . 125
4.3.4 Thermo-mechanical behavior of the laminate at the macro-scale . . . 125
4.4 Identification of each layer thermo-chemical properties and mechanical behavior at the meso-scale . . . 126
4.4.1 Estimation of the volume fraction of each layer . . . 127
4.4.2 The resin inter-layer cure dependent behavior . . . 127
4.4.2.1 Elastic modulus and Poisson's ratio . . . 127
4.4.2.2 Linear coefficients of thermal expansion and chemical shrinkage 131
4.4.3 The prepreg layer cure dependent behavior . . . 131
4.4.3.1 Mechanical elastic properties . . . 131
4.4.3.2 Coefficients of thermal expansion and cure shrinkage . . . 134
4.5 Comparison with experimental results and discussions . . . 135
4.5.1 Calculation procedure . . . 135
4.5.2 Results and discussions . . . 137
4.6 Partial conclusion and perspectives . . . 142

5 Characterization and modeling of the composite rheological behavior during the cure 145
5.1 Introduction . . . 147
5.2 Experimental procedure . . . 147
5.2.1 Sample preparation . . . 147
5.2.2 Methodology of characterization tests . . . 148
5.2.2.1 Curing cycle . . . 149
5.2.2.2 Loading mode definition . . . 150
5.2.2.2.1 Preliminary tests . . . 150
5.2.2.2.2 The adopted strategy . . . 151
5.2.3 Mechanical strains calculation strategy . . . 154
5.3 Experimental results analysis . . . 157
5.3.1 General aspect of the mechanical behavior . . . 157
5.3.2 Limitations due to the experimental setup compliance . . . 160

5.3.3 Influence of the sample initial section . . . 161
5.3.4 Influence of the degree of cure . . . 162
5.4 Modeling results and discussions . . . 169
5.4.1 Theoretical background: Brief reminders on creep behavior of viscoelastic materials . . . 169
5.4.2 Curve fitting and estimation of creep parameters of Burgers model during the cure . . . 172
5.4.3 Sensitivity analysis of Burgers model parameters to a creep-recovery loading path . . . 179
5.4.4 Parameters' evolution with cure and identification of the rheo-kinetic Burgers model . . . 183
5.4.4.1 Behavior before the gel point . . . 183
5.4.4.2 Behavior beyond the gel point . . . 186
5.4.4.3 Rheo-kinetic Burgers model . . . 187
5.5 Verification of the rheo-kinetic Burgers model predictions . . . 188
5.5.1 Creep-recovery test . . . 189
5.5.2 Loading-unloading test, denoted as test I . . . 189
5.5.3 Loading-unloading test, denoted as test II . . . 192
5.5.4 Axial strain responses in comparison with the three tests . . . 194
5.6 Partial conclusion . . . 197

General conclusion and perspectives **201**

Résumé étendu en français **205**

Bibliography **213**

List of Figures

1 Use of composite materials in commercial aircraft [1]. 2

1.1 Thermoset resin polymerization mechanism from a monomer stage to a fully cured (3D) cross-linked network [2]. 9
1.2 Microstructures of toughened epoxy resin systems showing the second phase of thermoplastic-rich particles in continuous epoxy-rich matrix. 10
1.3 Schematic of prepreg production by two steps hot melt process [3]. 11
1.4 Typical inter-laminar region containing rubber particles [4]. 12
1.5 Morphology of IMA/M21 carbon/epoxy toughened prepreg with thermoplastic inter-laminar dispersed particles through the laminate thickness. 13
1.6 Example of vacuum bag lay-up components for autoclave curing [5]. 14
1.7 Typical autoclave processing system [5]. 14
1.8 RTM Epoxy resin properties development and state transition during a typical cure cycle [6]. 15
1.9 Geometric deviation named as ¨warpage ″generated due to the induced residual stresses in flat laminates [7]. 17
1.10 Micrograph of composite laminates showing in-plane fiber waviness. 17
1.11 Schematic view of thermal deformation induced in laminates during cooling down due to differential thermal expansion [8]. 19
1.12 A reduction in enclosed angle eta due to contraction resulting in the well-known spring-in deformation pattern [9]. 19
1.13 Fiber waviness induced by chemical shrinkage in resin-rich areas (e.g., T-joints) [10]. 21
1.14 Effect of tool–part interaction on distortion of a flat part [7]. 21
1.15 Effect of tool–part interaction on distortion of a part with curved sections [9]. . 22
1.16 Schematic of different stages in a typical autoclave process cycle [11]. 22
1.17 Effect of resin flow on the warpage in flat laminates [9]. 23
1.18 General view of PVT-α device [12]. (1) Displacement sensor (2) Piston (3) Heat flux sensors (4) Mold cavity (5) Ejectors (6) Elastomer capsule containing sample 25
1.19 Variation of volume chemical shrinkage versus degree of cure of vinylester resin and associated composites with different fiber volume fractions [12]. 26
1.20 Measured through-thickness shrinkage plotted against the degree of cure related to UD and cross-ply precured samples [13]. 27
1.21 (a) Experimental bench based on (TMA) method employed for cure shrinkage measurements. (b) dimensions of the heating plates and used samples [14]. . . . 28
1.22 (a) Measured post-gelation cure shrinkage of AS4/8552 laminates [14]. (b) Measured through-thickness chemical shrinkage of an M21EV/IMA laminate [15]. . . 28

1.23 The working principle of FBG sensor [16] [17]. 29
1.24 Cross-sectional micrograph of FBG sensor embedded along the in-plane transverse direction of UD laminate [18]. 30
1.25 (a) Strain changes at different thickness after gelation of T300/Epoxy laminate. (b) Captured effective chemical shrinkage along the in-plane and out-of plane transverse directions after gelation. [16] 30
1.26 (a) DIC setup placed near the view-port of the autoclave. (b) Measured displacements along the in-plane direction of neat resin and composites samples. [19] . . 31
1.27 DIC experimental test setup [20]. 32
1.28 (a) Measured thermo-chemical strains by DIC during the cure of 4 ply prepreg sample. (b) Estimated CCS during the isothermal cure at 180°C. [20] 33
1.29 Micrograph of a sample edge made of IMA/M21 prepreg and consolidated at an isotherm of 90°C. Coexistence of both bleeding and shear flow mechanisms are observed [21]. 35
1.30 Schematic of the OoA prepreg lay-up consolidation process [22]. 35
1.31 SEM images of cross-sectioned AS4/8552 samples. Condition one corresponds to no applied pressure: (a) Isotherm hold at 40°C (b) Isotherm hold at 60°C (c) Isotherm hold at 80°C. Condition two corresponds to vacuum applied pressure during heating: (d) Isotherm hold at 40°C (b) Isotherm hold at 60°C (c) Isotherm hold at 80°C [23]. 37
1.32 The effect of pre-debulking conditions on the through-thickness compaction of the UD samples [14]. 38
1.33 Steady shear viscosity profile of an epoxy resin isothermally cured at 140°C [24]. 41
1.34 (a) Evolution of G' and G" during the 171°C isothermal curing of an epoxy resin at 10 rad/s and 10% strain. Gelation onset is identified as the cross-over point of G' and G" [25]. (b) Gel point criterion through complex shear modulus onset [26]. 41
1.35 (a) Loss tangent curves evolution as function of time for different frequencies during the curing of an epoxy resin at 70°C. Gelation is identified as the point where Tanδ is independent of frequency [27]. (b) Variation of Tanδ during the curing of glass/epoxy prepreg at 120°C. Gelation is identified as the peak in Tanδ curves for different frequencies [28]. 42
1.36 Measured stress-strain curves. (a) Assumed elastic behavior, $\varepsilon_r < 0.2\%$. (b) Assumed inelastic behavior, $\varepsilon_r > 0.2\%$ [29]. 44
1.37 (a) Yield stress as a function of cure degree for a curing at 160°C. (b) Obtained yield time as a function of isotherm cure temperatures [29]. 44
1.38 Material mechanical response taken at three different moments from the cure cycle. (a) Applied stresses with the oscillatory strain responses as function of time. Fitted strain data with a sinusoidal function (Blue) (b) The corresponding Lissajous plots [30]. 45
1.39 Yield stress measured values for different degree of cure levels of a vinylester resin [30]. 46
1.40 (a) Scheme of the measuring system in DMA with the single cantilever mode [31]. (b) Configurations of the prepreg samples for DMA testing [32]. 47

1.41 (a) DMA measurements, conducted on uncured laminates, of the storage modulus and Tanδ [33]. (b) DMA measurements conducted on partially cured samples. The evolution of storage modulus (E') over time at three different isothermal temperatures [33]. (c) DMA measurements of shear modulus through cure performed on precured prepregs [34]. (d) Viscoplastic shear strain development with time for precured sample using tensile creep tests [2]. 48
1.42 (a) Complex viscosity as a function of time for different isothermal cure at 110°C, 120°C, 130°C, and 140°C, (b) complex viscosity as a function of temperature during a heating ramp of 4.6°C/min, in comparison with the modified WLF chemorheological model [35]. 51
1.43 Schematic representation of the rheo-kinetic model based on the yield stress approach to describe the material gelation [30]. 51
1.44 Comparison of measured viscosity with time dependent model (denoted as TD) and Castro-Macosko model (denoted as CM) for different isotherm cure temperatures [36]. 52

2.1 IMA/M21 reinforcing material preimpregnated with epoxy resin. (a) Unidirectional preimpregnated sheets as standard roll form. (b) IMA/M21 UD prepreg ply. 56
2.2 Micrograph through the thickness of an IMA/M21 laminate cured sample. . . . 57
2.3 Scheme of curing reaction mechanism of Epoxy/Amine systems (1-3) and etherification (4) [37]. 59
2.4 DSC dynamic scan of M21 resin for a heating rate of 10°C.min^{-1}. Heat flux recorded as a function of temperature. 63
2.5 Baseline after removing the endothermic peak. 64
2.6 DSC experimental measurements of the cure degree (a) and the polymerization rate (b) for different heating ramps at 3, 5 and 10°C.min^{-1}. 65
2.7 An example of heat flux and surface temperature recorded as function of time during the cure of M21 resin sample (1) in the PvT-α mold. 67
2.8 Experimental conversion degree evolution as function of time calculated from equation 2.9 and obtained from PvT-α mold measurements, in comparison with the one predicted by the kinetics model from equation 2.10. 68
2.9 Experimental polymerization rate evolution as function of time calculated from equation 2.1 and obtained from PvT-α mold measurements, in comparison with the one predicted by the kinetics model from equation 2.10. 68
2.10 Typical dilatometric curve of volumetric behavior obtained with PvT-α apparatus of the M21 resin during a curing cycle (Obtained results from sample (2) testing). 69
2.11 (a) Variation of volume strains of the M21 resin as a function of the thermal cycle. (b) Variation of the volume chemical shrinkage of the M21 resin as a function of the predicted degree of cure. 70
2.12 Loss factor tan(δ) as a function of time at three different frequencies during the isothermal curing of the M21 resin at (a) 160°C and (b) 180°C. 73
2.13 Global overview of the PvT-HADDOC experimental setup. 3D conception (left) and a scheme of the mold cavity (right). 75
2.14 Scheme of the heating circuits of the PvT-Haddoc device. 76

2.15 Surface temperature evolution of the piston and the lower plate during a curing cycle: (a) Before thermal system improvement (extracted from Peron *et al.* work [38]). (b) Current study after thermal system improvement. 77
2.16 3D illustration of the PvT-Haddoc device - Highlight on added improvements. . 77
2.17 PvT-Haddoc device. 79
2.18 Example of performed oscillatory tests without sample showing (a) a hysteresis loop due to the presence of frictions, and (b) a hysteresis due to the stiffness of the metal bellows: elimination of friction. 79
2.19 Schematic of the isotropic compressive state performed through the combination of the applied compressive force and pressure around the sample during a curing cycle. 80
2.20 Schematic illustration of relative positions of the sample, the glass window and the laser profilometer. 82

3.1 Debulking set-up configuration of stacked laminate before cut. 87
3.2 (a) Final cut using a stainless steel die cutting. (b) Final compaction step using a compaction mold [38]. (c) Final shape of UD IMA/M21 prepreg sample. . . . 87
3.3 IMA/M21 sample placed in the PvT-HADDOC for the thermo-chemical characterization before mold closure. 88
3.4 Manufacturer's recommended cure cycle (named as cycle A) applied to sample I performed in the PvT-HADDOC device. 89
3.5 (a) Measured displacements by the piston according to the manufacturer's recommended cure cycle related to sample I experiment. (b) Through-thickness calculated strain of sample I after baseline subtraction. 90
3.6 The effect of time and temperature on the induced through-thickness strains due to the compaction mechanism in the uncured state of the material through the three tested thermal cycles names as A, B and C (Please note that the notations Th.Exp, Th.Cont and Ch.Sh are employed to refer to thermal expansion, thermal contraction and chemical shrinkage, respectively). 92
3.7 Viscosity evolution of the M21 resin during a heating ramp at $1°C.min^{-1}$ up to 180°C. (Supplier technical data [39]). 95
3.8 New proposed curing cycles: (a) named as cycle 1 and (b) named as cycle 2. . . 97
3.9 Axial displacements measured by the piston during the experiment of sample 3 including raw data, the baseline and the sample thickness variation, together with the performed thermal cycle 2. 99
3.10 In-plane variation of the lateral surface of sample 2 with time along the measuring line for a selected position of the sensor (x = 0) during the cure cycle 2. 100
3.11 Evolution of the in-plane displacements for the 5 selected points along the through-thickness measuring line with time of sample 2. 101
3.12 Comparison between the deformations along the three principal directions of the UD IMA/M21 laminate together with the estimated degree of cure and the thermal cure cycle 2. 102
3.13 Thickness reduction due to the compaction mechanism of the studied prepreg in the uncured state. 105

3.14 Optical micrograph of an uncured IMA/M21 UD laminate sample microstructure through its thickness. . . . 106
3.15 Optical micrograph of a cured IMA/M21 UD laminate sample microstructure through its thickness. . . . 106
3.16 Comparison between experimental and fitted data of the compaction kinetics as function of time for each isothermal dwell at 30°C, 60°C and 70°C in the uncured state of the material. . . . 107
3.17 Linear fit of the compaction kinetics parameters A and R_0 as functions of temperature. . . . 108
3.18 Comparison between the estimated compaction kinetics based on the proposed empirical fit and the experimental thickness reduction of sample I during the heating ramp only. . . . 109
3.19 The induced strains along both transverse directions during curing of sample 3 as function of the applied thermal cycle 2. . . . 110
3.20 (a) Example of cured IMA/M21 laminate sample. (b) Extracted specimens for linear dilatometric measurements. . . . 112
3.21 Linear thermal expansion behavior along three principal directions obtained with measurements conducted on cured specimens extracted from sample 2 using a linear dilatometer. . . . 112
3.22 Measured chemical shrinkage of sample 2 during the isothermal cure at 160°C of cycle 2. . . . 114
3.23 Transverse chemical shrinkage measured during a 180°C and 160°C isothermal cure (Sample 1 and 3 are taken as examples, respectively). (a) Along the in-plane direction. (b) Along the thickness direction. . . . 116

4.1 Different scales defined in a composite laminate structure [40]. . . . 121
4.2 (a) Schematic model of the multi-layer geometry with coordinate system and dimensions for a unidirectional IMA/M21 prepreg laminate. (b) A through-thickness micro-section of a cured sample. . . . 123
4.3 The evolution of an Epoxy resin modulus during a typical cure described by CHILE model as a function of T*= T-Tg [41]. . . . 128
4.4 The evolution of the Poisson's ratio with the degree of cure of an epoxy resin [42]. 129
4.5 (a) Comparison of predicted values of the transverse Young's modulus with fiber volume fraction for various theoretical methods. (b) Comparison between the proposed analytical models by Jacquet *et al.* [43] with numerical calculations. . 133
4.6 Comparison between measured and estimated deformations along both transverse directions of the UD IMA/M21 laminate. (Sample 2 is taken as example for the experimental data). . . . 138
4.7 Comparison between measured and estimated deformations along both transverse directions of the UD IMA/M21 laminate after shrinkage behavior adjustment at the prepreg ply scale. (Sample 2 is taken as example for the experimental data). 141

5.1 (a) Coordinate system and initial dimensions' notations for a unidirectional IMA/M21 prepreg sample. (b) Specimen placed in the PvT-Haddoc setup for the mechanical testing (before mold cavity closure). . . . 148

5.2 Predicted polymerization rates according to both adjusted thermal cycles. . . . 150
5.3 (a) Experimental procedure for the mechanical testing. (b) Preliminary oscillatory mode loading test. . . . 151
5.4 Loading path diagrams: (a) Compressive loading-unloading test procedure (denoted as test I). (b) Creep-recovery test procedure (denoted as test III). . . . 152
5.5 Experimental protocol of the mechanical testing procedure under controlled stress using the Pvt-HADDOC setup (focus on the isothermal hold). . . . 153
5.6 Through-thickness compaction behavior and reference state definition. . . . 155
5.7 Through-thickness strain measurements resulting from the mechanical testing of sample 4. . . . 157
5.8 Applied loading-unloading stress evolution with time during the isothermal hold at 160°C. Illustration of mechanical test I. . . . 158
5.9 Mechanical strains evolution with degree of cure obtained from testing of samples 1, 3, 4 and 6 as examples. . . . 159
5.10 Measured transverse axial displacements obtained from creep-recovery test of sample 6 at α=31% together with the device displacements and the corresponding applied load. . . . 160
5.11 Measured transverse axial displacements obtained from creep-recovery test of sample 6 at α=58% and α=67% together with the device displacements and the corresponding applied load. Illustration of compliance device limitations after gelation. 161
5.12 Axial mechanical strain evolution with time during a loading-unloading cycle at α=38%. Illustration of sample's initial section influence on the behavior. . . . 162
5.13 Experimental creep normalized strain ε_3^* evolution with time during creep-recovery test as functions of cure degree. . . . 164
5.14 Mechanical response of sample 1 obtained with loading-unloading applied stress according to test I at four levels of cure degree. Resulted stress and strain are normalized by the corresponding stress amplitude for more legibility. . . . 165
5.15 Experimental results of loading-unloading-recovery tests of samples 1 and 3. (a) Stress-strain curves at α = 34% of samples 1 and 3. (b) Corresponding strain evolution with time at α = 34%. (c) Stress - strain curve at α = 49% of sample 1. (d) Strain evolution with time of sample 1 at α = 49%. . . . 167
5.16 Response of the studied prepreg material to the compressive loading-unloading test with different rates of stress loading at α = 34%. . . . 168
5.17 Viscoelastic models' responses to creep-recovery testing. . . . 171
5.18 Comparison of experimental response to creep-recovery test with modeling results predicted by Burgers model at α = 18% and α = 26%. . . . 173
5.19 Comparison between creep-recovery experimental and fitted data predicted by Burgers model for an applied stress of 11 10^{-3}MPa at different α. . . . 176
5.20 Comparison between creep-recovery experimental and fitted data predicted by Burgers model for an applied stress of 15.8 10^{-3}MPa at different α. . . . 176
5.21 Comparison between creep-recovery experimental and fitted data predicted by Burgers model for an applied stress of 30 10^{-3}MPa at different α. . . . 177
5.22 Comparison between creep-recovery experimental and fitted data predicted by Burgers model for an applied stress of 45.5 10^{-3}MPa at different α. . . . 177

5.23 Comparison between creep-recovery experimental and fitted data predicted by Burgers model for an applied stress of 65 10^{-3}MPa at different α. 178
5.24 Sensitivity analysis of Burgers model parameters on creep-recovery response. (a) The influence of E_0. (b) The influence of E_1. (c) The influence of η_0. The influence of η_1. 180
5.25 Sensitivity analysis of Burgers model parameters on creep-recovery response through sensitivity coefficient S^* evolution during an applied loading cycle. Each parameter was varied at a time by +10% from the nominal value identified for a α = 31%. 182
5.26 Plot of a proposed regression dependency for dynamic viscosity $\eta_0(\alpha)$ of Maxwell branch for the Burgers model as an exponential function of degree of cure. . . . 184
5.27 Plots of proposed regression dependencies for modulus of elasticity of Maxwell branch $E_0(\alpha)$ and relaxing response $E_1(\alpha)$ for the Burgers model as exponential functions of cure degree. 184
5.28 Plot of a proposed regression dependency for dynamic viscosity $\eta_1(\alpha)$ of Kelvin-Voigt branch for the Burgers model as an exponential function of degree of cure. 185
5.29 Measured axial strains of sample 6 after gelation. 186
5.30 Plots of the exponential regression of the numerical viscosity $\eta_0^{num}(\alpha)$ together with calculated experimental values η_0^{exp} as function of cure degree along the whole isothermal curing. 188
5.31 Comparison between the experimentally determined creep-recovery behavior with those calculated according to rheo-kinetic Burgers model for different degrees of cure. Experimental results were obtained from sample 6 testing according to test III. 190
5.32 Axial average normalized strains ε_3^* for a loading-unloading applied stress performed on samples [1 - 4] according to test I. Superimposition of the response of the rheo-kinetic Burgers model for two levels of cure degree with experimental data. 191
5.33 Sensitivity analysis of rheo-kinetic Burgers model parameters on loading-unloading response through sensitivity coefficient S^* evolution during an applied loading cycle at α = 29% according to test I. 191
5.34 Axial normalized strains ε_3^* for a loading-unloading applied stress performed on sample 5 according to test II. Superimposition of the response of the rheo-kinetic Burgers model for two levels of cure degree with experimental data. 193
5.35 Sensitivity analysis of rheo-kinetic Burgers model parameters on loading-unloading response through sensitivity coefficient S^* evolution during an applied loading cycle at α = 29% according to test II. 193
5.36 Axial strain responses for loading-unloading stress according to tests I and II on samples [1 - 4] and 5, respectively, with obtained axial creep strain according to creep-recovery test III carried out on sample 6. Superimposition of the response of the rheo-kinetic Burgers model to each loading path at 41% of cure degree. . 194
5.37 Axial strains response for loading-unloading applied stress performed according to tests I and II on samples [1 - 4] and 5, respectively, with obtained axial creep strain according to creep-recovery test III carried out on sample 6. Superimposition of the response of the rheo-kinetic Burgers model to each loading path at 29% of cure degree. 196

List of Tables

1 Comparison between the properties of the main employed materials in the aerospace industry [44] - HR: High Resistance, IM: Intermediate Modulus, HM: High Modulus and UD 0° 0° is for unidirectional along the direction to fibers 2

1.1 Properties of reinforcing fibers used in aerospace grade composites [44]. 8
1.2 Properties of matrices used in aerospace grade composites [44]. 8

2.1 General properties of the preimpregnated IMA/M21 material [39]. 57
2.2 General properties of HexTow® IMA carbon fibers [45]. 58
2.3 Parameters of Bailleul's cure kinetics model modified by Msallem *et al.* [46]. . . 66
2.4 Measured volumetric CTE and CCS of the M21 Resin. 71
2.5 Gel point at different isotherms. 72

3.1 Details for tested thermal cycles B and C applied under 7 bars. 94
3.2 Strain drops due to compaction for the three tested thermal cycles performed under 7 bars. 94
3.3 Details of new curing cycles. 98
3.4 Tested specimens according to new curing cycles. 98
3.5 Estimated values of the CTE for the IMA/M21 material by the PvT-HADDOC set-up. 111
3.6 Estimated values of the CTE for the IMA/M21 material with linear dilatometer on cured samples. 113
3.7 Estimated values by the PvT-HADDOC device of the CCS for the IMA/M21 laminate. 115

4.1 Values of the resin interlayer mechanical and thermo-chemical properties. 130
4.2 Values of the prepreg layer mechanical properties. 134
4.3 Estimated values of the laminate macroscopic CTE by the multi-layer model. Comparison with experimental results gathered in table 3.5. 138
4.4 Computed values of the laminate macroscopic CCS by the multi-layer model. (See table 3.7 for comparison with experimental results.) 139
4.5 Adjusted values of CCS of the prepreg ply. 140
4.6 New calculated values of the laminate macroscopic CCS by the multi-layer model. (See table 3.7 for comparison with experimental results.) 140

5.1 Defined σ_a levels for tests I, II and III with degree of cure variation values. . . . 152
5.2 Mechanical testing details and specimens used for each test. 154

5.3 Applied stress amplitudes for each degree of cure (α). 163
5.4 Parameters of the Burgers model identified by curve fitting on the basis of creep-recovery test for each loading cycle during the cure. 179
5.5 Coefficient values of the exponential regressions given by equation 5.24. 186

GENERAL INTRODUCTION

Because of the ongoing challenges triggered by climate change over the past decades, besides the fact of fuel prices soaring, society and industries have been impelled to tend towards more constrained practices in fossil-fuel consumption. Part of the solutions, with regards to many engineering sectors as the automotive industries and aviation, lies in lightening the structure and thus improving its fuel efficiency, while ensuring that the mechanical properties are maintained or even improved. Thus, the most sustainable alternatives that have been adopted to reduce fuel consumption in the aviation industry, are making airplanes lighter [47]. This has been accomplished by introducing more advanced lightweight materials and optimizing structures' design. For example, by including more suitable joining techniques in aircraft assemblies as adhesive bonding technology and welding processes over riveting methods and other fasteners which are considered as significant sources of additional weight [48]. Within this context, the use of composite materials in aerospace sectors has undergone a remarkable rise at an ever faster pace due to the merits of lightweight. For about fifty years, composite materials have gradually replaced metal alloys in aircraft, and today nearly exceed 50% of the structures' weight in the Airbus A350 XWB and the Boeing 787 aircraft as illustrated by figure 1 and reported by Hexcel Corporation. They have been largely integrated in aircraft primary structures as upper fuselage skin panel structures, wing boxes, wing panels, keel beam, empennage and stabilizers [1].

To date, latest-generation aircraft consume 70% less fuel and are around 85% more efficient than those entering service in the 1960s [49]. This interest is justified by the promising properties that represent these reinforced materials as there are numerous benefits to be had. They provide long-term good resistance to severe chemical and temperature environments, they are naturally anti-corrosive and have long service life and minimum maintenance as compared to most competitive metallic materials. Their mechanical properties are sometimes inferior to those of some metallic alloys, however it has to be taken into account the weight of elements. Composites have a very high strength to weight ratio (named as specific modulus) that allows them to deliver more strength per unit of weight than most metals (see table 1).

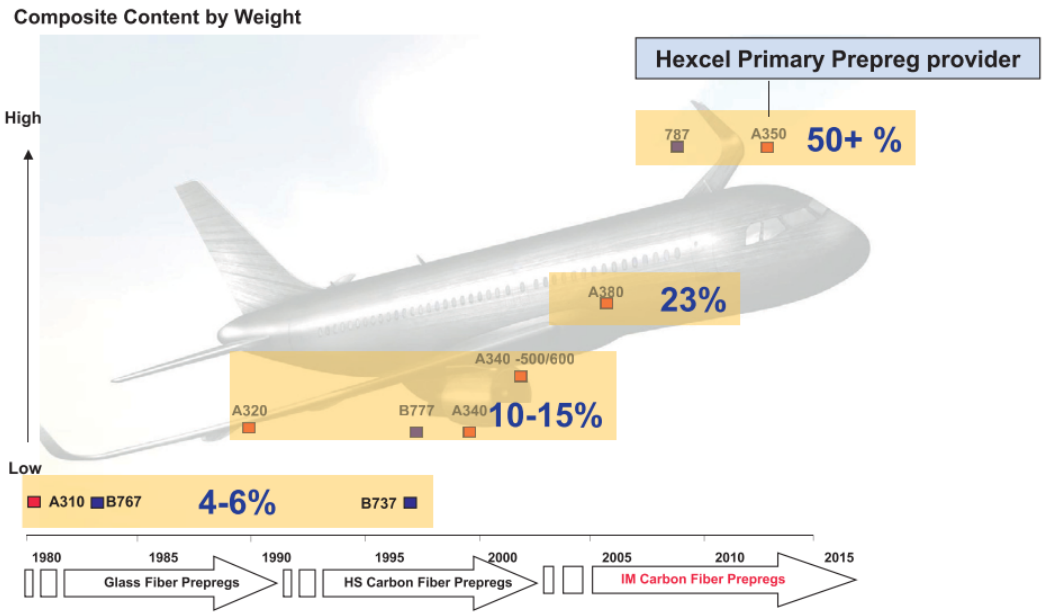

Figure 1: Use of composite materials in commercial aircraft [1].

They also withstand comparable loads better than certain aluminum especially in the highly tension-loaded environment. Their specific rigidity makes them so far the material of choice for lightening structures.

Table 1: Comparison between the properties of the main employed materials in the aerospace industry [44] - HR: High Resistance, IM: Intermediate Modulus, HM: High Modulus and UD 0° 0° is for unidirectional along the direction to fibers

Material	Density d	Tensile Modulus E UD 0° (GPA)	Tensile Strength UD 0° (MPA)	E/d
Aluminium	2.7	70	300 - 350	26
Steel	7.8	70	/	27
Titanium	4.5	120	1100	27
Epoxy - Carbon fibers (HR)	1.6	143	2000	89
Epoxy - Carbon fibers (IM)	1.6	174	2400	108
Epoxy - Carbon fibers (HM)	1.7	320	2000	188
Epoxy - Glass fibers 55% V_f	2	25	350	12.5

The composite material used in this research work is developed from a prepreg manufactured from a thermosetting matrix named as M21. The M21 is an epoxy grade matrix filled with thermoplastic particles whose interest will be detailed after. The studied composite system is indeed a toughened prepreg with extra layers of resin as distinct interleaves between plies. The reinforcements used are long unidirectional carbon fibers. The employed composite in this work, is a high performance aerospace-grade material reproduced by Hexcel which is commonly used in developing aeronautical structures by AIRBUS. The most used thermosetting polymers in the aviation sector are epoxy resins. During the late 1970s, carbon

reinforced epoxy composites were incorporated in secondary structures of the A300B1 [50]. Most recently, the fuselage of the Boeing 787 Dreamliner was based on an epoxy resin as well as the manufacturing of the primary structures of the A350 XWB [1,50]. They have come to dominate the market due to their high-performance with good mechanical properties, their high compatibility and wettability with carbon fibers plus to their design versatility with a variety of processing methods. Indeed, they have become the matrix of choice for high performance composites for use in highly demanding environments.

Due to their complexity and high anisotropy, composite materials are complicated to process. While thermoplastic-based systems are increasingly used, thanks, in part, to their processing and reshaping flexibility, thermoset based materials are still widely used for aeronautical primary structure parts. During the processing of thermosetting composites, the material undergoes several multi-physical phenomena throughout all the process stages. Quality of the final part is largely influenced by the manufacturing procedure. In most cases, the interplay of these multi-physical phenomena is responsible of process-induced stresses which often entail parts distortion and mechanical properties degradation. Often the magnitude of these internal stresses is consequential and ignoring them at the design stage may lead to a risky design. For aviation sector applications, dimensional stability is one of the major issues since parts geometry with tight tolerances is very required. The control of manufacturing costs for these structures continues to mobilize significant efforts as highly distorted parts are rejected entirely. Trial-and-error methods have been largely applied to compensate in certain cases the mold geometry for the expected distortions so that the composite part met the shape requirements. However, this technique involves large process parameters and generates very costly manufacturing trials and wastage even if it worked well for simple structures. For complex geometries with new generation developed materials, this approach took several iterations which highly amplify the time of production and therefore manufacturing costs. For this reason, simulations tool are required in order to predict the final geometry of composite structures. Hence, thorough understanding of the cure behavior of thermosetting composite and deep knowledge about the different phenomena involved during processing are crucial. Multitudes mechanisms have been identified to be responsible of internal stress generation and part deformations. Among these sources, thermal contraction and chemical shrinkage phenomena have a significant impact. The polymeric matrix changes from a liquid to a solid as the cure progresses which leads to important variations of its behavior accompanied by the development of the mechanical properties and cure shrinkage related to the crosslinking reaction. Due to the presence of fibers, these phenomena are often anisotropic and their intensity depends on whether it is about the resin or fiber dominated direction. Despite that several studies have been carried out on this particular subject and process models have been developed, there is still a need for more reliable direct measurements of these complex phenomena to ensure models validity. Commonly, experimental characterization of thermoset composites behavior has focused on the post gelation region due to the limitations that present some traditional testing techniques to capture the development of the material properties in the liquid state. Given the complexity that exists in the pre-gelation region, experimental tools capable of capturing the evolution of composites rheological properties and thermally or through curing induced strains are highly needed.

The work presented in this thesis has been conducted in the LTEN laboratory of Nantes (Laboratoire de Thermique et Energie de Nantes) and funded by Nantes University. The main research objective of this thesis is to contribute through new experimental strategies to a better understanding of the complex cure behavior of thermosetting composites by investigating the IMA/M21 epoxy based prepreg during the entire cure cycle. The present research is organized into five chapters. Chapter 1 gives a review of the literature on curing issues of thermosetting composites and the main multi-physical phenomena responsible of parts deformations. Then, the most employed experimental methods allowing the measurements of chemical shrinkage of thermoset composites are presented. The fourth part of this chapter is dedicated to a brief description of the consolidation phenomenon of thermoset composites in the uncured state since the compaction behavior of these materials during this stage still requires to be more elucidated. The last part of the first chapter is devoted to present the measurement methods and modeling approaches of rheological properties during the cure of thermosetting systems. The first part of chapter 2 is related to the studied prepreg material presentation. Then, the polymeric matrix thermo-chemical behavior is characterized during the cure in order to validate the most suitable kinetic model to be used in this work. Its properties, such as the coefficients of thermal expansion and cure shrinkage, are measured to be compared with the ones to be determined from the measurements on the composite. The gelation point of the matrix is also measured through a rheological characterization. The final part of this chapter is devoted to the presentation of the experimental set-up used in this research work for the characterization of the process-induced strains and the rheological behavior throughout the cure of the studied composite. Chapter 3 gives the analyses of the multi-axial measurements of the thermo-chemical deformations of the prepreg during the entire curing including the early pre-gelation stage. Chapter 4 proposes a new modeling approach that accounts for the presence of the extra interleaf layers of toughened resin within the prepreg plies in the calculation of the laminate macroscopic coefficients of thermal expansion and cure shrinkage. Finally, chapter 5 is divided into two main parts. The first part of this chapter includes two principal sections which describe the methodological experimental approach developed to characterize the rheological behavior during the cure of the studied prepreg. An analytical model is proposed in the second part of this chapter which also includes two sections in which the employed model parameters are identified from experimental data in order to give a description of the rheological properties of the material and their evolution with the degree of cure. Rheological model predictability during the curing of the studied material behavior is finally discussed.

CHAPTER 1

LITERATURE REVIEW AND OBJECTIVES

Contents

1.1 General presentation of thermosetting composites **7**
1.1.1 Reinforcements 7
1.1.2 Matrix 8
1.1.3 Prepregs 10
1.1.4 Autoclave processing of thermosetting prepregs 13
1.1.5 Physical and chemical properties of thermoset polymers 15
1.1.5.1 Gelation 15
1.1.5.2 Vitrification 15
1.2 Issues statement and scope of study **16**
1.2.1 Curing issues of thermoset composites 16
1.2.2 Multi - physical phenomena generating residual stresses and responsible of geometrical variation during composite processing . . 18
1.2.2.1 Differential thermal expansion 18
1.2.2.2 Chemical shrinkage 20
1.2.2.3 Tool - Part interaction 20
1.2.2.4 Resin flow 22
1.2.3 Synthesis and scope of study 23
1.3 Description of thermo-chemical strains measurement methods **24**
1.3.1 Volumetric measurements 24
1.3.2 Directional measurements 26
1.3.2.1 Dynamic Mechanical Analysis (DMA) 26
1.3.2.2 Thermomechanical Analysis (TMA) 27

1.3.2.3 Fiber Bragg Grating (FBG) sensors (optical fiber sensors) 29
1.3.2.4 Digital Image Correlation (DIC) 31
1.4 Consolidation phenomenon of thermosetting prepregs in the uncured state **33**
1.5 Measurement techniques and modeling approaches of rheological properties during the cure of thermosetting systems **39**
1.5.1 Experimental methods of rheological properties characterization . 40
1.5.1.1 Classical detection criteria of gel point 40
1.5.1.2 Yield stress based-approach to investigate the gelation in thermoset resins 43
1.5.1.3 Employed techniques to investigate thermoset composites rheological behavior during the cure 46
1.5.2 Modeling approaches of rheological behavior during the cure . . . 49
1.5.2.1 Rheo-kinetic models for thermosetting resins 49
1.5.2.2 Developed rheological models for thermoset composites 51
1.6 Outlines of this literature review and Objectives **53**

1.1 General presentation of thermosetting composites

A composite material can be defined as the result of the assembly of two or more non-miscible materials with different physical and chemical properties. One of them, comprises the "reinforcement" phase which is a resistant material embedded in the other constituent that represents the bonding element called "matrix" whose mechanical strength is much lower. This assembly enables to obtain better properties than those of the constituents used alone. Composites are therefore heterogeneous materials and are commonly highly anisotropic according to the reinforcement type and arrangement, which means that the mechanical properties depend on the direction in which the material is loaded. The final properties of composites depend on the characteristics of the elements that comprise it. This range of properties is due to the many possible combinations of reinforcements and matrices which results in "custom-made" materials for specific applications.

1.1.1 Reinforcements

The reinforcement is a strong material that comes in use for strengthening the composite. It contributes to the mechanical properties of the latter and will support most of the applied forces. In most cases, it is harder and stiffer than the matrix. A common type of composite includes usually fibers or particulates as reinforcement.

Particles, unlike to fibers, do not have a preferred size. In fact, they can be of various shape, size or configuration from simple spheres to complex shapes such as plates. In many cases, they are simply used as fillers to reduce the cost of composites or also with the purpose of improving certain properties of the matrix, such as stiffness, temperature resistance, electrical and thermal conductivity, corrosion resistance, shrinkage reduction, etc. Particulate composites tend to be less stiff than fiber reinforced composites but they are usually easy to process and much less expensive.

Fiber reinforcements are of various types. They can be employed as random-fibers, short fibers or long continuous fibers to reinforce the polymer matrix. Composites with continuous fibers normally have a preferred orientation and enable to have better mechanical properties when loaded through the longitudinal direction parallel to fibers. Thus, the arrangement of the fibers allows to modulate the mechanical properties of composites ranging from strongly anisotropic to isotropic materials according to certain plane direction. The main reinforcing fibers used for aeronautical structural composites are Carbon fibers (high resistance HR, intermediate modulus IM, high modulus HM), Aramid, Boron and Glass fibers. Some characteristics of these fibers are given in table 1.1. In the case of our study, we are dealing with long Carbon fibers with high performance and intermediate modulus [45]. Carbon fibers offer high stiffness and strength and can be five-times stronger than steel with low density thanks to their lightweight. They can offer many practical benefits such as good resistance to high temperatures, high chemical resistance and low thermal expansion with negative Coefficient of Thermal Expansion (CTE) along fibers direction. For these reasons they have been widely used in the manufacturing of aeronautical structural parts since they tend to give the best overall performance.

Table 1.1: Properties of reinforcing fibers used in aerospace grade composites [44].

Type of Fibers	Tensile Strength (MPA)	Tensile Modulus (GPA)	Ultimate Elongation at Failure (%)	Density	CTE along fibers direction ($10^{-6}K^{-1}$)
Carbon HR	3900	230	1.6	1.77	-0,1 to 0.3
Carbon IM	5300	300	1.8	1,78	-0.3 to -0.8
Carbon HM	3900	540	0.7	1,93	-0.8 to -1.5
Boron	3600	400	0.9	2.5	/
Aramid	3600	125	2.9	1.44	-5.2
S-Glass	4500	73	5	2.5	2

1.1.2 Matrix

The matrix constitutes the continuous phase of a composite and can be a polymer, metal, or ceramic. It has a main purpose to transmit loads to the reinforcement through shear loading at the interface. It also ensures the protection of fibers against abrasion and various environmental conditions and it enables to maintain them in the proper orientation. Besides, it allows to give the desired shape to the composite component, to maintain its geometry and to determine its surface quality. Two types of matrices are generally used for industrial applications of composites; thermosets and thermoplastics. The ones commonly used in aerospace industry are given in table 1.2. While thermoset polymers have long dominated the composites market especially in aviation thanks to their high mechanical properties among other matrices [50,51], improvements in the characteristics of thermoplastic resins are leading to an ever-increasing use. Thermoplastics usage is poised to grow more for current and future applications and are now more apparent in manufacturing advanced composites components for the aerospace industry.

Table 1.2: Properties of matrices used in aerospace grade composites [44].

Type of Matrix	Tensile Strength (MPA)	Tensile Modulus (MPA)	Ultimate Elongation at Failure (%)	Density	Glass transition Temperature Tg (°C)
Epoxy 180°C	80	3600	2.5	1.3	180
Bismaleimide	100	4100	2.4	1.3	260
Polyphenylene sulfide (PPS)	65	3800	1.6	1.35	90
Polyether Ether Ketone (PEEK)	100	3600	4.9	1.3	143

Thermosetting polymers represent a branch of polymers that undergo a chemical reaction that can be named as "curing" , which converts them into an infusible and insoluble material, due to their network formation through exchanging electrons to form new chemical bonds during the cross-linking reaction [52]. The action of heat and/or through the addition of a curing agent as catalysts and/or hardeners make it possible to initiate the chemical reaction of polymerization. This corresponds to the creation of covalent bonds between monomers

to obtain macro-molecular long chains that tend to grow gradually constituting a three-dimensional (3D) network structure as shown in figure 1.1. In this case, the crosslinks are recognized as chemical crosslinks. This reaction is therefore irreversible and it is no longer possible to melt the cured part by heating once it is polymerized. A rise in temperature can only lead to the degradation of the material which means that thermosetting resins can only be shaped once. As a result, thermoset resins have a strong and rigid structure due to their permanent networks and are rather difficult to reprocess, or recycle. However, they have outstanding mechanical properties such as their high-modulus and are very flexible for desired properties as environmental, thermal and chemical resistances because of their high cross-linking density [52, 53]. Unlike thermoset resins, thermoplastic are a specific class of polymers that do not exchange electrons and do not cross-link. They can be reheated above the melting temperature which results in better flexibility for additional processing of the same material that makes them more suitable for reshaping parts and recycling.

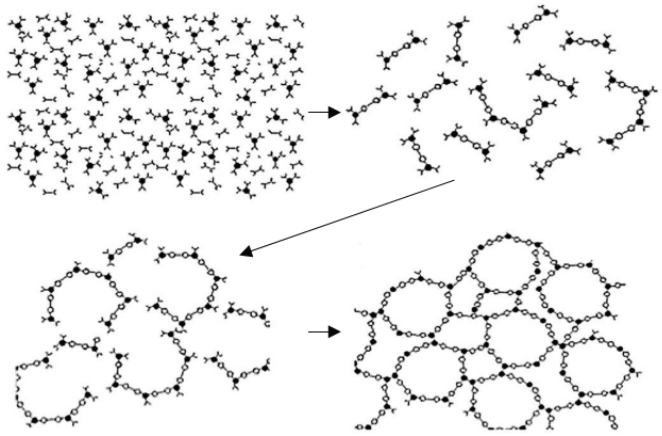

Figure 1.1: Thermoset resin polymerization mechanism from a monomer stage to a fully cured (3D) cross-linked network [2].

Toughened thermoset resins

Despite their good mechanical properties provided by the high crosslink density of the (3D) network structure, thermoset polymers suffer from poor fracture resistance since they are inherently brittle materials. Since the 1960s, efforts have been made to enhance thermoset toughness which is an important property that can be defined as the ability of a material to absorb energy and to plastically deform before fracture [52, 54]. High fracture toughness of epoxy resins is a very required property in designing parts for dynamic and structural applications where the material is submitted to encounter several mechanical shocks and vibration. Multitude strategies have been developed based on different approaches such as flexibilising the thermoset network. This was achieved by chemical modification of the resin through the introduction of more flexible chains into the network of macromolecules or the reduction in crosslink density of the network. These methods resulted however in a significant decrease in the glass transition temperature (T_g) which implied the limitation of cured resins applications at high service temperatures in view of thermal degradation issues.

Alternative solutions were developed which consist in introducing suitable fillers such as rubber, thermoplastic or rigid particles as separate phase that does not affect the bulk properties [52,55]. Nevertheless, rubber-based toughening method revealed some limitations when employed with multi-functional epoxy with high crosslink density. It leaded in some extent to decreasing the thermal stability of the material and its modulus while increasing resin viscosity and water absorption tendency. It was therefore interesting to search for more effective strategies which led to the development of thermoplastic-based toughening fillers for multi-functional epoxy resins. This technique was widely applied [52, 56–59] and allowed for significant improvement in toughness and fracture resistance without deterioration in thermo-mechanical properties of high cross-linked resins. Amorphous or crystalline high-performance ductile thermoplastic modifiers with high glass transition temperature and good thermal stability were commonly blended with epoxy resins. These thermoplastic additives can be whether soluble in the uncured resin composition or insoluble. Examples of thermoplastic particles included to epoxy resins are given in figure 1.2. We can clearly distinguish the epoxy-rich regions comparing to the second-phase thermoplastic particles where size and morphology of the latter significantly depend on the concentrations of added thermoplastic [4, 59].

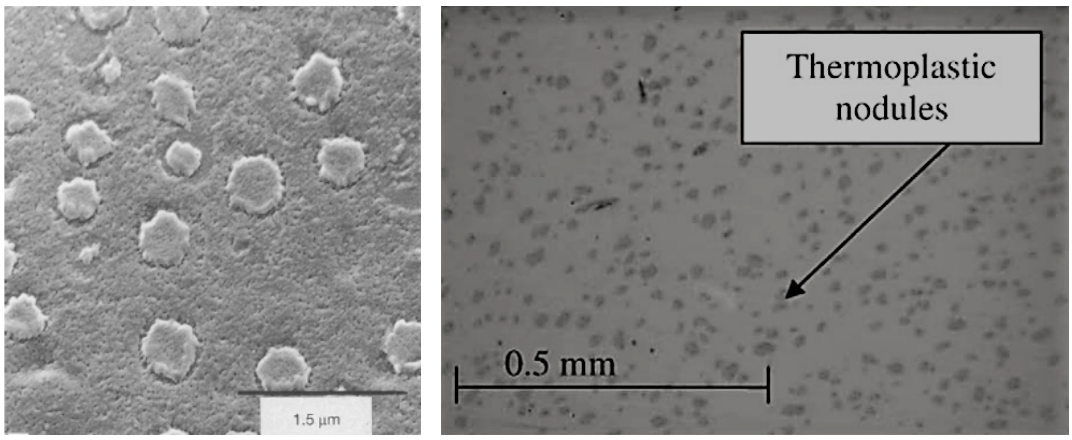

(a) [59] (b) [46]

Figure 1.2: Microstructures of toughened epoxy resin systems showing the second phase of thermoplastic-rich particles in continuous epoxy-rich matrix.

1.1.3 Prepregs

Prepregs are composite materials in which fibers are pre-impregnated with partially polymerized thermoplastic or thermoset resin matrix. The latter, generally reacts very slowly at room temperature enabling a significant work-time before curing. Prepregs are most commonly used in high-performance applications such in aerospace industries, as can be noticed from figure 1, with an exceptional interest in carbon-fiber-epoxy prepregs that have been recently more incorporated in aircraft primary structures [1].

The two most common employed procedures of thermosetting prepreg fabrication are hot melt and solvent impregnation [60]. In the solvent impregnation technique, the reinforcing material is passed through a resin solution bath and calendared to get desired resin content, and then heated to remove the solvent. Hot melt method can be proceeded in one step especially in the case of woven prepregs, or into two steps for unidirectional (UD) prepregs. The two-step hot melt process is illustrated by the schematic shown in figure 1.3. The first step consists in pre-coating a formulated resin at a controlled weight on a paper or film to produce a resin film with accurate and uniform thickness. Next, these films are impregnated during step 2 on the fiber tow and driven to infiltrate using heat and pressure. Holt melt prepreg processing enables accurate resin content control during impregnation.

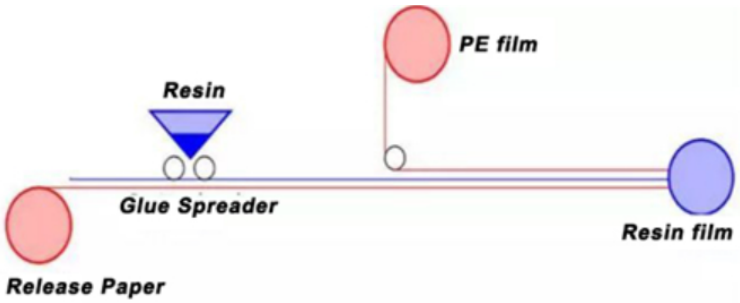

(a) Preparation of resin film

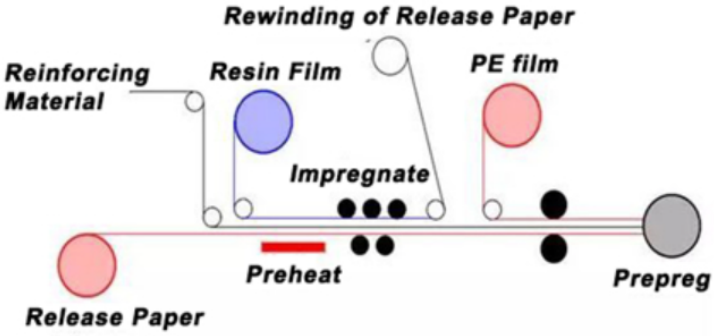

(b) Impregnation

Figure 1.3: Schematic of prepreg production by two steps hot melt process [3].

Prepregs have various advantages such as high strength-to-weight ratio, good resistance to corrosion, abrasion and allow simplified and rapid production time through the possibility of automation by draping machines. Prepregs enable a better control of fibers content in the final composite part which allow to obtain composites with high mechanical performances and to develop a wide range of aircraft components including fuselage panels, keel beam, wing and empennage [1]. Nevertheless, among the major predominant and life-limiting critical failure mechanism in these costly composite structures was found to be the issue of delamination. Inter-laminar separation in composites may develop during manufacturing due to the presence of residual stresses and it may also result from impact damage. The inherent brittleness of thermosetting matrices and thus the lack of toughness at fibre/matrix interfaces play a major role on the inter-laminar fracture of these materials and their low resistance to impact. As a result, efforts have been made over the past two decades in order

to enhance the mechanical properties of thermosetting prepregs. Hence, the development of toughened composites has had a far greater potential for overcoming the existent limitations of the current prepregs. Attempts have been made to modify the matrix toughness involving the use of thermoplastic particles. However, the resulted relative improvement in fracture toughness for composites was not as important as in the case of the bulk thermoset resin since fibers constraint reduced plastic deformation of the matrix at the crack front which resulted in poor translation of resin toughness into the composite [61]. As a consequence, the concept of interleaving of composites was introduced by American Cyanamid with the CYCOM HST-7 as their commercial product achieving improved toughness by the addition of a discrete high toughness epoxy layer on one side of the pre-impregnated material [61]. Modern prepreg systems have further introduced thermoplastic and rubber particles in the form of interleaves in between plies that achieved significant improvement in the material properties specifically in aerospace-grade carbon/epoxy composites [4, 54, 61–66]. They are commonly termed as third generation toughened prepregs. A typical scanning electron microscope (SEM) image of inter-laminar zone as distinct ply of a toughened carbon fiber/epoxy prepreg with rubber particles is given in figure 1.4. An example of micro-graphs captured through the thickness of toughened carbon/epoxy (IMA/M21) laminate with resin interlayer reinforced by thermoplastic particles are presented by figure 1.5.

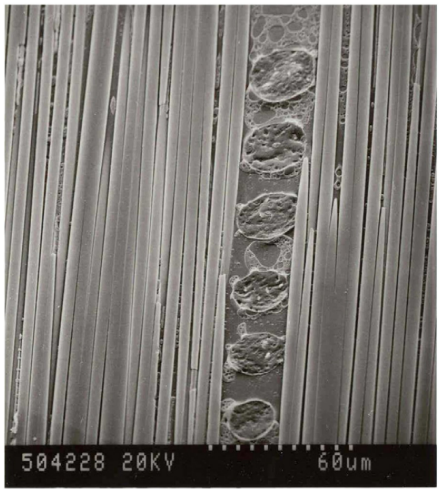

Figure 1.4: Typical inter-laminar region containing rubber particles [4].

Layers of carbon fibers are clearly represented by white color whilst the dark phases between plies represent the resin inter-layers. This method has proven to be extremely effective and it is assumed to give significant improvements of the inter-laminar fracture toughness. The interleaved system has a superior mechanical properties such as higher static strength and fatigue resistance, higher impact and delamination resistance, improvement of the matrix fracture toughness and inter-laminar shear strength [4, 61–63, 65]. There are currently a number of commercial toughened prepreg systems using interleaf layers toughening technique and have been widely introduced in manufacturing primary structures of aircraft as is the

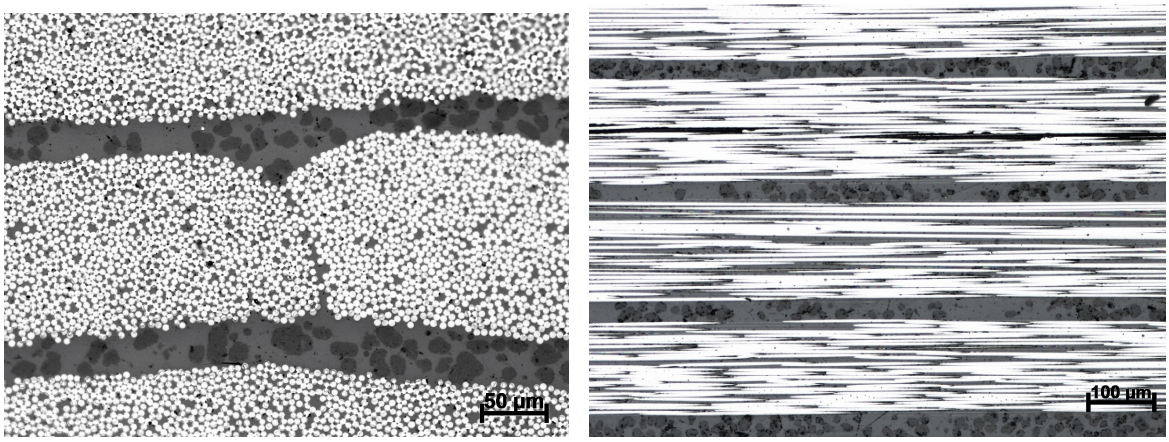

(a) Micrograph along the transeverse direction (b) Micrograph along the longitudinal direction

Figure 1.5: Morphology of IMA/M21 carbon/epoxy toughened prepreg with thermoplastic inter-laminar dispersed particles through the laminate thickness.

case of the Boeing 787 [67] supplied by Toray industries or the Airbus A350 [1] employing the HexPly IMA/M21E prepreg which is similar to the material used in this research work supplied by Hexcel.

1.1.4 Autoclave processing of thermosetting prepregs

Prepregs can be processed in different ways and the selection of the appropriate method can be influenced by multiple parameters including the particular application, matrix type, composite part size, cost and the quality of final parts performance requirements [60]. The most common techniques of thermosetting prepregs processing comprise forming with the use of autoclave, compression molding or more recently flexible vacuum bag oven or Out-of-Autoclav (OOA) processing that has become increasingly popular [60, 68, 69]. Autoclave-assisted prepreg is one of the most important fabricating process of high performance aerospace-grade materials because of the quality and lightness of the obtained component with high fiber volume and low void contents despite the high cost. Composite parts manufacturing from thermoset prepreg using autoclave process relies on the basic steps summarized briefly below:

- Prepreg lay-up: this step consists in stacking thin layers of prepreg to form a component of desired shape. Stacked laminate can be laid up by hand or machined onto a mold surface according to Automatic Tape Laying (ATL) technique which is suitable for large, low to medium curvature monolithic parts, or Automatic Fibre Placement (AFP) method for narrow unidirectional prepreg tapes that is more appropriate for medium to large complex curvature monolithic parts [68].

- Vacuum bag lay-up: After the layup is complete, the structure is covered with various layers, as can be noticed from the illustration in figure 1.6, placed in the vacuum bag and sealed. Vacuum bag processing is applied to encourage evacuating the entrapped

air from the layup with a consolidation pressure of up to 1 atmosphere. Vacuum bag debulking is typically performed at room temperature or at a slightly elevated temperature. The component of the vacuum bag lay-up are ideal for high quality aerospace parts [5,60,68]. In fact, the bleeder layer entails to achieving composites of known fiber volume by absorbing excess of the matrix. The breathers provide a path for removal of air and volatile from the whole assembly during cure.

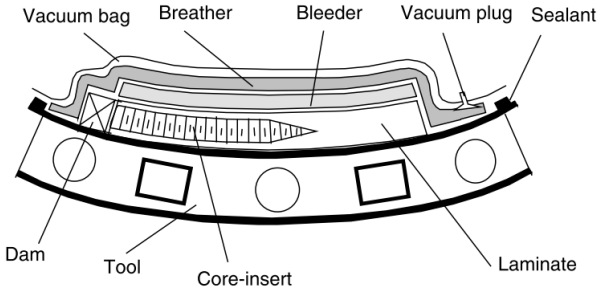

Figure 1.6: Example of vacuum bag lay-up components for autoclave curing [5].

- Autoclave curing: The consolidation of prepreg during curing requires high temperature/pressure cycles. During this stage, the tool–laminate assembly is placed in autoclave, as illustrated by figure 1.7, and the bag is connected to the vacuum system.

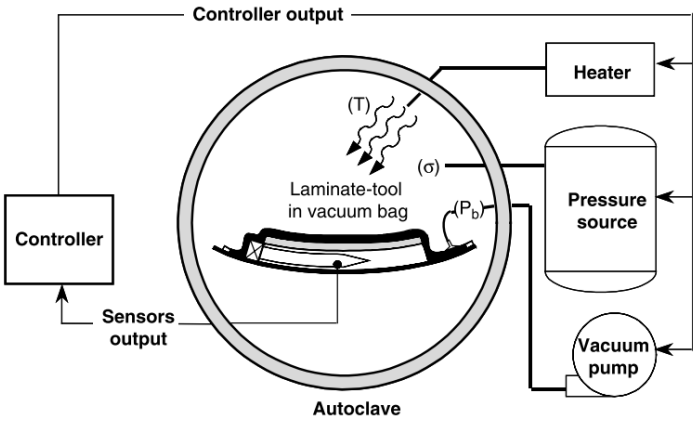

Figure 1.7: Typical autoclave processing system [5].

Autoclave processing cure relies on high consolidation pressure (0.3 - 0.8 MPa) to prevent void nucleation and growth. Usually, nitrogen or carbon dioxide is used to pressurize the autoclave. The assembly is heated to typically 120-180°C depending on the thermosetting matrix system to trigger the polymerization reaction. The heating system is either electrical or based on a gas-fired heat exchanger [5,60]. Consolidation of prepregs in autoclave process improves full resin saturation which significantly reduces dry spots and other defects arising from insufficient resin flow. This leads to achieve most desired performance and to contribute to the production of a high-quality, low-defected parts.

1.1.5 Physical and chemical properties of thermoset polymers

1.1.5.1 Gelation

During processing, thermosetting polymers undergo several physico-chemical phase transitions. The so-called gelation phenomenon in the case of thermoset systems results from the cross-linking reaction. It is considered as a chemical gelling mechanism since it is formed due to branched networks made of linear flexible chains attached by covalent bonds [70]. The structural transformation during gelation characterized by the formation of the (3D) molecular network is a characteristic stage of the polymerization reaction which leads to irreversible changes in the physical properties. During the latter, the resin behavior is assumed to transform from a viscous liquid to a rubbery viscoelastic solid behavior and eventually a glassy solid at a critical extent of reaction. The gelation phenomenon is classically assumed to take place at a precise moment of the cross-linking process, called gel time that corresponds to a specific advancement of cure degree commonly denoted as α_{gel} (see figure 1.8) [5, 71, 72]. This transition is associated with an increase of the resin mechanical properties like the viscosity which tends to infinite values once the material reached the gel point and an increase of the effective elastic modulus by several orders of magnitude. Chemical shrinkage is an other macroscopic consequence of gelation that can be referred to a decrease in the free space occupied by the polymer molecules and an increase in density that occur during polymerization.

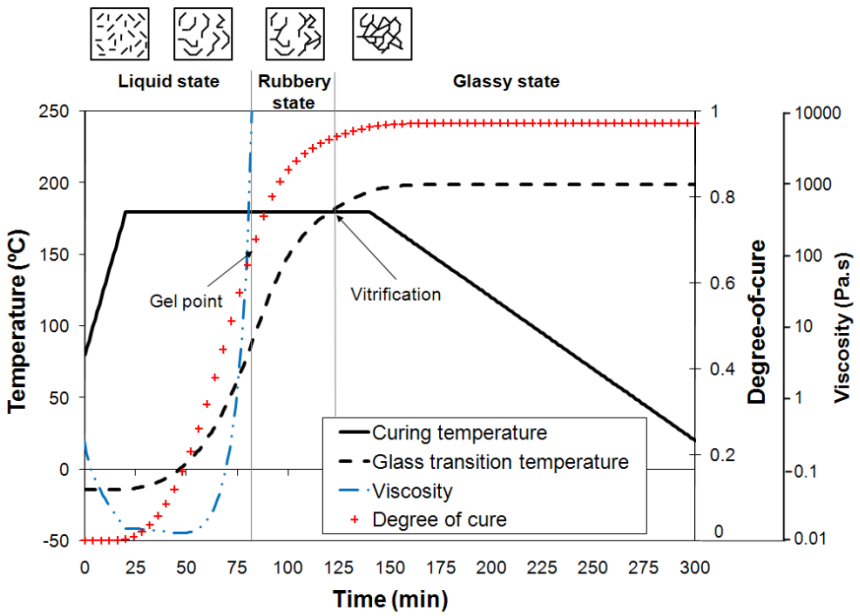

Figure 1.8: RTM Epoxy resin properties development and state transition during a typical cure cycle [6].

1.1.5.2 Vitrification

The glass transition temperature represents a phase change of the material and has an important influence on the reaction kinetic of thermosetting systems. It marks the temperature below which a material exhibits properties typical of a glass. During the cure of thermoset

polymers, the glass transition temperature (T_g) increases from the initial value that corresponds to the uncured monomer denoted as T_{g0} to $T_{g\infty}$ of the fully cured material [73–75]. Vitrification occurs when the glass transition increases and becomes equal to the temperature of cure (see figure 1.8). The vitrification time reveals the resin transformation from a rubber to a gelled glass (if gelation has occurred) or from a liquid to an ungelled glass (if gelation has not occurred). The occurrence of the vitrification phenomenon results in the cessation of the crosslinking reaction since the resin eventually solidifies and the reaction generally becomes diffusion controlled. Further resin reaction can take place if it is triggered by temperature cure increase. If the cure temperature exceeds the $T_{g\infty}$, thermal degradation may occur and the resin will be submitted to important reduction in most physical properties.

1.2 Issues statement and scope of study

1.2.1 Curing issues of thermoset composites

As described previously, during the processing of thermoset prepregs under prescribed curing cycles with controlled temperature, pressure and vacuum, the material undergoes several multi-physical phenomena throughout all the process stages including layup, consolidation and curing. Quality of the final composite components is largely influenced by the manufacturing procedure. The most challenging factor, for high performance composite manufacturing in aviation sector, is the ability to produce composite structures with high mechanical properties and stable geometries that match the required tight tolerances. Therefore, it is crucial to properly investigate the effect of manufacturing process on their mechanical behavior to provide a good understanding of the different aspects and phenomena responsible of the unexpected occurrence of defects of these costly high-performance composite parts. A good example, is residual stresses that exist with the absence of any external loads and develop during the processing of these materials, which often entail dimensional changes and generate shape distortions. Aside from geometric deviations, they have played an important role on reducing mechanical properties like low resistance to crack propagation and increasing delamination in produced laminate structures [7–9, 76–78]. Most notable shape distortions triggered by residual stresses can be summarized into, spring-in, warpage and fiber waviness defects that can be observed more clearly in the case of laminate structures [8, 10, 78, 79]. Particularly, flat thin laminates have been reported to exhibit large deformation during processing inducing extremely large curvatures defined by warpage defect as can be found in figure 1.9.

Cure-induced waviness has been widely inspected, particularly, in UD laminates in which fibers deviate from the mean direction of laminate to create wavy patterns usually in the in-plane direction as can be observed from figures 1.10a and 1.10b. Fibers waviness has been proven to significantly influence the strength of the component by decreasing the material compressive strength which further contributes to the degradation of the overall part quality.

Trial-and-error methods have been largely applied to compensate the mold geometry for the expected distortions like warpage and spring-in defects. However this technique involves numerous process parameters and generates very costly manufacturing trials and wastage.

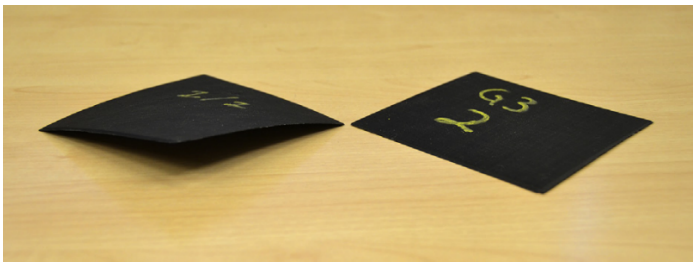

Figure 1.9: Geometric deviation named as "warpage "generated due to the induced residual stresses in flat laminates [7].

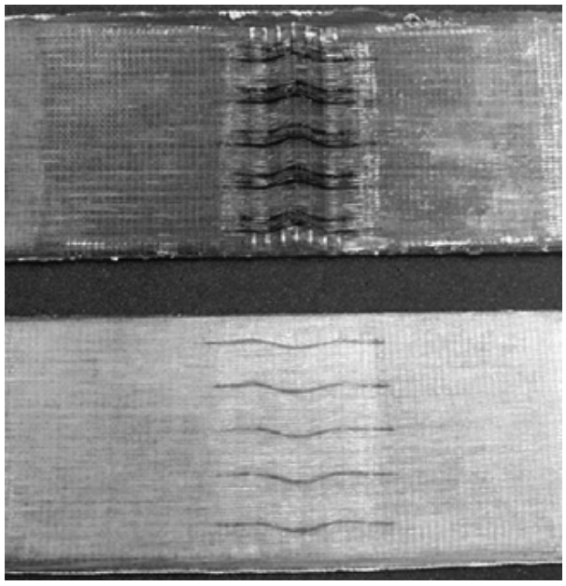

(a) Glass/Epoxy laminate [8]

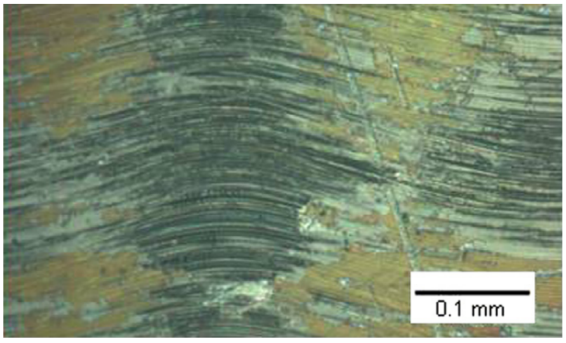

(b) UD laminate reinforced with carbon fibers [77]

Figure 1.10: Micrograph of composite laminates showing in-plane fiber waviness.

For this reason, models and simulations come in handy to predict the cure behavior of thermosetting materials during processing and therefore costs of mold manufacturing can be minimized by avoiding trial-and-error strategies. However, in order to accurately predict how these shape distortions would develop, a good description of the behavior of composite materials is quite required to allow to calculate the mechanical states induced during part

manufacturing. Besides, in order to get the best out of such costly materials, it becomes necessary to understand and identify the different reasons behind residual stresses generation. They can arise from several reasons and they can be generated on the macroscopic scale as well as on the microscopic scale. Multitudes multi-physical phenomena have been identified to be responsible of internal stress generation during cure and part distortions. Thermal anisotropy, chemical shrinkage of the resin, resin flow, consolidation, fiber volume fraction gradients, gradients in temperature and the degree of cure, moisture absorption and tool–part interaction are among the most important mechanisms affecting the stress creation during curing [7–9,78]. Residual stresses that develop at the macro-scale, like the anisotropic behavior of individual plies and tooling interaction with the material, are assumed to have the most significant impact on part deformations [78]. Moreover, as the thermoset system transforms during the cure from a liquid to a solid, the mechanical properties also develop. The evolution of the mechanical behavior through curing significantly affects the internal stresses evolution which depends on the viscoelastic properties of the resin as cure progresses [2,80,81]. Some of the most fundamental sources of shape deformation induced from internal stresses will be described below.

1.2.2 Multi - physical phenomena generating residual stresses and responsible of geometrical variation during composite processing

As we have seen above, many phenomena can be responsible of geometrical deformations during the manufacturing of composite parts. This subsection aims at presenting these multi-physical mechanisms.

1.2.2.1 Differential thermal expansion

During thermosetting systems' curing in autoclave, composite parts are subjected to strong variations in temperature in accordance with the thermal cure cycle's different stages of heating/cooling. The thermal expansion and contraction phenomena of fibers are very low in composites in comparison with the matrix. Particularly, carbon fibers used in high-performance composites usually exhibit an orthotropic behavior with a very small CTE in the transverse direction (in the range of 5 $10^{-6}K^{-1}$) and a slightly negative CTE along the longitudinal direction (in the range of -0.4 $10^{-6}K^{-1}$ for IM7 fibers) [82–84]. Nevertheless, thermoset resins, notably epoxy systems, have a CTE more than ten times higher in the case of M21 resins. This thermal expansion differential is a source of residual stress generation in both the microscopic and macroscopic scales. On the micro-scale, this difference of CTE between fibers and matrix does not cause any macroscopic distortions, whereas, it can affect the mechanical behavior and be source of failure [78,82]. However, on a ply-to-ply scale in composite laminates, residual stresses are built up with a much higher impact on shape distortions. In fact, micro-scale differential thermal expansion triggers a much larger thermal expansion in the transverse direction of a unidirectional ply than in the fibers direction. Thus, during cool-down step throughout the thermal cure cycle, the induced thermal deformation of one layer is rather constrained by other layers with different reinforcement orientations especially when 90° and 0° plies are cured together. This generates plies under tension and compres-

sion. Consequently, curvature of flat plate laminate at demoulding can be expected, known as warpage deformation, when the lay-up is balanced but unsymmetrical as illustrated by figure 1.11 [8, 78].

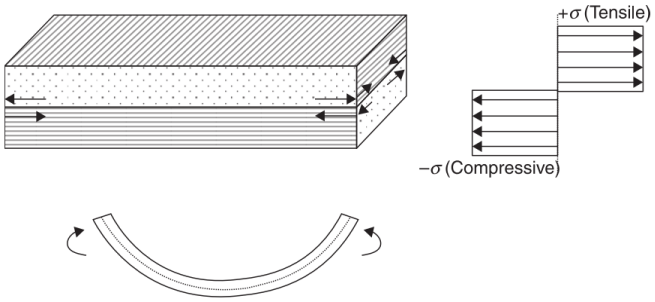

Figure 1.11: Schematic view of thermal deformation induced in laminates during cooling down due to differential thermal expansion [8].

In the case of curved laminates, thermal anisotropy plays a major role in the distortion of these geometries for any lay-up even with a symmetric and balanced stacked plies. Since CTE of the laminate is greater in the thickness direction (matrix dominated) compared with the strains and CTE values in arc length along fibers direction, a modification in the angles of the curved zones occurs with temperature change. This results in the well known spring-in phenomenon illustrated by figure 1.12 when the curved part is cooled-down [9, 78, 85, 86]. This distortion does not take place in the case of isotropic materials since thermal expansion/ contraction are uniform and thus, the angle is preserved, nor does it occur in flat plate laminates.

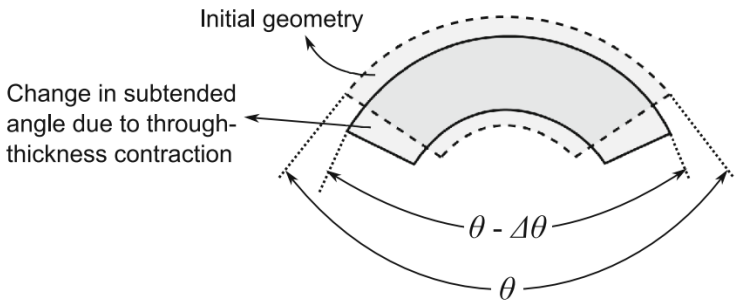

Figure 1.12: A reduction in enclosed angle eta due to contraction resulting in the well-known spring-in deformation pattern [9].

Nelson and Cairns [85] were the firsts to propose a relation that allows to estimate the magnitude of spring-in angle, $\Delta\theta$ by,

$$\Delta\theta = \theta \left[\frac{(CTE_I - CTE_T) \cdot \Delta T}{1 + CTE_T \cdot \Delta T} \right] \tag{1.1}$$

which is the result of residual stresses that develop during cool-down step, when the laminate is fully cured, with θ that represents the initial subtended angle of the part, ΔT is the temperature change, CTE_I and CTE_T are the coefficients of thermal expansion along the

in-plane (circumferential) direction and the out-of-plane (radial) direction, respectively. Note that, such phenomenon was found to be highly dependent on the material state. Indeed, the CTE of a thermoset resin is approximately 3-4 times [46] larger in the rubbery state (above the glass transition temperature) than the CTE value in the glassy state. Hence, the spring-in deformation was found to be much higher after cooling a material in its rubbery state which caused samples to shrink more in comparison with the glassy state [87].

1.2.2.2 Chemical shrinkage

As mentioned in the previous paragraph, chemical shrinkage of thermoset resins is an inherent phenomenon to the matrix polymerization. Due to the chemical cross-linking, covalent bonds are developed and a highly cross-linked resin network of polymer chains is formed which increases the density and reduces the volume of the matrix. This phenomenon ceases as soon as the matrix is fully cross-linked or when vitrification takes place. In contrast to the resin, fibers exhibit no chemical shrinkage. The amount of composite shrinkage during cure varies according to the structure anisotropy. In UD laminates, the amount of shrinkage through the thickness direction (matrix dominated) is generally much larger than shrinkage strains along fibers dominated direction. The anisotropy of chemical shrinkage can cause similar effects to thermal contraction at the micromechanical level, on the lamina-level and at the macroscopic scale. Cure shrinkage has also a significant contribution to the spring-in deformation for curved parts and was commonly treated in the same way as thermal contraction [88–90] by including an additional cure shrinkage term into equation 1.1 suggested by Radford and Rennick [86] as follows

$$\Delta\theta = \theta \left[\frac{(CTE_I - CTE_T) \cdot \Delta T}{1 + CTE_T \cdot \Delta T} + \frac{\varepsilon_I^{ch} - \varepsilon_T^{ch}}{1 + \varepsilon_T^{ch}} \right] \tag{1.2}$$

where ε_I^{ch} is the in-plane chemical shrinkage strain and ε_T^{ch} is the through thickness chemical strain. This empiric relation is limited to relatively simple shapes and implicitly assumes that the composite is a stiff elastic material without taking in account the development of the mechanical properties on such phenomenon and with no distinction between shrinkage before and after gelation. Chemical shrinkage was also reported to be responsible of the occurrence of fiber waviness [10, 77, 91] in particular composite geometries such as T-joint shapes in the thick-walled areas as presented in figure 1.13.

1.2.2.3 Tool - Part interaction

Tool part interaction phenomenon is considered as an extrinsic source of residual stresses and shape deformations. Composite parts are generally manufactured on metal tooling, taking the example of manufacturing process of a thermoset flat plate depicted in figure 1.14. During heating up, the tool plate expands and tends to stretch the part which induces tension stresses in the latter through friction/bonding due to the mishmash in their respective CTEs [7, 9, 78]. Shear interaction takes place at the tool-part interface. Some of the stress is relieved during the first stages of cure when the matrix is not cured yet through inter-ply slippage [7]. Gradients of in-plane stresses through the thickness of the part can arise and remain locked in the material during the cure progress since the non-interacting regions with

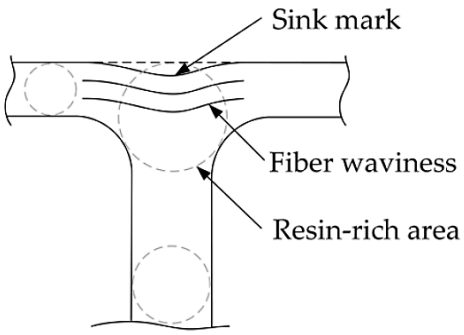

Figure 1.13: Fiber waviness induced by chemical shrinkage in resin-rich areas (e.g., T-joints) [10].

the tool are not submitted to shear interactions (see figure 1.14-b). Upon demoulding, some of the residual stresses are released and the formation of compressive residual stresses occurs inducing bending which leads to warpage in the case of flat plates (see figure 1.14-c) and large modification of angles in parts with corner sections [9,88] (see figure 1.15). Additionally, part-tool CTE mismatch and induced tool constraining have been reported to be among the most affecting sources that can cause fiber waviness in composite parts [8, 10, 77].

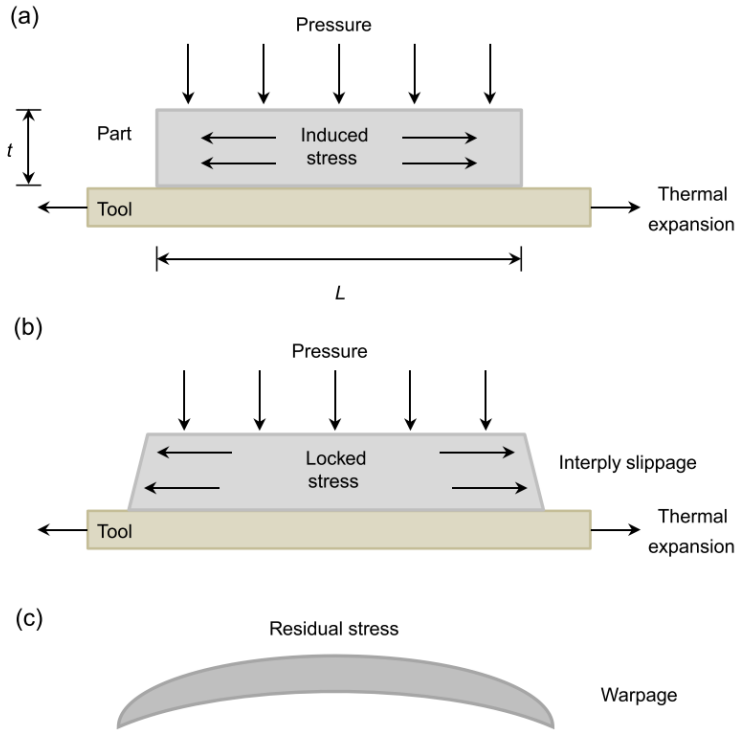

Figure 1.14: Effect of tool–part interaction on distortion of a flat part [7].

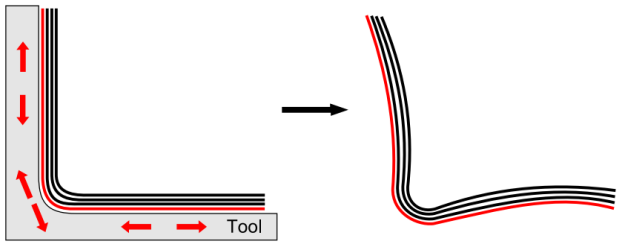

Figure 1.15: Effect of tool–part interaction on distortion of a part with curved sections [9].

1.2.2.4 Resin flow

During autoclave processing of thermoset composites, resin viscosity undergoes various transitions in line with the different steps of curing cycle. As schematically shown in figure 1.16, during a typical autoclave curing cycle, the resin goes through low viscosity states while the temperature is raised up to an intermediate level (denoted as stage 3) allowing it to flow and making it easier for trapped air and volatile to escape and to enhance the consolidation of plies. Within cure progress, resin viscosity increases significantly and rapidly through gelation and then reaches higher values during the isotherm cure as most of the resin has already cross-linked [11].

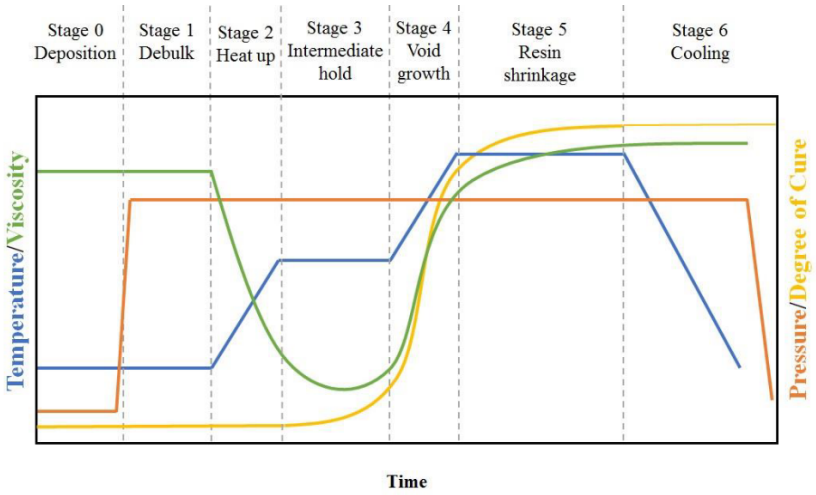

Figure 1.16: Schematic of different stages in a typical autoclave process cycle [11].

Resin flow in laminate structures has been widely investigated and assumed to be a critical parameter to control in composite processing. It can affect the distribution of fibers and hence fiber volume fraction which definitely has an important impact on the mechanical properties of the material. Resin flow through a laminate can also generate resin rich/ poor regions within the part and was considered as an other aspect among the multipyhsical sources affecting final dimensions of parts [9, 10, 92, 93]. In the case of flat composite components processing, resin rich/ poor regions are often formed due to resin movements along the thickness direction of the laminate through which it generates fiber volume fraction gradient. As presented in figure 1.17, resin rich regions are formed near to the tool plate while resin

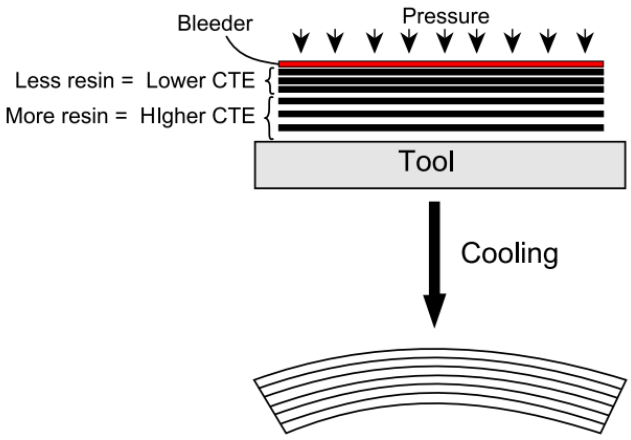

Figure 1.17: Effect of resin flow on the warpage in flat laminates [9].

poor regions are located on the upper side of the laminate. Hence, the laminate behavior becomes unsymmetrical with low CTE on the upper side due to low fiber fraction in contrast to much higher CTE in resin region area, which creates warpage of the flat parts during cooling down.

1.2.3 Synthesis and scope of study

As described in previous subsection, process-induced stresses often make it very challenging to achieve the specified dimensions of composite parts. In most cases, there exists an interplay of coupled multi-physical phenomena to be responsible of part distortions such as the example of spring-in deformation in curved geometries. Thermal-induced residual stresses in addition to internal stresses that arise due to the chemical shrinkage of the polymer matrix, named as the curing residual stresses, are among the most affecting mechanisms of shape distortions in composites. Controlling these stresses requires a deep understanding of their developing process within fiber-reinforced composite-laminates and accurate estimation of their magnitude. However, their measurement and modeling still present several scientific and technical issues that still need to be settled.

In order to determine the residual stresses, analytical, numerical, and experimental approaches have been applied. There exist many types of prominent works that have employed analytical or numerical approaches based on elastic behavior models for residual stresses calculation [94–96]. They commonly assumed that the majority of residual stresses are generated during the cool-down and the prediction of these stresses is based on considering the material as thermo-elastic without taking into account the chemical shrinkage of the matrix. Nevertheless, nearly all used composites exhibit some viscoelastic properties. There have been a number of studies that developed alternative methods for assessing residual stresses considering linear viscoelasticity to overcome elastic behavior models limitations [97, 98] (more recent studies are reviewed in [99]). As an example, it was reported by Harper and Weitsman [98], that by taking into account the viscoelastic relaxation of the epoxy matrix, residual stresses were reduced by about 20% and estimated curvature of the studied laminate plates

was rather overestimated according to the elasticity analysis. Although applied linear viscoelastic approaches were able to better predict residual stresses and part curvature, they only focused on the cooling stage of the curing cycle and do not accurately reflect the actual material behavior since anisotropic thermo-rheological models require extensive long calculation times. Modeling the whole cure cycle has been limited in the literature and relatively few works have considered chemical shrinkage and thermal expansion in residual stresses calculation [99]. Studies interested in analyzing residual stresses related to spring-forward phenomenon in L-shaped parts [100,101] based on thermo-chemo-viscoelastic models proved the importance of modeling gelation and how sensitive the simulated phenomenon was to cure shrinkage, resin flow and the viscosity profile of the matrix throughout the cure which emphasizes the need to simulate the entire curing process.

However, model ability to properly simulate the response of composite materials during processing requires precise characterization of the rheological properties development with cure, which are rarely available. The nonlinear rheological behavior of the material should be explored and taking the matrix shrinkage into account in the analysis are needed to implement a model able to simulate curing deformations. Moreover, information about the CTE to account for the thermal effect and the Coefficient of Chemical Shrinkage (denoted as CCS hereafter) to characterize the cure shrinkage are of big importance to predict shape distortions. Fine measurements of these parameters are necessary since the validity of most models must be determined by experiments that allow the assessment of the accuracy of the predicted phenomena. CTE and CCS are difficult properties to measure on a reacting anisotropic composite material throughout the whole cure cycle. Indeed, several of the different tested techniques presented in the literature were conducted on pre-cured or fully cured materials to overcome some experimental limitations, the most popular will be briefly outlined in the following section 1.3 of this chapter. Next, in section 1.4, we will provide a brief description about the consolidation phenomenon of thermoset composites. Section 1.5 takes a close look at the employed methods to measure the rheological properties during the cure of thermoset resins and composites and the related modeling approaches of these properties.

1.3 Description of thermo-chemical strains measurement methods

One of the difficulties associated with composite parts distortions during manufacturing is the monitoring of thermo-chemical deformations on a reacting material. A variety of test methods have been developed to characterize these deformations in thermoset composites and are concisely summarized in this section.

1.3.1 Volumetric measurements

Chemical shrinkage of thermosetting resins has been widely characterized by several types of techniques that have been classified into volume and non-volume dilatometric methods proposed by Nawab *et al.* in a review [102]. In contrast, not many studies have been conducted on the characterization of the volumetric behavior of thermosetting composites since the

overall drawback of the employed techniques was their lack of directional measurements in such anisotropic materials. Among the most used volume dilatometric techniques, capillary-type dilatometer are the simplest ones to provide global information about the volumetric chemical behavior of isotropic thermosetting matrices. Many studies involved the use of the PvT-α mold set-up in monitoring thermal strains and chemical shrinkage during the cure of various neat thermosetting resins [46, 103] and associated composites [12]. The configuration of the PvT-α device is given in figure 1.18.

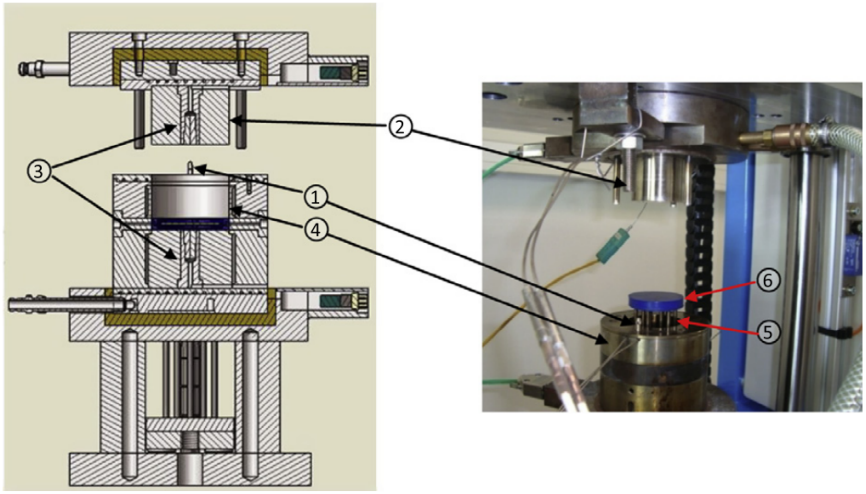

Figure 1.18: General view of PVT-α device [12]. (1) Displacement sensor (2) Piston (3) Heat flux sensors (4) Mold cavity (5) Ejectors (6) Elastomer capsule containing sample

This experimental bench is a home-built apparatus and consists of a piston (2) which is able to move in a cylindrical stainless steel cavity (4). The latter is placed between two plates of an electric press and it is designed so that heat transfers are one dimensional through the sample thickness. Before each experiment, the resin sample is infused in a low modulus elastomer capsule (6) and then placed in the PvT-α cavity under the piston. Two heat flux sensors (3) developed in our laboratory, each of them comprising three thermocouples, are embedded in the piston and the bottom of the mold. Data treatment of these sensors provide information on surfaces temperature of sample and heat flux density. The heating of the set-up is ensured by three heaters located at the top and bottom to heat the piston and cavity, respectively [12] with limited heating rates are employed in order to prevent temperature gradient along the sample thickness. The allowed temperature during cure can reach 200°C and the applied pressure can be adjustable up to 10 MPa. During the whole experiment, the position of the piston is adjusted in real time in such a manner that follows the variation of the resin volume in order to keep the applied pressure constant. The measured displacement by the piston are recorded by LVDT-type displacement sensor with a precision of 1 μm and a limit of 10 mm. The PvT-α device enables the determination of the enthalpy and degree of cure associated to the chemical reaction. It allows the estimation of the volumetric CTE at the uncured and cured state of the resin and the volumetric chemical shrinkage. Nawab *et al.* [12] studied the influence of fiber volume fraction of cross ply glass fibers/vinylester composites [0/90] on the volume chemical shrinkage in comparison with neat resin behavior, taking into account the thermal gradients effects. The volume shrinkage of the resin alone was found equal to

7.1% and evolves linearly with the degree of cure whilst the shrinkage values for composites were reduced since the volume fraction of resin was lower. Indeed, composites with 32% and 49% of fiber volume fractions reached 4.40% and 2.76% of volume shrinkage, respectively, as illustrated in figure 1.19. Although that this device and related methods proved to be useful in the case of characterization of the volumetric behavior during cure, there remains a need for more efficient techniques that can enable directional measurements of linear properties related to the thermo-chemical behavior of thermoset composites.

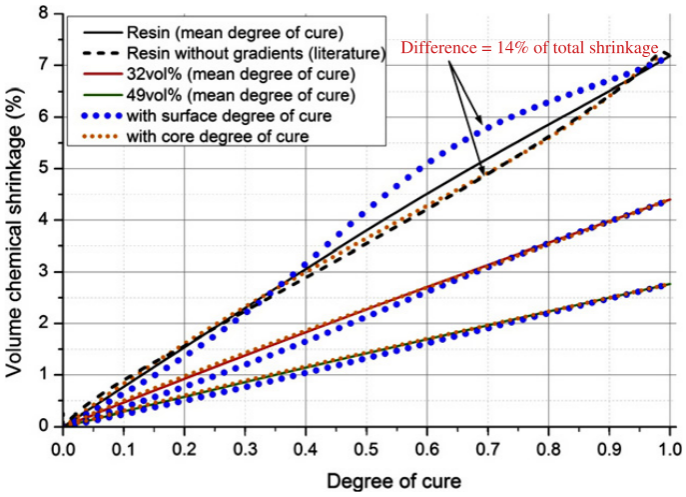

Figure 1.19: Variation of volume chemical shrinkage versus degree of cure of vinylester resin and associated composites with different fiber volume fractions [12].

1.3.2 Directional measurements

Many investigations have been conducted into evaluating potential directional techniques to measure the cure shrinkage and thermal strains in composite materials. However, these measurements are not easy to implement when dealing with a reacting thermoset material during the process. Some of the developed methods will be presented in this subsection.

1.3.2.1 Dynamic Mechanical Analysis (DMA)

Dynamic Mechanical Analysis (DMA) was employed by Ersoy and Tugutlu [13] in a compression mode test under atmospheric pressure in order to measure dimensional changes during cure of a thermosetting composite. The study was conducted on unidirectional and cross-ply samples prepared from a carbon/epoxy prepreg named as AS4/8552. Prepreg sample were firstly, partially cured in autoclave. The tested samples in DMA had 25×25 mm^2 of dimensions. Measurements of dimensional variation were conducted through the thickness directions of samples under a very small applied force of 0.1 N. The reported results of through the thickness chemical shrinkage of cross-ply (XP) and UD composite samples versus degree of cure are given in figure 1.20.

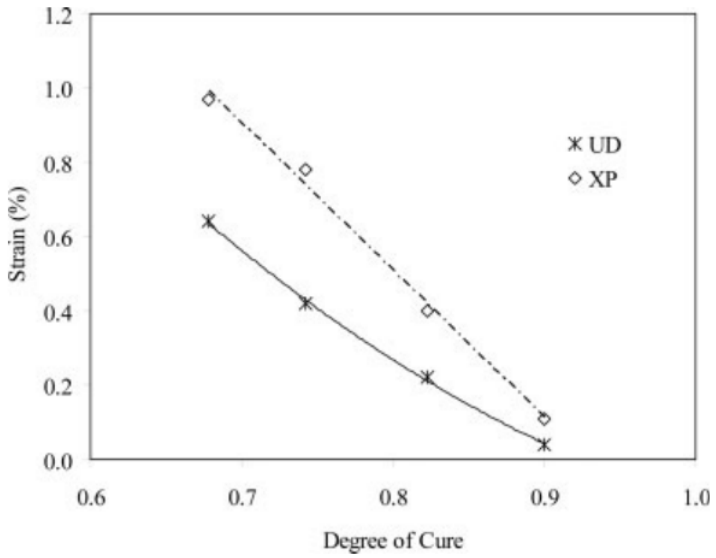

Figure 1.20: Measured through-thickness shrinkage plotted against the degree of cure related to UD and cross-ply precured samples [13].

The results showed a significant difference between measured through-thickness strains according to each stacking sequence. The cure shrinkage was doubled in the case of the XP laminates due to the constraints applied by fibers along both in-plane directions. Despite of the satisfying results, this method remains very limited to partially or totally cured prepreg samples and information on cure shrinkage are only available after the material gelation. Besides, the measurements on this setup were carried out on samples that are tested under conditions which are by no means representative of the manufacturing process.

1.3.2.2 Thermomechanical Analysis (TMA)

Studies employing TMA to characterize thermo-chemical strains on thermoset composites are scarce. Among the most prominent works, Olivier *et al.* [104] developed an original method employing TMA to determine the in-plane deformations of several stacked sequences of partly cured composite laminates. Experiments were performed without applied pressure during the cure nor vacuum. Garstka *et al.* [14] proposed the use of a similar system of a TMA which they called a video extensometer, where the prepreg samples were cured in between two heating plates as illustrated in figure 1.21. The through-thickness dimensional variations of UD and cross-ply samples made of a toughened epoxy prepreg AS4/8552 were captured by a non-interlaced camera by measuring the relative vertical motion of the steel plates.

It was possible to estimate the post-gelation cure shrinkage for both laminates (figure 1.22a). They found the average value of final shrinkage in the case of UD laminate is 0.48% and 0.98% for cross-ply samples. This method gave satisfying results about through-thickness CTE of the cross-ply laminate in the liquid and rubbery states which were equal to 373 $10^{-6}K^{-1}$ and 202 $10^{-6}K^{-1}$, respectively. Other authors [16, 105, 106] have also used TMA

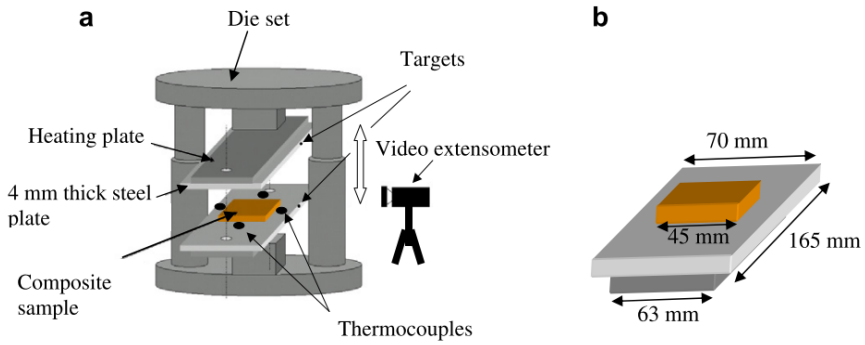

Figure 1.21: (a) Experimental bench based on (TMA) method employed for cure shrinkage measurements. (b) dimensions of the heating plates and used samples [14].

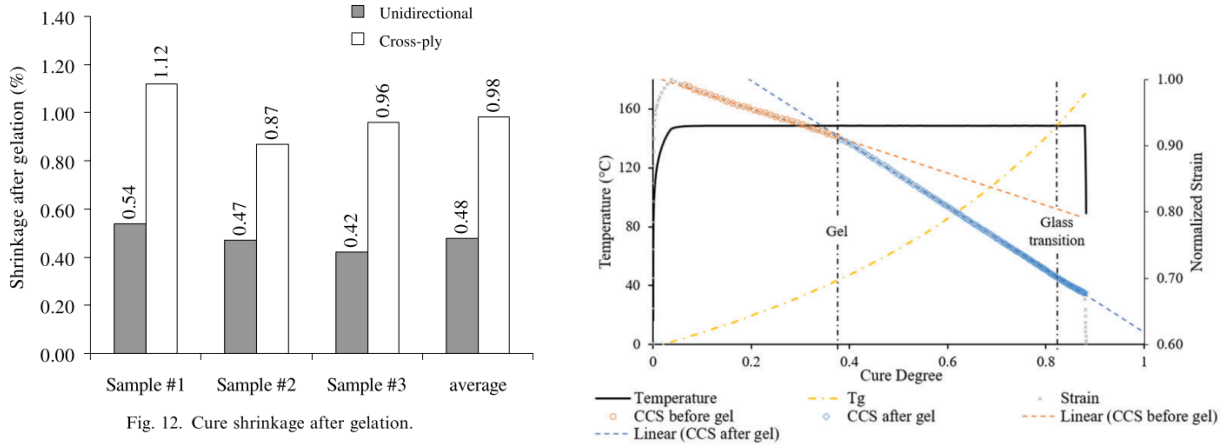

(a) (b)

Figure 1.22: (a) Measured post-gelation cure shrinkage of AS4/8552 laminates [14]. (b) Measured through-thickness chemical shrinkage of an M21EV/IMA laminate [15].

method to measure the in-plane dimensional changes due to thermal expansion/contraction and chemical shrinkage of partially cured samples. More recently Moretti *et al.* [15] developed an experimental method using TMA technique to measure the thermal and chemical strains during the cure of an M21EV/IMA prepreg. The investigation of the cure shrinkage was carried out using samples made of 16 plies cut from uncured quasi-isotropic compacted laminate dedicated to through-thickness measurements and samples of 40 plies cut from a unidirectional compacted laminate devoted to in-plane direction tests. The characterization was performed by applying an isothermal dwell during 6 hours to samples that were heated at 20°C/min from 20°C to 150°C assuming only chemical strains acted during the isotherm hold. Results about measured chemical shrinkage are gathered in figure 1.22b. Cure shrinkage evolution exhibits a linear dependency on the degree of cure with a slope change occurred at the gelation of the matrix.

1.3.2.3 Fiber Bragg Grating (FBG) sensors (optical fiber sensors)

Several studies reported the use of optical fiber sensors that have attracted considerable attention as an efficient method for in-situ monitoring of cure shrinkage and thermal expansion of complex shaped composite parts such as Distributed Optical Sensors (DOS) [107] and Fiber Bragg Grating (FBG) [17, 18, 108, 109]. They are highly sensitive and very thin with a coating diameter nearly less than 150 μm and thus can be directly placed inside the composite laminate. A FBG sensor is a single-mode optical fiber having periodic variation of the refractive index along a certain length named as grating. The grating is etched inside the fiber core by exposing the optical fiber to an interference pattern of intense ultra-violet (UV) light [17]. When light from a broadband source is transmitted into the FBG sensor, only a narrow spectral component is reflected back within the grating region that can be represented by a spectrum of wavelength as illustrated by figure 1.23a. When a FBG sensor is submitted to uniform strain along its axial direction or temperature variation, the peak wavelength shifts proportionally with the variation of these two parameters as shown in figure 1.23b. Due to this, these sensors have been used as a temperature or strain sensing element. An example of an embedded FBG sensor along the in-plane transverse direction of UD carbon/epoxy laminate is given by figure 1.24. It is clearly shown that the sensor's size is much larger than a fiber which makes them intrusive technique, even though it was assumed in some works that intrusiveness was not a problem anymore [18].

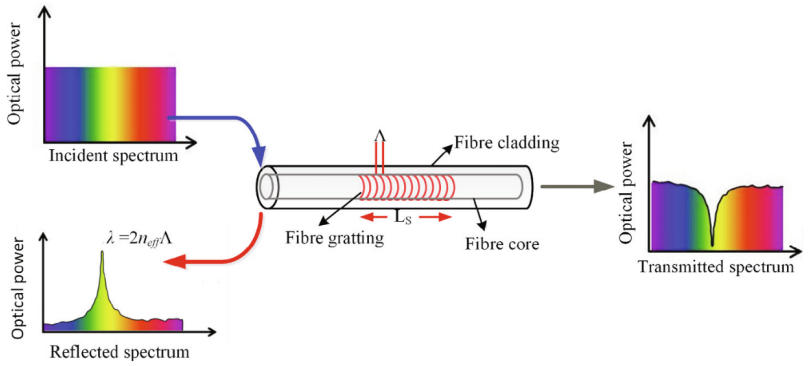

(a)

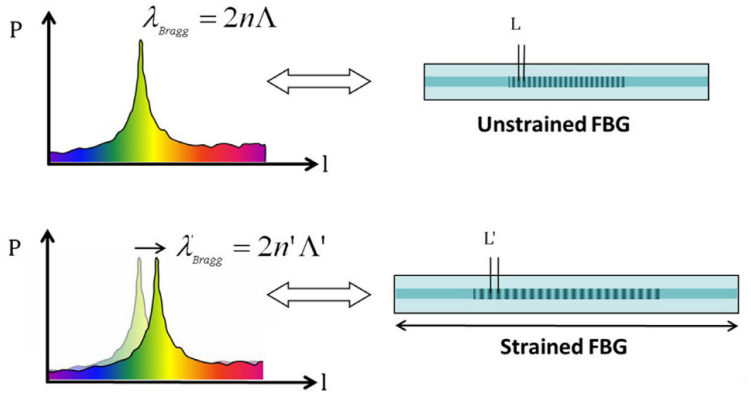

(b)

Figure 1.23: The working principle of FBG sensor [16] [17].

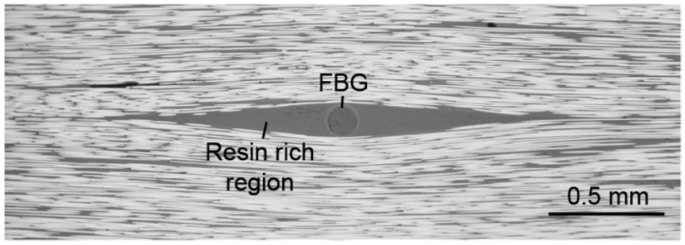

Figure 1.24: Cross-sectional micrograph of FBG sensor embedded along the in-plane transverse direction of UD laminate [18].

FBG sensors have been introduced in various applications such as the monitoring of temperature and cure-induced strain gradient in laminated composites [17], the investigation of the effect of non-uniform gelation on residual stresses in thick laminates [109] and the measurements of chemical shrinkage evolution in thermoset laminates [18, 108]. Hu *et al.* [16] employed FBG sensors as an in-situ method to capture the gel point and to measure the effective transverse chemical shrinkage development during the curing process of a UD carbon T300/Epoxy laminate in autoclave. FBG sensors were inserted at different thickness of the sample to obtain the internal temperature distribution along the thickness of the laminate. Also, FBG sensors were placed in-plane perpendicular to the fiber direction and along the thickness direction. Obtained results showed uniform distribution of temperature along the material thickness and thus assumption of uniform cure along the thickness was made. Figure 1.25a represents a uniform evolution of the obtained measured effective cure shrinkage in different positions along the thickness proving that no cure gradient occurred throughout the material thickness after gelation. The comparison between measured strain changes along both transverse directions indicated that the chemical shrinkage behavior of the studied prepreg was transverse isotropic (figure 1.25b).

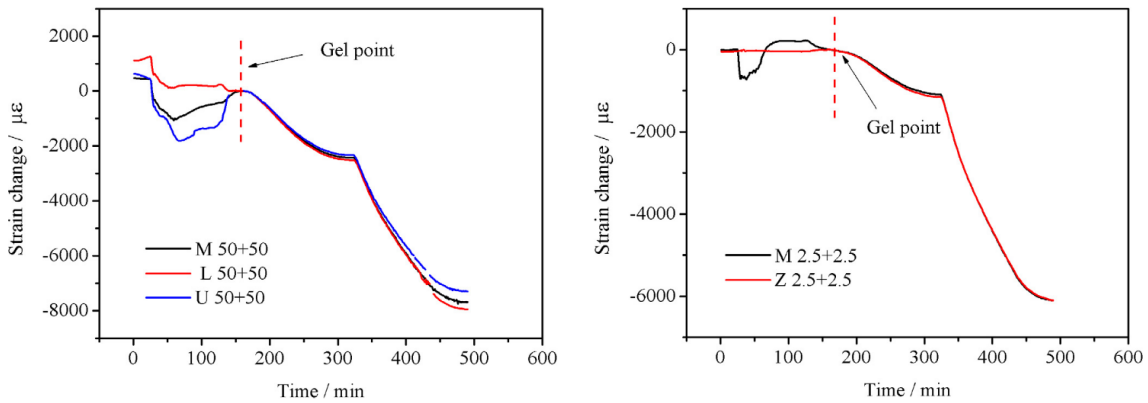

(a) (b)

Figure 1.25: (a) Strain changes at different thickness after gelation of T300/Epoxy laminate. (b) Captured effective chemical shrinkage along the in-plane and out-of plane transverse directions after gelation. [16]

The tailed FBG set proved to be a promising in-situ technique able to probe the gel point and to measure strains during the cure of thermoset prepregs with confirmed results commonly performed with TMA and DMA methods [16, 18, 110]. Unfortunately, the main drawback of this method is that the information about estimated local strains are only limited to the post-gelation stage of the curing behavior since the mechanical interlocking between the matrix and the sensor only develops after gelation.

1.3.2.4 Digital Image Correlation (DIC)

Another way to investigate cure induced thermo-chemical strains was introduced by using non-contact technique applied to polymers and composite systems termed as Digital Image Correlation or (DIC). It was developed in the early 1980's as a method for full-field optical-numerical analysis over a material surface strain under mechanical or thermal loading [111]. Recently, DIC technique has been employed for in-situ measurement of thermoset neat resin shrinkage [112–114] and monitoring of cure induced deformations in thermoset composites [19, 20, 23]. The DIC method principle is based on the comparison of a reference and a deformed speckled image by tracking random surface patterns displacement changes from the initial to the final deformed states. It also enables 2D and 3D deformation measurements. Motagi *et al.* [19] developed a new experimental approach employing DIC technique in order to analyze the processing induced strain of, a commercial epoxy resin, a carbon fiber and glass fiber composites. The approach is based on curing the material in an autoclave equipped with a borosilicate view-ports that facilitate the in-situ measurement using DIC. It includes two decent 6-megapixel cameras placed near the view-ports of the autoclave as shown in figure 1.26a.

(a)

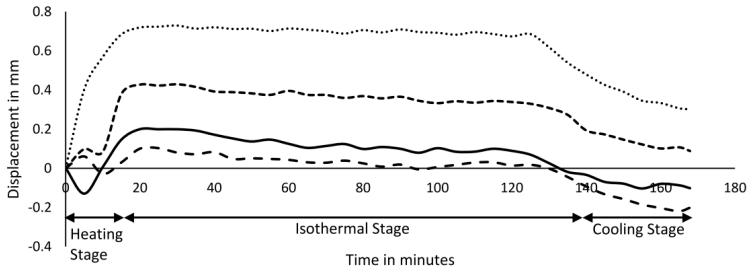

(b)

Figure 1.26: (a) DIC setup placed near the view-port of the autoclave. (b) Measured displacements along the in-plane direction of neat resin and composites samples. [19]

Before the testing, a speckle layer was sprayed on a thin layer of peel ply and introduced on the sample surface. During the curing, displacements in the speckle pattern were captured by the camera which enabled the estimation of material strains using the post-processing Vic-3D software [19]. The obtained first results were satisfying and revealed interesting information about in-plane and out-of plane transverse strains evolution during the whole curing cycle of the studied epoxy resin and related composites. The type of obtained results along the in-plane direction of the material is illustrated in figure 1.26b. Some limitations were reported like the convection effects resulting from airflow inside the autoclave, which induced some variation in measured strains due to sample movements during manufacturing.

Duffner *et al.* [20,23] suggested another way to employ DIC technique in order to investigate the induced cure deformations of thermoset composites. The experimental DIC setup consists of two digital cameras placed approximately 100 cm above the sample, as seen in figure 1.27 which are connected to a computer controlled by VIC-3D image acquisition software. Fine-tune adjustment of the camera's exposure were ensured to enable clear images of the sample during the test. 50mm × 50mm × 0.8mm UD square laminates were made of 4 plies from a UD AS4/8552 prepreg. Before the test, samples were debulked under vacuum pressure at room temperature. A speckle pattern of black and white spray paint was applied to the prepreg sample surface. Samples were cured according to the standard recommended cure cycle on a Peltier heating plate. The transverse in-plane strains were calculated by correlated Solutions DIC software. The method is based on the deformation of the speckle pattern captured through images taken every 30 seconds during the cure cycle.

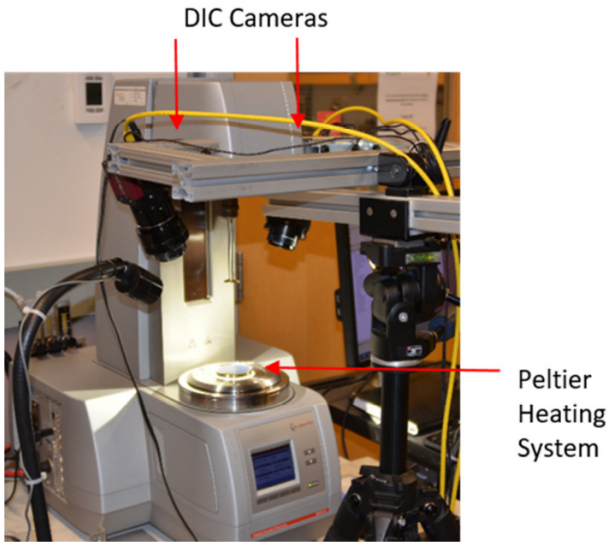

Figure 1.27: DIC experimental test setup [20].

The reported results showed the ability of the method to capture the whole curing behavior of the studied prepreg. As shown in figure 1.28a, five regions were identified according to the transverse in-plane strain evolution with temperature: (1) represents the initial expansion during the heating stage, (2) the compaction of the sample that occurred at the pre-gelation stage (will be further discussed in the next section 1.4), (4) material shrinkage

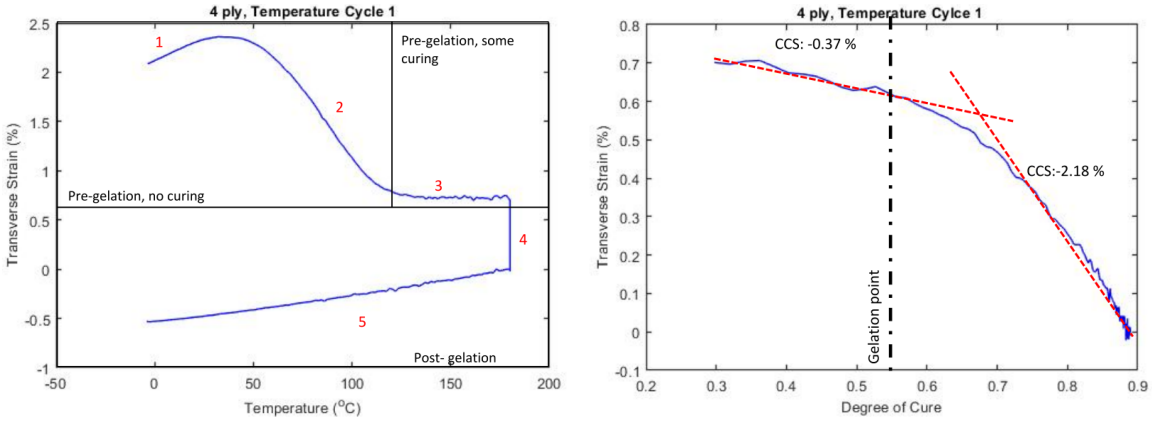

(a) (b)

Figure 1.28: (a) Measured thermo-chemical strains by DIC during the cure of 4 ply prepreg sample. (b) Estimated CCS during the isothermal cure at 180°C. [20]

during isothermal cure and (5) thermal contraction along the cool down step. The in-plane chemical shrinkage evolution with the cure degree (figure 1.28b) showed a non linear behavior with a much lower CCS equal to -0.37% before gelation compared to the estimated post gel CCS equal to -2.18%. The observed trend evolution of the chemical shrinkage with cure was attributed, by the authors, to the tool interaction with the sample. It was supposed that the latter prevents in-plane shrinkage before gelation during which the prepreg does not have any modulus. They assumed that the overall shrinkage took place along the sample thickness at pregelation stage. Despite the limitations of this method to be performed under atmospheric pressure, in addition to its restriction to the in-plane strains measurement only, it showed a satisfying ability to capture the evolution of the thermo-chemical strains throughout the whole curing of the thermoset prepreg.

1.4 Consolidation phenomenon of thermosetting prepregs in the uncured state

Consolidation phenomenon represents a key stage of composite laminates manufacturing process as it has a very significant impact on the final shape of parts and their dimensions accuracy. It plays a major role in eliminating inter- and intra-ply voids and porosity which therefore influences the mechanical performance of components. Consolidation process involves two stages according to the material state. The first one can be related to the early stages of the curing when the matrix remains a viscous fluid and the composite is no yet cured, during which the material consolidation is assumed to be mainly dominated by resin flow mechanism and voids elimination. In the second stage, the material cures and the structure solidifies. This section is rather about to provide brief description of the consolidation of thermoset composites in the uncured state. Understanding the physics that control this phenomenon is therefore of crucial importance in order to build more reliable predictive tools of dimension variation. This is notably essential when dealing with new aerospace grade

toughened prepregs. Providing in-situ multi-axial measurements of the induced compaction mechanism and/or widening throughout the consolidation phase of an uncured composite is therefore highly required. Thus, it permits to develop more accurate simulations by further understanding the existent mechanisms that drive the material consolidation. The latter is indeed influenced by multiple parameters that can be related to the cure process or the material properties. In the prediction of consolidation, several information must be provided, based on the type of process manufacturing, that include applied conditions as the applied pressure, the thermal cycle and/or vacuum, in addition to the material related parameters, like the nature of fibers, their permeability, type of lay-up, resin involved, its kinetics and the physical, thermal and mechanical properties of both fibers and matrix [115,116]. Thus, various flow and deformation mechanisms occur during the consolidation of these fiber-reinforced composites depending on the interplay of these multiple parameters which makes this phenomenon quite complicated to experimentally investigate during the early stages of cure.

In the autoclave case, cure relies on high consolidation pressure to keep the volatile species, air and moisture dissolved in the resin or compresses them to reduce void growth and prevent void nucleation. Composites are commonly treated as deformable fiber bed saturated with curing resin [117]. The compaction of the fibrous structure and the resin flow is assumed to take place simultaneously and the two phenomena thoroughly influence each other [93,118]. Most of the studies of the resin flow models are based on Darcy's law, which dictates the flow of viscous fluids through porous media [115,116,119]. As the resin viscosity drops during the early stage of the cure cycle, the flow into the fiber bed is assumed to be driven by the applied pressure gradient in the laminate ensuring the impregnation of dry areas and collapsing voids, simultaneously, fibers network compacts gradually. The compacting forces induces therefore the variation of the thickness and dimension changes of parts. Several flow and deformation mechanisms are found to be responsible factors of the compaction behavior depending on resin viscosity, but among the major ones, percolation flow (known as bleeding flow) is assumed typical for low-viscosity thermoset system, where under applied pressure the resin can escape from the ply and bleed out without shifting the fibers inducing fiber bed compaction. On the other hand, shear flow mechanism (known as squeezing flow) is mostly observed in the consolidation of thermoplastic prepregs during which the resin can push fibers transversely making the system deform as an incompressible fluid and the driving force is the deviatoric components of the applied stress [93]. The flow mechanisms determine the ability of the material to deform during autoclave consolidation. Recent works showed that new generation of toughened prepregs exhibit rather a more complex behavior during consolidation due to the presence of the thermoplastic particles [21,120,121]. Nixon *et al.* [21,120] investigated the compaction behavior of toughened prepreg as function of processing parameters like pressure, load rate, temperatures, and boundary constraints using DMA technique in addition to an Instron machine with temperature controlled hot plates. It was demonstrated that the material presents features typical to both; low-viscosity thermosets and high-viscosity thermoplastics. Both bleeding and shear flow patterns were captured along the through-thickness consolidation of the material (figure 1.29). Further experimental investigations of flow and deformation mechanisms, throughout the consolidation of these toughened composites, are still required in order to provide more accurate information of the compaction behavior and its development in the uncured state.

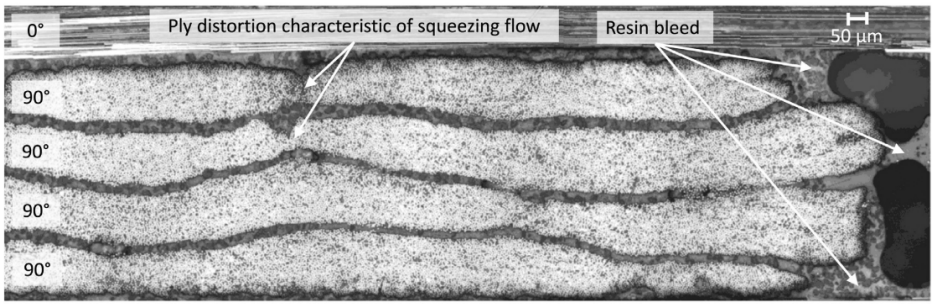

Figure 1.29: Micrograph of a sample edge made of IMA/M21 prepreg and consolidated at an isotherm of 90°C. Coexistence of both bleeding and shear flow mechanisms are observed [21].

During an out-of-Autoclave (OoA) curing process, considered of late, as an alternative even for aerospace applications, a low consolidation pressure of 1 atm is rather applied by vacuum and prepregs are vacuum bag-cured in conventional ovens. As an example, in late-generation Vacuum Bag Only (VBO) process intended for high performance applications, consolidation is considered as a three-step process consisting of coupled mechanisms: resin flow, fiber bed compaction and air evacuation [22,69]. As a consequence of low applied pressure in this type of processing and due to the need for high quality components having low porosity level, VBO prepregs are designed with a partially impregnated microstructure. The latter consists of both resin-rich and dry areas which serve as channels that facilitate the evacuation of entrapped gases in the laminate. The OoA prepreg consolidation process is illustrated schematically in figure 1.30.

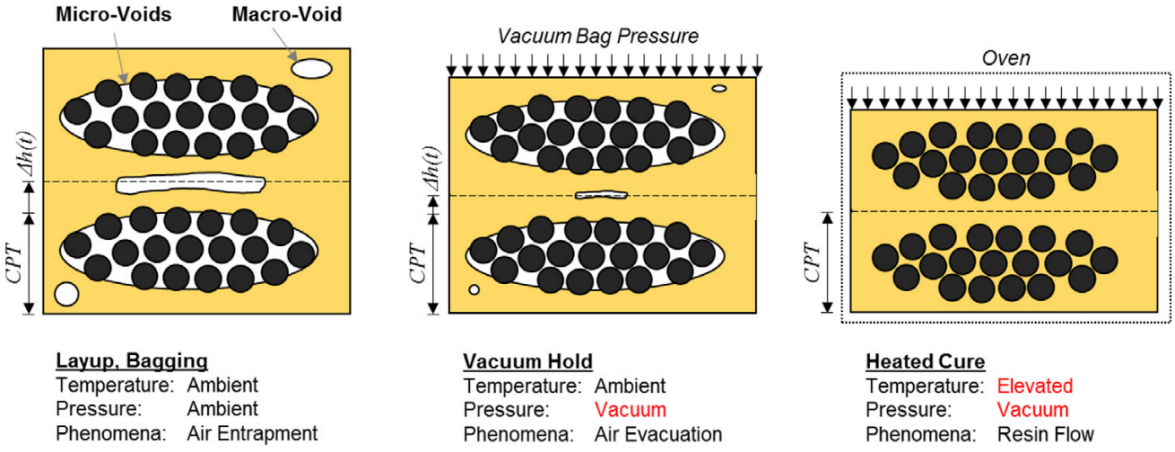

Figure 1.30: Schematic of the OoA prepreg lay-up consolidation process [22].

After lay-up, an unconsolidated laminate consists of; stacked plies that comprise fiber tows, resin rich areas that include macro-voids located within plies or around the tows and micro-voids located between individual fibers within the dry tow cores. When vacuum is applied, the gases are removed through the dry tow cores inducing a decrease in macro-voids content and fiber bed compaction. Then, when temperature is raised, the resin viscosity drops and it

gradually infiltrates the dry areas in the fiber network to produce, in the ideal case, a void-free microstructure. The flow is supposed to initially be driven by the applied atmospheric pressure through the gap between two fiber tows governed by the Darcy's law, but once the resin sufficiently impregnates the fiber bed, only capillary flow can enhance filling inside a fiber tow and complete the full laminate saturation [122–125]. The thickness of each ply is therefore reduced. The viscosity of OoA prepregs plays a major role on the compaction of the part and it has been demonstrated that it has a significant impact on flow times and fibers' impregnation which is directly correlated to the influence of the applied thermal cure cycle [22].

Differences have been reported in the thickness and fiber volume fraction when comparing in and out of an autoclave cured part which has been related in some extent to the low pressure (vacuum) applied during the processing of VBO prepregs [22, 126]. It has been proved that Void formation in VBO processes represents the principle major issue [127]. Thickness reduction evolution has been widely modeled as a means to evaluate the induced compaction and therefore to assess the consolidation and final part qualities, not only of OoA prepreg processing [128, 129] but also of autoclave-cured composites [116, 130]. However, experimental measurements of thickness reduction are scarce, notably for uncured materials and are commonly performed on partially cured samples or after curing [131–135]. Autoclave and OoA consolidations require a more thorough investigation. More quantitative experimental and prediction methods are yet needed to elucidate the complexity of the involved phenomena which will yield in more accurate simulations tools of these manufacturing processes.

A number of efforts have been undertaken to understand the effect of capillary pressure on resin infiltration for liquid composite molding processing [136–138] but to a lesser extent for prepreg processing. Researchers have seen that due to capillary pressures, in addition to the total applied pressure gradient, the microscopic flow of the resin increases in dry spots of the fiber bed in regions far from the outer surfaces of the ply. In recent studies carried out by Duffner *et al.* [20] and Zobeiry *et al.* [139], it was found that capillary pressures effect results in a reduction of the inter-ply separation at elevated temperatures in prepregs revealing the ability of the material to self-consolidate without the application of external compacting pressure. Duffner *et al.* [20] examined the influence of applied stress by performing tests on uncured prepreg plies based on toughened epoxy system under two evaluating conditions: the first, without applying external stress and the second, through employing vacuum pressure. Each pressure condition was tested at three different temperatures in order to assess the influence of different viscosities on resin flow which varies from approximately 3000 Pa.s, correlated to a testing temperature of 20°C, until 102 Pa.s, for a selected temperature equal to 80°C. The investigation consisted in examining the cross section of each uncured one-ply sample of AS4/8552 prepreg cut into $50 \times 50 \times 0.2\, mm^3$ square. Thickness variation of tested samples was observed through SEM (Scanning Electron Microscopy) analysis. Obtained SEM images are gathered in figure 1.31. The results showed that comparing to 40°C and 60°C hold, at 80°C the ply was fully saturated with resin with a lower content of voids and the thickness was significantly reduced in both conditions even when no vacuum was applied. Authors assumed that the compaction of the ply was due to the resin flow into dry regions resulting in the consolidation of the latter. They additionally supposed on the basis of the

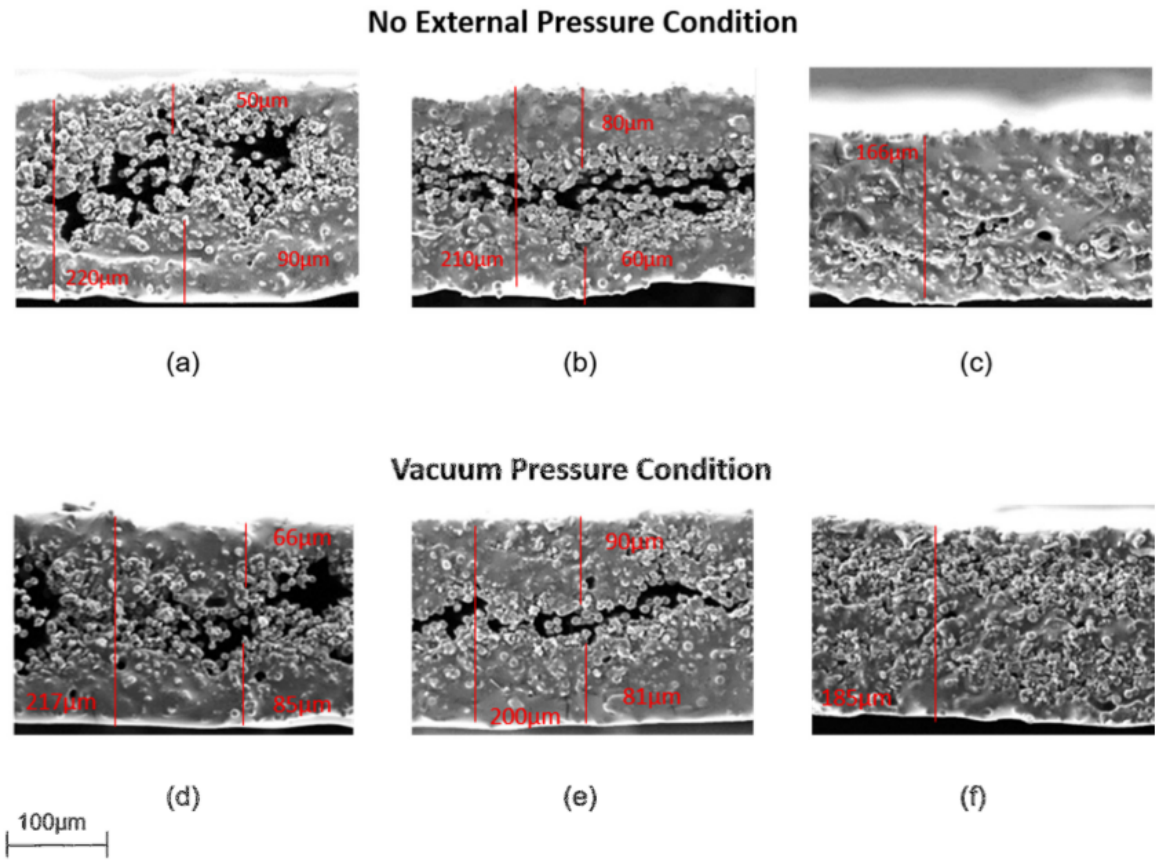

Figure 1.31: SEM images of cross-sectioned AS4/8552 samples. Condition one corresponds to no applied pressure: (a) Isotherm hold at 40°C (b) Isotherm hold at 60°C (c) Isotherm hold at 80°C. Condition two corresponds to vacuum applied pressure during heating: (d) Isotherm hold at 40°C (b) Isotherm hold at 60°C (c) Isotherm hold at 80°C [23].

SEM results, when no external stress is applied to the sample, capillary pressure, caused by the surface tension between resin and fiber, acts as the only driving force that enables resin infiltration into the fiber bed.

The developed DIC method by Duffner *et al.* [20,23] described earlier (see section 1.3) allowed to capture the same compaction phenomenon of the studied prepreg sample at the pre-gelation stage. It was observed that a significant strain drop along the transverse in-plane direction took place (denoted by region 2 on figure 1.28a) during the heating of the material. The authors suggested that the observed compaction of the 4-ply sample was related to the self-consolidation of the material which was assumed to be only induced by the effects of surface tensions and the resulting capillary pressure since there was no applied stress during the curing tests.

Garstka *et al.* [14] reported similar results when studying the cure behavior of the AS4/8552 prepreg whose experimental method (see figure 1.21) was previously described in section1.3. Obtained results of the UD laminate cure behavior evolution is given in figure 1.32. During the pre-gelation regime (t<5000s) when the resin is still a viscous fluid, a drop in strains along

the thickness direction was noticed as the temperature increased for both laminate configurations of the investigated material. As reported by the authors, no external compressive stress was additionally applied to the samples during the testing expect the atmospheric pressure. The authors attributed this behavior to the consolidation of the material declaring that no resin bleed-out took place. Three different debulking conditions before curing were tested and did not appear to eliminate this strain drop. In the first case, the sample was not pre-consolidated. The second condition consists in applying an 8 hours vacuum debulking step under 0.069 MPa at a temperature of 30°C (denoted as vac-preconsolidation according to the authors). In the third case, laminate samples were compacted under 0.074 MPa pressure when heated at a temperature of 100°C (referred as jig-preconsolidated according to the authors). The obtained results (figure 1.32) showed that the effect of debulking at higher temperature and pressure before cure induced lower thickness reduction of the laminate. This was indeed attributed to the improvement of voids migration outside the sample during debulking resulting in more consolidated laminate in the uncured state.

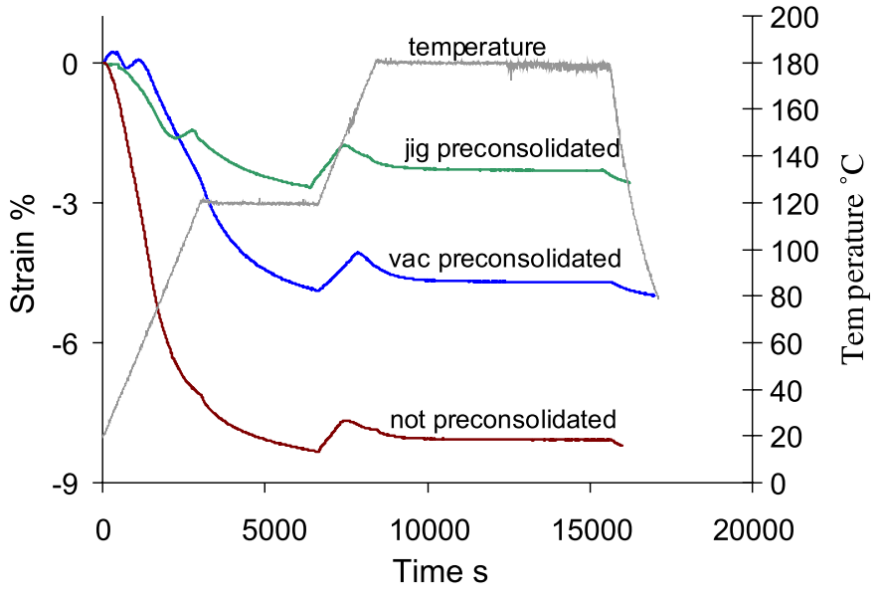

Figure 1.32: The effect of pre-debulking conditions on the through-thickness compaction of the UD samples [14].

The observed findings about consolidation phenomenon highlighted the need for greater understanding of the compaction behavior that occurs at the pre-gelation regime of thermosetting composites, regardless of the employed manufacturing process. Dimensions change induced by consolidation are important to know in order to gain more insight into the involved fundamental mechanisms in the curing behavior and hence to better identify the parameters that control this stage. Real-time monitoring of composites whole cure cycle considering the material anisotropy within representative conditions of real manufacturing processes is therefore of prime importance.

1.5 Measurement techniques and modeling approaches of rheological properties during the cure of thermosetting systems

Knowledge about the evolution of the mechanical properties, throughout all the different stages of the manufacturing process, is a very essential step in understanding the development of certain mechanisms controlled by the presence of multiple multi-physics phenomena. As discussed in earlier sections, for autoclave processing or OoA fabrication, information about the composite rheological properties before gelation is a key issue in the composite industry. Indeed, it can give guidance on when certain parameters should be applied during the cure cycle. For instance, the onset of the applied pressure prior to matrix gelation, has a major role on parts consolidation, regarding voids suppression and resin flow mechanisms. Otherwise, full knowledge about the mechanical behavior at the early stages of curing process of these anisotropic materials, could provide large contribution in promoting the predictable tools of composite manufacturing, notably, when dealing with toughened prepregs that exhibit complex rheological behavior. Hence, it seems necessary to further understand the mechanical behavior during curing of thermosetting composites. Several authors have employed different standard measurement techniques in order to obtain more precision on the evolution of rheological properties during curing of thermoset resins but to a lesser extent related to composites.

Chemorheology is defined as the study of the viscoelastic behavior of these reacting systems during curing [72, 140]. Various chemo-rheological techniques and measurement systems have been employed for the study of the gelation phenomenon and rheological properties which mainly include standard methods like rheometer, DMA and TMA. The determination of the gel point has been a key issue in thermosetting processing from the manufacturing point of view. It is an essential parameter for the controlling and monitoring of any processing operation. There exist multiple criteria in literature that have been developed to identify the time to gelation of thermosets.

This section will be therefore divided as follows. The first subsection will be focused on presenting in the first part, the most used criteria for the determination of the gel point, which commonly involve measuring the rheological properties over time of the matrix. Most common research works that have been interested in the investigation of gelation in thermoset systems, including resins and composites, will be then briefly described along the last two sub-subsections. Finally, the second subsection will be concerned with the presentation of some developed rheological models that have been proposed in literature to describe the mechanical behavior during the cure of thermoset systems.

1.5.1 Experimental methods of rheological properties characterization

1.5.1.1 Classical detection criteria of gel point

The gel time can be determined according to different criteria that have been widely used in literature for several types of thermosetting resins and related composites [71, 141]. The most commonly used ones will be briefly presented thereafter.

Divergence of the steady shear viscosity

This method implies the use of isothermal steady shear rheological tests. During the liquid phase, the thermoset polymer is subjected to a constant shear rate. The viscosity, being recorded as a function of time, continues to increase with the progress of the crosslinking reaction, as a result of the extension of the molecular chains, until it diverges to high values. The latter commonly exceed the capacity of the rheometer as the material approaches the gel point within the formation of a 3D molecular chains network. The inspection of the onset of gelation was defined by the moment related to the sudden increase in the extrapolated viscosity towards infinity, as illustrated by figure 1.33. This figure represents the viscosity profile of an RTM6 epoxy resin cured during an isotherm of 140°C. However, the extrapolation of the steady viscosity brings difficulties to accurately define the gel point since it may depend on the shear rate. In addition, near to the gel point, relaxation times became very long and the steady state conditions may not be reached during the relatively short time of the experiments. The transition in the viscosity values may also appear earlier due to the stiff developing material, hence, the resulting rising stresses may overload the rheometer and therefore only an apparent gel point would be estimated. Moreover, the divergence of viscosity may also relate to the vitrification of the material. Despite the multitude difficulties and inaccuracy of this method, it was largely employed, primarily, because of its simplicity [70, 71, 141, 142].

Curves crossover point of the elastic modulus (G') and viscous modulus (G") or when tan(δ) equals 1

Dynamic mechanical measurements have been an interesting alternative to follow the rheological properties during curing of thermosetting resins and to detect the onset of gelation. Oscillatory shear flow measurements have been preferred to those of the steady shear, since they revealed better ability to be applied to thermoset polymers not only in the liquid state but also in the rubbery and glassy states. Many authors have adopted oscillatory testing regime using rotational rheometer, often at a small amplitude oscillatory shear. Typical obtained evolution of dynamic viscoelastic moduli during the crosslinking process is gathered in figure 1.34a.

The viscous properties are dominant in the liquid state, *i.e.*, the loss modulus (G") is larger than the storage modulus (G') that is still negligible during the initial part of the experiment. With the cure progression, the storage modulus keeps rising until it intersects and then exceeds the loss modulus. Tung and Dynes [25] were the first to introduce a correlation

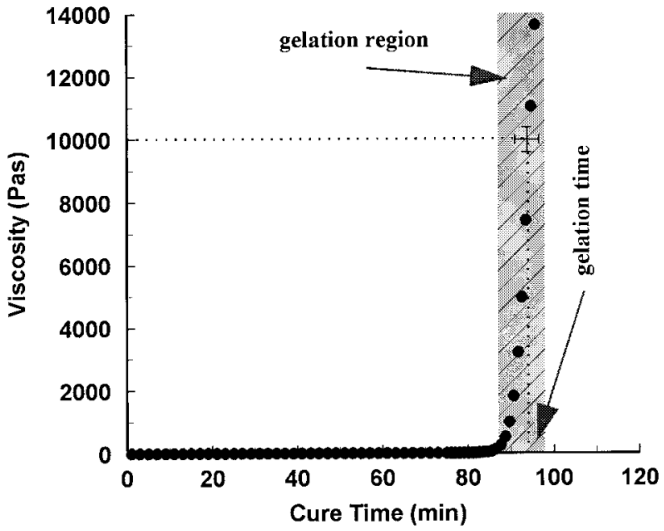

Figure 1.33: Steady shear viscosity profile of an epoxy resin isothermally cured at 140°C [24].

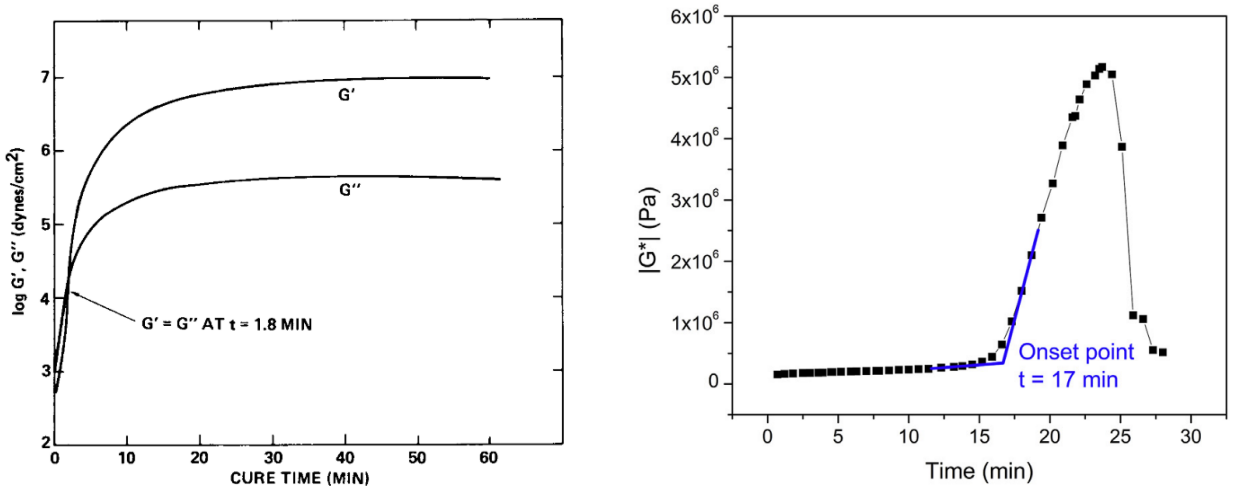

(a) (b)

Figure 1.34: (a) Evolution of G' and G" during the 171°C isothermal curing of an epoxy resin at 10 rad/s and 10% strain. Gelation onset is identified as the cross-over point of G' and G" [25]. (b) Gel point criterion through complex shear modulus onset [26].

between the gel point and the intersection of the recorded dynamic moduli of several thermosetting systems. They considered that the cross-over point of G' and G" ($\tan(\delta)$ = G"/G' = 1) could be expected near to the gel point. However, it was afterwards demonstrated that the crossover point of moduli depended on frequency of the oscillatory shear measurement. Winter and Chambon [71, 143] revealed that the validity of this criterion could be possible only in the case of stoichiometrically balanced network polymer system, at temperatures

significantly above its T_g. This method has been widely employed by several authors using thermoset resins [141, 144] and also epoxy prepregs [145, 146]. Earlier experiments [26] conducted on carbon fiber/epoxy prepreg, under isothermal and non-isothermal conditions, by means of rheological tests, suggest that the onset in complex shear modulus (G*) increase marked the gel point of the preimpregnated material more accurately than G'-G" cross-over point or the viscosity increase criteria. The proposed method to define the gel point is illustrated in figure 1.34b. It was proved that obtained results are independent of the frequency, geometry diameter and strain.

Tanδ is independent of frequency

Winter *et al.* [142, 147] generalized the previous criterion in order to overcome the stated limitations. The authors demonstrated that the evolution of the loss tangent (Tanδ) measurements with cure time, for a given isotherm cure temperature and at different frequencies, enables to obtain various curves that would coincidence at a single point, corresponding to the time of gelation onset (see figure 1.35a). This criterion was almost the most used one to identify the gel point of thermoset resins [27, 141, 144, 148]. Other authors have further developed this criterion and proved the ability to identify the gel point in thermoset reinforced polymers as the peak in Tanδ curve by using DMA method [33, 149–151] or by employing a parallel plate rheometer [28]. They have demonstrated that the identified gelation time was independent of frequency (see figure 1.35b).

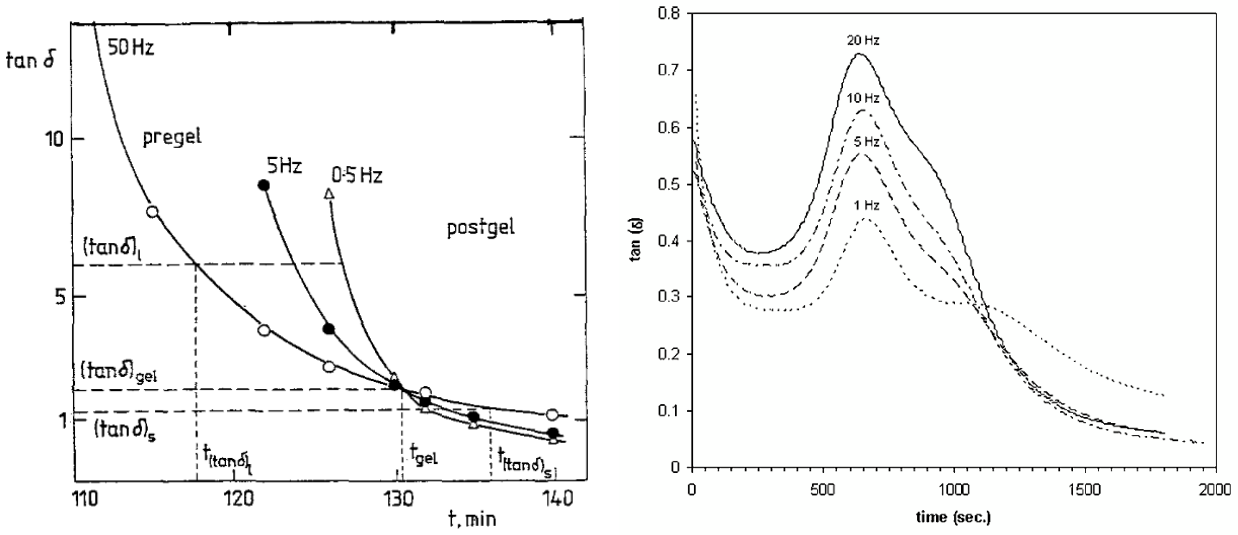

(a) (b)

Figure 1.35: (a) Loss tangent curves evolution as function of time for different frequencies during the curing of an epoxy resin at 70°C. Gelation is identified as the point where Tanδ is independent of frequency [27]. (b) Variation of Tanδ during the curing of glass/epoxy prepreg at 120°C. Gelation is identified as the peak in Tanδ curves for different frequencies [28].

1.5.1.2 Yield stress based-approach to investigate the gelation in thermoset resins

Outside of the large number of studies discussed above, mainly based on the assumption that the resin behavior is linear viscoelastic that transforms from viscous liquid to viscoelastic solid at gel point, a new approach has been proposed by Msallem *et al.* [29] to elucidate the resin gelation. The authors assumed that resin transformation during this phase could be assimilated to yield stress materials behavior. In order to explain further in-depth the introduced approach, here is a quick reminder about yield stress materials. In fact, the notion of yield stress fluids was firstly established by Bingham and coworkers [152]. These materials represent a category of non-Newtonian fluid characterized by having a yield stress. They have the particularity to exhibit properties of either solids or liquids, depending on the external forcing [153]. At small stress level, these materials are able to sustain finite deformations prior to flowing and deform essentially in an elastic way, but once a critical stress is exceeded, they flow and the material could behave as a viscous Newtonian fluid (case of Bingham fluid) or differently (see [154] for more details). The specific value of stress is called the yield stress. These materials commonly include concentrated emulsions like cosmetic creams, polymer gels like Carbopol and some composites. In his study, Msallem *et al.* [29], considered that since epoxy resins are reactive systems with a changing state during the crosslinking reaction, gelation could be assimilated to a transformation from an initial viscous liquid state, which ¨flows¨ under low stress levels, to a solid state characterized by a yield stress that evolves with curing. Once this specific stress level is reached, the material flows again and the behavior could be assimilated to a viscoelastic-viscoplastic solid after the gel point. It was crucial to investigate the evolution of the resin yield stress levels with degree of cure as a way of investigation of the gelation phenomenon. The yield stress approach was introduced by the authors in order to assess residual stress development during the cure process of thermoset composites. They supposed that residual stresses remain in the composite part if they are lower than the yield stress of the matrix, on the other hand, if they exceed this one, a relaxation is possible. Indeed, it has been reported, even in very limited way, that irreversible viscoplastic strains could contribute to stress relief during the cure cycle and thus it counter-act the build-up of residual stresses [2, 155].

His method consists in performing cyclic charge-discharge test under applied shear stress, as linear ramp form using the creep mode of rheometer, during the isothermal cure of an epoxy resin. As illustrated in figure 1.36, based on stress-strain curve during an applied loading-unloading cycle, it was supposed that an elastic recovery of strain $\varepsilon_r < 0.2\%$ (ε_r for residual strain) (figure 1.36a) indicates that the yield stress was not reached. Tests were repeated with increased applied stress amplitude as the polymerization reaction progressed. This allowed to detect inelastic recovery as $\varepsilon_r > 0.2\%$ (figure 1.36b). According to the authors, this implied that the imposed stress was beyond the resin yield stress. The corresponding flow time is therefore deduced and correlated within the degree of cure (based on developed cure kinetic model) which enabled to establish a relation between measured yield stresses and cure degree for a given isotherm temperature.

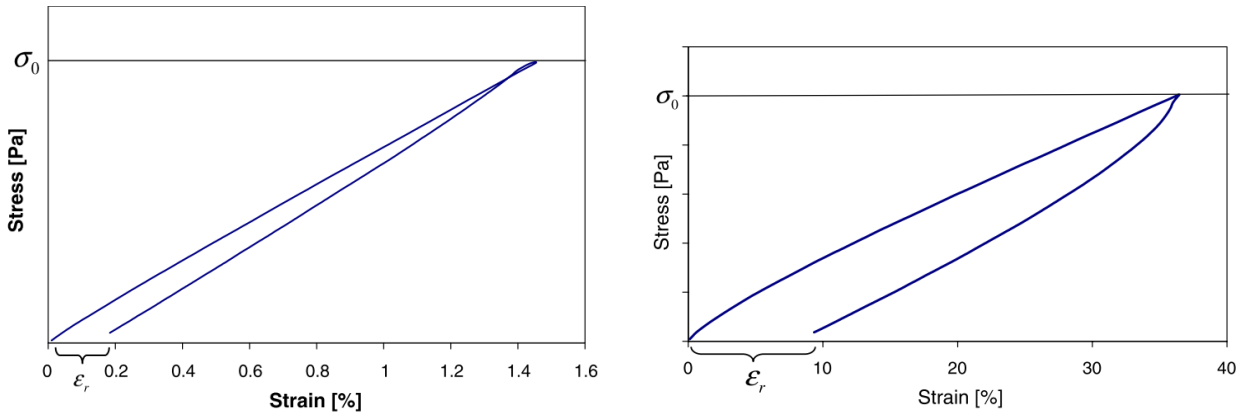

(a) (b)

Figure 1.36: Measured stress-strain curves. (a) Assumed elastic behavior, $\varepsilon_r < 0.2\%$. (b) Assumed inelastic behavior, $\varepsilon_r > 0.2\%$ [29].

The evolution of the resin yield stress during the cure is given by the curve plotted in figure 1.37a determined for a curing at 160°C. It proved the increasing tendency of the yield stress with cure correlated with the resin progressive transformation to a rigid solid with the crosslinking reaction. The time corresponding to the start of formation of yield stresses was proved to be coherent with the gel time determined by other methods ($\alpha_{yield} = \alpha_{gel} = 0.52$ for the studied M21 epoxy resin). Figure 1.37b depicts the yield time as a function of isotherm cure temperatures.

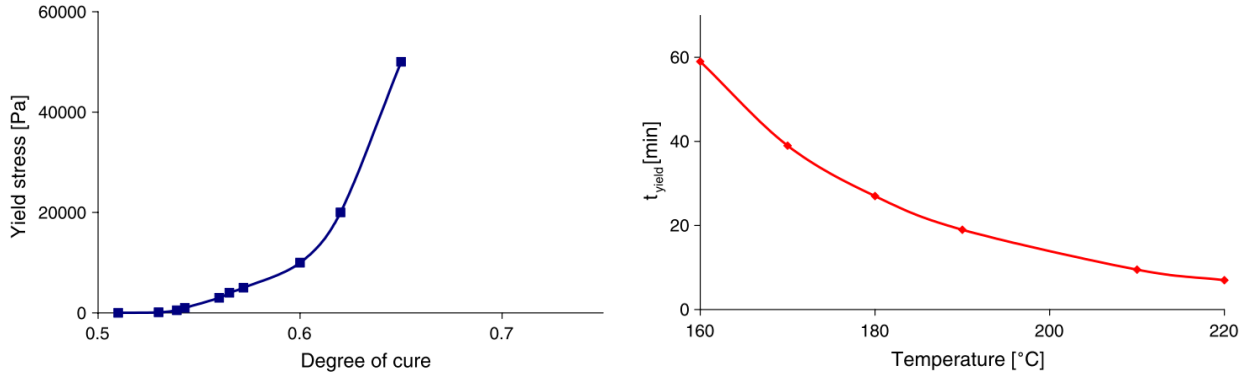

(a) (b)

Figure 1.37: (a) Yield stress as a function of cure degree for a curing at 160°C. (b) Obtained yield time as a function of isotherm cure temperatures [29].

In a more recent research work carried out by Cardinaud [30], the same yield stress approach was adopted to investigate the cure behavior of a vinylester thermoset resin. The employed protocol was however different from the one described above. The authors rather performed dynamic oscillatory shear measurements in a stress-controlled rheometer. The material was subjected to a sinusoidal stress with an increasing stress amplitude at a fixed frequency, throughout the whole isotherm curing for a given temperature. The inspection of the resin

flow mechanism, once the applied stress exceeded the resin yield stress, was mainly based on the analysis of the resulting mechanical response as Lissajous plot of the stress as a function of strain. Such method of understanding the yielding and flow phenomena, by means of oscillatory measurements, has been of great interest and was largely applied within the context of exploiting large amplitude oscillatory shear (LAOS) to investigate and assess the nonlinear viscoelastic behavior of a complex fluid such as yield stress fluids [156]. An example of the obtained experimental results are gathered in figure 1.38.

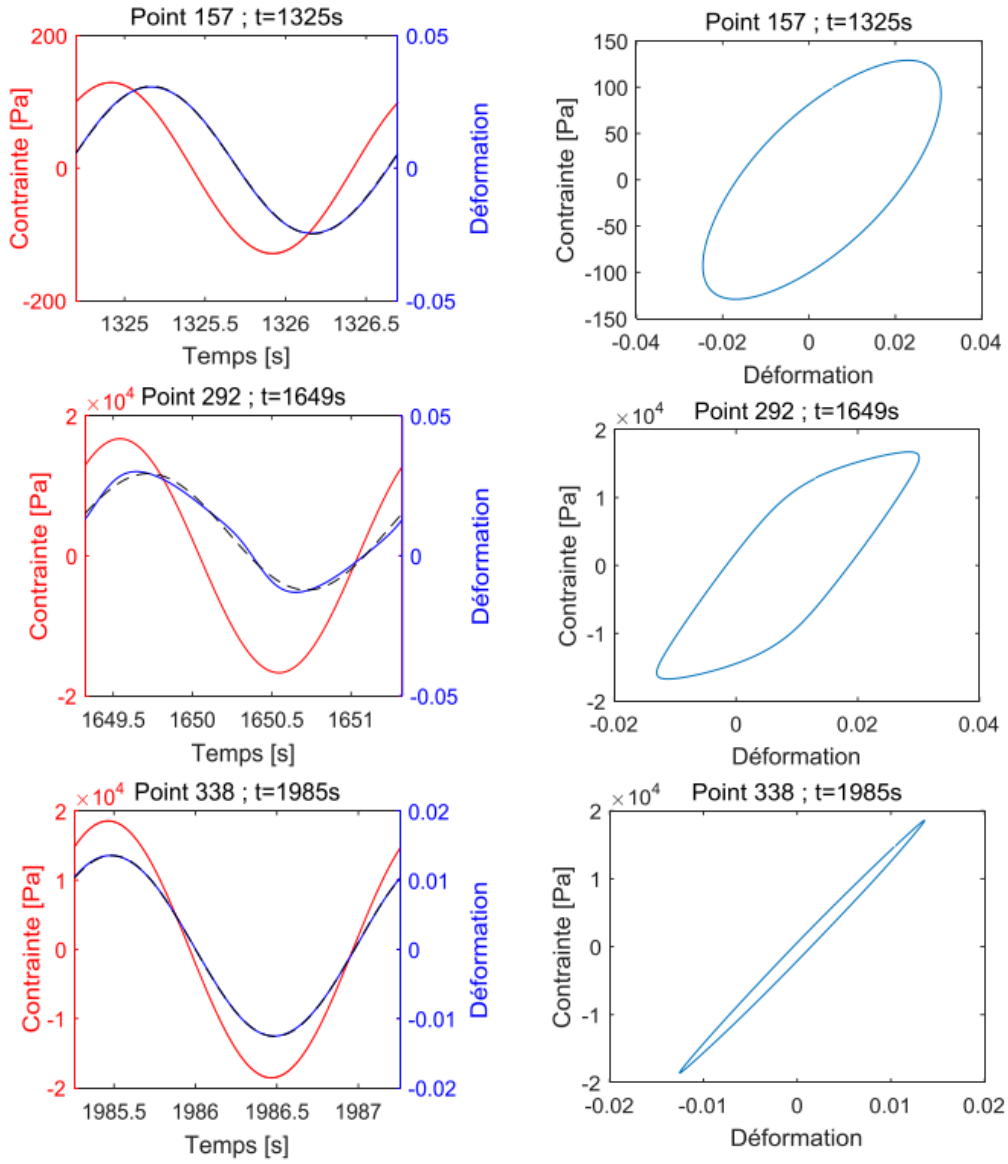

(a) (b)

Figure 1.38: Material mechanical response taken at three different moments from the cure cycle. (a) Applied stresses with the oscillatory strain responses as function of time. Fitted strain data with a sinusoidal function (Blue) (b) The corresponding Lissajous plots [30].

Three different moments from the rheological testing are taken as examples. Oscillatory strain response as a function of time during a period of oscillation within the applied oscillatory stress are given in figure 1.38a, while figure 1.38b depicts the corresponding Lissajous plots for each given moment. According to the authors, at t=1325 s and t=1985 s, the material behavior response was considered as linear viscoelastic solid (elliptic Lissajous loop) and elastic dominated solid behavior (straight line on the Lissajous curve), respectively. At t=1649 s, a non-linear viscoelastic response appeared illustrated by a distortion of the Lissajous curve and the resulting oscillatory strain waveform is no longer sinusoidal (compared with data). It was presumed that such behavior is triggered by the resin flow once the applied stress exceeded its yield stress. Based on this method, it was possible to estimate an evolution of the resin yield stress over an interval of cure degree that ranges from 0.2 and 0.4 (see figure 1.39). The first captured value of the resin yield stress (around 0.2) was close to the matrix α_{gel} corresponding to 8%. It was assumed according to authors' opinion that the investigation of the yield stress built up by means of oscillatory measurements allowed to have an original perception about the resin onset of gelation and the curing process.

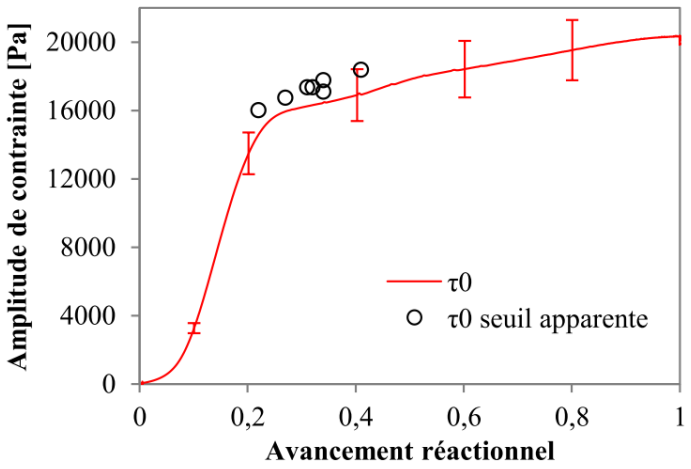

Figure 1.39: Yield stress measured values for different degree of cure levels of a vinylester resin [30].

1.5.1.3 Employed techniques to investigate thermoset composites rheological behavior during the cure

Although there is an increasing need to study the pre-gelation region, according to the authors' knowledge, studies that look into this area are very scarce and the number of experiment-based investigations on composite rheological behavior during the early stages of cure is rather limited. The low capacity of thermoset matrix to withstand stresses before gelation always makes the characterization of composites behavior particularly complicated. The challenges come especially from finding the appropriate measuring methods, that enable to accurately capture the material mechanical response, without influencing the latter. Moreover, it is necessary to perfectly control the stress or strain state of the material and to know its thermo-chemical behavior in order to decorrelate the contribution of each of the

material properties from the overall thermo-chemical-mechanical behavior. It is therefore very common to approximate the mechanical properties of the matrix before the gel point, or, to consider that the stresses developed in this state are rather negligible. Most of the developed mechanical constitutive models in literature are based on tests rather performed on fully or partially cured specimens. The composite mechanical behavior before gelation is consequently, either approximated or considered equivalent to the matrix cured state behavior, assumed in most cases linear elastic. Otherwise, when viscoelastic models are chosen to describe the composite behavior, the use of a DMA device is very common.

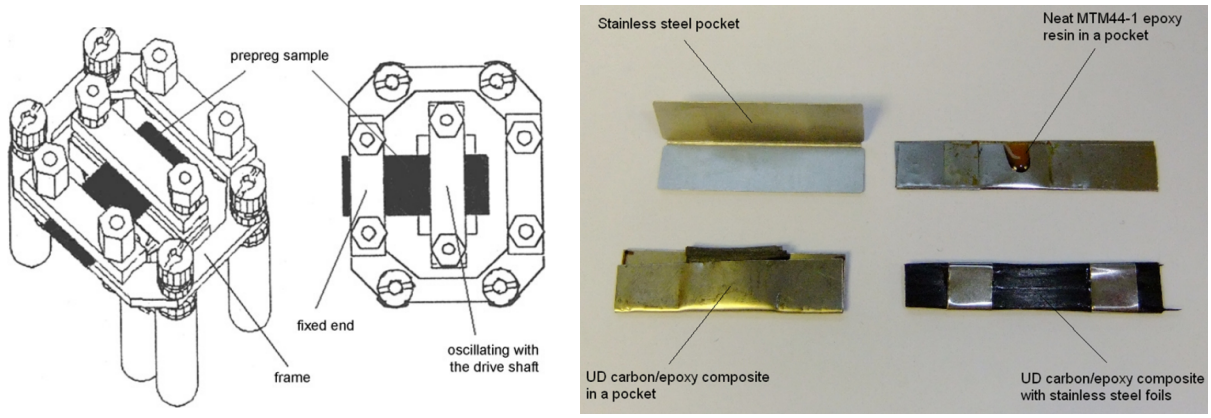

(a) (b)

Figure 1.40: (a) Scheme of the measuring system in DMA with the single cantilever mode [31]. (b) Configurations of the prepreg samples for DMA testing [32].

It was largely employed to investigate the viscoelastic properties, to determine the influence of the frequency on the mechanical response of prepregs [157, 158] and also the effect of time and temperature [146, 159]. Nevertheless, the characterization is always performed under atmospheric pressure. Samples preparation and setting-up in DMA device are also quite complicated when investigating uncured materials. Xie *et al.* [31] used a single cantilever holder configuration (figure 1.40a), commonly used for prepreg characterization, and one-layer sample of a prepreg whose longitudinal direction of fibers are parallel to the length of the latter. The end of uncured samples are usually wrapped. In that case of study, aluminum foils were used in order to avoid undesired deformations during the test. Depending on the resin viscosity, it was also reported by Jakobsen *et al.* [33], the use of thin nylon films that envelop the prepreg in order to prevent resin dripping inside the DMA. Kister *et al.* [32] performed a similar DMA investigation of a carbon/epoxy prepreg mechanical behavior. They rather used stainless steel pockets, in which four-ply samples were packaged before the test, in comparison with other samples, that were instead wrapped with thick stainless steel foils, so as to avoid their bonding to the clamps, as illustrated in figure 1.40b. In contrast, other authors used precured specimens to the gelled state to overcome such difficulties [34, 158, 159].

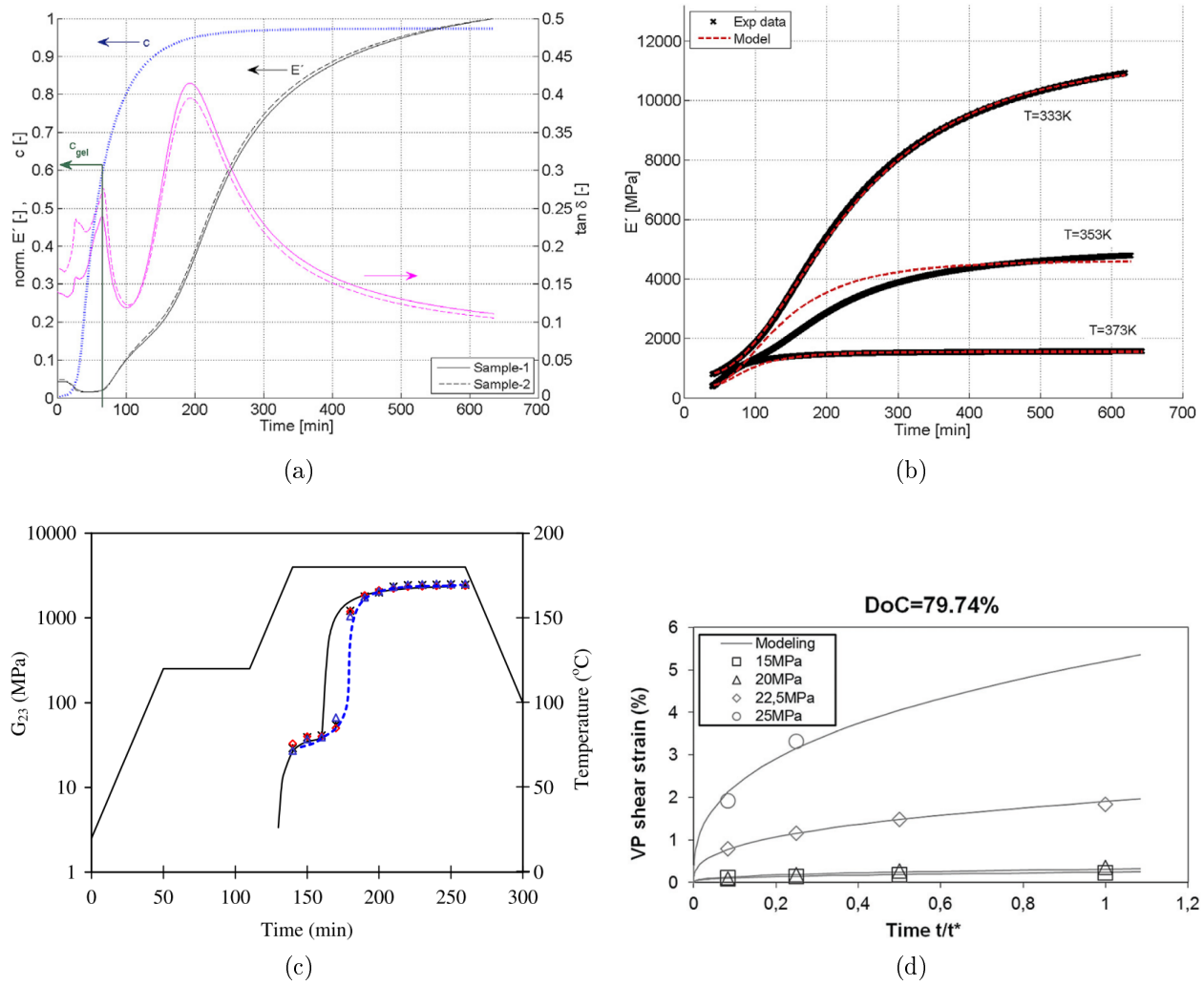

Figure 1.41: (a) DMA measurements, conducted on uncured laminates, of the storage modulus and Tanδ [33]. (b) DMA measurements conducted on partially cured samples. The evolution of storage modulus (E') over time at three different isothermal temperatures [33]. (c) DMA measurements of shear modulus through cure performed on precured prepregs [34]. (d) Viscoplastic shear strain development with time for precured sample using tensile creep tests [2].

Typical obtained results from DMA can be found in figure 1.41. A normalized storage modulus together with Tanδ are plotted as a function of the test duration of two tested samples in figure 1.41a. Jakobsen *et al.* [33] were able to estimate the gel point taken as the onset in storage modulus and from the peak in Tanδ. The authors reported that appeared discrepancies in data before gelation were due to the low values of the storage modulus in the liquid state. The authors performed additionally DMA tests, on precured prepreg samples, in order to estimate the evolution of the material Young's modulus, during the isotherm curing, through storage modulus measurements. The corresponding results are gathered in figure 1.41b and showed the influence of the temperature on the parameter evolution.

When the sample is cured under glass transition temperature (at T=373), vitrification does not occur and the Young's modulus values remain low. Kister *et al.* [32] reported in their study that disparities between the packaged and unpackaged samples were found to induce a decrease in the measured storage modulus amplitudes, in addition to, significant delays in time/temperature due to the thermal diffusivity of the stainless steel pocket. Ersoy *et al.* [34] performed DMA tests on precured samples using the transverse shear mode and were able to capture the shear modulus variation, during post-gelation stage before and after vitrification (figure 1.41c).

Testing methodologies of composite, irreversibly changing with cure measurements, are almost non-existing. Hence, models and developed predictive tools are mostly theoretical and lack experimental proof of their adequacy in regard with the materials real behavior. Viscoplastic shear strain developments with cure were recently investigated in a study conducted by Saseendran [2]. They performed tensile creep tests on precured postgel glass/epoxy prepreg samples, for a degree of cure that ranges from 79.7 to 100%, using tensile machine Instron. Their results were compared to a visco-plasticity model and it was shown that, for a cure degree lower than 80%, the viscoplastic strains were much more sensitive to the increase of the applied shear stress and consequently grew much faster (figure 1.41d).

1.5.2 Modeling approaches of rheological behavior during the cure

1.5.2.1 Rheo-kinetic models for thermosetting resins

Chemo-viscosity models

As described earlier, the chemorheology term was used for describing the viscoelastic behavior of chemically reacting polymers. Rheo-kinetic models, also called chemorheological models, cover different conditions depending on the temperature and the curing step, but also on the studied variable considered to describe the rheological behavior. These models are commonly called as chemo-viscosity models since the material viscosity is the principal rheological property used to describe the mechanical behavior with the reaction progress. Note that, both terms are not synonyms, chemo-viscosity models are always rheo-kinetic models but the opposite is not true. The models, relating viscosity and cure degree described in the literature, range mostly from models based on free volume theory, probability based models to empirical models. A more extended summary of the overall developed chemo-viscosity models of thermosets during their curing can be found in [72, 160]. In this paragraph, only some of the most common chemorheological models will be described. These models are in most cases based on using complex viscosity. Much work has been done to determine the appropriate empirical models that best describe the viscosity behavior of the reactive matrix and Arrhenius model was among the first mathematical relation that were used. It was initially developed to describe isothermal conditions curing and was subsequently improved into a more general form of 5 and 6 parameters to be more suitable for non-isothermal curing applications. However, they have not been widely used to describe viscosity evolution and the original first order *four-parameters model* remained the main used expression under isotherm conditions. Another expression that has been used extensively in chemo-viscosity modeling is the Williams-Landel-Ferry (WLF) approach based on the polymer free-volume theory to

describe the viscosity dependence on temperature which consists in a two-parameter relation described by

$$\eta(T,\alpha) = \eta_{Tg}\ \exp\left(\frac{-C_1(\alpha)\ (T - T_g(\alpha))}{C_2(\alpha) + (T - T_g(\alpha)}\right) \tag{1.3}$$

where η is the steady viscosity variable, α is the degree of cure, η_{Tg} is the viscosity at the glass transition, $C_1(\alpha)$ and $C_2(\alpha)$ are fitting parameters that only depend on the cure degree of the resin and $T_g(\alpha)$ is a function that relates the glass transition temperature change with cure, commonly defined according to the Di Benedetto equation as being the most widely used function [160]. Another expression of a chemo-viscosity model was developed to predict the viscosity evolution as a function of cure degree in the pregel stage derived by Castro and Macosko as

$$\eta(T,\alpha) = \eta_0(T)\left(\frac{\alpha_{gel}}{\alpha_{gel} - \alpha)}\right)^{A+B\cdot\alpha} \tag{1.4}$$

where $\eta_0(T)$ is the initial viscosity of the resin, at a given temperature T before curing which often can be measured, nevertheless, in non isotherm condition, it can be estimated by the Arrhenius relation to predict the viscosity change at any temperature. A and B are fitting parameters and α_{gel} is the degree of cure at the gel point. This model has commonly been applied under isothermal conditions which further simplifies its application. Several works [72] revealed that a modified WLF equation was more appropriate to predict the viscosity development with cure of epoxy-based systems, by combining together both the WLF (equation 1.3) and Castro-Macosko (equation 1.4) models described by the following form

$$\eta(T,\alpha) = \eta_{Tg}\ \exp\left(\frac{-C_1(\alpha)\ (T - T_g(\alpha))}{C_2(\alpha) + (T - T_g(\alpha)}\right)\left(\frac{\alpha_{gel}}{\alpha_{gel} - \alpha)}\right)^{a} \tag{1.5}$$

where a is a constant to be determined by regression analysis of the experimental data. This model was also successfully applied to describe the chemorheological behavior of a carbon nanotube epoxy nanocomposites [161] and a low-viscosity epoxy based system [35] under both isotherm and non-isotherm conditions. Typical obtained results are gathered in figure 1.42 of the complex viscosity evolution, at pregelation stage, of an epoxy resin predicted by the modified WLF model.

Yield stress based-approach model

In order to support the developed experimental investigation of the resin curing behavior, based on the yield stress approach, Cardinaud *et al.* [30] proposed a rheo-kinetic model integrating the resin yield flow threshold to describe the gelation process. The proposed approach is based on the coexistence of a viscoelastic solid type behavior, that describes the formed cross-linked network (solid phase), and a viscous liquid behavior, that is associated with the polymer macromolecules not yet included in the cross-linked network chains which flow once the applied stress exceeded the specific yield stress of the material for a given degree of cure. The developed rheo-kinetic model is schematically illustrated in figure 1.43. G is related to the spring element that represents the elastic modulus of the solid behavior, η is related to the viscous behavior by the dash-pot element that constitutes the model's fluid unit, η_{num} is a numerical constant related to the second dash-pot element included to prevent some discontinuities in the model response and τ_y represents the material yield stress. The preliminary

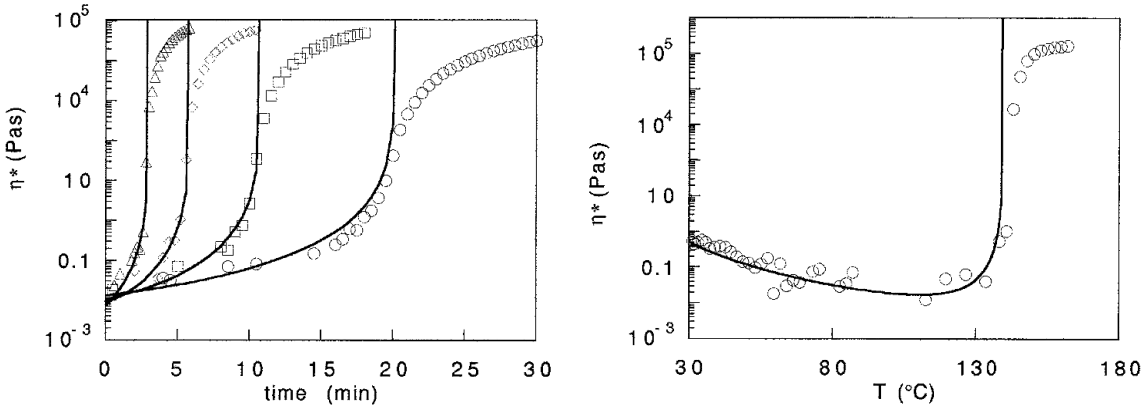

(a) (b)

Figure 1.42: (a) Complex viscosity as a function of time for different isothermal cure at 110°C, 120°C, 130°C, and 140°C, (b) complex viscosity as a function of temperature during a heating ramp of 4.6°C/min, in comparison with the modified WLF chemorheological model [35].

obtained results from this model showed satisfactory ability to simulate the transition in the resin behavior from viscoelastic solid to a plastic fluid, once the characteristic yield stress value is exceeded, by analyzing the simulated Lissajous plot of the mechanical response. The prediction of the yield stress evolution with the degree of cure showed satisfactory agreement with the measured experimental values. However, further experimental tests are still needed to validate the proposed approach and hence to improve the developed model.

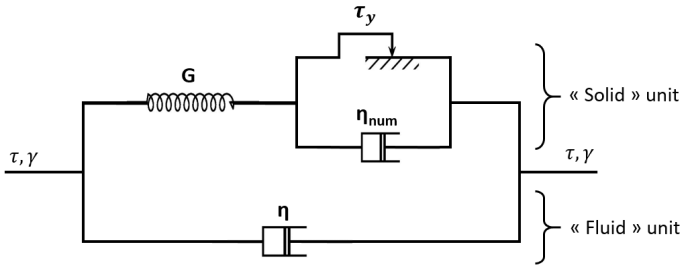

Figure 1.43: Schematic representation of the rheo-kinetic model based on the yield stress approach to describe the material gelation [30].

1.5.2.2 Developed rheological models for thermoset composites

Although a large number of rheo-kinetic models has been developed in literature in order to predict rheological properties evolution with cure of thermoset resins, even if they were all limited to the gel point and only based on viscoelastic approaches, in the case of thermoset composites, these models are significantly scarce. Since experimental investigations are difficult to conduct on a reacting composite before material gelation, it was therefore easier to implement purely elastic models to describe the material behavior which required less experimental characterizations to validate the developed approaches. On the other hand,

much research works have been interested in developing viscoelastic and viscoplastic models to characterize composite materials behavior. Nevertheless, most of these models are more difficult to implement, and require complicated experimental characterization and intensive calculations for parameters identification. Moreover, they commonly describe the time-dependent or temperature-dependent mechanical response only of the composite during the cure, with partially or fully-cured resins, thus, the mechanical behavior before gelation is either approximated or considered negligible [97, 99].

In order to validate their experimental investigation, Ersoy *et al.* [34] estimated the prepreg effective shear modulus evolution, during the post gel stage, by means of micromechanical model. And this, on the basis of the resin post-gel properties evolution with temperature, before and after verification, assumed as an elastic material. The obtained results of the simulated data (illustrated with black solid line) are presented in figure 1.41c together with the measured shear modulus values (illustrated with red points) after gelation. They reveal significant disparities between the predicted and the experimental onset of vitrification. Jakobsen *et al.* [33] developed an incremental formulation of a linear elastic constitutive law, accounting for the chemical and temperature changes in the prepreg properties during the post-gel stage cure, by decoupling the modulus increments due to the chemical reaction from increments resulting from temperature change. The fitted data are presented in figure 1.41b with the experimental measurements of the Young's modulus evolution. In a recent study [36], an attempt to employ the Castro-Macosko (equation 1.4) chemo-viscosity model to estimate the viscosity evolution with cure of a thermoset composite was made. A comparison was also performed, with a developed rheological model based on time dependent mathematical approach of viscosity evolution without integrating a cure model but rather by fitting data from experimental measurements in non isotherm conditions of cure. The experimental investigation was based on using an oscillating plate-plate rheometer. The predicted evolution with both models of the measured viscosity revealed nevertheless remarkable accuracy for different isothermal cure (see figure 1.44).

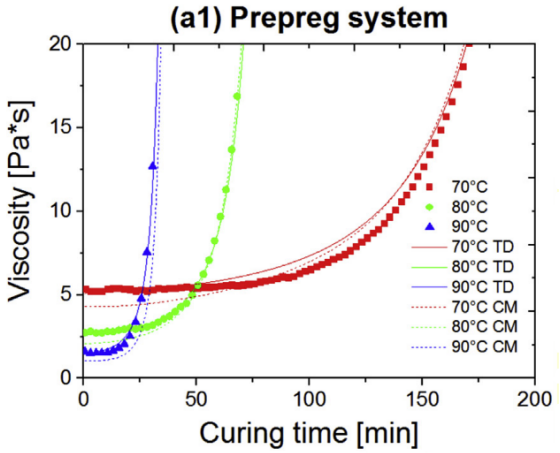

Figure 1.44: Comparison of measured viscosity with time dependent model (denoted as TD) and Castro-Macosko model (denoted as CM) for different isotherm cure temperatures [36].

1.6 Outlines of this literature review and Objectives

This bibliographic study has allowed to present the fundamental notions and concepts involved in cure-induced issues of thermoset composites. It highlighted that the phenomena responsible for residual stresses generation, resulting in composite part deformations, are multi-physical and rather complex. The most impacting ones seem to be those related to the material thermal anisotropy, chemical shrinkage, resin flow and consolidation. However, accurate experimental measurements of these phenomena is of crucial importance in order to correctly predict dimension variations of these anisotropic materials. An increased ability to predict shape distortions will therefore result in more cost efficient development, improved performance and optimized manufacturing of composites. Based on the employed techniques reviewed in literature and the reported obtained results in this area, it is clearly evident that it remains an essential need for more sophisticated methods, that allow to perform cure monitoring of these materials in more representative and realistic conditions of manufacturing processes. In that case, the developed simulation tools can be validated by in-situ measurements that would provide more elaborate and precise validations. On the other hand, as presented in the previous section, there are limited studies that looked in-depth into the material rheological properties evolution during the pre-gelation region, although the increasing requirement to investigate this phase among the whole cure process of thermoset composites. As the challenges come from finding the appropriate method that can accurately capture the strains induced in the material, notably during this phase without influencing the latter, the overall objective of this study is therefore to further understand the development of the multi-physical phenomena that occur during the whole cure process of a thermoset composite. To achieve this objective, it will be necessary to characterize the induced strains throughout the consolidation of the uncured material and the induced thermo-chemical deformations. Moreover, a new experimental procedure that allow to characterize the rheological behavior of the studied composite through curing will also be developed.

CHAPTER 2

MATERIALS AND METHODS

Contents

2.1 Introduction **56**

2.2 Studied material: IMA/M21 toughened prepreg **56**

2.2.1 IMA carbon fibers 57

2.2.2 M21-Epoxy resin: Composition and Curing reaction mechanism . 58

2.3 Literature review: Reminders on cure kinetics models of Epoxy/Amine systems **59**

2.4 Thermo-chemical characterization and model validation of the M21 resin cure kinetics **62**

2.4.1 Model validation of the curing kinetics 62

2.4.1.1 Dynamical Scanning Calorimetry (DSC) characterization 62

2.4.1.2 Characterization using the PvT-α mold 65

2.4.2 Characterization of the volumetric behavior of the M21 resin during the cure by using the PvT-α mold 69

2.5 Rheological characterization of the M21 resin: Gel point determination . **71**

2.6 Presentation of the PvT-HADDOC set-up and the imported improvements **74**

2.6.1 Design and global working principle 74

2.6.2 Thermal control 75

2.6.3 Mechanical state 78

2.6.4 Displacement measurements 81

2.7 Partial conclusion **83**

2.1 Introduction

In the previous chapter, we have seen that thermoset composites are complex materials whose manufacturing processes require a good control of the material transformations. For this purpose, it is crucial to focus on the physico-chemical properties of the matrix and to characterize them precisely. The first part of this chapter deals with a general presentation of the composite used in this research work and its constituents. A detailed understanding of the mechanisms governing the resin transformations through the crosslinking reaction is also presented. Sections 2.3 and 2.4 will be devoted to the study of the polymerization kinetics of the matrix and the application of a cure model will be discussed. The volumetric behavior of the latter is additionally characterized. The final part of this chapter is dedicated to the presentation of the laboratory scale bench employed in this thesis work and designed for the investigation of the thermoset prepreg thermo-chemo-rheological behavior during the cure.

2.2 Studied material: IMA/M21 toughened prepreg

The material used in this study is a unidirectional prepreg supplied by Hexcel Composite France known as HexPly®M21/34%/UD194/IMA-12K. The latter belongs to the family of high performance OMC (Organic Matrix Composite) and more specifically, to the family of thermosetting CFRP (Carbon Fiber Reinforced Plastic). This material is an aerospace-grade composite commonly used in elaborating primary and secondary aeronautical structural parts. It was delivered as unidirectional preimpregnated sheets in a standard roll form, as it is represented in figure 2.1.

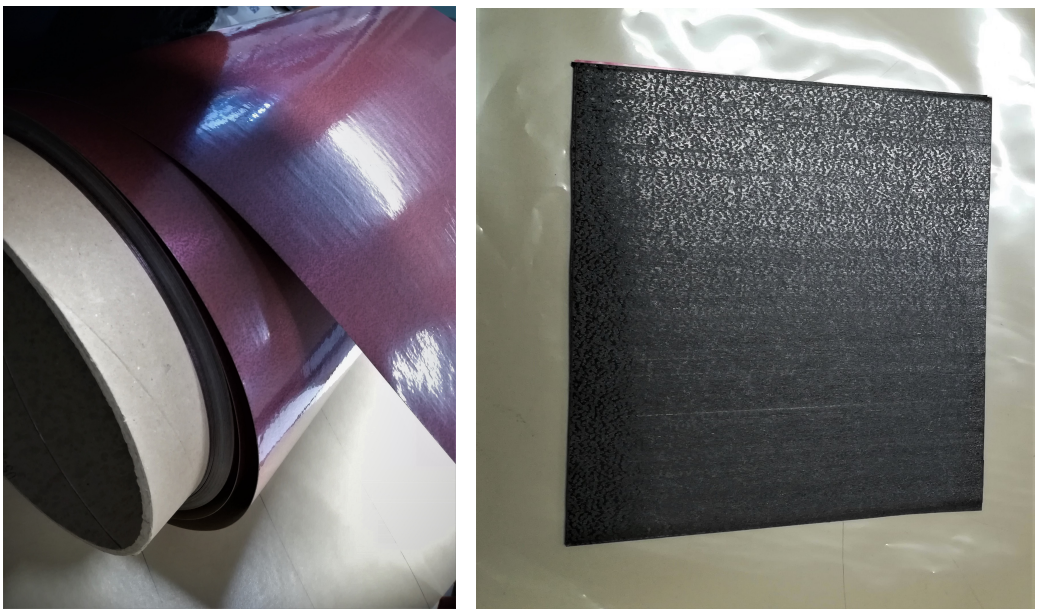

(a) (b)

Figure 2.1: IMA/M21 reinforcing material preimpregnated with epoxy resin. (a) Unidirectional preimpregnated sheets as standard roll form. (b) IMA/M21 UD prepreg ply.

This prepreg is made of M21 epoxy resin and long unidirectional IMA carbon fibers. The final resin content of the cured material is 34% by weight for an areal weight of fibers of 194 g/m^2. The manufacturer's data sheets indicate a nominal cured ply thickness of approximately 0.184 mm [39]. The main properties of the IMA/M21 prepreg are summarized in table 2.1.

Table 2.1: General properties of the preimpregnated IMA/M21 material [39].

Physical Property	Symbol	Unit	Value
Theoretical calculated laminate density	ρ_c	g.cm^{-3}	1.58
Cured ply thickness	h_{cured}	mm	0.184
Theoretical calculated fiber volume fraction	V_f	%	59.2
Resin density	ρ_m	g.cm^{-3}	1.28
Fiber density	ρ_f	g.cm^{-3}	1.79

The IMA/M21 system is in fact a third generation toughened prepreg that includes extra layers of epoxy resin in the form of distinct interleaves in between plies. These discrete epoxy layers are filled with thermoplastic particles. As it was detailed in chapter 1 (see subsection 1.1.3), this technique of interleaving has been widely used as a solution to enhance cured laminate toughness. A typical micrograph image captured through the thickness of an IMA/M21 prepreg sample, presented in figure 2.2, highlights the inter-laminar resin rich zones incorporating thermoplastic particles as heterogeneous distinct plies between the fiber rich layers.

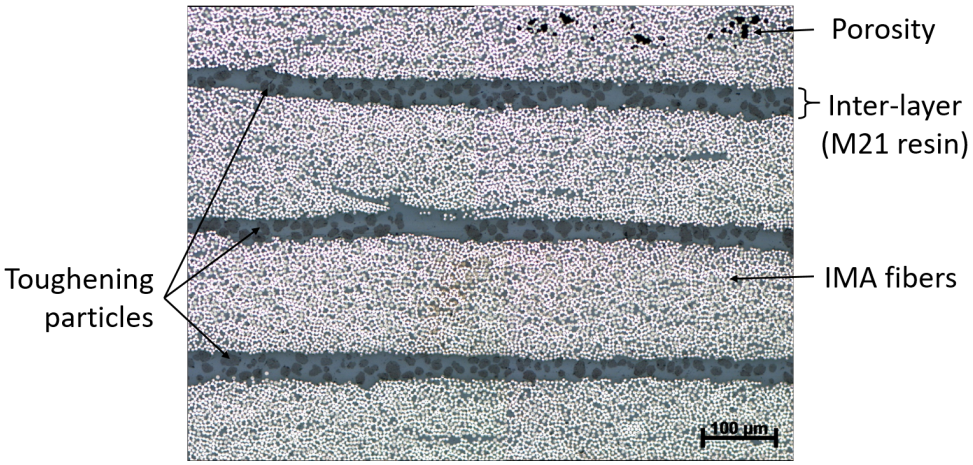

Figure 2.2: Micrograph through the thickness of an IMA/M21 laminate cured sample.

2.2.1 IMA carbon fibers

HexTow® IMA carbon fibers, also produced by Hexcel, are continuous, high performance and intermediate modulus fibers. The properties reported by the supplier are detailed in table 2.2 for tows of 12k (12000) filaments. This type of fibers has been surface treated and is known for its high tensile modulus and good shear strength.

Table 2.2: General properties of HexTow® IMA carbon fibers [45].

Fiber Property	Unit	Value
Tensile strength (12K)	MPa	6,067
Tensile modulus	GPa	297
Ultimate elongation at failure (12K)	%	1.8
Filament diameter	Microns	5.1
Carbon content	%	95.0

2.2.2 M21-Epoxy resin: Composition and Curing reaction mechanism

Epoxy resins are the most employed thermosetting polymers in the manufacturing of high performance composites, especially in the aviation industry. Their use is also important in surface coatings and structural adhesives. The HexPly® M21 epoxy resin used in the impregnation of the supplied prepreg was also provided by Hexcel and delivered as a roll of a thin film. The supplied neat resin included also undissolved thermoplastic particles similar to those present in the interleaf layers of the IMA/M21 prepreg. Data on the composition of the M21 system comes from a written patent by Hexcel [64] on toughened prepreg with thermoplastic particles. However, the exact proportions of the resin constituents remain unknown until now. According to the patent and recent research works [46, 162, 163] conducted on similar M21 systems, high melting temperature and low melting temperature thermoplastics are incorporated in the epoxy matrix with proportions that range from 3 to 10% by weight. These thermoplastics essentially include copolymers of polyamide 6 (PA6) and polyamide 12 (PA12) whose contents depend upon the desired properties. Particles containing more PA6 typically have melting temperatures between 190°C and 194°C, or even 217°C for compounds containing 100% PA6, which is well above typical epoxy prepreg curing temperatures. Low melting thermoplastics are present as PA12 or copolymers (PA6/12) with more (PA12) content and a melting temperature less than 160°C.

The crosslinking process of the M21 resin consists of quite complex reactions' system of several components such as epoxy pre-polymers of different functionalities, curing agents and other various additives. Epoxy pre-polymers have the particularity of reacting with diverse functional groups such as amines, phenols, etc. Amine hardeners are still the most commonly used ones with epoxy systems. Knowledge acquired notably from studies [46, 162, 163] carried out on the well-known T700GC/M21 prepreg type supplied also by Hexcel Composite revealed that the crosslinking of the M21 system is a classic epoxy/amine polyaddition reaction, thermally activated. Epoxy/amine based systems have the advantage of presenting high glass transition temperature above 200°C, a good thermal stability and minimal chemical shrinkage. They are characterized by excellent chemical resistance and promising mechanical properties. The cross-linking of the epoxy/amine system takes place in two or even three chemical steps [37, 164, 165]. The cure rate and the formed 3D network are strongly influenced by the relative speeds of the different chemical reaction steps, which depend mainly on the reactivity of the epoxy pre-polymers and the crosslinking agent. The reaction of the primary amine with the epoxy groups to produce a secondary amine (illustrated by reaction

1 in figure 2.3) which further reacts with the epoxide to form a tertiary amine (denoted as reaction 2) are the main chemical reactions that take place (see figure 2.3). At each reaction between an epoxide and an amine group there is a continuous addition of secondary alcohols, in addition to catalyst hydroxyl groups -OH (alcohol, phenol, water, acid) initially present. This considerably increases the interaction between the epoxy pre-polymers and the amines resulting in typical autocatalytic behavior. The tertiary amine group exerts an additional catalytic effect and causes the epoxide group to self-polymerize to form a poly-ether (reaction 3, figure 2.3). Other possible elementary reactions as the etherification (reaction 4, figure 2.3) between epoxy and formed hydroxyl groups can take place and competes with the epoxy-amine other elementary curing reactions.

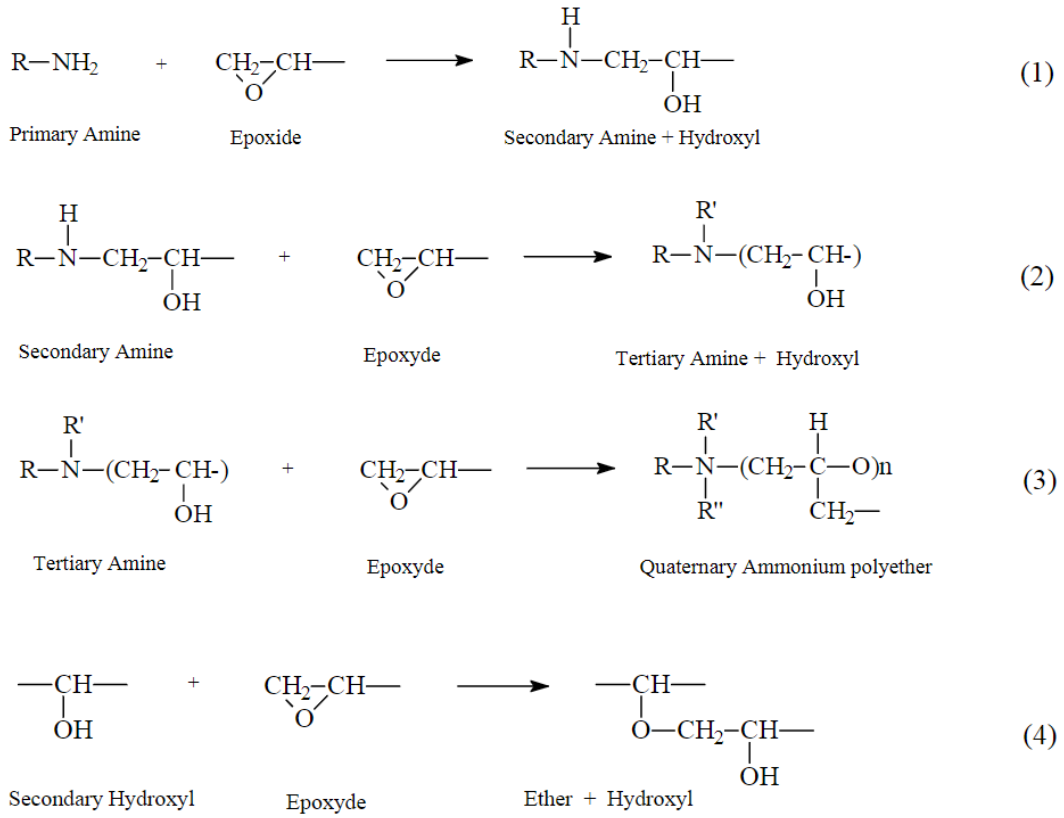

Figure 2.3: Scheme of curing reaction mechanism of Epoxy/Amine systems (1-3) and etherification (4) [37].

2.3 Literature review: Reminders on cure kinetics models of Epoxy/Amine systems

The crosslinking reaction of the epoxy matrix is triggered via external heating that results in an increase in its rate. The thermal history of the resin cure plays a major role on the kinetics of the different competing chemical reactions that can take place during the polymerization (figure 2.3). In the case of Epoxy/Amine systems, the cure kinetics can vary depending on the reactivity of the chosen amine hardener and the amount and functionality of the epoxy

pre-polymers. The presence of the hydroxyl catalysts in the reaction system, either initially introduced or produced during the reaction, also highly influences the kinetics of the cure mechanism. An appropriate characterization and modeling of the polymerization kinetics of thermosetting resins is necessary in order to provide a better representation of the changes that these reactive systems undergo during a curing cycle. The cure kinetics is defined as the rate of polymerization and is expressed by the derivative form of the conversion degree denoted by α as

$$\alpha(t) = \int_0^t \frac{d\alpha}{dt} dt \tag{2.1}$$

The purpose of a kinetics model of the curing reaction is to determine the polymerization rate of the material. The latter is commonly considered as function of time, temperature and the cure degree. A number of models have been reported in the literature for thermoset resins and can be applied to the Epoxy/Amine reaction system. These models can be divided in two categories: mechanistic and phenomenological models [166]. On the one hand, the mechanistic models describe precisely the crosslinking mechanisms by following all the elementary reactions likely to occur and are obtained from balances of reactive species involved in the reaction. According to works carried out by Stevenson and Lee [167, 168], these models have proved their ability to describe accurately the reaction kinetics of the unsaturated Polyester/Styrene system, taking into account the effect of the concentration of the introduced initiators and inhibitors on the polymerization rate. Nevertheless, such models remain more complex and require a thorough knowledge of the reaction system components which cannot be applied to the studied M21 system due to the lack of precise data on its formulation. On the other hand, phenomenological models are the most preferred for simplicity reasons since they require less kinetics parameters and generally expressed in a relatively simple rate equation. Indeed, they rely on experimental data to identify the parameters of the model. They are based on global considerations derived from the nature of the crosslinking of the systems ignoring the details of how reactive species take part in the reaction. There exist empirical models which are based on the principle of separation of variables. In this case, the polymerization rate of the reaction is expressed as the product of a function of temperature K(T) and a function of the cure degree $f(\alpha)$ as follows

$$\frac{d\alpha}{dt} = K(T) \cdot f(\alpha) \tag{2.2}$$

Among these models, we find the one proposed by Prime [169], described by equation 2.3, which is the simplest to use and correlates the kinetics of the reaction with the cure degree (α) by an n^{th} order rate equation

$$\frac{d\alpha}{dt} = K(T) \cdot (1-\alpha)^n \tag{2.3}$$

where n represents the reaction exponent and K(T) is the rate constant obeying an Arrhenius temperature dependency

$$K(T) = k_0 \cdot \exp\left(\frac{-E_a}{RT}\right) \tag{2.4}$$

with k_0 is a constant, E_a [J.mol^{-1}] is energy of activation, R [J.K^{-1}.mol^{-1}] is ideal gas constant and T[K] is the temperature. The author assumed that the entire polymerization of the Epoxy/Amine system can be described by a single overall reaction mechanism without

considering the effects of the catalytic present species or auto-catalytic components produced during the reaction. However, this is not always true given the multiple mechanisms that may be involved in the polymerization of epoxy/amine systems which may limit the reliability of this model to describe the autocatalytic behavior of this type of reaction. Kamal and Sourour [170, 171] proposed the first comprehensive empirical model that was the most widespread later on in several studies. These authors based their work on the assumption that the crosslinking of the epoxy/amine system occurs according to catalytic and auto-catalytic mechanisms, neglecting the etherification reaction. The model's mathematical expression is described by

$$\begin{aligned} \frac{d\alpha}{dt} &= (K_1(T) + K_2(T) \cdot \alpha^m) \cdot (1-\alpha)^n \\ \text{with } K_i(T) &= k_i \cdot \exp\left(\frac{-E_{ai}}{RT}\right),\ i = 1,2 \end{aligned} \tag{2.5}$$

where K_1(T), K_2(T) are cure rate constants obeying the Arrhenius temperature dependency and (n+m) represents the overall order of the reaction. This model has been widely applied to unsaturated polyester [172] and diamine-coupled epoxy thermoset systems. It has proved good agreement with experimental measurements and has also been modified in some cases to take into account other physical phenomena, such as vitrification. The polymerization reactions of thermosetting resins are rarely 100% achieved due to the decrease of free functions of present species or possible diffusion effects related to the verification phenomenon as well as a probable degradation of the matrix at high cure temperatures [73]. In order to take into account the incomplete polymerization for advanced crosslinking rates and to have more reliable predictions of the reaction kinetics, some authors [173, 174] have defined a variable $\alpha_{max} < 1$ to replace the unit value in equation 2.5, so that the modified Kamal and Sourour model became as follows

$$\frac{d\alpha}{dt} = (K_1(T) + K_2(T) \cdot \alpha^m) \cdot (\alpha_{max} - \alpha)^n \tag{2.6}$$

α_{max} illustrates the final reached limit of the crosslinking reaction for a given temperature. Its value is usually determined according to the corresponding used isothermal cure temperature on the basis of $\alpha_{max}(T_{iso})$ function experimentally identified. The latter generally follows an increasing linear regression of maximum reached levels of cure degree as a function of different isothermal cure temperatures T_{iso}. This empirical model has been particularly applied to the modeling of the curing kinetics of related derivative systems of the M21 resin with very similar behavior as M21E and M21EV systems and proved good agreement between experimental data and cure kinetics simulations [15, 162, 175, 176]. Bailleul [177] proposed an other phenomenological model stating the kinetics rate as a product of an Arrhenius temperature function K(T) and degree of cure polynomial function G(α) as presented by equations 2.7 where T_{ref}(K) is a temperature chosen arbitrarily in the considered curing temperature range to which is associated the parameter k_{ref} and a_i are the coefficients of

polynomial function.

$$\begin{aligned} \frac{d\alpha}{dt} &= K(T) \cdot G(\alpha) \\ \text{with } K(T) &= k_{ref} \cdot \exp\left(-A\left(\frac{T_{ref}}{T} - 1\right)\right) \\ \text{and } G(\alpha) &= \sum_{i=0}^{n} a_i \alpha^i \end{aligned} \tag{2.7}$$

This model has been widely used and proved its ability to predict the cure kinetics of different reaction systems. It was extended in certain works to account for the effect of vitrification on the reaction kinetics and to include the effects of diffusion associated to network formation. This model was also modified by the addition of an inhibition function that allows to consider the effect of inhibitor on the curing kinetics as in the case of polymerization of unsaturated Polyester/Styrene systems [178] or vinylester resins [12]. Bailleul's model has been particularly improved by Msallem *et al.* [46] to predict the cure kinetics of a similar M21 Epoxy/Amine based resin system which will be further detailed in the next section.

2.4 Thermo-chemical characterization and model validation of the M21 resin cure kinetics

2.4.1 Model validation of the curing kinetics

Please note that, the objective of this section is not to identify a novel cure kinetics model for the studied resin, but to validate the most suitable one that allows to accurately describe its cure degree development during a curing cycle. On the basis of the previous brief reviewing on developed cure kinetics models applied to similar systems as M21 resin, but most importantly, according to what is available as non confidential data (*i.e.*, model parameters) concerning this aerospace-grade resin, the Bailleul's model modified by Msallem *et al.* was chosen to be employed. For this, a comparison between obtained results in Msallem's work and the experimental thermo-chemical behavior of our matrix is carried out to justify the model choice.

2.4.1.1 Dynamical Scanning Calorimetry (DSC) characterization

DSC tests were firstly conducted on M21 resin samples in order to provide an objective point of comparison with the available information about the different M21 systems' physical properties in literature. A TA Instruments Q200 differential scanning calorimeter was used in our case of study. Samples of M21 resin with less than 10 mg of weight were used and aluminum hermetic pans were employed. Only non isothermal dynamic scans were carried out with ramp rates of 3, 5 and 10°C.min^{-1}. Performed thermal cycles consist of an initial isothermal of 2 min at -30°C, then the material is heated up to 310°C which is also maintained during 2 min before the cooling stage. The analysis of DSC thermogram obtained by temperature scanning at the rate 10°C.min^{-1} is presented in the figure 2.4.

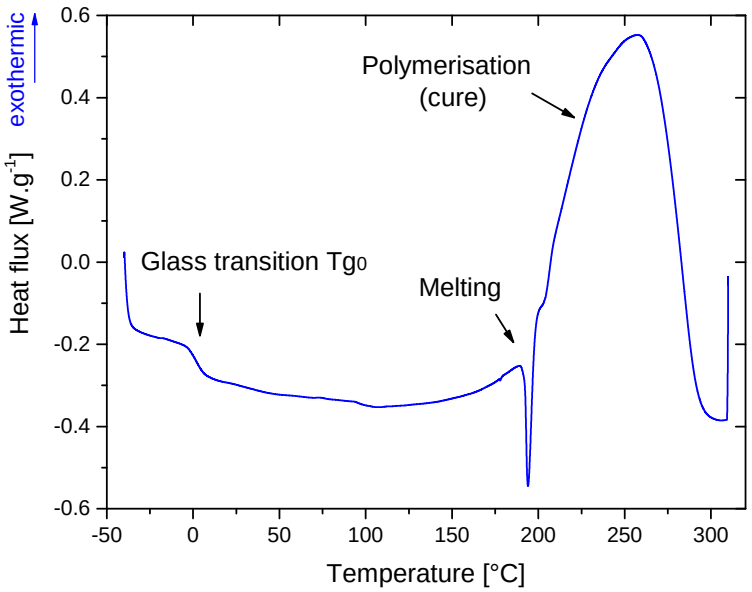

Figure 2.4: DSC dynamic scan of M21 resin for a heating rate of 10°C.min^{-1}. Heat flux recorded as a function of temperature.

The heat flux curves present systematically a large exothermic peak that starts nearly to 120°C showing the cross-linking reaction of the resin. We can also observe, starting from the lowest temperatures, the inflection point related to the glass transition T_{g0} of the uncured resin around 0°C. This temperature was also detected around 0°C in Paris *et al.* works [162] and at -4.15°C in the study carried out by Msallem *et al.* [46]. We can notice from this thermogram, the presence of an endothermic peak situated at 192°C. The temperature corresponding to this endothermic peak varies slightly with the applied heating rate. Indeed, we obtained a melting temperature T_F = 197°C for 5°C.min^{-1} of ramp rate and T_F = 205°C for 3°C.min^{-1}. Similar results were obtained in [46]. Based on the data present in the patent [64] of the M21 resin in addition to the reported similar results in literature, one can admit that this melting peak corresponds to the thermoplastic particles incorporated in the M21 system. More precisely, this endothermic peak is consistent with the melting temperature of high-melting thermoplastics as discussed in subsection 2.2.2, which may be related to copolymers that contain significant contents of polyamide 6.

The total enthalpy of the cross-linking reaction denoted as ΔH_{tot} is obtained by integration of the area under the exothermic peak which can be done using a classical method such as the trapezoid rule. However, the presence of the endothermic peak masks a part of the heat flux released at the beginning of the polymerization which alters the final value of the total transformation enthalpy of the resin sample. The choice was made to remove this endothermic peak by a post-processing (see figure 2.5). The integration of the area under the exothermic peak after removal of the endothermic peak is done by defining a sigmoid as baseline [81, 177] since the specific heat Cp evolves with the polymerization degree of the resin which passes from a raw uncured state to a cured state. The sigmoid integration line is defined between two points m_1 and m_2, and whose equation can be written by the following form

$$C_p(\alpha) \quad = \quad (1-\alpha)\ Cp_{m1} \quad + \quad \alpha\ Cp_{m2} \tag{2.8}$$

where α is the degree of cure advancement, Cp_{m1} and Cp_{m2} are respectively, the specific heats at the beginning and at the end of the crosslinking reaction. Since the evolution of the cure degree over time is unknown, an iterative treatment was conducted based initially on a linear integration baseline to tend progressively towards the sigmoid.

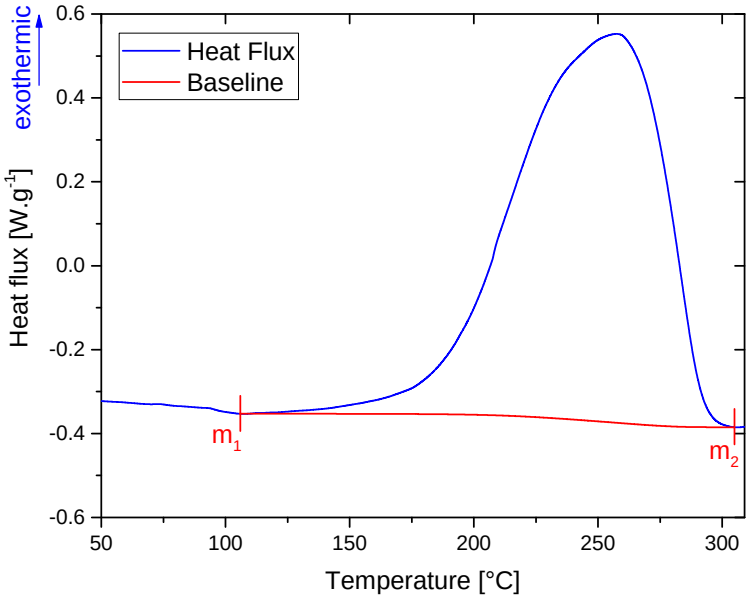

Figure 2.5: Baseline after removing the endothermic peak.

The average value of the total enthalpy of the reaction $\Delta H_{tot-DSC}$ obtained according to the different heating rates is estimated equal to 412 ± 8 J.g^{-1}. This value is consistent with the measurement obtained in the literature for the epoxy system M21. Ledru *et al.* [176] determined an average value of ΔH_{tot} = 420 ± 20 J.g^{-1}. It was estimated equal to 424.5 ± 10.2 J.g^{-1} and 445.1 ± 5.9 J.g^{-1}, respectively, in the works of Paris and Msallem [46, 162] on the basis of dynamic DSC analysis. The degrees of cure development related to the crosslinking reactions as well as the different polymerization rates are calculated from the experimental data provided by the DSC for the applied 3 heating rates according to equations 2.9 and 2.1, respectively. $\alpha(t)$ can be calculated as the ratio between the instantaneous and the total transformation enthalpy:

$$\alpha(t) = \frac{\int_0^t \Delta H(t)dt}{\Delta H_{tot}} \tag{2.9}$$

Analysis of the evolution of cure degrees as function of temperature in figure 2.6a shows that the curves shift to higher temperatures as the heating rate increases. The evolution of the polymerization rates presented in figure 2.6b reveals that the cross-linking kinetics increases with the heating rate as well as it shows that the maximum peak moves towards high

temperatures. Indeed, it is verified that a slow heating rate favors the cross-linking of a large number of chemical groups which induces the onset of the polymerization reaction to occur at lower temperatures for slower heating rates (auto-catalytic effect of the reaction) [146, 179]. Thus, lower heating rate promotes lower gel temperature values.

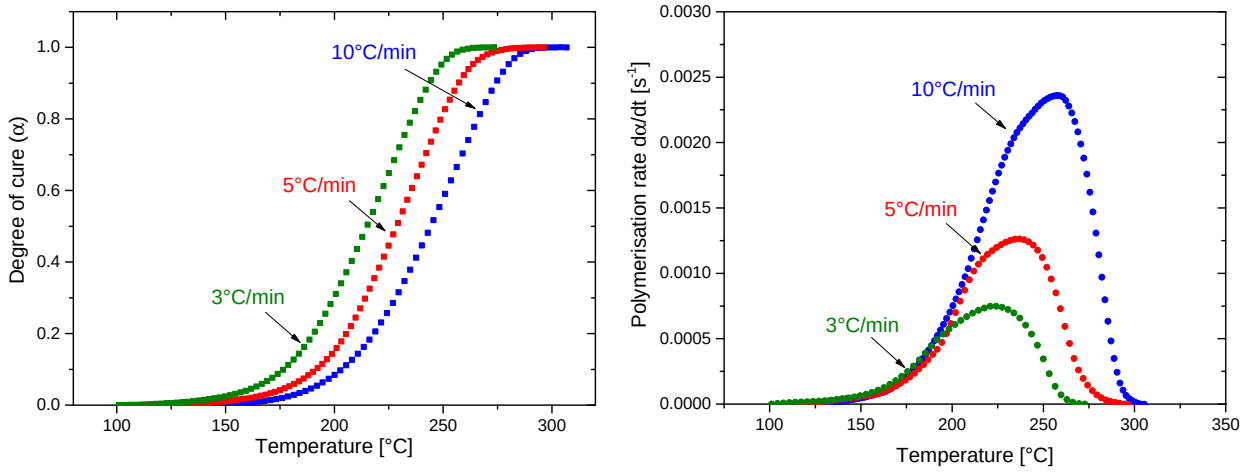

(a) (b)

Figure 2.6: DSC experimental measurements of the cure degree (a) and the polymerization rate (b) for different heating ramps at 3, 5 and 10°C.min^{-1}.

2.4.1.2 Characterization using the PvT-α mold

The experimental procedure employed by Msallem *et al.* [46] in developing the cure kinetics model for the M21 epoxy system was rather based on tests performed with the Pvt-α mold (see subsection 1.3.1 for more details about the experimental bench). The author choice was derived from the requirement of providing a more accurate simulation of thermoset composites material cure kinetics. Hence, the PvT-α mold presents a good candidate that allows the establishment of an empirical kinetics model on the basis of experimental tests carried out on resin samples with more representative dimensions, during an industrial and real thermal cycle under high pressure. It also enables to overcome some limitations faced with DSC measurements, commonly employed in such context, that cannot attain accurate and continuous measurement of the cure kinetics limited to only few milligrams of samples weight. The developed kinetics model by Msallem *et al.* [46] is in fact an extended version of Bailleul's model described by equation 2.7 that takes into account the effects of the glass transition temperature on the polymerization rate. Model parameters were identified on the basis of experimental curing tests of more representative volume element of matrix. The identification of model parameters was conducted using a specific software named as Polykinetic®. Used resin samples in the investigation conducted by Msallem *et al.* were 6 mm thick cylinders with diameter of 45 mm. The cure kinetics model is described by the following equations as

$$\begin{cases} \frac{d\alpha}{dt} &= G(\alpha)\cdot K_A(T)\cdot K_D(T,\alpha) \\ G(\alpha) &= \sum_{i=0}^{i=7} a_i\cdot\alpha^i \\ K_A(T) &= K_{ref}\cdot\exp\left(-A\left(\frac{T_{ref}}{T}-1\right)\right) \\ K_D(T,\alpha) &= K_2\cdot\exp\left(C_1\left(\frac{T-T_{g(\alpha)}}{C_2\lvert T-T_g(\alpha)\rvert}\right)\right) \\ T_g(\alpha) &= T_{g0}+\frac{(T_{g\infty}-T_{g0})\cdot\lambda\cdot\alpha}{(1-(1-\lambda)\cdot\alpha)} \end{cases} \tag{2.10}$$

where α is the degree of cure, $d\alpha/dt$ is the crosslinking rate and $G(\alpha)$ is a polynomial function. $K_A(T)$ is the Arrhenius law that describes the dependence of the cure rate on temperature (T). $K_D(T,\alpha)$ is an exponential function that describes the effect of glass transition on the diffusion of macromolecules and the cure kinetics rate [74] where $T_{g\infty}$ and T_{g0} are the glass transition temperature for the cured and uncured resins respectively. λ is a material constant. The values of the model parameters are gathered in table 2.3.

Table 2.3: Parameters of Bailleul's cure kinetics model modified by Msallem *et al.* [46].

G(α)	a_0 = 0.88	a_1 = 1.81	a_2 = -5.48	a_3 = 29.26
	a_4 = 138.39	a_5 = -232.08	a_6= 177.59	a_7= -52.37
K_A(T)	T_{ref} = 493.13 K	K_{ref} = 0.00164 s^{-1}	A = 19.113	
K_D(T)	K_2 = 0.335	C_1 = 2.3	C_2 = 60 K	
$T_g(\alpha)$	$T_{g\infty}$ = 215° C	T_{g0}=-4.15° C	λ = 0.551	

In our case of study, model adequacy was ascertained by measurement conducted with the M21 resin using the PvT-α mold during the curing under a constant pressure of 50 bars and according to the manufacturer's recommended thermal cycle. The latter consists of a heating ramp of 2°C/min up to 180°C followed by an isothermal curing dwell, commonly of 120 min. In these testings, the applied isothermal cure was held for 200 min. One should mention that such high pressure applied around the neat resin sample was used as recommended in previous work [12,103,180] conducted on PvT-α mold and has no particular effect on the resin thermo-chemical behavior during the cure. Please note that, the experimental tests conducted on the neat resin using the PvT-α mold were carried out by the team of Capacités® SAS, the Engineering and Research valuation subsidiary of the University of Nantes.

Two samples were tested for this investigation to ensure the reproducibility of results with initial thickness of 6 mm and diameter equal to 44 mm for each. Resin samples' weights are 11.431 g for sample (1) and 12.274 g for sample (2). As described in chapter 1, PvT-α mold enables to simultaneously measure the surface temperature and the heat flux exchanged between the sample and the mold during the cure. The latter is determined thanks to the heat flux sensors embedded inside the piston and the cavity. Figure 2.7 gives an example of the sample surface temperature related to the prescribed thermal cycle and the measured heat flux plotted versus time brought by sample (1) response. The matrix transformation is characterized by the exothermic peak related to the heat flux generated during the crosslinking reaction. It seems to start during the heating ramp at a temperature nearly to 85°C at

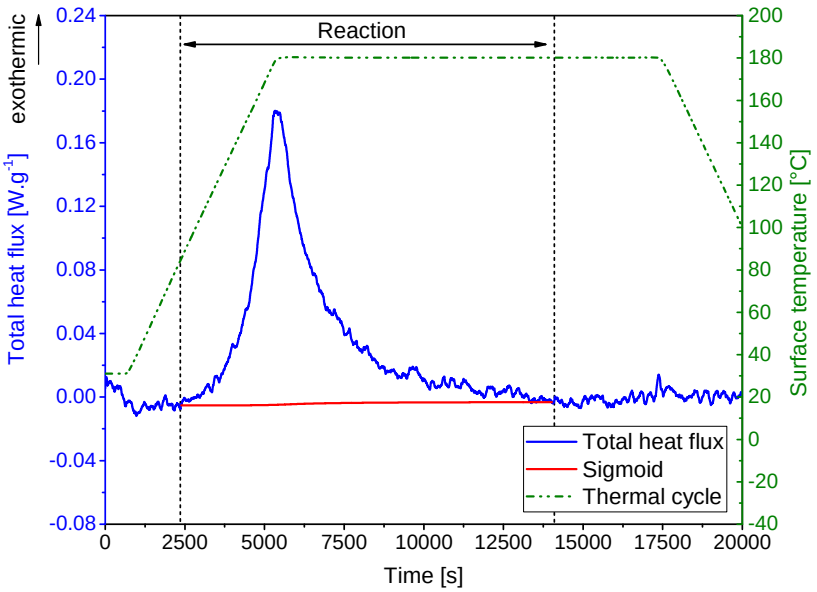

Figure 2.7: An example of heat flux and surface temperature recorded as function of time during the cure of M21 resin sample (1) in the PvT-α mold.

approximately t = 2350s and ends by t = 14100s, since no variation in the heat flux is observed after this time. The calculation of the area under the corresponding exothermic peak, delimited by a defined sigmoid curve adjusted during the reaction, gives an estimation of the total transformation enthalpy ΔH_{tot}. The latter is calculated on the basis of both tested resin samples by $\Delta H_{tot-PvT} = 417 \pm 15$ J.g^{-1} which is consistent with the value obtained from DSC analysis. According to the classical approach in DSC analysis it is possible to estimate the experimental conversion degree according to equation 2.9. The latter is calculated between t = 2350s and t = 14100s. The obtained degree of cure evolution with time is plotted in figure 2.8 and is compared to the estimated one using the kinetic model from equation 2.10. The experimental data are presented by an average curve obtained from resin samples (1) and (2) responses. The scattering of measured degree of cure is given by standard deviation error bars that remain below $\pm$ 2 10^{-2}. As indicated in figure 2.8 there is a very good agreement between experimental data and the model prediction for the degree of cure evolution during the applied thermal cycle. It is evident from this example, the model prediction of α_{max} at the end of the reaction is rather different from the unit value and equal to 94%. The incomplete polymerization can be related to the vitrification phenomenon (Tg(α) becomes $\geq$ 180°C) that takes place nearly to t = 11500s according to the model prediction of glass transition evolution with curing. From that moment, the resin transforms from a rubber to a gelled glass which resulted in the cessation of the crosslinking reaction. At the end of the performed isothermal hold, the cured material glass transition temperature is estimated equal to 200.2 °C.

In figure 2.9 are given the experimental average curve of the polymerization rate calculated according to equation 2.1 and the predicted one by the kinetic model altogether with the prescribed thermal cycle. Plotted error bars give standard deviation of the variation in measured curing rates with reference to both resin samples which remain below $\pm$ 2.2 10^{-5}.

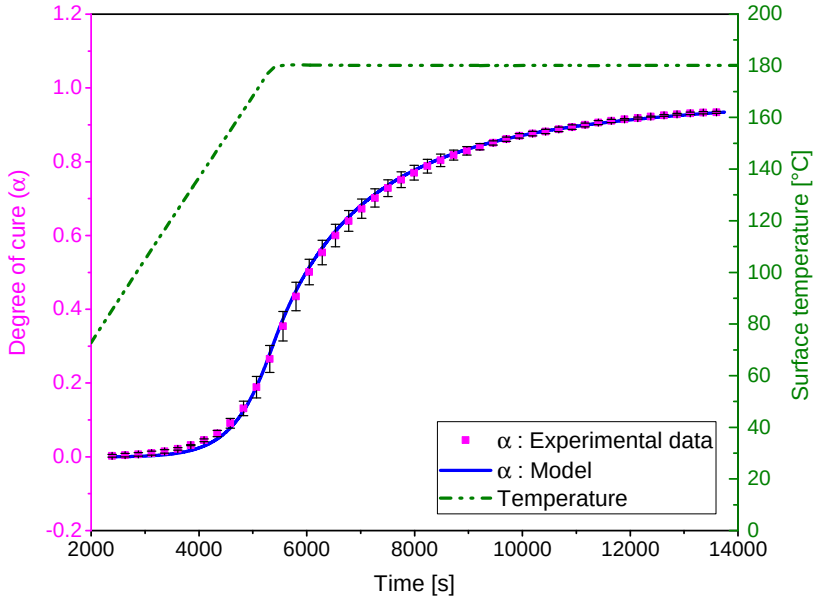

Figure 2.8: Experimental conversion degree evolution as function of time calculated from equation 2.9 and obtained from PvT-α mold measurements, in comparison with the one predicted by the kinetics model from equation 2.10.

Again, experimental data obtained from PvT-α measurements show very good consistency with the model prediction of the polymerization rate during the total thermal cycle which validates the choice of the kinetic model for our M21 resin system.

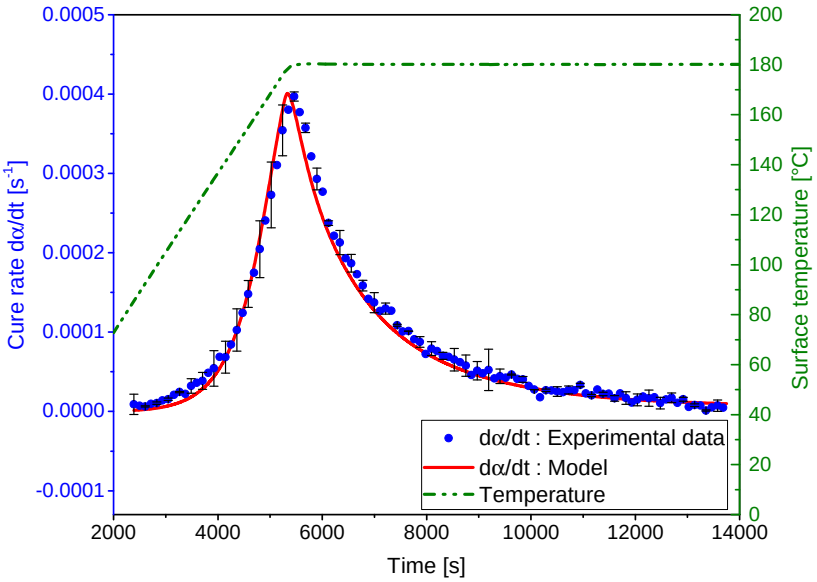

Figure 2.9: Experimental polymerization rate evolution as function of time calculated from equation 2.1 and obtained from PvT-α mold measurements, in comparison with the one predicted by the kinetics model from equation 2.10.

2.4.2 Characterization of the volumetric behavior of the M21 resin during the cure by using the PvT-α mold

As previously mentioned, other than the measurements of the heat flux and the surface temperature, the PvT-α mold allows to simultaneously record the volumetric change of the resin sample during the cure for a given cycle. As described in chapter 1, the resin sample is inserted in an elastomer capsule placed in the mold cavity during the cure. The applied pressure around the sample is assumed to be constant and hydrostatic and the elastomer surface remains constant since it is deformable. As a consequence, the measured displacement by the LVDT sensor through the thickness of the sample that can be denoted as Δh, is directly related to the increment of sample volume variation as $\Delta V = S \times \Delta h$ where S is the sample section. Figure 2.10 depicts the evolution of the measured volume change (ΔV) versus time during the whole scanning temperature run of sample (2) taken as example. This curve has a classical behavior where three main parts can be distinguished:

1. During the heating ramp, the increase of temperature leads to a large increase of the sample volume which is mainly attributed to the thermal expansion of the material.
2. During the isothermal cure, a steep drop in the sample volume is observed because of the shrinkage induced by the resin polymerization.
3. During the cooling step, the volume decrease is due only to thermal contractions.

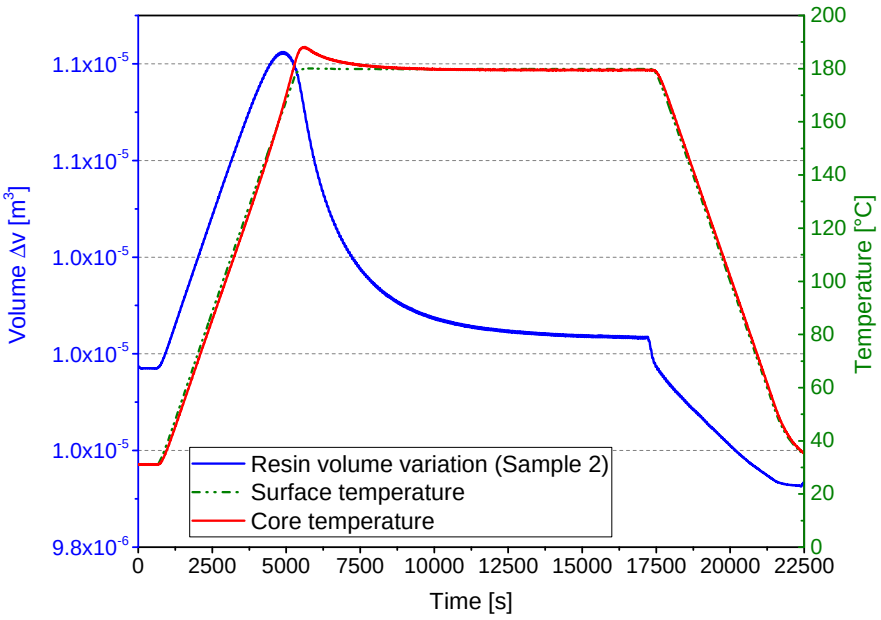

Figure 2.10: Typical dilatometric curve of volumetric behavior obtained with PvT-α apparatus of the M21 resin during a curing cycle (Obtained results from sample (2) testing).

Figure 2.10 also shows a comparison between the evolution of the temperature measured at the surface and core of the resin during the cure cycle. The latter was recorded by a 80 μm-diameter thermocouple (K-type) located in the middle of sample 2. The steps identified

from the volume variation are identical to those of sample 1 which is not presented here for the sake of clarity. From this figure, we can observe that the exothermicity of reaction generates a temperature difference between the surface and the core at the beginning of the isothermal stage. The latter reached up to 6°C (for 6 mm thick sample), which is considered negligible.

Assuming that temperature and transformation gradients are negligible, the overall change in the volume of the resin sample throughout the cure cycle is defined as a combination between the volumetric variation due to the thermal effects and chemical shrinkage as described by equation 2.11:

$$\frac{\Delta V}{V_0} = \frac{S \times \Delta h}{S \times h_0} = CTE_V \cdot \Delta T + CCS_V \cdot \Delta\alpha \tag{2.11}$$

Where $\Delta V/V_0$ is the volume deformation of the resin sample. CTE_V is the volumetric coefficient of thermal expansion and CCS_V is the volumetric coefficient corresponding to the chemical shrinkage of the resin. Please note that, the thickness variation measured by the LVDT displacement sensor of the PVT device integrates the variation of the resin, the elastomer capsule, as well as the thermal expansion of the mold. A calibration of the displacement sensor in the temperature range of the test is thus carried out beforehand. Δh is the variation along the thickness direction of the elastomer and the resin. h_0 is the initial measured thickness by the sensor and S is the in-plane capsule section assumed constant [181]. A subtraction of the contribution of the elastomer capsule displacements is also conducted knowing its coefficient of thermal expansion (evaluated independently). In order to estimate the volumetric CTE of the resin, the volume deformation $\Delta V/V_0$ is plotted versus the temperature as it is illustrated by figure 2.11a.

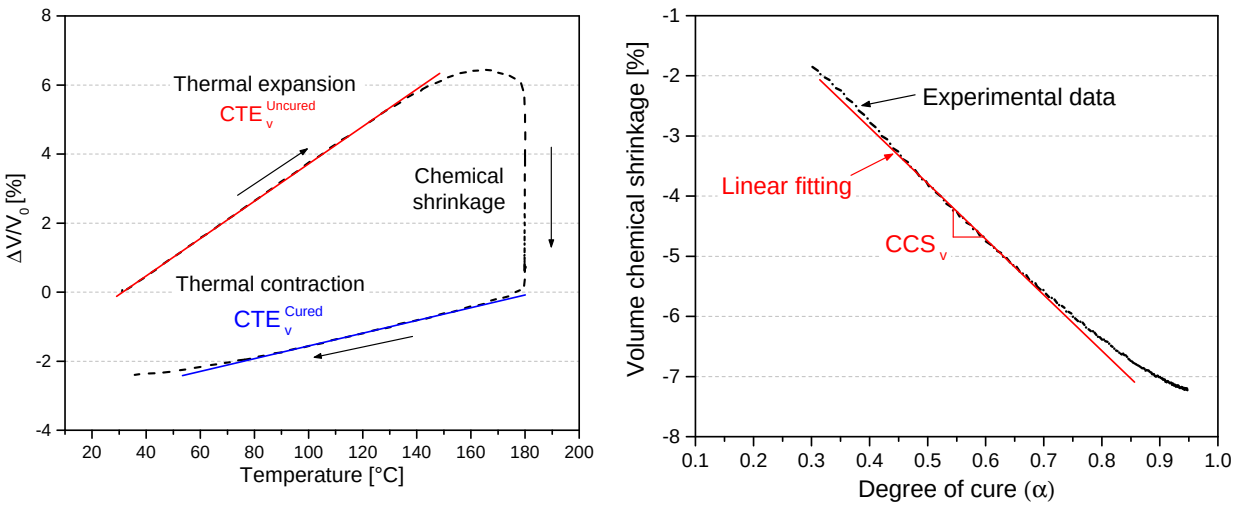

(a) (b)

Figure 2.11: (a) Variation of volume strains of the M21 resin as a function of the thermal cycle. (b) Variation of the volume chemical shrinkage of the M21 resin as a function of the predicted degree of cure.

During the heating ramp, the increase of the sample volume is mainly driven by thermal effects. The resin is assumed to be at the uncured state until nearly T = 130°C and chemical shrinkage still be negligible. Above this temperature, curing effects start to become more prominent and the polymerization reaction starts to induce a non linear behavior in the curve. The slope of the linear zone below T = 130°C represents the volumetric CTE of the resin at its liquid state. During cooling, the slope of the curve gives the volumetric CTE in the cured glassy state (below Tg). The estimated values are reported in table 2.4.

Table 2.4: Measured volumetric CTE and CCS of the M21 Resin.

Property	Symbol	Unit	Value
Volumetric CTE in the uncured state	$CTE_V^{Uncured}$	10^{-6} K^{-1}	537
Volumetric CTE in the cured glassy state	CTE_V^{Cured}	10^{-6} K^{-1}	188
Volumetric CCS	CCS_V	%	-9.17

Assuming a linear dependence of CTE_V with the degree of cure following a rule of mixture between the uncured and the fully cured values as described in equation 2.12, it is possible, by subtracting the thermal part from the total volume variation (according to equation 2.11), to estimate the free strains due to the chemical shrinkage only.

$$CTE_V(\alpha) = \alpha \quad CTE_V^{Cured} + (1-\alpha) \quad CTE_V^{Uncured} \tag{2.12}$$

In order to estimate the volumetric CCS of the neat resin, the variation of the volume shrinkage during the isothermal step is plotted versus the predicted degree of cure. Thus, data in figure 2.11b suggest a linear relation between the volumetric chemical shrinkage and the degree of cure. The slope is directly related to the volumetric CCS of the resin. The estimated values of the material parameters, CTE and CCS, are gathered in table 2.4. The obtained results are consistent with the estimated values by Msallem *et al.* [46] who reported a volumetric CTE at the uncured state equal to 606 10^{-6} K^{-1} and a cured CTE_V equal to 135 10^{-6} K^{-1}. The reported volumetric CCS is equal to -6 %.

2.5 Rheological characterization of the M21 resin: Gel point determination

A rheological characterization is performed to correctly identify the gel point of the studied M21 resin since available information in the literature are not well consistent. α_{gel} value was reported by Ledru and Paris [162,176] to be equal to $34 \pm 0.5\%$ and 36% respectively, however, Msallem *et al.* [46] estimated a gel point equal to 52 ± 1 %. For the characterization of the gel point, dynamic rheological measurements were performed using a HAAKE™MARS™ Rheometer. Parallel-plate geometry was used with 20 mm of plate diameter. The preparation of samples proved to be quite difficult since the resin was supplied in thin layers on paper films. It was absolutely necessary to scrape the resin from the films to obtain the required quantities. Such procedure induced large amount of air bubbles entrapped inside the formed samples. It was essential to perform a compaction step under applied pressure at a temperature equal

to 50°C for a short period of time $\leq$ 10 min. For this, sufficient quantity of resin was placed in a specific mold, on which the pressure was applied, and that allows to obtain resin pellet of approximately 0.9 mm of thickness and around 18 mm of diameter. Resin pallets were stored in sealed bags before the testing for at least 12 hours to ensure that solicitation effects related to the preforming step are completely removed in order to have the same initial state of samples before rheological measurements.

The criterion that seems to have the best accuracy to assess the gel point, according to the literature, was assumed to be the independence of $\tan(\delta)$ of frequency. Performed tests were carried out at different isotherms: 160, 170 and 180°C. Each test for a given temperature was undertaken on 2 samples to probe the reproducibility of measurements. For each given isotherm cure, frequency sweep of three different levels were performed on the same sample. The rheological multi-wave method provides an opportunity to obtain, in a single experiment, simultaneously, multiple information data. The chosen frequencies are 1, 10 and 100 rad/s with 5% applied strain amplitude. The time of the scanning test must be small enough to make the assumption that the degree of cure remains constant during the test which is not easy for high temperatures. That's why the maximum level of isotherm was chosen equal to 180°C. Higher temperatures were difficult to manage and would have induced more uncertainties in the measuring procedure.

Figures 2.12a and 2.12b, depict the plotting of the loss factor $\tan(\delta)$ as a function of time for the three different frequencies at 160°C and 180°C isotherm temperatures, taken as examples, respectively. Results obtained from T = 170°C test are also similar. The gel time is observed as the crossover of $\tan(\delta)$ curves for each given temperature. We can now determine the gel point α_{gel} that corresponds to each estimated gel time by using the kinetics model (equation 2.10) to estimate the corresponding degree of cure. The obtained results for all tested temperatures are gathered in table 2.5. The gel point is assumed equal to an average value $\alpha_{gel} = 52 \pm 1.4\%$ which in agreement with the estimated value by Msallem *et al.* [46].

Table 2.5: Gel point at different isotherms.

Temperature	°C	160	160	170	170	180	180
α_{gel}	%	51	53	53	50	54	52
Mean value of α_{gel}	%			52 ± 1.4			

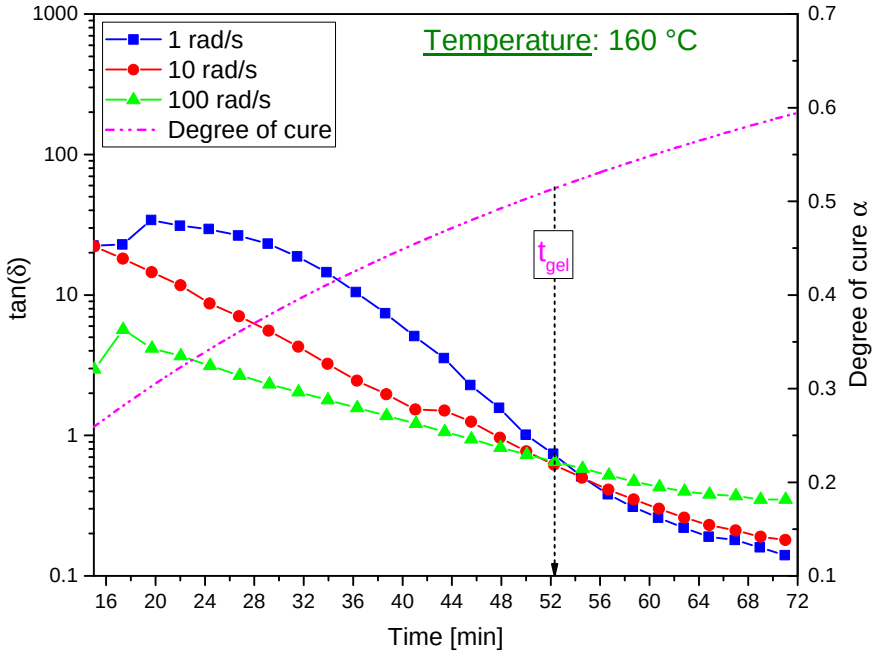

(a)

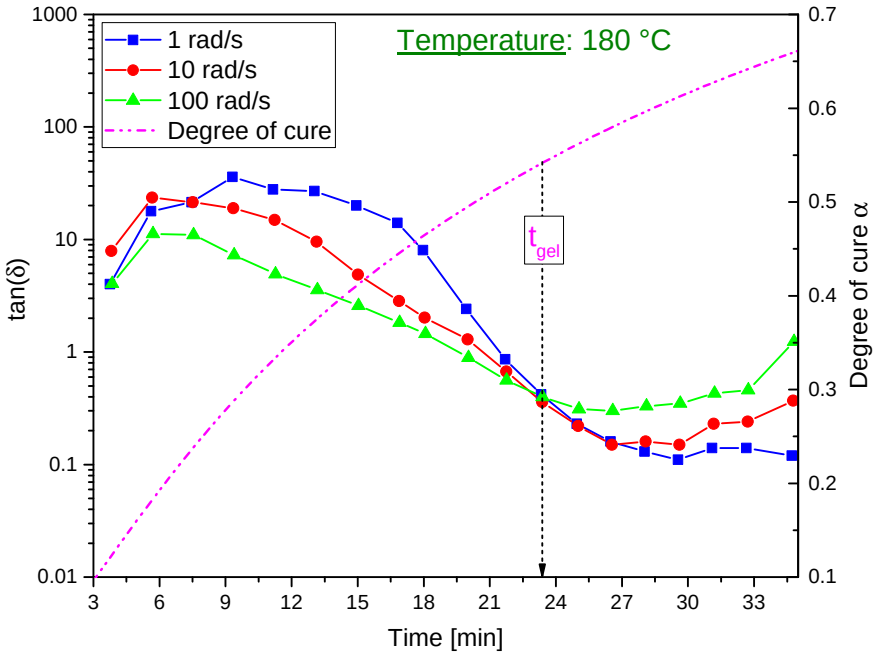

(b)

Figure 2.12: Loss factor tan(δ) as a function of time at three different frequencies during the isothermal curing of the M21 resin at (a) 160°C and (b) 180°C.

2.6 Presentation of the PvT-HADDOC set-up and the imported improvements

2.6.1 Design and global working principle

The overall characterization of the thermo-chemo-rheological behavior throughout the curing of the IMA/M21 studied composite is conducted using a home-made laboratory apparatus named as PvT-HADDOC for Pressure, Volume and Temperature - Homogeneous Anisotropic Deformation and Degree Of Cure monitoring. The device enables the measurements of the induced curing strains of anisotropic thermosetting composites during the whole cure, simultaneously along the out-of-plane and the in-plane directions. Based on controlled homogeneous mechanical and thermal conditions, this set-up can provide an analysis of the intrinsic behavior of thermoset composites along the cure cycle, independently of the particular bagging conditions commonly used in the case of autoclave manufacturing process. In addition, other physical quantities such as the reaction progress, the temperature of the sample surfaces and the performed pressure can be measured with the device.

The PvT-HADDOC is indeed an already existing bench that has been initially designed during the thesis work carried out by Peron [38]. Relying on previous obtained results, it was pointed-out that some improvements of the first developed version of the device are necessary in order to enable ideal homogeneous thermal and mechanical states around the samples while curing. An outline of the introduced improvements is given in next subsections. As the characterization of the process-induced strains through multi-axial measurements is the main objective of this work, the adopted experimental protocol of displacement measurements will also be detailed in subsection 2.6.4.

The PvT-Haddoc bench consists essentially of a mold cavity that was designed specifically to enable the curing during the experiment of composite samples with more representative dimensions than the ones commonly used in classical methods like DMA. The curing is ensured under high pressure and temperature, as typically recommended for high performance thermoset composites. The mold cavity is attached to an Instron ElectroPuls E10000 Electrical Press and placed on its fixed frame, as it is illustrated by both figures in 2.13. The Instron machine is controlled by a computer on which the Console software control interface and WaveMatrix™ specific software are installed. The latter enables to perform the desired conditions during the testing as it controls the applied displacements and the desired applied force level by the piston during the cure. This universal testing machine is designed for dynamic and static testing with a load cell of ± 10 kN. The WaveMatrix™ software allows a large flexibility to run complex multi-step tests from a simple static ramp to cyclic wave-forms. It is in fact the assembly mold-cavity/Instron-Press that allows the monitoring of the material behavior throughout a whole thermo-mechanical curing cycle. Used composite samples in this set-up may have as maximal square base dimensions equal to 105×105 mm^2 and several millimeters thick ideally that do not exceed 10 mm. During the experiment, the sample is placed between the piston which is assembled to the moving frame of the machine and a plate that is attached to the lower heat exchanger of the cavity (see figure 2.13-*right*). Both, the

piston and the lower plate are made of stainless steel. This cavity can be filled with silicone oil, allowing on the one hand, to apply pressure on the lateral surfaces of the sample and on the other hand, to ensure the control of the surface temperature of the tested sample.

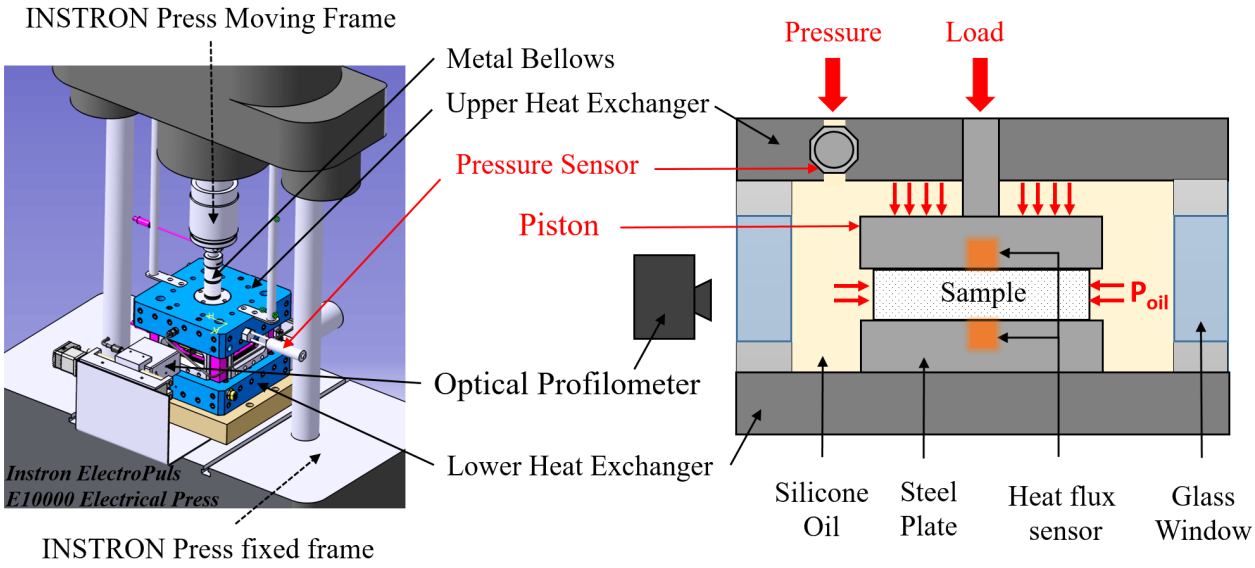

Figure 2.13: Global overview of the PvT-HADDOC experimental setup. 3D conception (left) and a scheme of the mold cavity (right).

2.6.2 Thermal control

The curing of tested samples takes place inside of the mold cavity only when the latter is filled up with a silicon oil named as CALSIL™IP 50. The employed oil is in fact totally colorless, chemically inert and has stable physical properties from -40°C to 200°C [182]. During the experiment, the sample is surrounded by the silicon oil and its lateral surfaces are in direct contact with the latter. The application of the selected thermal cure cycle inside of the cavity is ensured by both heat exchangers that are connected to a Vulcatherm thermo-controller unit, as schematically illustrated in figure 2.14. The latter allows the heating/cooling of the system by circulating a heating oil through the exchangers. Note that, the heating oil circuit in the system is different from the one related to the silicone oil. A PT100 sensor is placed in one of the exchangers in order to serve as input for the thermo-controller PID. The allowed temperature in the present system can reach up to 200°C. The thermo-controller enables a fast heating/cooling rate that can reach to 16°C.min^{-1}. The latter is however limited to 5°C.min^{-1} in order to diminish induced temperature gradients through the composite sample thickness for the current investigations.

The silicon oil circulates continuously inside the pressurized cavity and through both exchangers due to a circulator pump inserted inside the cavity (see figure 2.16 for more clarity) in order to provide the thermal homogeneity around the sample. As it is depicted in figure 2.14, the silicone oil circuit is controlled by hydraulic and pneumatic actuators system that allows the filling of the cavity and also ensure the application of the desired pressure during the test. A PT100 sensor is also placed in the cavity so as to obtain information

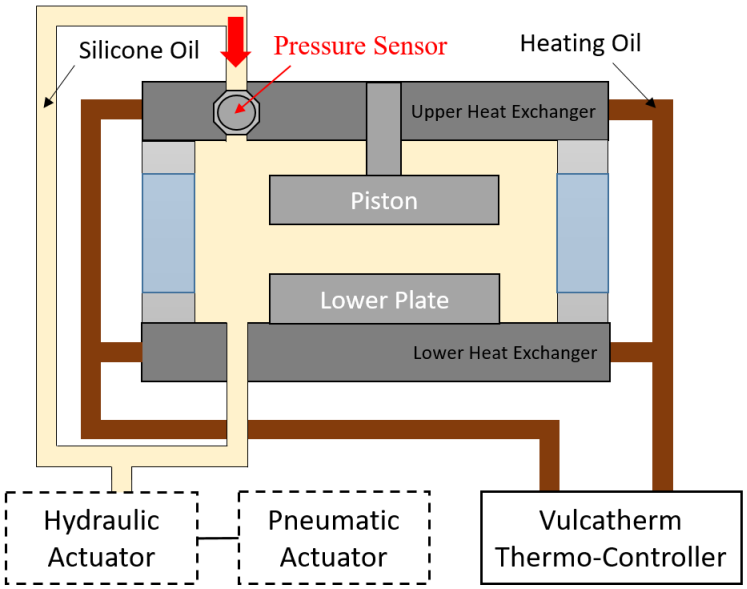

Figure 2.14: Scheme of the heating circuits of the PvT-Haddoc device.

about the oil temperature during the curing. As presented in figure 2.13-*right*, two heat flux sensors are embedded in the piston and the steel plate so that they are in contact, respectively, with the upper and lower sample surfaces. Data treatment of these sensors, as it is described in [183], provides information about the surface temperatures of the sample and the heat flux exchanged between the latter and the device. It is then possible to estimate the experimental degree of cure of the sample by analyzing these fluxes during the chemical reaction of the material.

First experiments carried out by Peron *et al.* [38] showed the insufficiency of the heating system to provide accurate thermal control for the piston and the lower plate during a curing cycle. Measurements of surface temperatures of the piston and the lower plate revealed significant disparities compared to the applied thermal cycle as presented by figure 2.15a. The performed thermal cycle by Peron *et al.* [38] consists of a first isothermal hold at 30°C during 10 min, then the system is heated at 3°C.min^{-1} up to 90°C where an isotherm of 10 min is performed, followed afterwards by a second heating step up to 100°C with the same rate. An isothermal dwell at this temperature is applied for 40 min, then the system is cooled at 3°C.min^{-1} until 30°C. Revealed temperature deviations between the piston and the plate reached up to 19°C. This can lead to high temperature gradients through the thickness of the sample and consequently gradients in the degree of cure which can be responsible for process induced residual stresses.

In order for the surface temperature of the piston to better follow the curing cycle, cartridge heaters were inserted into the latter to compensate the deficiency of convective heat exchanges between the piston and the silicone oil (see figure 2.16). The temperature of the piston is then better controlled during the heating ramp as well as during the isothermal hold, by means of a power compensation based on a PID regulation. The latter tends to limit temperature disparities between the piston and the oil. The cooling-down phase is also improved by the

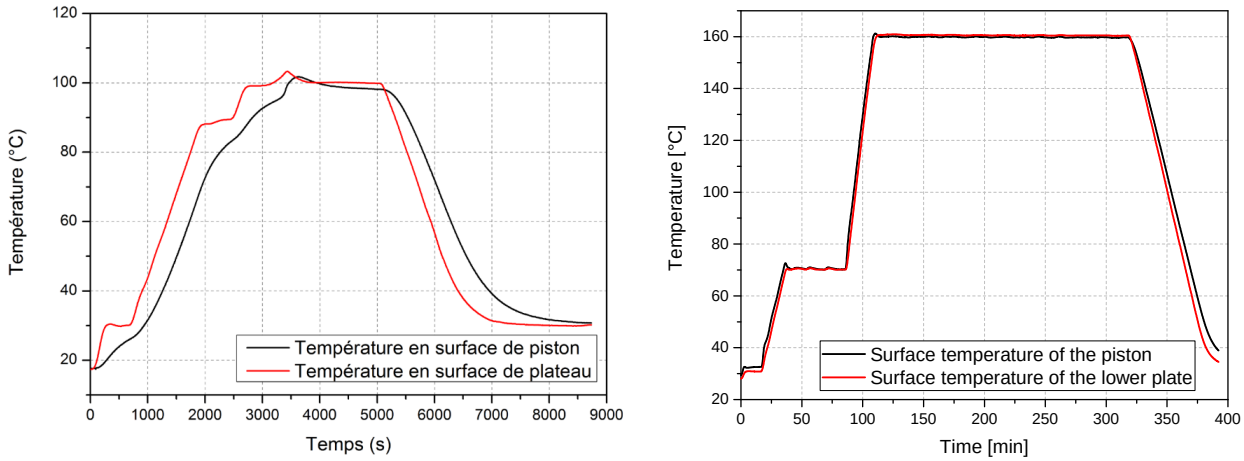

(a) (b)

Figure 2.15: Surface temperature evolution of the piston and the lower plate during a curing cycle: (a) Before thermal system improvement (extracted from Peron *et al.* work [38]). (b) Current study after thermal system improvement.

insertion of a rectangular aluminum fin on the piston (see figure 2.16) that increases the surface exchange between the latter and the silicone oil. This allowed to maximize the heat transfer during the cooling of the system and to follow more precisely the imposed curing cycle.

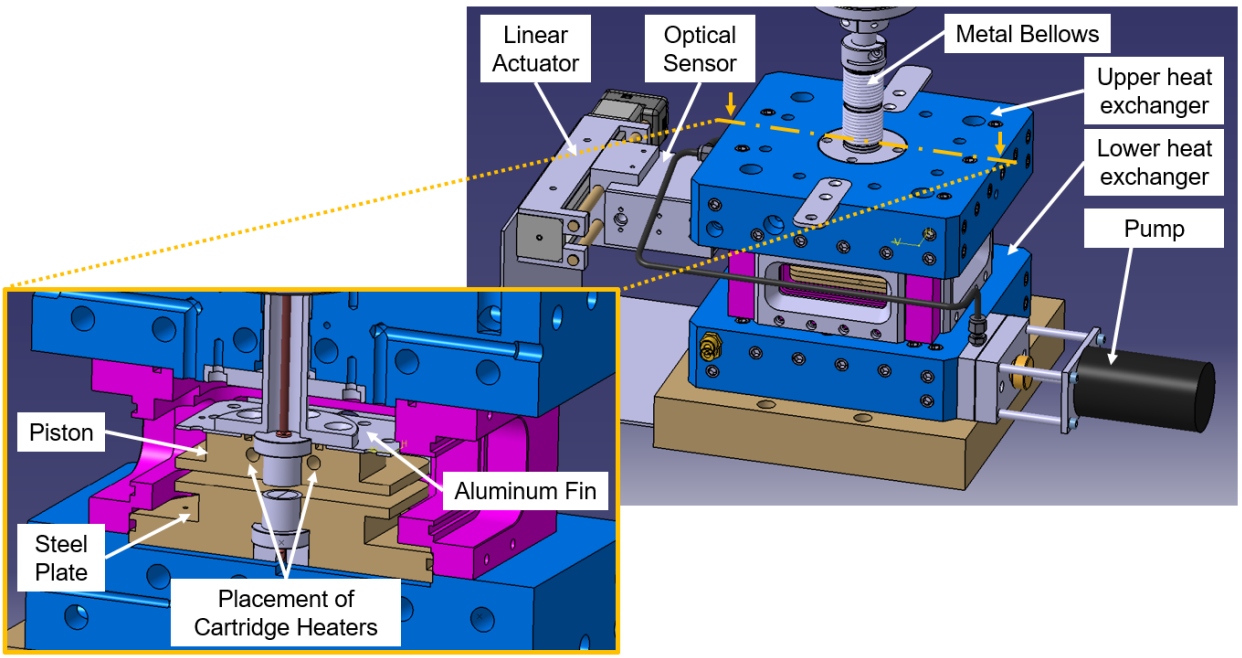

Figure 2.16: 3D illustration of the PvT-Haddoc device - Highlight on added improvements.

Figure 2.15b shows the results of these improvements for a given thermal cycle which consists of a heating ramp from 30°C (after an isotherm at this temperature during 20 min) to 70°C at 2°C.min^{-1} followed by a first isothermal hold during 50 min. Afterwards, a second heating step is applied at 4°C.min^{-1}, later, an isothermal curing at 160°C is performed followed by a cooling step of the system to 30°C at 2°C.min^{-1} of cooling rate. It can be noticed from the measured surface temperatures of the piston and the lower plate, that temperature discrepancies are highly reduced. The maximum attained temperature difference ΔT during the heating ramps and along the isothermal dwells is equal to 2°C. Slight variations are obtained during the cooling phase, more precisely when approaching the ambient temperature, that reach up to 6°C.

2.6.3 Mechanical state

Thanks to the assembly mold-Cavity/Instron-machine, it is possible, from the one hand, to control through to the piston the applied force on the sample along its thickness direction. On the other hand, the applied hydrostatic pressure inside the cavity by means of silicone oil pressure, which also acts on the through thickness direction as well as along the in-plane direction of the sample, constitutes the second important parameter that controls the mechanical state of a studied sample during the cure. Hence, it is important to accurately measure the evolution of the applied oil pressure inside the cavity, especially when dealing with reacting thermosetting composites, which are highly sensitive to the applied stress in the liquid state. The control of the latter was initially ensured by a pressure sensor installed at the outlet of the oil cylinder, which itself is controlled by a second pneumatic actuator as it can be seen from figure 2.14. In order to avoid possible pressure decrease, due to frictional losses because of the oil circulation in the connecting circuit between the cavity and the hydraulic cylinder and in order to increase the reactivity of the system, a new pressure sensor has been inserted in the cavity (see figure 2.17). It is indeed a KELLER 35 X HTC piezoresistive sensor that allows pressure measurements of fluids at high temperature up to 300°C with a maximum level of pressure of 10 bars. The pressure sensor is placed on the upper exchanger of the molding cavity. Hence, it directly measures the pressure of the silicone oil as it circulates in the appropriate circuit through the exchanger which allows to have a more precise control of the local applied pressure on the sample.

Preliminary mechanical tests, that were carried out in oscillatory mode to investigate the rheology of the material during the cure (see chapter 5 section 5.2), revealed the existence of dry frictions. The latter appear between the piston surface sliding across the contact surface of the upper exchanger. Figure 2.18a shows the presence of an hysteresis loop related to frictions of nearly 40 N measured during a test performed without inserting a sample with an imposed oscillatory displacement of 0.5 mm. This amplitude of friction was too important compared to the characterization required in the investigation of the rheological behavior of the studied prepreg, what motivated an additional improvement. Thus, in order to eliminate frictions in the connection between the piston and the mold cavity, two stainless steel bellows were inserted in series configuration as visible from figure 2.17. They act as leak-tight seal while ensuring high resistance to pressure and high temperature endurance with great chemical resistance. The axial stiffness of a single bellows is 20 N.mm^{-1}, what

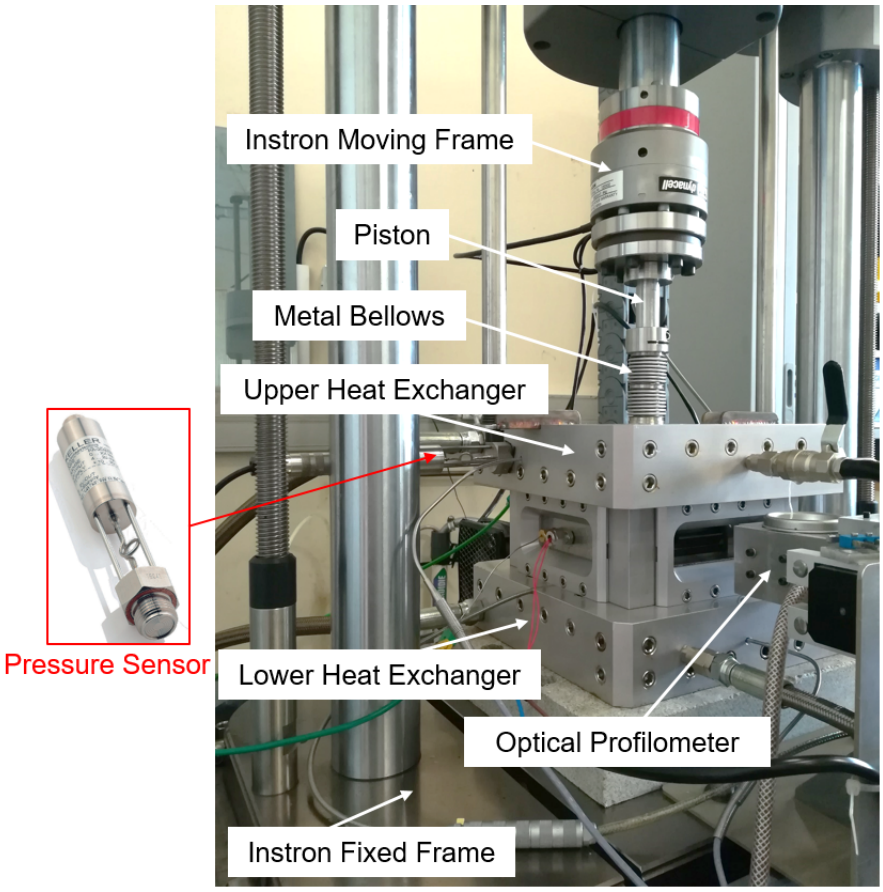

Figure 2.17: PvT-Haddoc device.

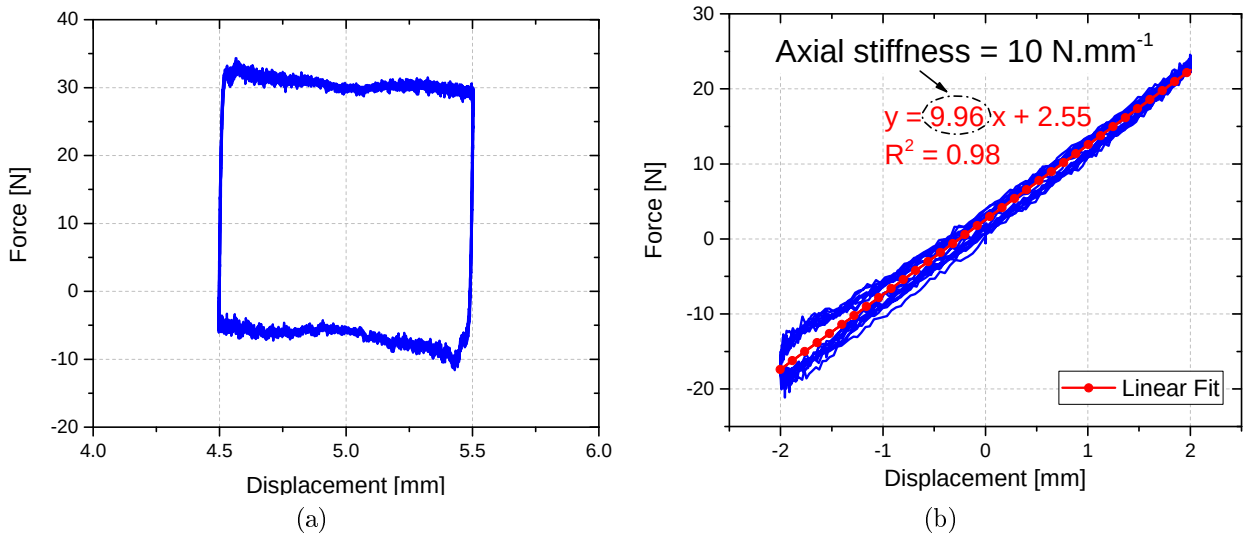

(a) (b)

Figure 2.18: Example of performed oscillatory tests without sample showing (a) a hysteresis loop due to the presence of frictions, and (b) a hysteresis due to the stiffness of the metal bellows: elimination of friction.

provides a total stiffness of 10 N.mm^{-1} and a maximum allowable axial displacement of 9 mm. An oscillatory loading mode test with imposed displacement of 2 mm was performed without a sample to assess frictions presence after bellows addition in the set-up.

In figure 2.18b, we can notice the reduction or almost total elimination of frictions through the obtained force-displacement curve. The presence of the hysteresis this time is simply due to the total stiffness of the metal bellows. The measured stiffness from the slope of the linear fit presents a relative deviation of 0.4% compared to the theoretical stiffness. We can therefore admit that the addition of metal bellows in the connection between the piston and the mold cavity to eliminate friction is a well validated solution.

By improving both the piston force control and the oil pressure measurements, the stress state around the sample has been accurately adjusted, which is of particular interest when a homogeneous compressive hydrostatic stress state around the sample is desired. The conducted investigations in this research work are basically based on applying a compressive stress state throughout the whole cure cycle assuming that frictions on the sample surfaces are negligible. As can be seen from figure 2.19, such stress state can be performed when the sample is simultaneously submitted to the compressive force applied by the piston along its thickness combined to the lateral oil pressure.

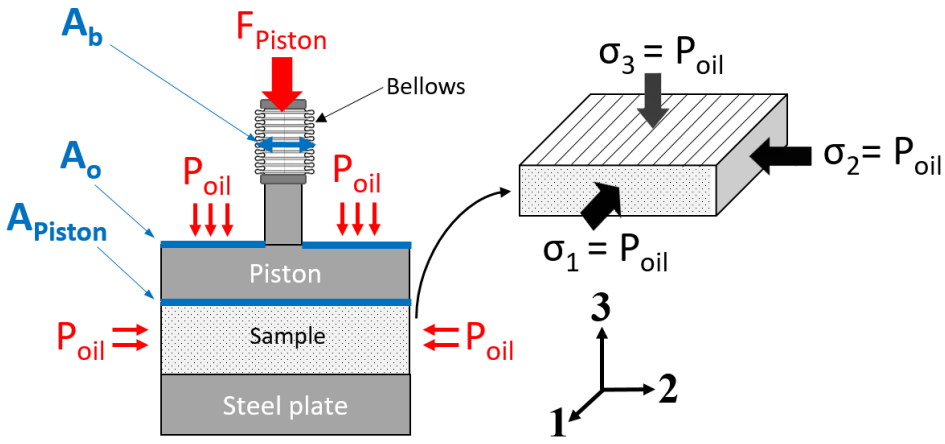

Figure 2.19: Schematic of the isotropic compressive state performed through the combination of the applied compressive force and pressure around the sample during a curing cycle.

The isotropic compressive state around the sample is only ensured throughout the equality between the applied stresses through its thickness, which are a combination between the applied force by the piston and the oil pressure, in addition to the lateral stresses applied by the oil. Therefore, it is crucial to accurately determine the piston force related to the applied oil pressure which can be estimated through the relations given below in equations 2.13 and 2.14:

$$\sigma_{1,2,3} = P_{oil} \quad and \quad \sigma_3 = \frac{F_{Piston} + P_{oil} \cdot A_o}{A_{Piston}} \tag{2.13}$$

$$F_{Piston}[N] \quad = \quad A_b[mm^2] \cdot P_{oil}[MPa] \tag{2.14}$$

where P_{oil} is the applied oil pressure around the sample according to the selected cure cycle, A_{Piston} is the lower area of the piston, A_o and A_b are the upper areas of the piston where the pressure oil is/ is not applied, respectively. In fact, the surface of the piston where the oil pressure is not applied (denoted by A_b), had initially a diameter of 22 mm, which makes a surface of about 380 mm^2. Due to the introduced modifications of the set-up by the addition of the bellows, this surface now corresponds approximately to the one related to the [bellows + piston] connection which was obtained empirically through calibration tests that made it possible to find the surface A_b estimated equal to 700 $\pm$ 10 mm^2.

2.6.4 Displacement measurements

A brief description of the measuring principle of the method involved in this study is given in this subsection. For further details about the undertaken calibrations steps and validation tests of these techniques, the reader is referred to [183].

Along the in-plane direction

These measurements are provided by a laser profilometer KEYENCE LJ-V 7080 placed in front of the glass window of the mold cavity made out of a borosilicate glass (see figure 2.17). The optic sensor ensures the recording of the lateral displacements of the sample surface variation as a function of time with a resolution of 0.5 μm. It also allows the recording of the lateral surface variation through vertical lines of about 39 mm in length along axis 3 parallel to the thickness of the sample as shown in the representative illustration of the emitted laser beam in figure 2.20. Note that, the profilometer can additionally move along axis 1 since it is fixed on a linear actuator (see figure 2.16), then, it is possible to record the evolution of the in-plane displacements (along axis 2) with time for several positions throughout the width (along axis 1) of the sample. In the studied case, only three positions are selected along axis 1 (x_1 = -5 mm, x_2 = 0 mm, x_3 = 5 mm). Hence, throughout the curing cycle, the sensor sweeps along the three positions continuously with a speed movement equal to 5 mm.s^{-1} and a sampling frequency of 10 Hz.

The estimation of the transverse in-plane deformations of the sample throughout the cure requires essentially two corrections steps of raw displacements data that can be detailed below:

1. Optical correction of the raw data coming from the profilometer is firstly required. In fact, refraction phenomena take place while the received rays propagate through the three different transparent media, *i.e.* ambient air, glass window and silicone oil since the emission and the reception zones of the profilometer are non coincident. Considering a point M taken on the lateral surface of the material. The correction of the virtual measured displacement with time related to this point along axis 2, referred by D^{virtual}(M), in order to obtain the real displacement, denoted as D^{real}(M), can be

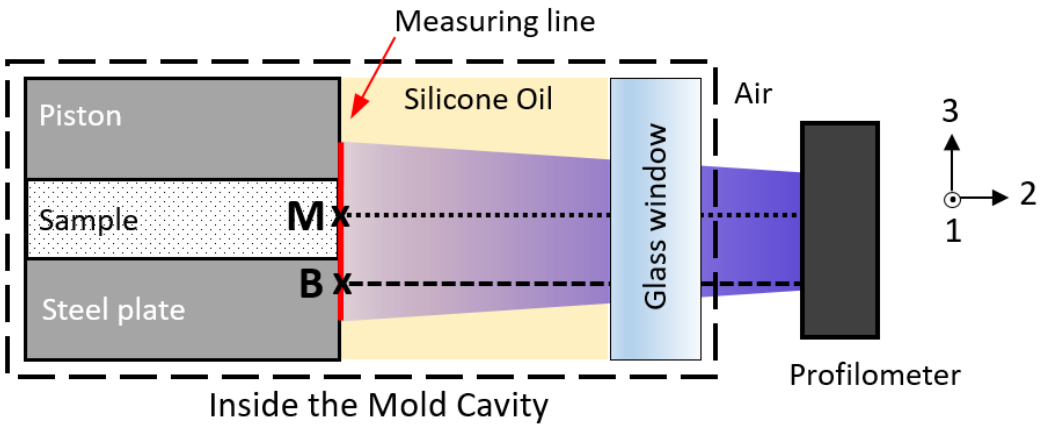

Figure 2.20: Schematic illustration of relative positions of the sample, the glass window and the laser profilometer.

calculated as follows by equation 2.15

$$D^{real}(M) = D^{virtual}(M) \cdot \frac{n(oil)}{n(air)} \tag{2.15}$$

which only involves the refractive indexes of the ambient air (n_{air}) and the silicone oil (n_{oil}) which is, according to [182], equal to 1.402.

2. Due to the thermal expansion/ contraction of the mold cavity including the glass window, a second correction of the measured real displacements is needed to overcome thermal effects in the in-plane direction. In fact, $D^{real}(M)$ can be expressed as

$$D^{real}(M) = d(M) + d^{Th}(cavity) \tag{2.16}$$

where d(M) includes only the material in-plane displacements response as it can be of thermal, chemical or mechanical origins (or coupled effects), whereas, d^{Th}(cavity) are the displacements of the mold cavity induced by thermal effects during the whole cure with time. In order to subtract these thermal effects, a baseline is taken as a reference. The latter is referred by point B on the lower steel plate (see figure 2.20) whose displacement along axis 2 during a curing cycle can be defined as

$$d(B) = d^{Th}(plate) + d^{Th}(cavity) \tag{2.17}$$

By estimating the thermal displacements of the lower plate d^{Th}(plate), the material response can be deduced as follows

$$d(M) = D^{real}(M) - \left[d(B) - d^{Th}(plate)\right] \tag{2.18}$$

Along the thickness direction

The dimensional variations of the sample through the thickness direction are measured throughout the displacement of the piston, recorded by the Instron Press Optical Encoder, that enables a linear resolution of 1 nm. The estimation of the through-thickness strains

relies on a correction of the raw data recorded by the press through a baseline-test. This test is performed without any sample and under the same conditions in order to remove the thermal effects related to the device during a selected curing cycle.

2.7 Partial conclusion

In order to better understand the complex behavior during processing of thermosetting composites, it is crucial to be able to estimate the degree of cure and to obtain a better understanding of the shrinkage development of the studied neat resin since the evolution of the composite properties during the cure directly depend on the state and cure degree of the matrix. For this purpose, this chapter firstly dealt with the thermo-chemical characterization of the M21 resin. The cure kinetics model of Bailleul modified by Msallem *et al.* [46] was assessed to be finally adopted for the M21 resin used in this study. The cure volumetric behavior of the resin was characterized using the PvT-α mold enabling the estimation of its volumetric CTE and CCS. The identification of the gel point of the M21 resin was also performed through dynamic rheological measurements. The obtained value revealed good agreements with Msallem *et al.* [46] results which can further validate the similarities between both studied M21 systems. The final part of this chapter was dedicated to the presentation of the PvT-HADDOC experimental bench employed in this work with the aim of characterizing an interlayer toughened thermoset Carbon/Epoxy prepreg during the entire cure cycle. An overview of the working principle and the principal components of the device are described in the last section of this chapter revealing the main introduced improvements.

CHAPTER 3

MEASUREMENTS OF THE ANISOTROPIC THERMO-CHEMICAL STRAINS OF THE IMA/M21 PREPREG DURING THE CURE

Contents

3.1 Introduction **86**
3.2 Sample preparation and set up **86**
3.3 Analyses of preliminary tests and definition of new adjusted cure cycles . **89**
3.3.1 Preliminary test analysis 89
3.3.2 Separation of coupled phenomena 93
3.3.3 Definition of new curing cycles 96
3.4 Analyses of cure-induced strains along the three directions **98**
3.4.1 Through-thickness displacement measurements and strains calculation 98
3.4.2 In-plane displacement measurements and strains calculation . . . 100
3.4.3 Comparison between the deformations along the three directions . 102
3.5 Compaction behavior in the uncured state through the thickness direction **104**
3.5.1 Compaction behavior analysis 104
3.5.2 Compaction kinetics 107
3.6 Anisotropic thermal expansion and shrinkage measurements results **110**
3.6.1 Thermal expansion behavior and CTE measurements 110
3.6.2 Chemical shrinkage behavior and CCS measurements 114
3.7 Partial conclusion ans perspectives **117**

3.1 Introduction

This chapter deals with the presentation of the developed experimental procedure used to characterize the interlayer toughened Carbon/Epoxy prepreg during the entire cure cycle. As the aim of the study is to better understand the complex behavior during the material whole transformation, the investigation must allow the monitoring of induced thermo-chemical deformations including the early pre-gelation stage. The next section of this chapter is devoted to a detailed presentation of the employed experimental protocol of prepreg samples' preparation. In section 3.3 are discussed the first results obtained from preliminary tests conducted on the IMA/M21 prepreg that show the complex behavior of the material during the cure. The interplay of several multi-physical phenomena impelled the modification of the manufacturer's recommended thermal cure cycle and the new proposed ones are also described in this section. The principle of strains calculation through a multi-axial characterization is detailed in section 3.4 which gives an overview of the total behavior during the cure through the analyses of cure-induced deformations. The investigation of the induced strains throughout the consolidation of the uncured material is discussed in section 3.5 which suggests further understanding of its compaction behavior in the liquid state. The analyses of the thermal induced strains and chemical shrinkage during the cure are detailed in the final section 3.6 of this chapter.

3.2 Sample preparation and set up

The processing route used to produce IMA/M21 prepreg samples for the thermo-chemical characterization during the cure relies on different steps that can be described as follows. Firstly, the prepreg roll is removed from the freezer and kept at room temperature for 24 hours so that the material gets completely reheated inside of the sealed storage bag to prevent condensation. Please note that, all the tested samples in this investigation are only produced as unidirectional stacking sequences [0°] of 30 plies. For each specimen, prepreg sheet squares of 140 × 140 mm^2 are then cut from the whole prepreg roll. Afterwards, layers are positioned manually into a UD configuration. After hand lay-up, the stacked laminate is placed against a flat aluminum tool. The entire compaction set-up is presented in figure 3.1.

The bottom side of the sample is supported by a release film to limit adhesion and ensure easy demoulding. On the upper side, before introducing the vacuum bag, the sample is covered with perforated release film plus a breather, and is additionally surrounded by Mosites rubber sheets to enable the uniform distribution of the vacuum throughout the laminate. It is highly recommended to perform regular debulking steps under a vacuum of about -0.9 bar for 15-20 min every 4 to 5 plies in order to ensure the good adhesion of layers and to remove the entrapped air during lay-up. In our case, the choice was made to perform a one-step debulking procedure for the entire stacked laminate at room temperature during 2 hours. The removal of air forces the bag down onto the laminate ensuring a debulking pressure of up to 1 atmosphere. After this step, the compacted sample is cut using a stainless steel die cutting (see figure 3.2a) and compacted again in a specific mold with desired final dimensions (figure 3.2b) at room temperature using a hydraulic press.

The obtained final sample shape is given in figure 3.2c with in-plane section of $L_0 \times L_0 = 105 \times 105$ mm^2 where L_0 is the initial in-plane length. Thickness measurements of each sample was performed using a Keyence laser sensor IL-100 by taking 9 measures along the flat surface of the sample. The obtained average initial height of all tested samples is $h_0 = 5.950 \pm 0.045$ mm. Samples are generally prepared a day before the testing due to the long preparation procedure. In this case, the uncured prepreg sample is stored in sealed bag at room temperature in order to prevent any moisture regain before the test. As the crosslinking reaction kinetics of M21 epoxy system is very slow at room temperature, no curing takes place during the whole 24 hours before the test. The exact information about the Out Life of this type of prepregs was not precised by the manufacturer but for the M21 based systems, it can vary from 5 to 30 days [39]. This procedure allows us to assume that all tested prepreg samples have nearly the same initial conditions.

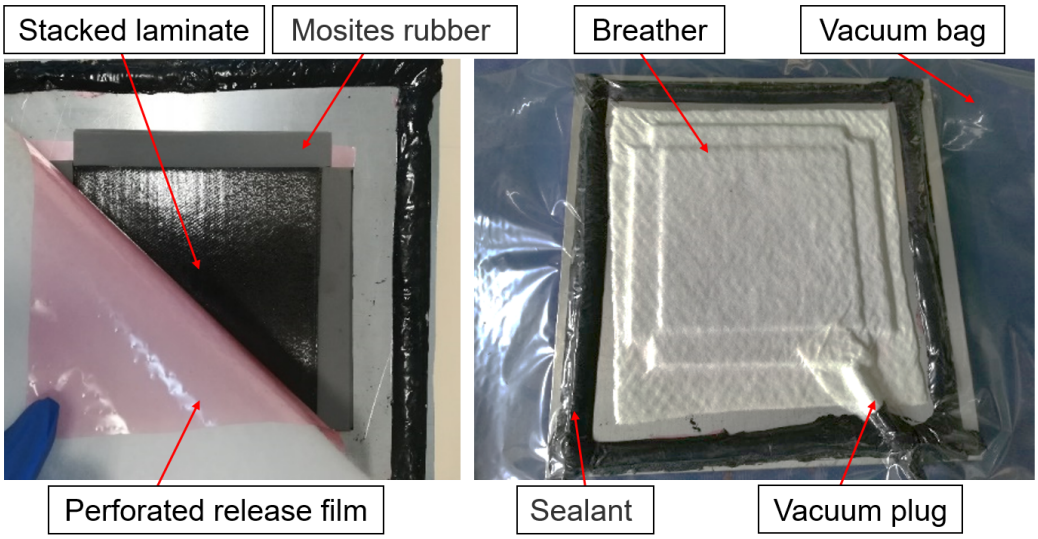

Figure 3.1: Debulking set-up configuration of stacked laminate before cut.

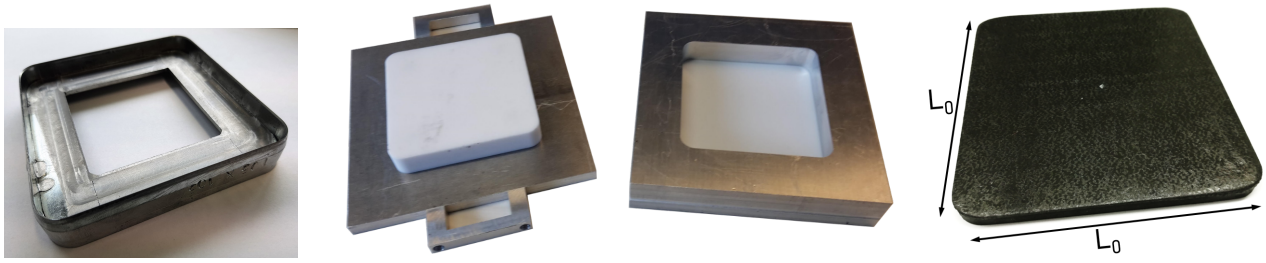

(a) (b) (c)

Figure 3.2: (a) Final cut using a stainless steel die cutting. (b) Final compaction step using a compaction mold [38]. (c) Final shape of UD IMA/M21 prepreg sample.

Before inserting the sample in the PvT-HADDOC device, the steel plate and the piston are lubricated with silicone grease as it was detailed and validated by Peron *et al.* [183] in order to reduce frictional effects by ensuring a frictionless contact between the surfaces and the sample during the cure. Afterwards, the sample is placed on the lower plate and the piston is

put in contact with the sample. A pre-compressive stress of 2 KPa is generally applied on all tested specimens which can be adjusted manually via the Console software. The cavity is then closed and filled with silicone oil while maintaining the piston's position constant during this stage to ensure that no sample movements are induced. The final step of the set up procedure is the application of the desired mechanical state around the sample. As it is described in chapter 2 (see section 2.6), an isotropic compressive state is preferred to be performed along the whole material curing. Once the mold cavity is filled with silicone oil, the latter is closed and screwed to the lower part of the device. The oil pressure is gradually increased to the desired value simultaneously with the piston applied compressive force whose position is kept constant during pressure adjustment stage. Once the latter reaches the desired value, the piston force is fine-tuned to the related applied oil pressure according to equation 2.14. At this step, the piston compressive load is set constant in WaveMatrix software in order to enable the recording of induced displacement variations through the curing test.

An example of IMA/M21 sample is shown in figure 3.3 before the mold closure. 1, 2, 3 are the three principal directions of a UD prepreg laminate. Hereafter, axis 1 runs parallel to the direction of fibers, axis 2 will be referred to the in-plane transverse direction and axis 3 defines the through-thickness transverse direction.

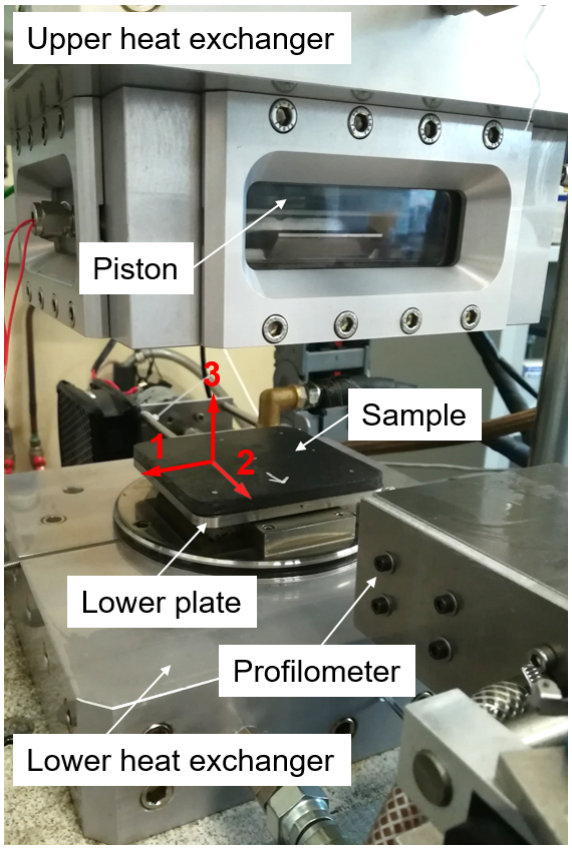

Figure 3.3: IMA/M21 sample placed in the PvT-HADDOC for the thermo-chemical characterization before mold closure.

3.3 Analyses of preliminary tests and definition of new adjusted cure cycles

In this section, we mainly focus on the analysis of through-thickness behavior on the basis of the performed preliminary characterizations.

3.3.1 Preliminary test analysis

The manufacturer's recommended thermal cure cycle according to our samples thickness [39] consists of a heating ramp of 2°C.min^{-1} up to 180°C followed by an isothermal curing of two hours at this temperature before the cooling step performed at the same rate 2°C.min^{-1} (see figure 3.4). Hereafter, this thermal cycle will be called as cycle A. The applied pressure according to autoclave processing for this aerospace-grade resin system is commonly 7 bars which corresponds to the saturated vapor pressure of water at 180°C which enables to prevent the development of porosity by keeping the volatile species, air and moisture dissolved in the resin. The first performed test in the PvT-HADDOC was carried out by applying these curing conditions of pressure and temperature. The compressive hydrostatic mechanical state of 7 bars around the sample was ensured by the application of oil pressure at this value with a corresponding compressive piston force of 490 N. The first tested UD IMA/M21 laminate sample is named as sample I.

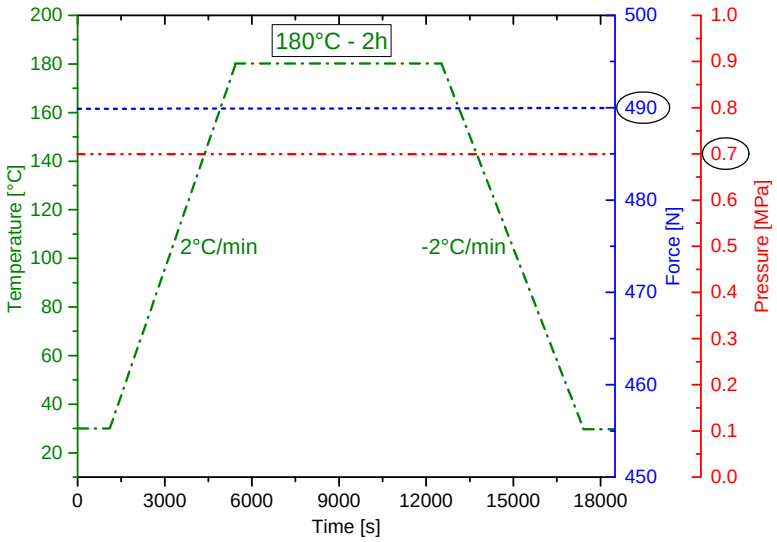

Figure 3.4: Manufacturer's recommended cure cycle (named as cycle A) applied to sample I performed in the PvT-HADDOC device.

The obtained transverse through-thickness displacements recorded by the Instron Press of sample's I experiment are given in figure 3.5a referred by raw displacements, altogether with displacement data coming from the baseline-test and the imposed thermal cure cycle. As described in chapter 2 (see subsection 2.6.4), the baseline presents the summation of the thermal induced displacements of the whole axial line during the test which includes the piston, lower plate and other different components that form the axial measuring line. It can

be observed from this figure, that the displacements of the latter follow well the evolution of the temperature during the whole cycle as expected. Raw axial displacements related to the sample experiment include, in fact, the material response in addition to the device induced thermal displacements. Since the first imposed isothermal hold at 30°C for 15 min, it can be noticed that raw displacements show a decrease comparing to the baseline. During the heating ramp, nearly at t = 2000 s, a second drop in the piston displacements become significantly noticeable. This phenomenon seems to occurs until approximately t = 2800 s and will be further analyzed in next paragraphs.

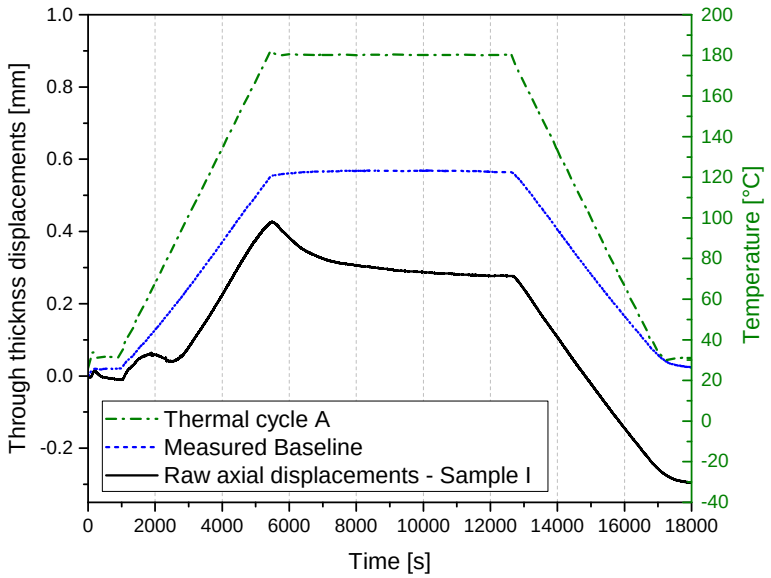

(a)

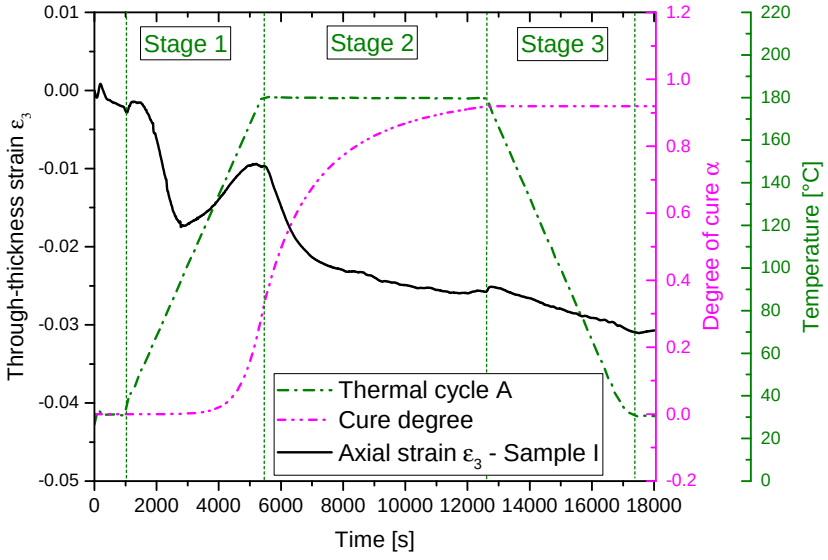

(b)

Figure 3.5: (a) Measured displacements by the piston according to the manufacturer's recommended cure cycle related to sample I experiment. (b) Through-thickness calculated strain of sample I after baseline subtraction.

After this instant, the piston displacements continue to increase following the temperature raise during the heating step which is due to the thermal expansion phenomenon of both, the sample and the device. Once the isothermal dwell is reached, an important decrease in piston displacements is observed because of the chemical shrinkage of the sample along its thickness direction. Displacements decrease seems to continue until t = 11500 s, afterwards, slight decrease might be observed during the rest of the isothermal step. Along the cool-down step, displacement drop recorded by the piston are mainly a consequence associated to thermal contractions of the device plus the prepreg sample.

The subtraction of the baseline from raw displacements data provides the sample thickness variations only during the curing test. Hence, the estimation of the through-thickness deformation with time of the material, denoted by $\varepsilon_3(t)$, can be deduced according to the equation below

$$\varepsilon_3(t) = \frac{\Delta h(t)}{h_0} \tag{3.1}$$

where $\Delta h(t)$ is the material height variation measured at time t, and h_0 is the corresponding initial height of the sample before the experiment.

Please note that, based on obtained results in chapter 2 from M21 resin testing, we assumed that temperature and transformation gradients are negligible along the resin samples thickness. Thus, for the upcoming analyses, we assume that there are no significant temperature differences between the surface and the core of composite samples and therefore temperature and degree of cure gradients are negligible along the thickness direction in composite samples which present lower volume fraction of resin comparing to the neat resin samples [12]. In the remainder of this report, the calculated degree of cure will be based on the resin curing behavior only by means of the cure kinetics model given in chapter 2 (see equation 2.10). The applied temperature program and the calculated cure degree are presented in figure 3.5b. The through-thickness deformation of sample I is calculated according to equation 3.1 and is also given in this figure. Three main stages can be then distinguished along the whole thermal cycle. Stage 1 corresponds to the heating step of the laminate that proved to include more than the thermal expansion phenomenon as been observed from raw displacements data in figure 3.5a. Strains drop sharply while the material is expected to expand with the increment of temperature. During stage 2, the sample is isothermally cured at 180°C and the induced cure shrinkage is now more evident through the high decrease in the measured strain after baseline subtraction. At the start of the isothermal dwell, the degree of cure reaches nearly 30% which means that the crosslinking reaction of the matrix has been already advanced during the heating step. The material gelation occurs approximately at t = 6100 s according to rheological measurements in chapter 2. The axial strain continues to decrease afterwards and remains rather constant during the rest of the isothermal step beyond t = 11400 s. Throughout stage 3, the material is thermally contracted when cooled from 180°C to the ambient temperature which is revealed by strain decline over time.

During the first stage of the cure cycle, the material proved to exhibit a complex behavior when submitted to a heating ramp. In order to gain more insight into the physics that control this phase, the calculated axial strain of sample I is plotted as function of temperature in figure 3.6/1-a and a more focus on the behavior evolution with time during stage 1 is accorded with a zoomed-in graph given by figure 3.6/1-b.

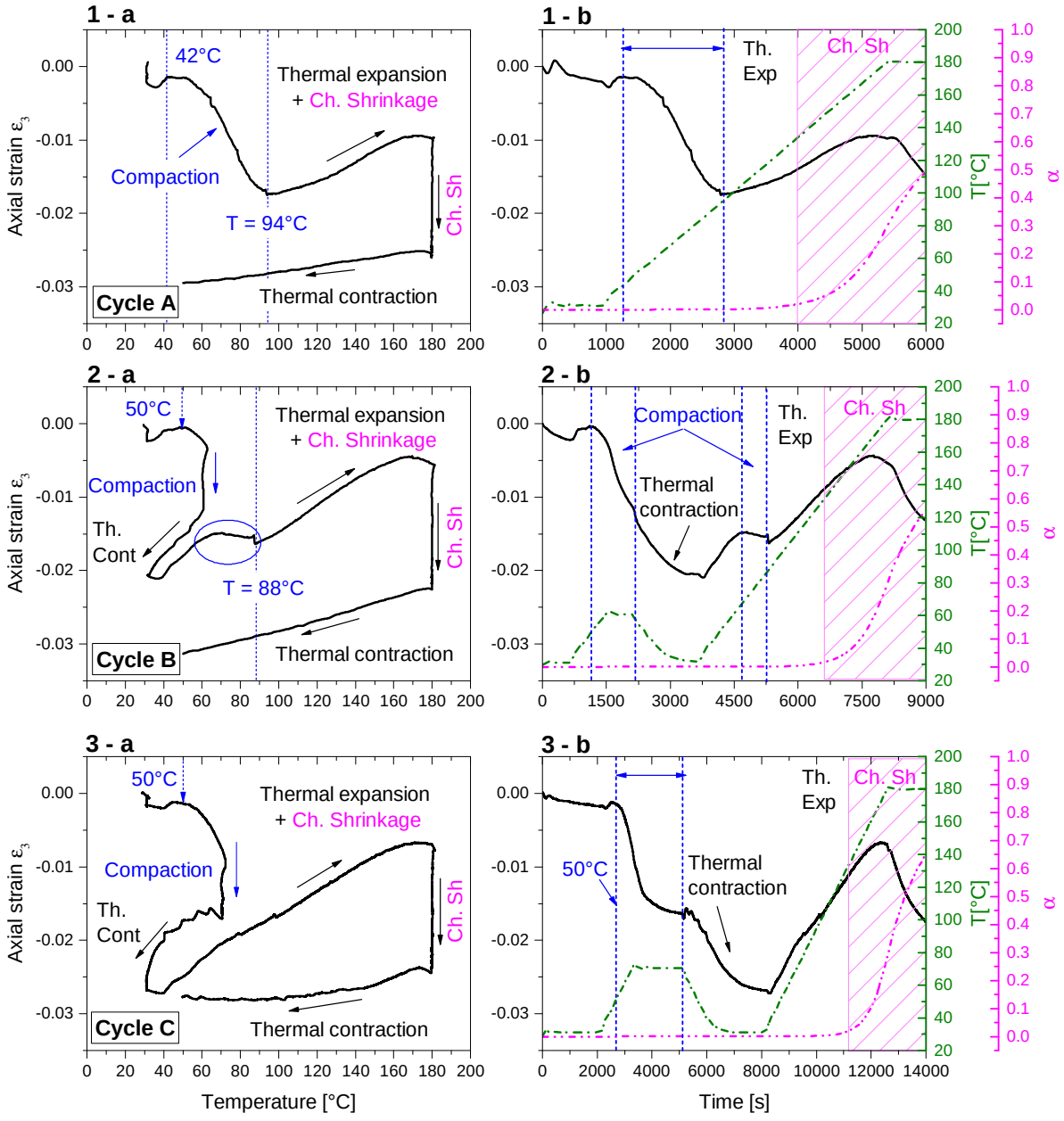

Figure 3.6: The effect of time and temperature on the induced through-thickness strains due to the compaction mechanism in the uncured state of the material through the three tested thermal cycles names as A, B and C (Please note that the notations Th.Exp, Th.Cont and Ch.Sh are employed to refer to thermal expansion, thermal contraction and chemical shrinkage, respectively).

It can be clearly deduced from this figure, the through-thickness strain is mainly driven by three competing mechanisms. First of all, the evolution of the degree of cure with time shows that until almost t = 4000 s, the polymerization reaction has not yet advanced since $\alpha = 0$. Thus, no contractions of chemical origin can take place at this phase of stage 1. The two mechanisms observed until t = 4000 s during the heating are mainly the thermal expansion in the liquid state of the material and compaction along the axial direction. From figure 3.6/1-a, it can be easily noticed that the sample contraction starts even during the first isothermal hold at 30°C. The material axial strain is reduced of about 0.25% during this step. The compaction phenomenon takes place at an early stage of the heating ramp. Measured axial strain seems to go constant from T = 42°C due to the competing phenomena. The compaction starts to dominate over the thermal expansion of the material upon T = 50°C when an important drop through the thickness of the sample is observed. Around 94°C, the latter is compacted about 1.5% and just after, the measured strain starts to increase again mostly due to the thermal expansion. Starting from t = 4000 s with corresponds approximately to T = 132°C, the crosslinking reaction of the epoxy matrix is activated with temperature and the estimated degree of cure starts to increase during the heating (α starts to become ≥ 0). Consequently, at this stage the cure induced strain is affected by small amount of chemical shrinkage coupled to the thermal expansion of the material.

3.3.2 Separation of coupled phenomena

As it is obvious from the analysis of the first experiment, the simultaneous occurrence of the three physical mechanisms: thermal expansion, compaction and chemical shrinkage during the heating ramp prevents from analyzing the uncured state of the material. In order to distinguish the relative contributions of the thermal expansion driving the through-thickness induced strain during the cure cycle of the IMA/M21 laminate, further experiments were performed to separate these phenomena.

Two different thermal histories were tested to cure the prepreg samples. The applied mechanical conditions around the sample remain unchanged, a compressive isotropic state is performed with 7 bars pressure for both new experiments. Samples were prepared according to the same protocol described in section 3.2. At this stage, we focused on modifying the first heating step of the thermal cure cycle A. Therefore, a second thermal cycle was proposed named as cycle B, as detailed in table 3.1, conducted on sample II. The latter consists in heating the sample from the ambient temperature to 60°C with a rate of $2°C.min^{-1}$. This temperature was held during 10 min, thereafter, the sample was cooled with same heat rate to 30°C. This temperature was kept for 10 min to ensure the thermal homogeneity of the sample, then, the latter was re-heated again at $2°C.min^{-1}$ up to the curing temperature 180°C.

As a way of comparison with obtained results from the first experiment, stage 1 of the cure induced axial strain of sample II as well as the thermal cycle and the estimated degree of cure are presented in figure 3.6/2-b. Figure 3.6/2-a gives the evolution of strains as function of the thermal cycle but only the first and the second steps among the cycle B (as detailed in table 3.1) are analyzed in this paragraph during which the prepreg is still in the uncured state.

Table 3.1: Details for tested thermal cycles B and C applied under 7 bars.

Cycle	Steps	Starting Temperature	Heating Ramp	Hold Temperature/Time	Cooling Ramp	Sample
B	1/3	30°C (15 min)	2°C.min^{-1}	**60°C/10 min**	-2°C.min^{-1}	II
	2/3			30°C/10 min		
	3/3	30°C	2°C.min^{-1}	180°C/120 min	-2°C.min^{-1}	
C	1/3	30°C (30 min)	2°C.min^{-1}	**70°C/30 min**	-2°C.min^{-1}	III
	2/3			30°C/10 min		
	3/3	30°C	2°C.min^{-1}	180°C/120 min	-2°C.min^{-1}	

At the beginning of the cycle, it can be observed that the material shrinks slightly during the first isothermal hold at 30°C. During the first heating ramp, the compaction mechanism starts to take place since T = 45°C but becomes more evident when the temperature reaches almost 50°C upon which the contraction dominates over the thermal expansion. The compaction process continues with a faster kinetics rate during the isothermal dwell at 60°C and the sample is compacted through its thickness direction by almost 1.2%. The estimated drops through ε_3 strains of tested samples are gathered in table 3.2. During step 2/3 of the cure cycle B, the observed contraction can be mainly attributed to thermal shrinkage during the cool-down stage. Once re-heated during step 3/3, axial strain increases again due to thermal expansion of the material which exhibits a second compaction stage that starts around 65°C with a lower degree of compaction about 0.1%. This mechanism is likely to end when the temperature reaches 88°C instead of 94°C as it is observed from the tested cycle A. However, we cannot conclude whether the material reached a final limit of compaction during the second heating ramp. Hence, after 90°C and before the start of the crosslinking reaction (around T = 132°C), the compaction mechanism could still alter the thermal expansion of the material that only seems to have major effect on the material behavior beyond 88°C over compaction.

Table 3.2: Strain drops due to compaction for the three tested thermal cycles performed under 7 bars.

Cycle	Sample	Thickness reduction (%)			
		1^{st} Heating Ramp	1^{st} Hold	2^{nd} Heating Ramp	Total
A	I	-1.5	/	/	-1.5
B	II	-0.27	-0.83	-0.1	-1.2
C	III	-0.62	-0.96	0	-1.58

In order to overcome this issue and ensure more accurate separation of coupled phenomena, a third thermal cycle was tested. The latter is called as cycle C as it is given in table 3.1. The isothermal dwell at 60°C after the first heating ramp was consequently adjusted and fixed at 70°C during 30 min. The cooling step (2/3) was maintained as in cycle B after the first isothermal hold at 30°C along 10 min. The sample was next re-heated to 180°C at 2°C.min^{-1}. Measured axial strain of experiment III is also plotted as function of the thermal cycle (see figure 3.6/3-a) for more legibility of the evolution of the material behavior before the isothermal cure at 180°C. The latter is also given in figure 3.6/3-b as function of time with

the estimated degree of cure evolution and the thermal cycle C. As expected, the material is slightly compacted since the first isotherm at 30°C as it was observed in the case of samples I and II. During the first heating ramp up to 70°C (step 1/3), the compaction process starts at the same temperature level around 50°C such as during the previous experiments. Sample III is compacted by 1.58% through its thickness until the end of the isothermal dwell (see table 3.2). After being cooled at 30°C during step 2/3, the latter is thermally contracted. Along the second heating ramp, axial strain evolution does not reveal any drop and continues to increase until the isothermal dwell. A slight inflection in $\varepsilon_3(T)$ evolution can be however noticed around T = 70°C, but the thermal expansion mechanism seems to be the predominant phenomenon until T = 132°C where cure shrinkage starts to take place.

The obtained results from the three experiments allow us to assume that the observed compaction phenomenon along the thickness direction of samples is an irreversible mechanism. The latter can only be attributed to the densification of the laminate structure as a consequence of the material consolidation in the uncured state. As it can be noticed from table 3.2, a higher induced drop in strains can be related to the increase in the time allowed for the resin to flow at higher temperature (30 min hold at 70°C in cycle C compared to 10 min hold at 60°C in cycle B). Obtained results from experiments conducted on sample I and III reveal that the material could reach similar compaction levels whether when heated through a one step heating ramp up to a temperature that exceeds 90°C or when submitted to an isothermal dwell at 70°C held for a sufficient time. A typical evolution of the M21 matrix viscosity during a heating ramp of 1°C.min^{-1} is given in figure 3.7 as a way of comparison with obtained results.

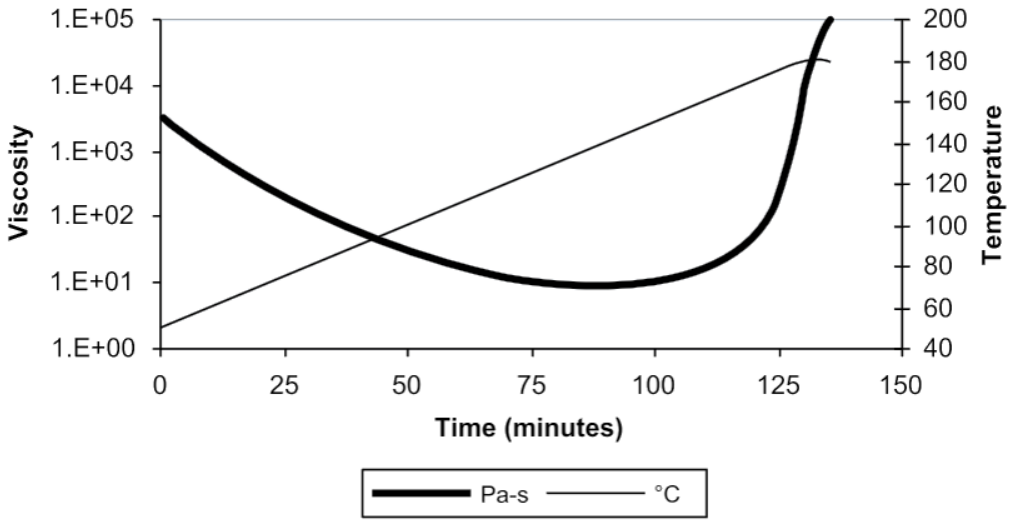

Figure 3.7: Viscosity evolution of the M21 resin during a heating ramp at 1°C.min^{-1} up to 180°C. (Supplier technical data [39]).

There is a pronounced drop in viscosity between 50°C and 90°C from about 1.5 10^3 Pa.s to less than 10^2 Pa.s. The strong decrease of the resin viscosity through this temperature range can clearly validate the dependency of the estimated compaction limits in table 3.1 on resin flow. Due to the increase in temperature, the prepreg viscosity drops. Hence,

the resin impregnation of the fiber bed is enhanced with the increase in resin's flow that results in more densification of the reinforcement and thickness reduction of the laminate. Indeed, the zero drop in the ε_3 of sample III during the second ramp demonstrates that once the laminate sample reaches a certain level of saturation, compaction is likely to end and becomes dominated by the thermal expansion phenomenon. As we can see from figure 3.7 the minimum of the resin viscosity is rather reached nearly to T = 120°C at 1°C.min^{-1}. As the beginning of the crosslinking reaction of the M21 matrix during heating at 2°C.min^{-1} is estimated approximately around T = 132°C, it would be impossible in the case of an isotherm hold at T = 120°C to investigate the intrinsic expansion of the composite in the uncured state. Therefore, the isothermal hold at 70°C seems to be in more adequacy with the objective of this research work to investigate the whole thermo-chemical behavior of the material by separating the coupled phenomena in the uncured state.

3.3.3 Definition of new curing cycles

Based on the obtained results from previous experiments and the stated assumptions, the isothermal hold at 70°C was expanded to allow a more sufficient time for the resin to flow. As a consequence, the standard manufacturing thermal cycle (denoted as cycle A) is adjusted and an isothermal dwell at 70°C is chosen to be held during 50 min. Such duration is considered sufficient to ensure the saturation of the laminate samples without affecting the thermal expansion of the material nor generating coupled chemical shrinkage by advancing the cure reaction. Consequently, two new curing cycles are proposed to be performed in this investigation and are presented in figures 3.8a and 3.8b.

Both adjusted cure cycles consist in applying a first isothermal hold at 30°C during 15 min to ensure the thermal homogeneity of the prepreg sample. The material is then heated at a constant rate of 2°C.min^{-1} up to 70°C. An isothermal dwell at 70°C is applied during 50 min for both new cycles to get rid from voids compaction phenomenon observed in the early stages of heating. The effect of the curing temperature on the induced chemical shrinkage is assessed by testing two curing temperatures, 180°C and 160°C which correspond to cycles 1 and 2, respectively. During the second heating steps, 2 heating ramps are performed 2°C.min^{-1} and 4°C.min^{-1}. The latter are chosen to be in line with the curing temperatures 180°C and 160°C, respectively. Cycle 2 is aimed at enabling the chemical reaction to start only during the isothermal dwell since a higher heating rate leads the onset of the crosslinking reaction to take place at a higher temperature as been discussed in chapter 2. Thereby, by separating the induced chemical shrinkage from the thermal expansion, one can prevent the conflicting effects of both mechanisms during the heating stage. Please note that the polymerization rate at 160°C is much lower than at 180°C as it is illustrated in figure 3.8. Cure rates for both thermal cycles are estimated by means of the kinetics model whose evolutions with time reveal a polymerization rate at 180°C almost more than twice the one related to a curing at 160°C. Therefore, the isothermal dwell at 160°C for cycle 2 was applied during 210 min in order to enable the investigation of the post-gelation chemical shrinkage. Such isothermal hold leads to a different maximum degree of cure of about 82% compared to 92% for cycle 1.

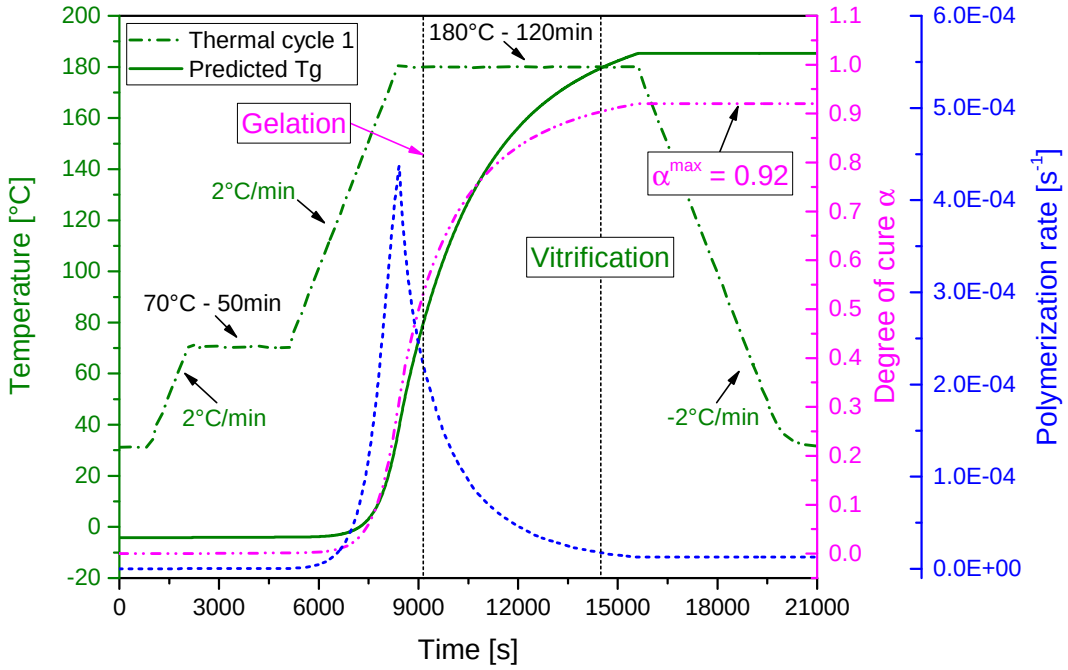

(a)

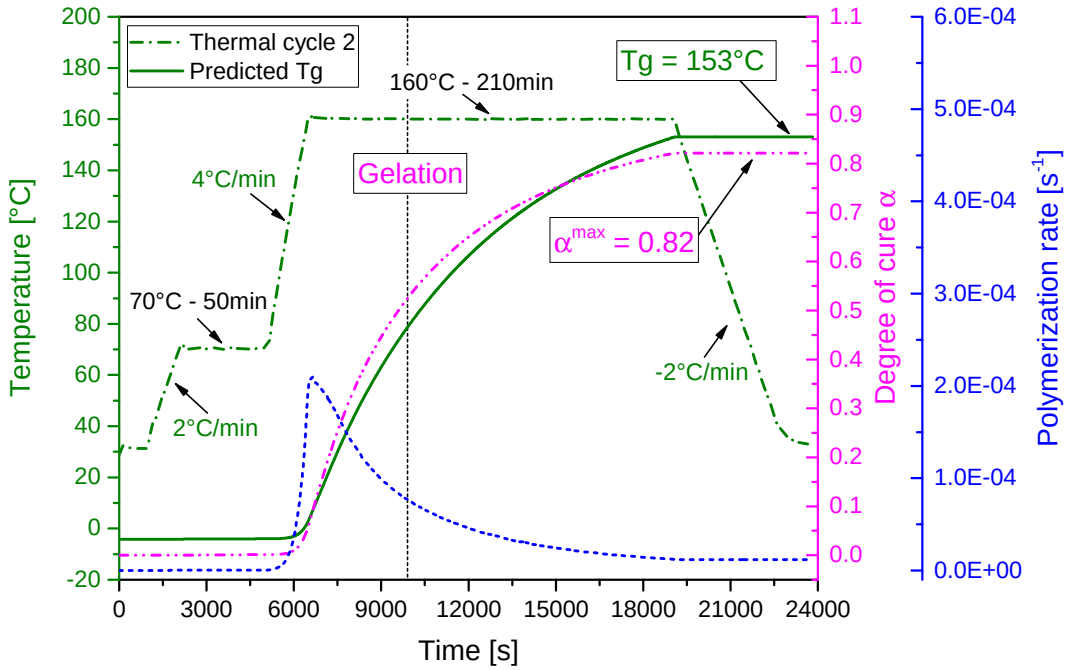

(b)

Figure 3.8: New proposed curing cycles: (a) named as cycle 1 and (b) named as cycle 2.

The predicted glass transition temperatures related to each thermal cycle are also given in figures 3.8a and 3.8b as function of time. It can be noticed that according to the cure cycle 1, material vitrification takes place at the end of the isothermal dwell at t = 14500 s. On the contrary, samples cured according to the proposed cycle 2 remain in the rubbery state during the whole isothermal cure.

The applied pressure related to the cure cycle 1 for a curing at 180°C is 7 bars. The corresponding compressive force applied by the piston is 490 N. On the other hand, samples cured according to cycle 2 at 160°C were submitted to 5 bars pressure. The latter is chosen to correspond approximately to the saturated vapor pressure of water at 160°C in order to prevent voids growth as recommended in [176, 184] and therefore to ensure the same curing conditions for all the tested samples. Details regarding the two adjusted curing cycles examined during this study are gathered in table 3.3. Sample 1 is cured according to cycle 1. Samples [2-5] are submitted to the cure cycle 2 as detailed in table 3.4. In an attempt to look into the effect of the debulking step under vacuum bag on the observed compaction behavior of the material, sample 5 was pre-compacted differently before cure from other samples. The latter was debulked 20 min approximately every subsequent 4 plies under a constant vacuum at room temperature.

Table 3.3: Details of new curing cycles.

Cure Cycle	Curing Temperature	Applied Pressure	Applied Piston's Force
1	180°C	7 bars	490 N
2	160°C	5 bars	350 N

Table 3.4: Tested specimens according to new curing cycles.

Sample's Number	Vacuum Bag Debulking Duration	Cure Cycle
1	2h	1
2	2h	2
3	2h	2
4	2h	2
5	20 min/4 plies	2

3.4 Analyses of cure-induced strains along the three directions

3.4.1 Through-thickness displacement measurements and strains calculation

Raw through-thickness displacements recorded during the cure experiment of sample 3 (taken as example) by the Instron machine and the displacement of the baseline related to the cure cycle 2 are given in figure 3.9. Thickness variations of sample 3 are obtained by subtracting the baseline displacement from raw measured data.

It can be noticed from this figure that the displacements of the baseline follow exactly the evolution of temperature along the whole cycle. Measured raw data which include the sample's thickness variation plus the baseline are globally lower than the baseline since the first stages of the thermal cycle due to the material compaction that takes place from the first

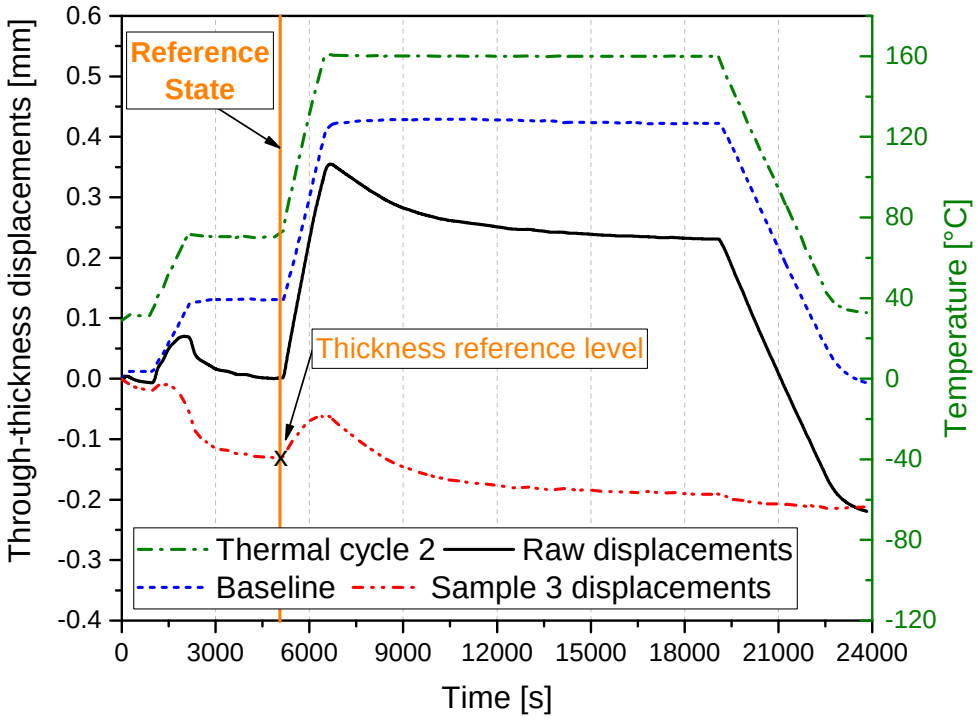

Figure 3.9: Axial displacements measured by the piston during the experiment of sample 3 including raw data, the baseline and the sample thickness variation, together with the performed thermal cycle 2.

isothermal hold at 30°C. Calculated displacements of sample 3 show very well thickness reduction that occurs from the beginning til the end of the applied isothermal dwell at 70°C. The sample height is reduced by around 2.2% after compaction. In order to take into account this consolidation stage that takes place at the fluid state, which can be considered as a preconditioning step in the laminate structure, one can define a reference state from which the material curing behavior can be accurately examined. By doing so, the material reference state is considered by the end of the isothermal dwell at 70°C for each tested sample according to both curing cycles 1 and 2. In the example considered here, sample's 3 reference state is taken at t = 5060 s as illustrated in figure 3.9. On that basis, a new height reference level, denoted by h_{ref}, is defined, which corresponds to the difference between the measured initial thickness h_0 of each sample before the test and the thickness reference level after compaction as follows

$$h_{ref} = h_0 - \mid \text{reference level} \mid \tag{3.2}$$

Therefore, through-thickness strains $\varepsilon_3(t)$ can be estimated by

$$\varepsilon_3(t) = \frac{\Delta h(t)}{h_{ref}} \tag{3.3}$$

where $\Delta h(t)$ is the axial measured displacements at time t of the sample during the cure.

3.4.2 In-plane displacement measurements and strains calculation

Raw displacements recorded along the in-plane direction during the cure experiment of sample 2 according to the thermal cycle 2 are taken as example in this subsection. Data are captured by the optical profilometer and are corrected according to the detailed steps in chapter 2 in order to estimate the real induced material displacements. As described in section 2.6, during the whole experiment of a given sample, the laser sensor sweeps throughout the width of the latter along three selected positions continuously with a speed movement equal to 5 mm.s^{-1}. In this example, the analyzed displacements are taken for the sensor's position x = 0 related to axis 1. Figure 3.10 gives a 3-D plot of the evolution of the in-plane displacements along axis 2, with time, through a vertical line along the sample thickness that corresponds to the sensor position x = 0.

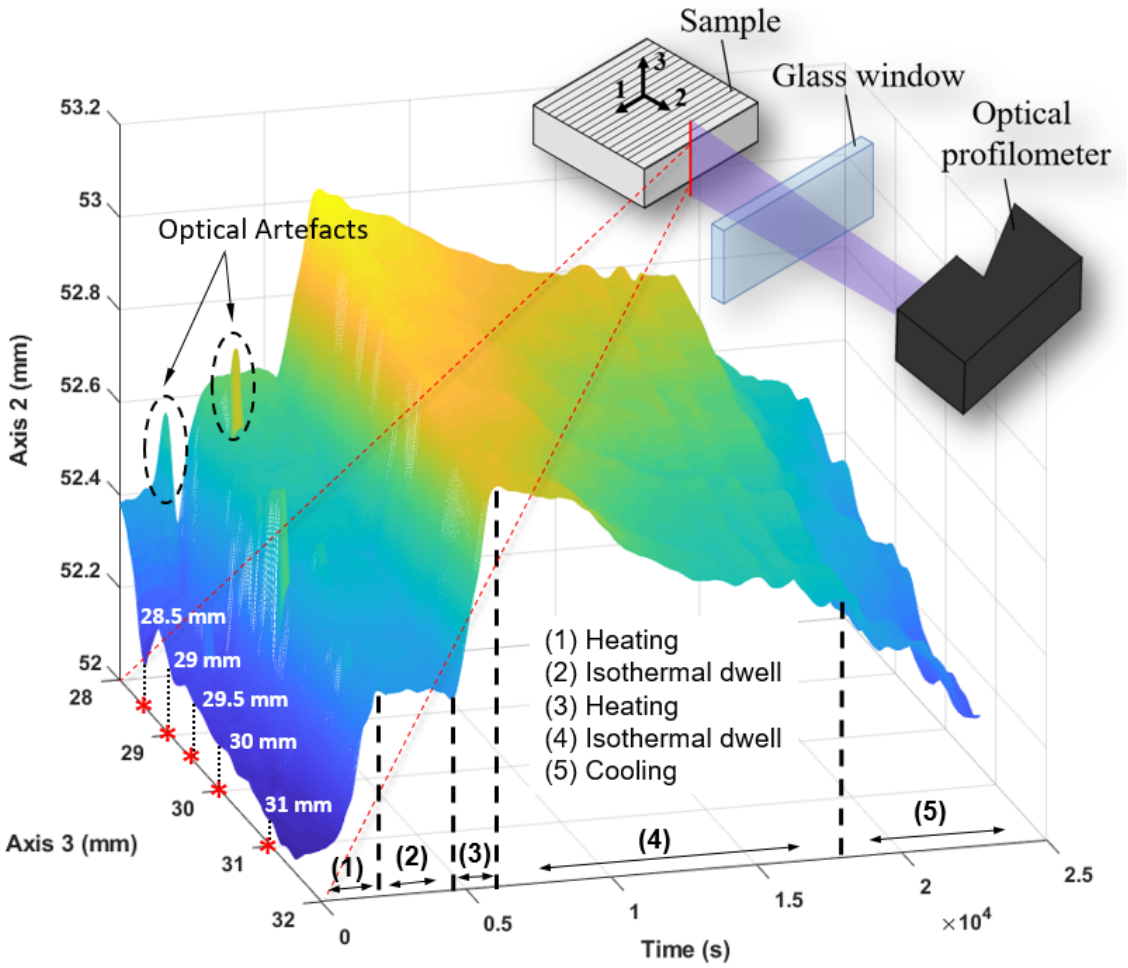

Figure 3.10: In-plane variation of the lateral surface of sample 2 with time along the measuring line for a selected position of the sensor (x = 0) during the cure cycle 2.

The different stages of the thermal cycle are also illustrated for more clarity. Indeed, the variation of the sample's lateral surface during the cure is given by means of a measuring segment along the through-thickness direction of 4 mm long throughout axis 3. Please note that, as described in chapter 2, the sensor enables in reality the recording of the lateral surface

variation through vertical lines of about 39 mm in length. This means that the emitted laser line beam also covers the lateral surfaces of the piston and the lower plate. In this case of sample 2, during the cut step using the die cutting, the final lateral surface presented a defect of less than 2 mm thick. Moreover, the presence of the metallic parts creates sort of optical artifacts captured by the sensor at the edges between the piston/sample's upper surface and the plate/sample's lower surface. Therefore, the analysis area of each sample has to be extracted from the whole measuring line by taking into account the non-defective lateral surface plus the optical artifacts, which explains the 4 mm long only throughout axis 3 taken in this example.

Through the selected measuring line, we can follow the material in-plane displacements throughout different points up to 20 points per mm. 5 points with different positions along the measuring line are extracted: p_1=28.5 mm, p_2=29 mm, p_3=29.5 mm, p_4=30 mm, p_5=31 mm, and the cure-induced in-plane displacement for each position is plotted versus time in figure 3.11. The performed cure cycle is also given in this figure. More detailed analysis of the in-plane behavior will be given in the next subsection. Displacements are zeroed at the end of the isothermal dwell at 70°C (t = 5100 s) in order to account for the new reference state obtained after compaction. During the second heating ramp up to 160°C, it can be seen that all the displacements follow the same evolution and increase with the temperature due to thermal expansion. During the isothermal cure at 160°C, the drop in the measured displacements indicates the chemical shrinkage phenomenon. From t = 19000 s, the displacements decrease following the cool-down step. As visible from these results, the displacements evolution for the 5 selected points reveal a homogeneous in-plane variation along the thickness of the sample.

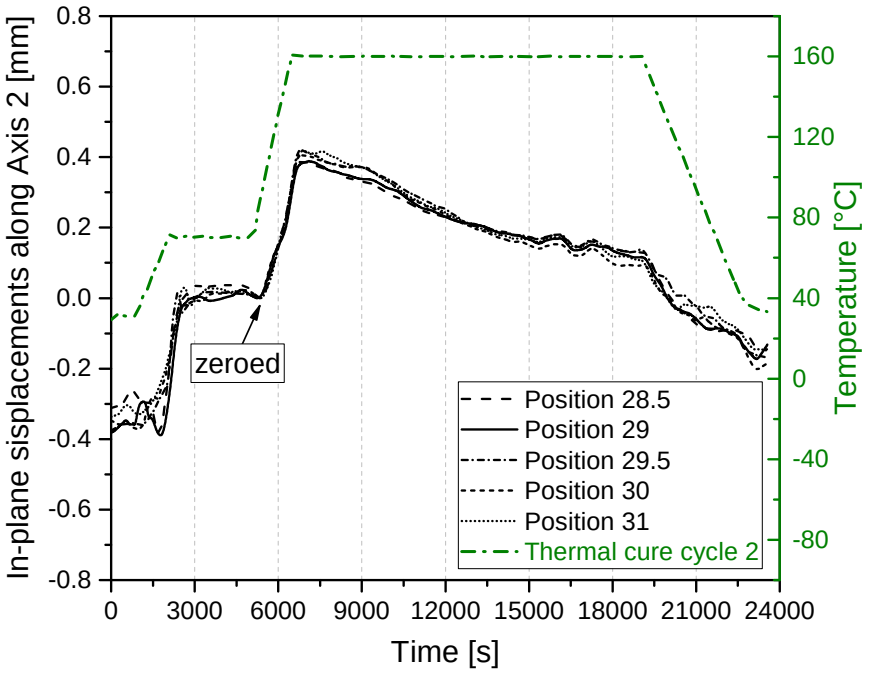

Figure 3.11: Evolution of the in-plane displacements for the 5 selected points along the through-thickness measuring line with time of sample 2.

Please note that the same results are found for the three swept positions of the lateral surface by the sensor along axis 1. From this, the in-plane strains during the cure are calculated by averaging the induced displacements along the selected measuring line for the three positions of the sensor. The latter can be denoted as $\Delta L(t)$ measured at time t. The in-plane deformations along axes 1 and 2 are therefore calculated according to equation 3.4 where L_0 is the initial in-plane dimension of the sample.

$$\varepsilon_{1,2}(t) = \frac{\Delta L(t)}{L_0/2} \tag{3.4}$$

3.4.3 Comparison between the deformations along the three directions

Now that we detailed in previous subsections strains calculation principle using the PvT-HADDOC device along the thickness and in-plane directions of tested samples, it is possible to analyze the anisotropic dimensional variations along the three directions of space of the studied UD IMA/M21 prepreg during the whole cure. To do so, samples [2-4] cured according to the adjusted cycle 2 are taken as examples in this subsection in order to analyze the entire curing behavior of the studied material which is presented in figure 3.12.

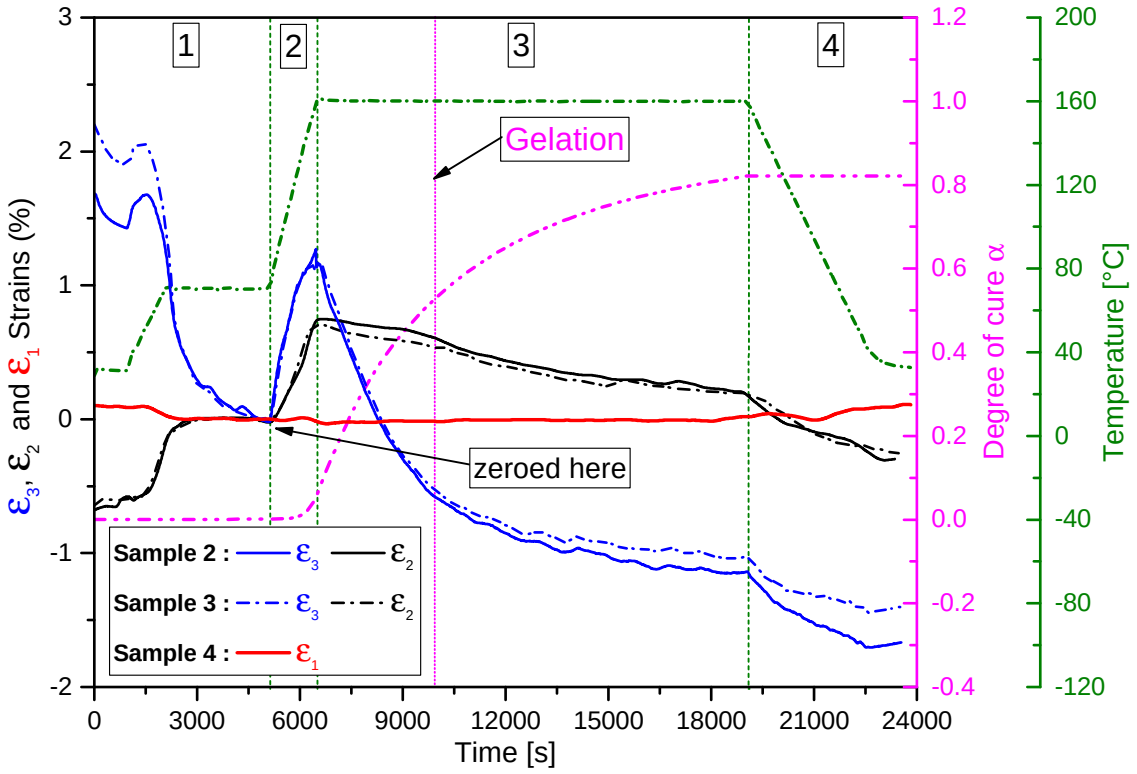

Figure 3.12: Comparison between the deformations along the three principal directions of the UD IMA/M21 laminate together with the estimated degree of cure and the thermal cure cycle 2.

The measured strains along the three directions are given together with the thermal cycle and the simulated degree of cure. Note that, as described earlier, the PvT-Haddoc only enables the measuring of cure induced strains along two directions at once. Therefore, during the experiment of sample 2 (and 3 as well), the latter was placed on the lower plate in a way that the transverse in-plane direction runs parallel to the laser beam direction of the sensor (see figures 3.3 and 3.10). The curing induced strains of samples 2 and 3 are presented to demonstrate the good reproducibility of results. The cure induced in-plane strain through the longitudinal direction of the studied laminate was recorded thanks to the optical sensor by performing an additional experiment conducted on sample 4. Only the measured in-plane strain of this sample is shown in figure 3.12 for the sake of clarity.

The curing behavior of prepregs is typically divided into two phases, before and after gelation of the matrix. In view of the results presented here, we suggest a further breakdown of the pre-gelation stage. Therefore, the induced strains will rather be analyzed depending on the evolution of the material state in line with the thermal cycle and physical phenomena that drive the cure behavior during the entire cycle. Consequently, 4 stages can be distinguished as indicated in figure 3.12.

During **'stage 1'** the material is heated up to 70°C at 2°C.min^{-1} and was held isothermally at this temperature during 50 min under isotropic compressive pressure of 5 bars in order to enable the compaction process to occur in the early stage of the uncured state. As it can be observed from this figure, strains are all zeroed at the end of the defined stage 1 considered as the pre-conditioning region of the laminate structure at $\alpha = 0$. Along the longitudinal direction, ε_1 strain shows a small contraction during the first heating ramp which may be attributed to the negative coefficient of thermal expansion of carbon fibers that controls the thermal behavior in the axial direction. As expected, the studied prepreg exhibits a through-thickness contraction while heated during this first stage illustrated by a significant drop in ε_3 strains for both samples. Indeed, the thickness decrease starts to take place steadily during the first isothermal dwell of 15 min at 30°C. A slight increase in ε_3 strains is then observed with the increment of temperature during the heating ramp. The compaction process begins at 50°C for both samples 2 and 3 as it was observed in the case of samples I, II and III analyzed in previous section which can confirm again the reproducibility of this phenomenon. Thickness reduction persists until the end of the isothermal step. On the contrary, through the transverse in-plane direction, the material is likely to follow the thermal cycle as visible from the increase in the ε_2 strains for both samples. On the basis of these observations, one can presume that the studied laminate only compacts through its thickness during this stage. As the material is still uncured, the main competing mechanisms in this region are therefore compaction and thermal expansion which clearly develop differently along both transverse directions.

During **'stage 2'** the material is heated from 70°C to 160°C at 4°C.min^{-1}. As can be seen from figure 3.12, the evolution of the estimated degree of cure proves that the material remains uncured up to 145°C. Indeed, at the end of the heating ramp, the cure degree only reaches nearly 5%. The increase in transverse strains ε_2 and ε_3 of both samples is only driven by thermal effects. As evident, no compaction occurred during the second heating ramp through the thickness direction which confirms the separation of the coupled phenomena thanks to

the proposed new cycle. We assume that compaction at this stage has already stopped. It can be observed that the UD laminate rather expands much more through its thickness than along the in-plane transverse direction. The latter shows an anisotropic thermal expansion behavior. Along the axial direction, the material does not expand further. ε_1 remains almost constant. This stage will be of use to estimate the CTE of the uncured material in subsection 3.6.1.

During **'stage 3'** the isothermal dwell at 160°C is performed during 210 min. Almost the whole polymerization reaction takes place during this stage. Transverse strains evolution is directly linked to the chemical shrinkage of the material. A large drop is visible in the through-thickness direction while it is less drastic in the in-plane direction approving the anisotropic behavior of the material. The change in deformation through the longitudinal direction is rather insignificant during the isothermal dwell. In subsection 3.6.2, this stage will be further analyzed in order to quantify the chemical shrinkage response of the prepreg, its dependency on temperature and degree of cure and therefore to estimate the CCS.

'Stage 4' depicts the material behavior during the cool-down step. The observed transverse strains drop along both directions is only due to thermal contractions. Strains along the axial direction show however a slight increase during cooling related to the negative CTE of the IMA carbon fibers. The estimation of the CTE in the solid state of the studied material are gathered in subsection 3.6.1.

3.5 Compaction behavior in the uncured state through the thickness direction

3.5.1 Compaction behavior analysis

In order to gain more insight into the compaction behavior observed in the uncured state of the studied material further analyses are given in this section by comparing the behavior of all tested samples. In figure 3.13 we only compare the induced through-thickness reduction that took place during the first heating ramp (started around 50°C for all samples) and along the isothermal dwell applied for 50 min at 70°C. Thus, extracted thickness reductions for all samples, denoted as $\Delta\varepsilon_3(t)$ are given as function of time while t = 0 s corresponds to the onset of the compaction process for each specimen.

The observed trend of the thickness reduction with time can validate the choice of 50 min isothermal dwell at 70°C. Indeed, the material compaction begins to flatten after 40 min and decreases steadily towards the end of the isothermal hold reaching approximately a constant value. Note that, samples [1-4] were prepared under the same conditions and debulked alike before the testing. During the first stage of the curing experiment, sample 1 was held at 70°C and submitted to an isotropic compressive pressure of 7 bars whilst 5 bars were applied to samples [2-4] (see table 3.4). At the end of the isothermal step at 70°C, sample 1 reaches a total compaction limit of -1.84%. Samples 2, 3 and 4 are compacted of -1.76%, -2.06% and -1.7%, respectively. The estimated strain drop limit values reveal in this case that the applied isotropic pressure level has an insignificant impact on the thickness reduction of the studied

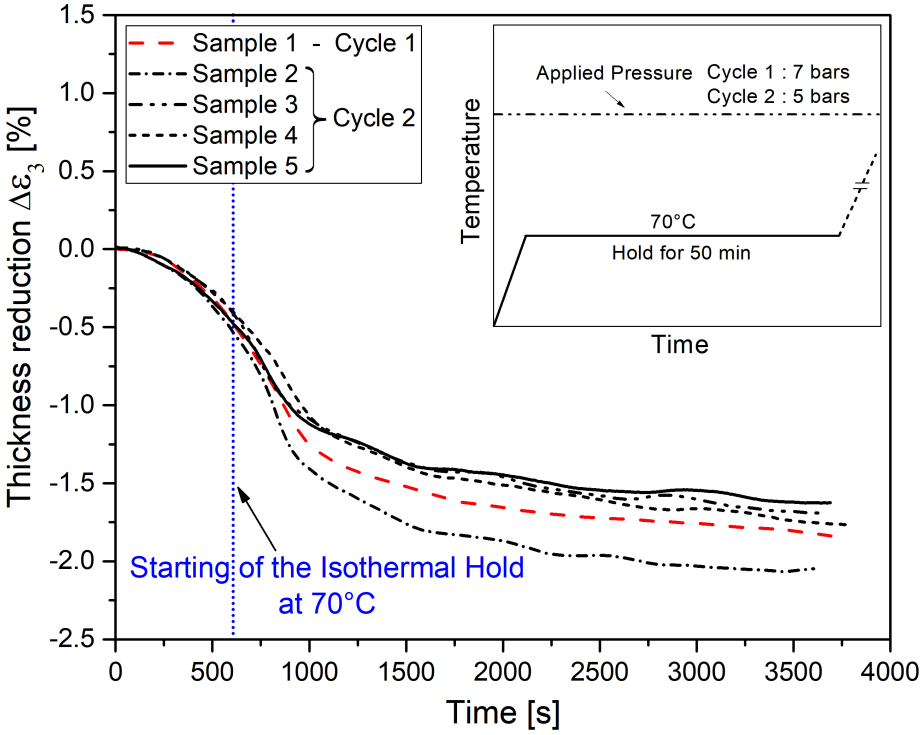

Figure 3.13: Thickness reduction due to the compaction mechanism of the studied prepreg in the uncured state.

prepreg. Sample 5 was pre-compacted under a constant vacuum in the order of 20 min every 4 plies at room temperature. The thickness reduction evolution of the latter shows a similar compaction behavior with a final limit level equal to -1.62% which is slightly lesser than other samples. However such difference cannot enable to conclude the effect of the debulking step on the compaction behavior. In this case, and regarding the tested conditions in this study, the compaction mechanism seems to be highly dependent on the thermal history applied to the sample, as been detailed in subsection3.3.2, but to a lesser extent on the pre-cure debulking step with no significant dependency on the applied isotropic pressure.

The microstructure of an uncured prepreg sample was studied by optical microscopic Zeiss Axio Observer in order to investigate the initial state of samples. To do so, a stacking sequence of 30 plies $[0]_{30}$ sample debulked under vacuum bag for 2 hours was used. Figure 3.14 displays an optical micrograph taken through the thickness of the uncured sample. Evidently, the microscopic inspection of this section reveals 2 types of voids: voids between plies which were mechanically entrapped during the lay-up and an important amount of dry fibers regions including micro-voids within the core of plies. A comparison with a cured sample micrograph is presented in figure 3.15. We clearly notice the absence of the dry fibers regions with barely some micro-voids within the core of the cured ply. Almost no voids are present in the resin interlayer between plies.

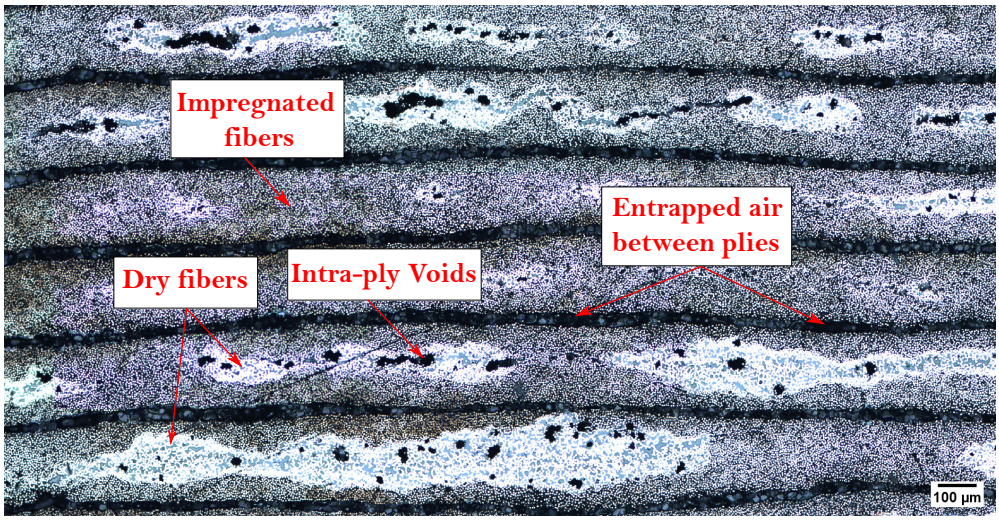

Figure 3.14: Optical micrograph of an uncured IMA/M21 UD laminate sample microstructure through its thickness.

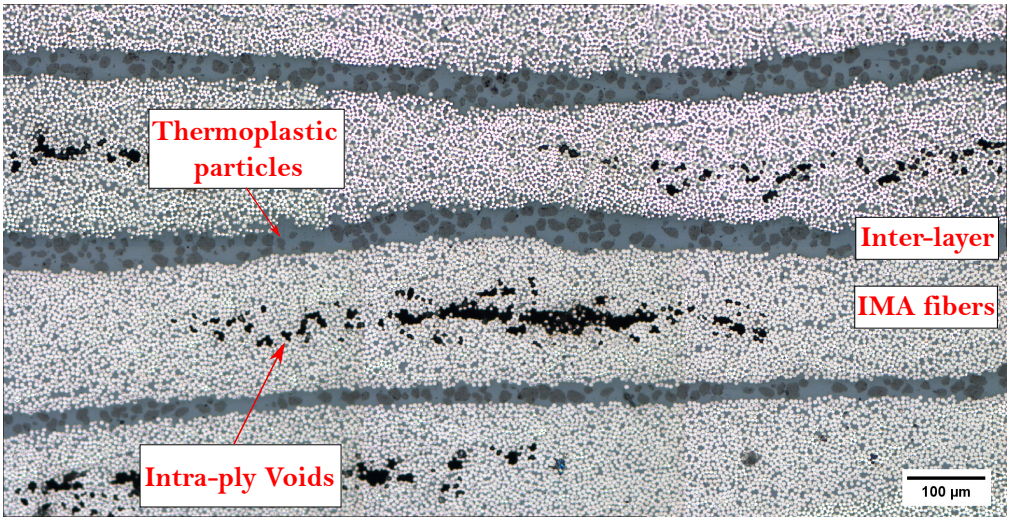

Figure 3.15: Optical micrograph of a cured IMA/M21 UD laminate sample microstructure through its thickness.

In light of this qualitative analysis, it could be concluded that the induced compaction is directly linked to the impregnation of the fiber bed and the elimination of voids which generate the densification of the laminate structure. Besides, visual observation of all tested specimens after curing did not reveal any resin leakage which can also confirm this assumption. We also presume that only capillary pressure could be the driving force to enhance resin infiltration due to the viscosity drop while heating as it was supported by recent research works carried out on toughened prepregs [20,139] (see section 1.4). As illustrated in figure 3.13, the quick drop in strains observed at the beginning of the heating ramp can prove that the capillary effects are decreasing as voids are being filled at the end of the isothermal dwell at 70°C. The observed variation in the reached compaction levels can be attributed to the variability of the initial morphology due to disparities in the amount of dry regions between the tested samples.

It seems plausible to consider that compaction limits are proof of a saturated material. The intra-ply voids that remain in the cured state could prove the insufficient effects of capillary pressure to drive the resin into the micro-cavities to fully impregnate these areas before gelation. The impact of the cure pressure on the compaction behavior couldn't be noticeable regarding the observed results. However, we assume that the isotropic compressive pressure of ≥ 5 bars has an important effect on promoting the solubility of the mobile species in the resin and limiting void growth during the heating ramp. The pre-cure debulking step seems to also have a negligible impact on the compaction behavior. We presume that as the samples were pre-compacted at room temperature, this can only eliminate a small amount of voids entrapped during lay-up in a way that it cannot be prominent during compaction. Since the resin viscosity of interlayer toughened prepreg is too high at room temperature, dry fibers will not get impregnated during debulking, consequently, there will still be voids inside the laminate before curing.

3.5.2 Compaction kinetics

In an attempt to identify the compaction kinetics as function of time and temperature of the uncured material, 3 temperatures related to the applied isothermal holds are identified among the all tested cycles: 30°C which represents the starting temperature for each cure cycle, 60°C and 70°C (see table 3.1). For each isotherm, the mean of thickness reduction ($\Delta\varepsilon_3$) is extracted and plotted against the holding time as shown in figure 3.16.

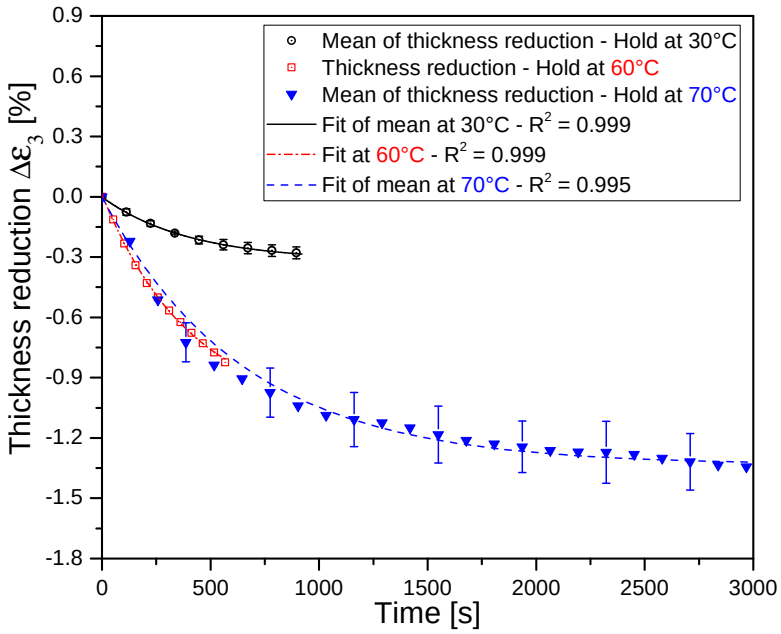

Figure 3.16: Comparison between experimental and fitted data of the compaction kinetics as function of time for each isothermal dwell at 30°C, 60°C and 70°C in the uncured state of the material.

The standard error of the means are only included to the measurements of thickness reduction according to 30°C and 70°C temperatures since only one sample was tested at 60°C. From this, we can observe the dependency of the compaction limit on the applied temperature level in relation with the hold duration. For each temperature, experimental data of thickness reduction are compared to the following expression fit. An exponential regression is proposed to find the best fit of $\Delta\varepsilon_3(t,T)$ (see equation 3.5). A good match between the experimental and the fitted kinetics for each temperature can be observed. The parameter A represents the compaction limit and R_0 is the compaction kinetics rate. Linear regressions are employed to predict the evolution of both parameters in terms of temperature than can be found in figure 3.17.

$$\Delta\varepsilon_3(t,T) \quad = \quad A(T)\left[1-\exp(R_0(T)\cdot t)\right] \tag{3.5}$$

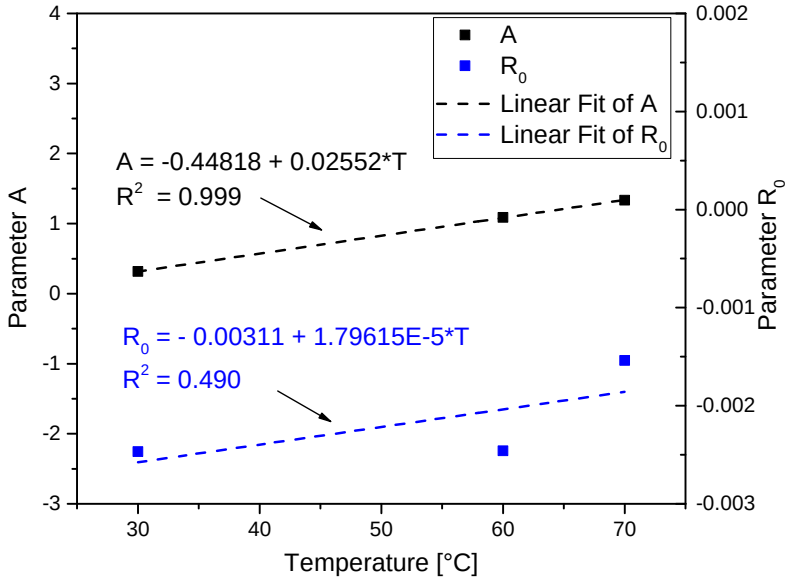

Figure 3.17: Linear fit of the compaction kinetics parameters A and R_0 as functions of temperature.

Data in figure 3.18 suggest an attempt to evaluate the accuracy of the proposed empirical relation (equation 3.5) to predict the compaction limit during a heating ramp only. The induced drop in transverse axial strains during the compaction of sample I are presented in this figure. For the sake of simplicity, only the range of temperature during which the compaction takes place is presented (the full curve can be found in figure 3.5b). As can be seen from this graph, the comparison between the experimental and the predicted data shows the ability of the proposed model to predict the maximum of strain drop for a given heating ramp estimated in this case equal to -1.5%. Nevertheless, the model's predicted kinetics shows significant differences between the experimental data at the start of heating which can be explained by the interplay of thermal expansion and the compaction mechanism of the material.

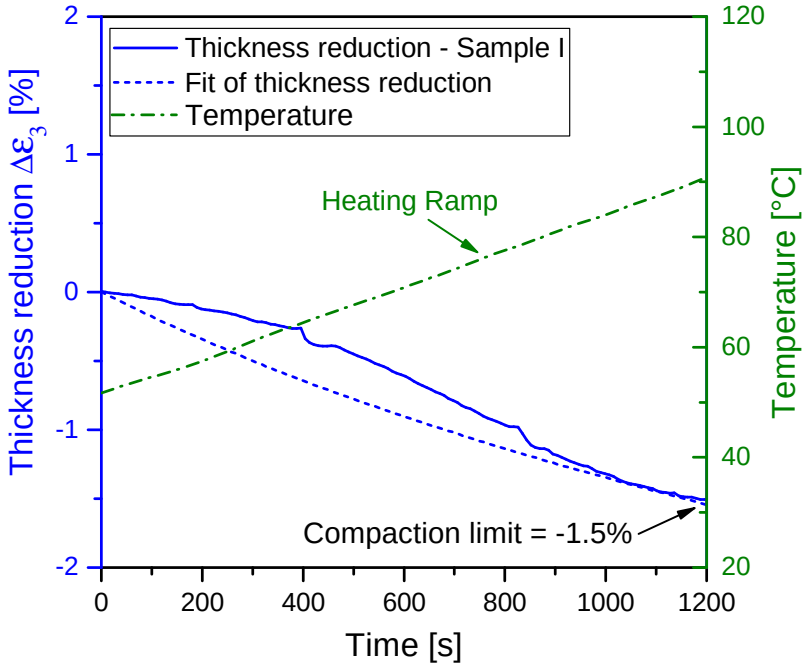

Figure 3.18: Comparison between the estimated compaction kinetics based on the proposed empirical fit and the experimental thickness reduction of sample I during the heating ramp only.

From a practical point of view, the estimation of thickness reduction evolution for a given temperature range or an isothermal dwell could be encouraging to predict the change in dimensions induced by the consolidation in the uncured state. Experimental measurements of thickness reduction are scarce in the literature, notably for uncured materials and are commonly performed on partially cured samples or after curing as a means to evaluate the consolidation and final part qualities. In the presented case, further investigations are required to better identify the most suitable model. Changing the heating ramp temperatures could be interesting to improve the prediction of the whole compaction behavior. As a perspective, an improved phenomenological model could be proposed from the experimental identification of the thickness reduction as function of the initial state of material in relation with the pre-debulking step and the porosity level of the samples.

3.6 Anisotropic thermal expansion and shrinkage measurements results

3.6.1 Thermal expansion behavior and CTE measurements

PvT-HADDOC measurements

In this subsection, we focus on stages 2 and 4 among the whole described curing behavior in section 3.4 in order to estimate the coefficients of thermal expansion of the IMA/M21 material. Figure 3.19 gives the induced strains along both transverse directions and their evolution with the thermal cycle. The curing behavior of sample 3 is taken as an example for the analysis.

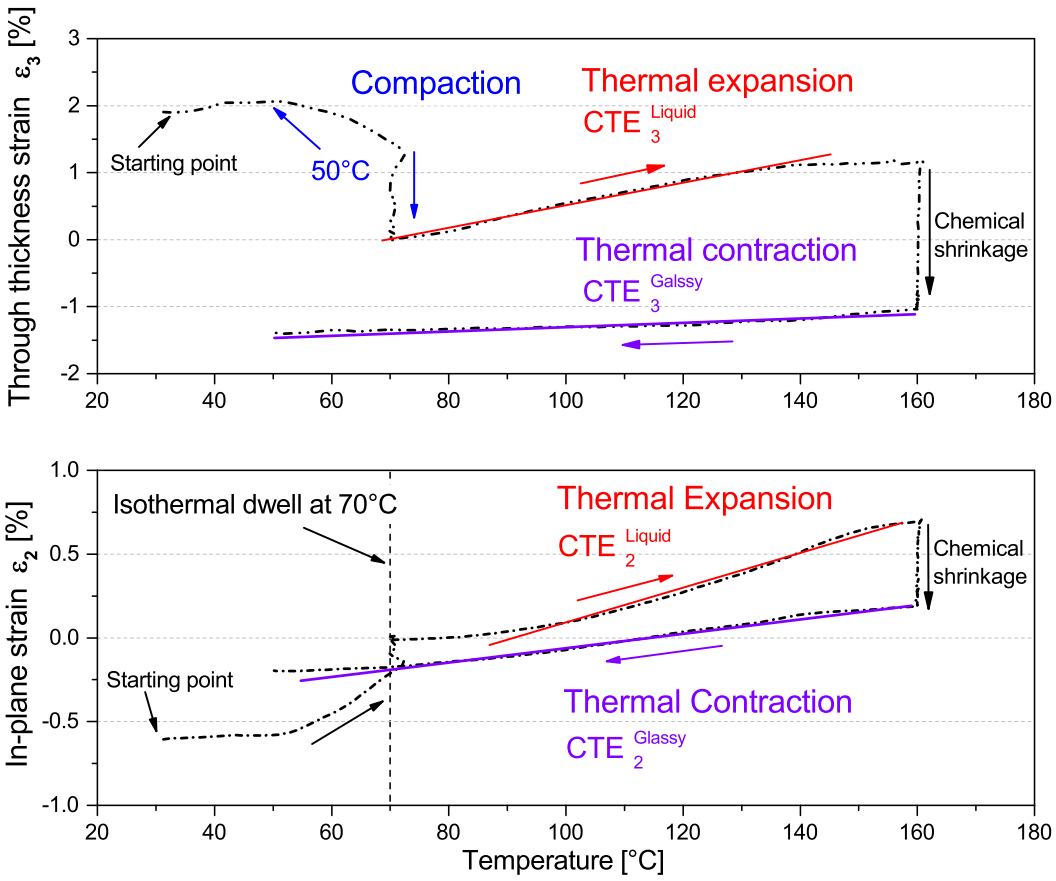

Figure 3.19: The induced strains along both transverse directions during curing of sample 3 as function of the applied thermal cycle 2.

As the material is heated, we can notice the through-thickness compaction that starts when the temperature reaches approximately 50°C. Along the transverse in-plane direction, the material expands and somewhat follows the thermal cycle up to 70°C. During the applied isotherm at 70°C, thickness reduction is again observed through the sharp drop in ε_3, while a small increase in ε_2 of 0.17% can be noticed. It is worth noting that throughout the

compaction stage, the transverse in-plane behavior still needs more investigations to further understand the origin of the induced strains whether they are only due to the thermal effects or there is also a triggered widening related to the through-thickness compaction. Nevertheless, this effect seems to be negligible compared to the compaction phenomenon.

The CTE in the liquid uncured state (denoted by CTE^{Liquid}) of the material can be estimated from the expansion phase during stage 2. As we can see from figure 3.19, during the heating ramp, the increase in both ε_2 and ε_3 is only linked to the temperature increment. The slopes of the linear regressions represent the CTE of the material in its liquid state. During the isothermal dwell at 160°C we can notice the strain drop which is driven by the crosslinking reaction of the matrix. During the cooling step, the only prominent phenomenon is the thermal contraction of the prepreg illustrated by the decrease in both strains ε_2 and ε_3. The value of the glass transition at the end of cure predicted by the kinetics model for samples cured according to cycle 2 is T = 153°C. The slopes of the linear fitting relations during cooling from 160°C to ambient temperature give therefore the CTE of the cured glassy state of the prepreg (denoted as CTE^{Glassy}). The values of the CTE in both states are calculated through the curing of all the tested samples [1-5] and the average values are gathered in table 3.5.

Table 3.5: Estimated values of the CTE for the IMA/M21 material by the PvT-HADDOC set-up.

Material state	Through-thickness CTE_3	In-plane CTE_2	Unit
Uncured Liquid	178±9	100±11	$10^{-6}K^{-1}$
Cured Glassy	55±4	39±4	$10^{-6}K^{-1}$

The estimated values of the CTE through the thickness are proved to be much higher than the in-plane direction in the liquid state and also when the material is fully cured. Such results support previous observations as it is clearly visible from figure 3.12. During stage 2, the material expands much more along its thickness. More thermal contraction along direction 3 is also observed throughout stage 4.

Measurement of CTE in the cured state with linear dilatometer

The CTE of the cured tested samples in this work were also measured using a linear dilatometer Linseis L 75 HXLT as a way of verification. The three directions are investigated using specimens that were cut from each laminate sample after the curing experiment. In figure 3.20a, we can find an example of a cured laminate sample according to cycle 2 and the extracted specimens for dilatometric measurements are given in figure 3.20b.

The tested samples were heated from ambient temperature up to 200°C with a heating rate of 2°C.min^{-1}. A typical variation of linear strains ($\Delta L/L_{ini}$) related to the expansion of specimens extracted from sample 2 is illustrated in figure 3.21 as a function of temperature. L_{ini} represents the initial length of used samples. Along the longitudinal direction, the measurements of ε_1 strain do not reveal any expansion of the material during heating but rather a slight contraction of about zero that could not be noticeable and which is in accordance with

(a) (b)

Figure 3.20: (a) Example of cured IMA/M21 laminate sample. (b) Extracted specimens for linear dilatometric measurements.

the observed tendency of the axial strain measured with the PvT-HADDOC device. The estimation of the CTE along this direction was difficult to identify due to the very low variation of ε_1 with temperature. Along both transverse directions, the strains evolution exhibit a change in slope approximately around the estimated value of Tg = 153°C. The point at which the strains change matches perfectly the predicted glass transition temperature which reflects the differences between the cured glassy and cured rubbery expansion coefficients.

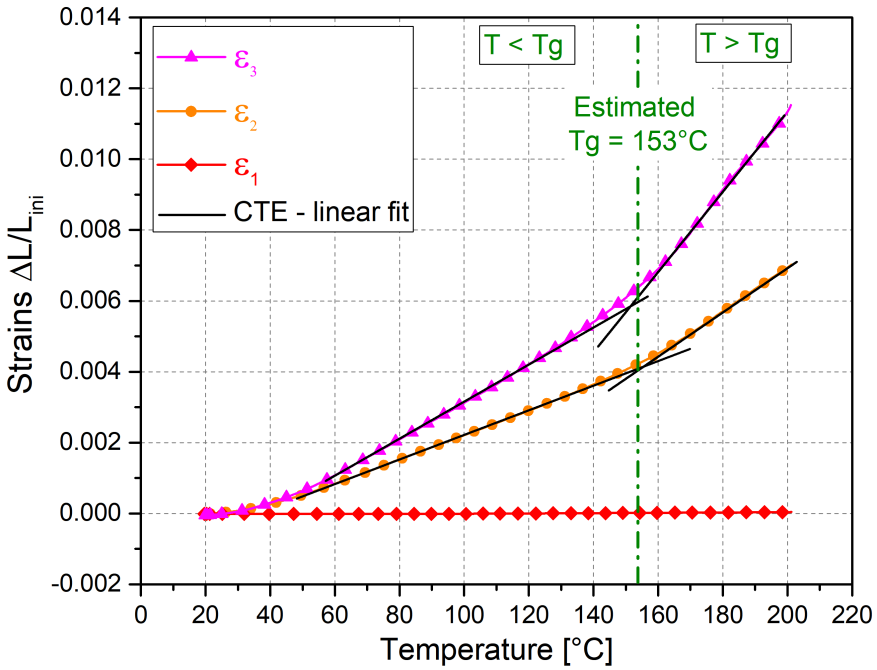

Figure 3.21: Linear thermal expansion behavior along three principal directions obtained with measurements conducted on cured specimens extracted from sample 2 using a linear dilatometer.

The estimated values of the CTE in the cured glassy (T<Tg) and cured rubbery (T>Tg) states are calculated from the slope of each linear fit of the linear strains according to the following equation

$$CTE_i = \frac{\Delta L_i}{L_{ini} \times \Delta T} \quad \text{with} \quad i = 2, 3 \tag{3.6}$$

The obtained values for each material state are gathered in table 3.6. Only the coefficients related to the cured glassy state can be compared to the measurements conducted with the PvT-HADDOC device since the cured rubbery state was difficult to examine during the cooling ramp from 160°C to the ambient temperature with the PVT tests. According to the results depicted in table 3.5 and table 3.6, one can conclude that the measurements of the CTE along both transverse directions with both methods are in excellent agreement.

Table 3.6: Estimated values of the CTE for the IMA/M21 material with linear dilatometer on cured samples.

Material state	Through-thickness CTE_3	In-plane CTE_2	Unit
Cured Glassy (T<Tg)	52±1	39±1	$10^{-6}K^{-1}$
Cured Rubbery (T>Tg)	87±5	61±3	$10^{-6}K^{-1}$

Discussions

The obtained disparities between the thermal expansion coefficients measured along the thickness direction and the transverse planar one given in tables 3.5 and 3.6, reveal that the IMA/M21 prepreg investigated in this research might have rather an orthotropic behavior than transversely isotropic, contrary to what a UD stacking may suggest. As the reported works in literature lack such *in-situ* multi-axial characterizations and due to the limitations of the employed techniques to capture the liquid expansion of toughened prepregs, the material behavior is commonly considered as transversely isotropic. Nevertheless, similar orthotropic behavior in the cured state was found in a recent research work [185] conducted on similar system of IMA/M21 interlayer toughened UD prepreg using TMA technique. Also, other recent works [186, 187] were interested in modeling the behavior of interlayer toughened prepregs. The obtained results have indeed shown in comparison with the measured CTE of cured UD laminate samples with linear dilatometer along the transverse directions an orthotropic behavior of the material.

Considering the obtained results in this work and some of the reported studies from the literature, one can presume that the orthotropic behavior of the unidirectional IMA/M21 laminate could be mainly arisen from the presence of the extra inter-leaf layers of resin between the fiber rich prepreg plies. In such case, the laminate could not exhibit a symmetric structure in the fiber direction which may explain the differences between the measured properties along both transverse directions. This assumption will be further verified in next chapter.

3.6.2 Chemical shrinkage behavior and CCS measurements

The dimension changes of the material that take place during the isothermal hold at stage 3 are directly generated by the crosslinking reaction of the matrix which are the subject of this subsection. The chemical shrinkage is a reflection of the polymerization and therefore it is much more useful to elaborate the relationship of cure shrinkage with the degree of cure. We assume that during the isothermal dwell there is no effect of thermal expansion of the material and thereby the measured strains during stage 3 are mainly related to the chemical shrinkage (denoted $\Delta\varepsilon^{chem}$). In figure 3.22, the effect of curing along both transverse directions is isolated and zeroed at the beginning of the isothermal cure at 160°C. The induced strains from the curing of sample 2 are taken as example and presented as a function of the estimated degree of cure.

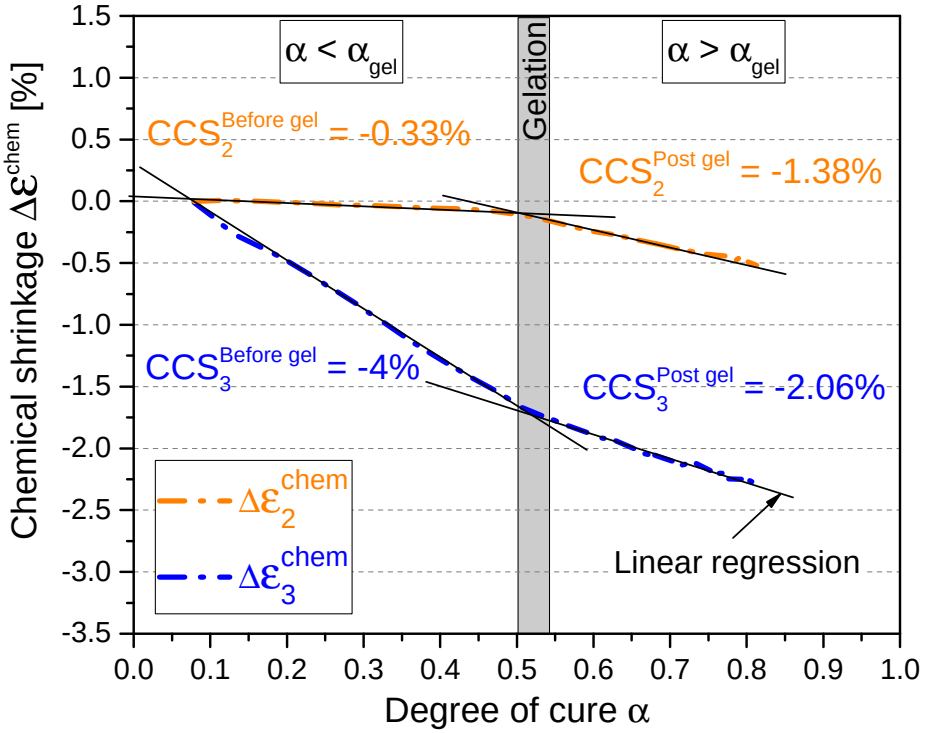

Figure 3.22: Measured chemical shrinkage of sample 2 during the isothermal cure at 160°C of cycle 2.

As illustrated in this figure, the dependence of the chemical shrinkage on the degree of cure follows as expected a linear trend, however, it exhibits a change of slope around a specific point. It has been reported in [46] that the gel point of the studied M21 system can range between $\alpha = 0.51$ and 0.55. In the present study, it estimated equal to 52±1.4 % (see section 2.5). Therefore, we assume that the deviation of the chemical shrinkage is attributed to the gelation of the matrix. The slope of each linear regression gives the CCS of the unidirectional laminate and hence allows for two coefficients of cure shrinkage to be found along both transverse directions as described in the equation below where 'BG' refers to before gelation stage and 'PG' denotes the post gelation one:

$$\Delta\varepsilon^{Chem} = CCS \cdot \Delta\alpha \tag{3.7}$$

$$CCS_i = \begin{cases} CCS_i^{BG} & \text{if } \alpha < \alpha_{gel} \quad \text{and} \quad i = 2,3 \\ CCS_i^{PG} & \text{if } \alpha \geq \alpha_{gel} \quad \text{and} \quad i = 2,3 \end{cases}$$

As it is visible from figure 3.22, the material does not display the same behavior through both transverse directions. Firstly and in line with the observed results in the previous subsection, the chemical strains evolution reveals again an orthotropic behavior of the studied unidirectional laminate. The total shrinkage through the thickness direction reaches -2.29% whereas the material only shrinks of about -0.5% along the in-plane direction. Secondly, the estimated values of the CCS reveal an unusual behavior that, to our knowledge, has not been captured before according to the reported works in literature, simultaneously along both directions. Before the gelation, the material tends to shrink entirely through its thickness with a higher rate of -4% comparing to the in-plane direction where the shrinkage evolves steadily with only -0.33% of rate. With further increase of degree of cure, the rate of the chemical shrinkage increases in the in-plane direction and still shows a linear relation with the degree of cure with a rate of -1.38%. However, through the thickness direction, the after gelation behavior is rather characterized by a much slower kinetics with a CCS of -2.06% which is almost half of the CCS before gelation.

The effect of the curing temperature was also investigated to further understand the shrinkage behavior. Sample 1 was cured under an isothermal dwell at 180°C. In the same manner, the induced strains captured during the isotherm hold are extracted from the overall induced strains to represent the chemical shrinkage only. In figure 3.23 are illustrated the cure induced shrinkage along the in-plane direction (figure 3.23a) and through the thickness direction (figure 3.23b) respectively, for the two cure temperatures. The estimated values of the CCS along each direction and for each temperature are presented on these graphs. Results show that for a given direction, the chemical shrinkage kinetics follows the same trend regardless of the cure temperature. These expected results support previous reported observations in literature that assume that the cure shrinkage is only a function of the degree of cure regardless of the cure temperature and time [14, 188]. Consequently, it is possible to estimate average values of the calculated CCS for all the tested samples according to both cure temperatures which are gathered in table 3.7.

Table 3.7: Estimated values by the PvT-HADDOC device of the CCS for the IMA/M21 laminate.

	Through-thickness CCS_3	In-plane CCS_2	Unit
Before gelation	-3.83±0.3	-0.27±0.04	%
After gelation	-2.07±0.1	-1.4 ±0.09	%

Discussions

From the results described above, we conclude that, thanks to the experimental device used in this work, it was possible to capture in an original and precise way how a UD laminate can shrink, along both transverse directions, before and after gelation, and under applied isotropic

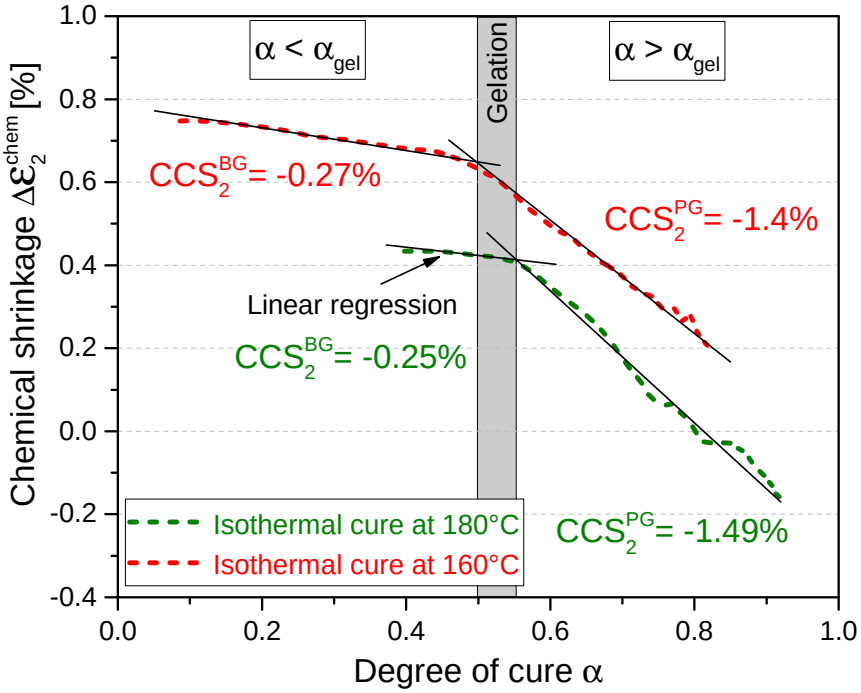

(a)

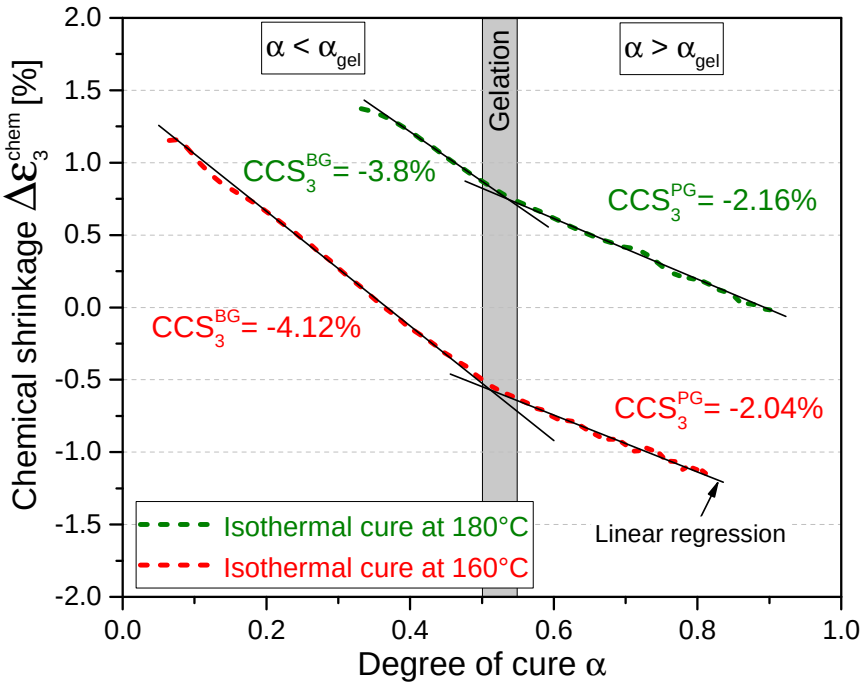

(b)

Figure 3.23: Transverse chemical shrinkage measured during a 180°C and 160°C isothermal cure (Sample 1 and 3 are taken as examples, respectively). (a) Along the in-plane direction. (b) Along the thickness direction.

compressive state. Like for CTEs, the presence of the interlayers in the laminate structure is expected to be the cause that triggers such discrepancies between reached level of shrinkage along both transverse directions. Nevertheless, there is no reported data in the literature that allow similar comparison between both linear chemical shrinkage of toughened prepregs since, according to the author knowledge, almost all available methods enable measurements along only one direction at one time. Therefore, the influence of the presence of resin interleaves on the induced orthotropic cure shrinkage behavior of the studied IMA/21 laminate will be further assessed in next chapter.

Moreover, due to the deficiency of the experimental tools commonly used to study the chemical shrinkage of thermoset composites, it has been generally considered that the material shrinks likewise during both regions before and after gel. Shrinkage rate change around the gel point has been already reported in few research works conducted on pure thermoset epoxy resins [188,189] or recently on thermosetting composites based on epoxy system [15,20]. However, their results are not totally in agreement with the findings presented in this work. In a study carried out by Moretti *et al.* [15] on a similar inter-layered prepreg IMA/M21EV using the TMA technique and conducted on samples laid-up in a quasi-isotropic configuration, it was reported that the through-thickness chemical shrinkage follows a completely different behavior. In the pre-gelation region, the material displayed a slow shrinkage rate, whereas after gelation the cure shrinkage progressed with a higher rate. In an other recent research work reported by Duffner *et al.* [20], the investigation was conducted on unidirectional samples made of the AS4/8552 prepreg system with dissolved thermoplastic particles that are rather dispersed within plies throughout the bulk phase of the epoxy resin. Thus, the laminate could be considered as transversely isotropic since it does not include resin interlayers between the prepreg plies. Only the in-plane chemical shrinkage was measured through curing and the obtained results showed a similar behavior compared to the studied material in this work. The average value of the pre-gelation CCS was found to be equal to -0.68% and the post gelation CCS to -1.45% which is comparable to the values of the CCS measured along the in-plane direction in this work.

Note that, the cure shrinkage behavior of the investigated neat resin did not exhibit any shrinkage rate change around the gel point as can be found in subsection 2.4.2 of chapter 2. Besides, the studied AS4/8552 prepreg does not include extra-interlayers. Hence, considering the results reported by the above-mentioned authors in addition to the present work, the change of the cure shrinkage rate cannot be thoroughly explained by the presence of these resin interleaves in the laminate which will be further discussed in next chapter.

3.7 Partial conclusion ans perspectives

Thanks to the PvT-Haddoc experimental bench the whole cure behavior of the studied IMA/M21 prepreg has been investigated in this chapter. The analysis of the multi-axial measurements of the thermo-chemical deformations allowed us to depict the complex behavior of this third generation unidirectional prepreg. The latter proved to be rather fully orthotropic. In order to get rid from the compaction phenomenon that has been identified through the thickness reduction in the early stages of heating, the standard curing cycle was

modified. By doing so, it was possible to separate the coupled physics. The cure behavior of IMA/M21 material has been divided into 4 stages that include the laminate consolidation in the uncured state, the thermal expansion during the heating step, the whole chemical shrinkage behavior, *i.e.*, before and after gelation, and also the material thermal contraction along the cooling step. The analysis of each stage enabled to obtain further understanding of the behavior during the cure.

The compaction of the material in the viscous uncured state is proved to be anisotropic. Thickness reduction is assumed to be dependent on the resin flow driven by capillary pressures effects. Such phenomenon is supposed to be correlated to the impregnation of fibers and voids suppression. Further developments on these hypotheses remain as future work. For example, the investigation of the effect of the pre-cure debulking step needs additional tests as to pre-compact the samples at different temperatures under different compaction pressure. In our case of study, the cure pressure is applied since the beginning of the cure cycle. Further investigations with different curing conditions like various time of pressure application or different cure pressure values are required to justify the impact of temperature/pressure on the material consolidation in the uncured state. Besides, the compaction behavior of the fiber bed for uncured materials still need more accurate studies according to recent research works on toughened prepregs [21, 120]. Hence, changing the mechanical state around the sample would be of great impact on the comprehension of the consolidation behavior during the early stages of thermoset composites processing.

The analyses of stages 2 and 4 among the cure cycle allowed us to estimate the material CTE parameters along both transverse directions and in both states, uncured liquid and cured glassy. As a perspective for future research, further investigations will be carried out in order to determine the evolution of the CTE through the full cure along both transverse directions. The measured chemical shrinkage of the studied IMA/M21 prepreg revealed the importance of such original in-situ multi-axial characterization. It is proved that the studied UD laminate does not shrink likewise before and after gelation along both transverse directions in the contrary to what has been commonly assumed. Indeed, the linear dependency of the chemical shrinkage on the degree of cure exhibits a change of slope around the gel point. Moreover, the shrinkage behavior showed an independence on the curing temperature. Such findings about the CTE and CCS parameters of the studied complex material reveal the crucial need to provide fine measurements of these parameters to properly account for the thermal effects and cure shrinkage in the prediction of shape distortions and residual stresses development during the cure of thermosetting composites.

CHAPTER 4

MULTI-LAYER MODEL CONSIDERING THE PRESENCE OF RESIN INTERLEAF LAYERS

Contents

4.1 Introduction **120**
4.2 Brief review on homogenization models employed for composite materials **120**
4.3 Multi-layer model and laminate constitutive equations **122**
4.3.1 Formulation of the multi-layered structure and model description 122
4.3.2 Application to thermo-chemo-elasticity 124
4.3.3 Volume fraction of each lamina 125
4.3.4 Thermo-mechanical behavior of the laminate at the macro-scale . 125
4.4 Identification of each layer thermo-chemical properties and mechanical behavior at the meso-scale **126**
4.4.1 Estimation of the volume fraction of each layer 127
4.4.2 The resin inter-layer cure dependent behavior 127
4.4.2.1 Elastic modulus and Poisson's ratio 127
4.4.2.2 Linear coefficients of thermal expansion and chemical shrinkage 131
4.4.3 The prepreg layer cure dependent behavior 131
4.4.3.1 Mechanical elastic properties 131
4.4.3.2 Coefficients of thermal expansion and cure shrinkage . . 134
4.5 Comparison with experimental results and discussions **135**
4.5.1 Calculation procedure 135
4.5.2 Results and discussions 137
4.6 Partial conclusion and perspectives **142**

4.1 Introduction

A single continuous fiber-reinforced unidirectional ply is commonly assumed as transversely isotropic. When no interleaf layers are introduced, the whole laminate is expected to exhibit a symmetric structure in the fiber direction and thus to represent the same properties along the in-plane and the through-thickness directions. In this chapter, we suggest a new approach that accounts for the presence of the extra interleaf layers of toughened resin within the prepreg plies in the calculation of the laminate coefficients of thermal expansion and cure shrinkage. From this, we firstly attempt to provide a way to assess the validity of the assumption made in the previous chapter on the basis of the experimental measurements which states that the studied material behavior is rather fully orthotropic. The second objective of the new proposed approach is to verify whether the presence of the resin interleaves plays a significant role on the strange shrinkage evolution around gelation. The first part of this chapter given by section 4.2 provides a brief reminder of the literature on the most employed typical micromechanical models in the case of composites that allow to estimate their effective properties. The third section deals with the presentation of the proposed approach. Thereby, the global architecture of the multi-layer model and the derived constitutive law of the defined laminate are detailed. In section 4.4 are given the thermo-chemical properties and mechanical behavior assumed for each layer of the studied IMA/M21 prepreg required for the estimation of the macroscopic effective thermo-chemical properties. In the final section of this chapter (section 4.5), the obtained results with the model are discussed and compared with the experimental properties determined in chapter 3.

4.2 Brief review on homogenization models employed for composite materials

Composite materials typically comprise a matrix phase and the reinforcement phase that can be of various types such as particulates with varied shape, size or configuration and fibers which can be incorporated as random, short or long continuous fibers. Regarding such composition and depending on the geometrical arrangement of the constituents, composites generally present an anisotropic behavior and their thermo-mechanical properties are conventionally analyzed through multi-scale approaches. It is necessary here to specify the different scales commonly employed for the study of composites. The scale of the constituents is referred as the microscopic scale that considers the smallest heterogeneities present in the material and which is of lower order than the scale of the resulting structure called as the macro-scale as it can be found through the illustrations given in figure 4.1. In the case of laminate composites, an intermediate scale called as mesoscopic scale can also be defined in which the plies are viewed as separate entities.

Micromechanics models which can also be referred as homogenization models, allow to evaluate the composite thermo-mechanical macroscopic properties (also called as homogenized properties) from the microscopic behavior, *i.e.* by taking into account the individual component properties of the material at the microscopic scale (such as the geometrical arrangements, the different phases constituting it, etc.) [190, 191]. Their objective is therefore to replace

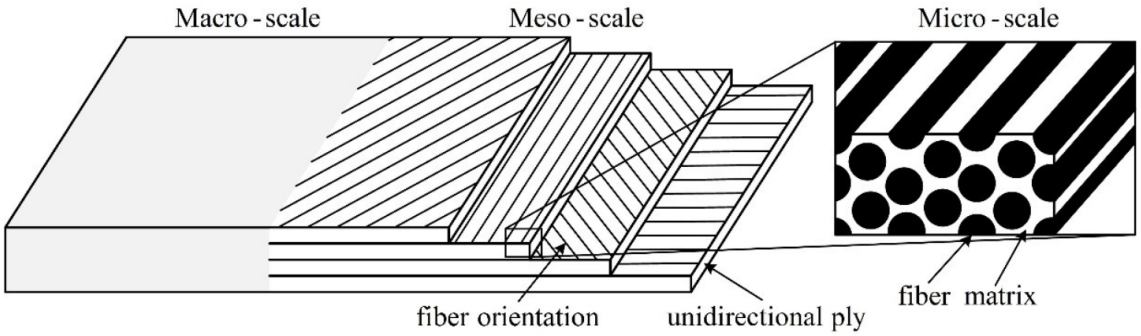

Figure 4.1: Different scales defined in a composite laminate structure [40].

the heterogeneous media at the micro-scale by an equivalent homogeneous medium which would have the same physical properties from a macroscopic point of view. This could be achieved through a combination of macroscopic-microscopic computational methods that replace in a more efficient way the fact of solving the full microscopic model. Unidirectional fiber laminated composites made from only prepreg layers are commonly analyzed using effective ply properties by means of a homogenization method of choice. Many engineering problems are solved at the macroscopic scale with such homogenized properties which are usually difficult or expensive to measure. The homogenization strategy mainly requires a well-defined field of application which commonly imply the use of the concept of a Representative Elementary Volume (REV) also called as the Representative Volume Element RVE. Depending on the geometry of the composite at the micro-scale and thereby on the statistical distribution of the properties, various approaches have been developed to solve the elastic problem of the transition from the micro-scale to the macro-scale either by analytical or numerical methods [190, 191]. Mean field approach based on the solution of the inclusion problem pioneered by Eshelby [192] which proposes a solution for the elementary problem of an assumed elastic ellipsoidal inclusion (fiber for example) immersed in an infinite isotropic medium, *i.e.* the matrix, has been the starting point of many micromechanical models. In these approaches, average fields are considered for each phase in the material such as the so-called Self-Consistent (SC) model [193] and the Mori-Tanaka (MT) model [194] that have been well adapted for heterogeneous materials with a random microstructure distribution at the micro-scale. The (SC) homogenization approach has been proved successful in the study of unidirectional continuous fiber reinforced composites to predict cure residual deformations [18,29,34,90,195] such as the example proposed by Msallem *et al.* [29]. It allowed the determination of the effective tensors of stiffness, thermal expansion and chemical shrinkage of the composite ply from the properties of the constituents. The laminate behavior during the cure was deduced by means of a thermo-chemo-elastic description based on classical laminate plate theory. The (MT) micromechanical model was applied in addition to the (SC) approach as a two-steps scale transition procedure in an other study proposed by Lacoste *et al.* [196] in order to carry out a multi-scale analysis of the behavior during the cure process of a meso-structured thermoset composite with complex microstructure made of UD strips randomly disposed in the layout. Some other analytical models are also well-known and have been largely employed. The determination of bounds of the effective properties of heterogeneous media is a complementary approach to the estimation of their effective behavior. We

find the bounds of Voigt and Reuss [197, 198] which represent the upper and lower bounds of the effective behavior of the material, and Hashin-Shtrikman bounds [199] which are an extension of the latter method and can be applied when the material behavior is considered as isotropic at the macro-scale. These bounds are known to give closer solution intervals than the Voigt and Reuss bounds. These methods only require the knowledge of the elastic behavior of the constituents and the respective volume ratio of the inclusions in the matrix composing the heterogeneous medium and are based on simple assumptions on the geometry of the structure. These bounds are obtained by assuming either the strain tensor or the stress tensor uniform in the material. In the first case, we obtain the Voigt bounds and in the second the Reuss bounds. The classical rule of mixtures has been then applied in several engineering applications owing to its simplicity for the determination of the elastic properties, thermal properties and effective coefficients of thermal expansion of unidirectional composite plies knowing the properties of its constituents [178, 200]. None of the stated classical homogenization models, according to the authors knowledge, has been applied to toughened prepregs with extra interleaf layers of resin as is the case with the studied material in this research work. The main objective here is therefore to propose a simple multi-layer model considering the interleaves presence to be usable with our experiments.

4.3 Multi-layer model and laminate constitutive equations

4.3.1 Formulation of the multi-layered structure and model description

The IMA/M21 UD laminate samples produced in this research work and used for the characterization of the thermo-chemical behavior during the cure exhibit a small thickness compared to the planar dimensions with a thickness to width ratio of about 0.05. Considering this point, classical laminate theory (abbreviated as CLT) based on the Kirchhoff–Love approach appears as a good candidate to translate the in-plane material behavior during the cure. As we do not consider here the full plate theory, but only the membrane kinematics, this approach can be here considered as a simple Voigt bound approach. The in-plane strain is assumed identical for all layers. However, to consider the effect of the interleaf layers on the induced through thickness thermo-chemical strains, some assumptions are additionally made to estimate the material behavior along the axial transverse direction. In the following, the assumptions made in CLT theory along with the assumptions made for considering the presence of the resin interlayers are stated below:

1. The principal laminate axes (1, 2, 3) are aligned with the coordinate system: 1 indicates the direction of fibers and 3 the normal direction to the plane of samples (see figure 4.2).
2. The laminate is considered as a multi-layer composite that has a microstructure consisting of alternating layers made up from unidirectional IMA/M21 prepreg plies and toughened resin inter-layers as it is illustrated in figure 4.2. The laminate is assumed to be made of 2N layers. Hereafter, the index "ply" refers to the dominant fiber rich

prepreg layer and "il" is associated to the resin interleaf layer toughened with thermoplastic particles. Thereby, one can assume that the structure of the material involves three different scales defined as follows:

- Microscopic scale which comprises the IMA fibers and the epoxy resin as the matrix phase for the prepreg ply and thermoplastic particles plus the epoxy resin for the interlayer.
- Mesoscopic scale in which the prepreg ply and the interleaf layer are viewed as separate laminae.
- Macroscopic scale which is related to the multi-layered laminate.

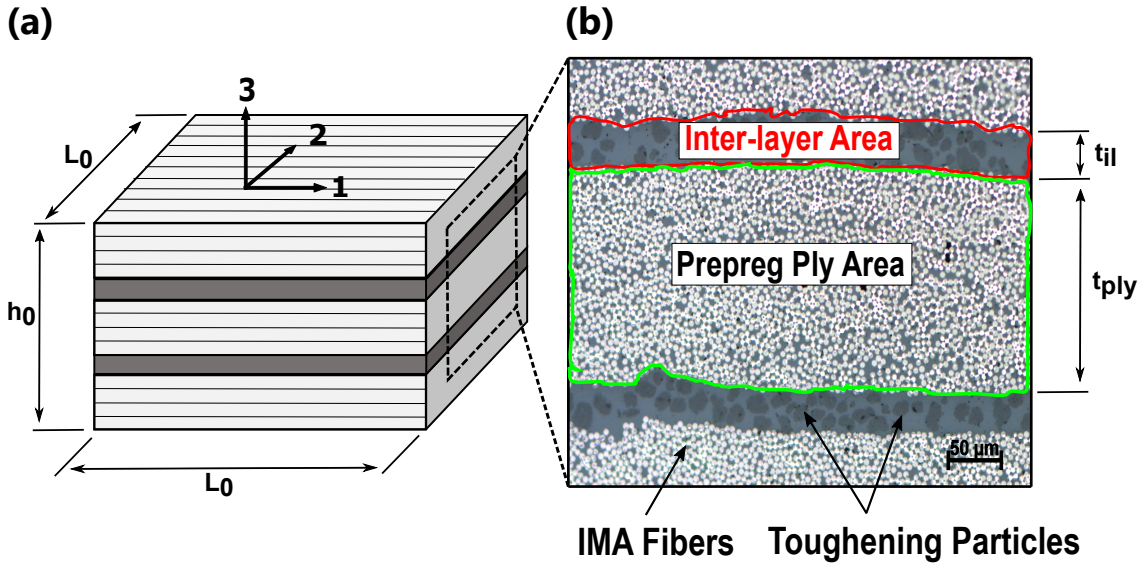

Figure 4.2: (a) Schematic model of the multi-layer geometry with coordinate system and dimensions for a unidirectional IMA/M21 prepreg laminate. (b) A through-thickness micro-section of a cured sample.

3. Each layer is assumed in a state of plane stress which is characterized by the following relations

$$\left\{ \begin{array}{rcrcrcl} \sigma_3^{ply} & = & \sigma_{23}^{ply} & = & \sigma_{31}^{ply} & = & 0 \\ \sigma_3^{il} & = & \sigma_{23}^{il} & = & \sigma_{31}^{il} & = & 0 \end{array} \right. \tag{4.1}$$

4. Note that, only homogeneous states of stress and strain are considered, just like in the PvT-HADDOC experiments. In the plane, the laminate is assumed to deform according to the Kirchhoff-Love assumptions, in which the normal to the middle surface before deformation remain normal to the same surface after deformation. Thereby, the midplane curvatures are neglected resulting in nil distortion strains for all layers. Moreover, a perfect bonding is assumed between the layers and the complete laminate is presumed to act as a single layer. Considering the kinematics connection between the laminae, the midplane elongation strains are equals for all layers resulting in

$$\left\{ \begin{array}{rcrcl} \varepsilon_1 & = & \varepsilon_1^{ply} & = & \varepsilon_1^{il} \\ \varepsilon_2 & = & \varepsilon_2^{ply} & = & \varepsilon_2^{il} \end{array} \right. \tag{4.2}$$

5. One should mention that according to Kirchhoff-Love assumptions, the strain perpendicular to the middle surface is ignored since the lines perpendicular to the mid-plane are presumed to have a constant length even after deformation. Nevertheless, in this case of study, nonzero transverse normal strains are assumed in order to account in a consistent manner for the expansion and shrinkage phenomena that occur in the out-of-plane direction, which means

$$\begin{cases} \varepsilon_3^{ply} & \neq & 0 \\ \varepsilon_3^{il} & \neq & 0 \end{cases} \tag{4.3}$$

6. A shear-free state is assumed which can be justified by the homogeneous boundary conditions (frictionless) and the homogeneous thermal expansion and shrinkage resulting in

$$\{ \sigma_{12}^{ply} = \sigma_{12}^{il} = 0 \tag{4.4}$$

Consequently, by adopting an orthotropic linear elastic behavior for each layer and by taking into account the stated assumptions above, the constitutive law of each lamina denoted by "k" for the ply or the interlayer, can be written in matrix from as strain-stress relations in principal axis by

$$\{\sigma^k\} = \begin{bmatrix} \sigma_1^k \\ \sigma_2^k \\ \sigma_3^k \end{bmatrix} = \begin{bmatrix} C_{11}^k & C_{12}^k & C_{13}^k \\ C_{12}^k & C_{22}^k & C_{23}^k \\ C_{13}^k & C_{23}^k & C_{33}^k \end{bmatrix} \begin{bmatrix} \varepsilon_1 \\ \varepsilon_2 \\ \varepsilon_3^k \end{bmatrix} \tag{4.5}$$

where $[C_{ij}]^k$ is the stiffness matrix whose components depend on each layer behavior.

4.3.2 Application to thermo-chemo-elasticity

For the studied composite material, cure strains highly depend on temperature variations that occur along the whole thermal cycle in addition to the chemical shrinkage induced by the crosslinking reaction of the matrix. To correctly describe the macroscopic behavior of the laminate during the cure process, these phenomena have to be considered in the elastic law (equation 4.5) used to describe each lamina behavior. Therefore, the latter can be described by the chemo-thermo-elastic constitutive law written in matrix form as

$$\{\sigma^k\} = \begin{bmatrix} \sigma_1^k \\ \sigma_2^k \\ \sigma_3^k \end{bmatrix} = \begin{bmatrix} C_{11}^k & C_{12}^k & C_{13}^k \\ C_{12}^k & C_{22}^k & C_{23}^k \\ C_{13}^k & C_{23}^k & C_{33}^k \end{bmatrix} \left(\begin{bmatrix} \varepsilon_1 \\ \varepsilon_2 \\ \varepsilon_3^k \end{bmatrix} - \begin{bmatrix} \varepsilon_1^{tc,k} \\ \varepsilon_2^{tc,k} \\ \varepsilon_3^{tc,k} \end{bmatrix} \right) \tag{4.6}$$

where $\{\varepsilon^{tc,k}\}$ contains the thermo-chemical strain tensor components for each layer. In practice, the latter is calculated based on CTE_i^k and CCS_i^k which are the coefficients of thermal expansion and chemical shrinkage, respectively, associated to each lamina along the direction

"i". For the sake of simplicity, the constitutive law for each lamina will be written as

$$\{\sigma^k\} = \begin{bmatrix} \sigma_1^k \\ \sigma_2^k \\ \sigma_3^k \end{bmatrix} = \begin{bmatrix} C_{11}^k & C_{12}^k & C_{13}^k \\ C_{12}^k & C_{22}^k & C_{23}^k \\ C_{13}^k & C_{23}^k & C_{33}^k \end{bmatrix} \begin{bmatrix} \varepsilon_1 \\ \varepsilon_2 \\ \varepsilon_3^k \end{bmatrix} - \begin{bmatrix} \sigma_1^{tc,k} \\ \sigma_2^{tc,k} \\ \sigma_3^{tc,k} \end{bmatrix} \tag{4.7}$$

4.3.3 Volume fraction of each lamina

We define the volume fraction of each layer in the entire volume of the fiber-reinforced laminate, denoted as ϕ_k, by:

$$\phi_k = \frac{V_k}{V_{tot}} = \frac{N \times t_k \times S}{N \times (t_{ply} + t_{il}) \times S} = \frac{t_k}{t_{ply} + t_{il}} \tag{4.8}$$

with

$$\phi_{ply} + \phi_{il} = 1$$

where V_k is the volume related to the layer k divided by the total volume of the composite referred by V_{tot}. N is the number of layers, t_{ply} is the prepreg ply thickness, t_{il} is the resin interlayer thickness as illustrated in figure 4.2 and S is referred to the surface of the sample.

4.3.4 Thermo-mechanical behavior of the laminate at the macro-scale

According to the defined constitutive law for each layer at the mesoscopic scale (see equation 4.7), note that the problem implies the determination of 4 unknown parameters for a given temperature and degree of cure: the out-of-plane elongations related to each lamina ε_3^{ply} and ε_3^{il}, and the in-plane macroscopic strains ε_1 and ε_2.

During the curing tests, the composite material was submitted to an isotropic compressive stress state which is assumed to lead to negligible deformations of the samples, *i.e.*, the applied pressures are low compared to the compressibility of the material when compacted. Therefore, in order to simplify the analysis without loosing any precision, the mechanical state around the laminate will be assumed stress free which results in

$$\{\sigma\} = \begin{bmatrix} \sigma_1 \\ \sigma_2 \\ \sigma_3 \end{bmatrix} = \begin{bmatrix} 0 \\ 0 \\ 0 \end{bmatrix} \tag{4.9}$$

where σ_1, σ_2 and σ_3 are the components of the macroscopic stress field related to the composite according to each principal direction.

Consequently, on the one hand, the midplane average stress field of the laminate can be estimated as a function of the corresponding local stresses of the prepreg ply and the interlayer since the overall in-plane stress is distributed between both constituents and can be defined as follows:

$$\{\bar{\sigma}\} = \begin{bmatrix} \sigma_1 \\ \sigma_2 \end{bmatrix} = \phi_{ply} \begin{bmatrix} \sigma_1^{ply} \\ \sigma_2^{ply} \end{bmatrix} + \phi_{il} \begin{bmatrix} \sigma_1^{il} \\ \sigma_2^{il} \end{bmatrix} = \begin{bmatrix} 0 \\ 0 \end{bmatrix} \tag{4.10}$$

We introduce the average stiffness matrix $[\bar{C}]$ of the multilayered structure as a function of the elasticity matrices related to the prepreg ply denoted by $[C_{ij}]^{ply}$ and the resin interlayer denoted by $[C_{ij}]^{il}$ as follows

$$[\bar{C}] = \phi_{ply}[C_{ij}]^{ply} + \phi_{il}[C_{ij}]^{il} = \begin{bmatrix} \bar{C}_{11} & \bar{C}_{12} \\ \bar{C}_{12} & \bar{C}_{22} \end{bmatrix} \tag{4.11}$$

Now by using the constitutive law of each layer described by equation 4.7 and considering the equation 4.11, one can compute the midplane average stress field components' expressions defined by equation 4.10. This leads to obtain the following relations

$$\begin{cases} \bar{C}_{11}\varepsilon_1 + \bar{C}_{12}\varepsilon_2 + \phi_{ply}C_{13}^{ply}\varepsilon_3^{ply} + \phi_{il}C_{13}^{il}\varepsilon_3^{il} &= \phi_{ply}\sigma_1^{tc,ply} + \phi_{il}\sigma_1^{tc,il} \\ \bar{C}_{12}\varepsilon_1 + \bar{C}_{22}\varepsilon_2 + \phi_{ply}C_{23}^{ply}\varepsilon_3^{ply} + \phi_{il}C_{23}^{il}\varepsilon_3^{il} &= \phi_{ply}\sigma_2^{tc,ply} + \phi_{il}\sigma_2^{tc,il} \end{cases} \tag{4.12}$$

On the other hand, along the through-thickness direction, a serial connection between the prepreg plies and resin interleaf layers is assumed. Therefore the normal stresses along axis 3 are identical in all laminae and we can obtain the following additional relations

$$\sigma_3 = \sigma_3^{ply} = 0 \Leftrightarrow C_{13}^{ply}\varepsilon_1 + C_{23}^{ply}\varepsilon_2 + C_{33}^{ply}\varepsilon_3^{ply} = \sigma_3^{tc,ply} \tag{4.13}$$

$$\sigma_3 = \sigma_3^{il} = 0 \Leftrightarrow C_{13}^{il}\varepsilon_1 + C_{23}^{il}\varepsilon_2 + C_{33}^{il}\varepsilon_3^{il} = \sigma_3^{tc,il} \tag{4.14}$$

Finally, by multiplying equation 4.13 and equation 4.14 by ϕ_{ply} and ϕ_{il}, respectively, we obtain an equation system comprised of equations 4.12, 4.13 and 4.14 defined as follows:

$$\begin{bmatrix} \phi_{ply}\sigma_1^{tc,ply} + \phi_{il}\sigma_1^{tc,il} \\ \phi_{ply}\sigma_2^{tc,ply} + \phi_{il}\sigma_2^{tc,il} \\ \phi_{ply}\sigma_3^{tc,ply} \\ \phi_{il}\sigma_3^{tc,il} \end{bmatrix} = \begin{pmatrix} \bar{C}_{11} & \bar{C}_{12} & \phi_{ply}C_{13}^{ply} & \phi_{il}C_{13}^{il} \\ \bar{C}_{12} & \bar{C}_{22} & \phi_{ply}C_{23}^{ply} & \phi_{il}C_{23}^{il} \\ \phi_{ply}C_{13}^{ply} & \phi_{ply}C_{23}^{ply} & \phi_{ply}C_{33}^{ply} & 0 \\ \phi_{il}C_{13}^{il} & \phi_{il}C_{23}^{il} & 0 & \phi_{il}C_{33}^{il} \end{pmatrix} \begin{bmatrix} \varepsilon_1 \\ \varepsilon_2 \\ \varepsilon_3^{ply} \\ \varepsilon_3^{il} \end{bmatrix} \tag{4.15}$$

Solving the equation system for a given increment of temperature variation ΔT or degree of cure $\Delta\alpha$, allows us to acquire an estimation of the macroscopic CTE or the CCS of the defined multilayered laminate by calculating the unknown parameters including the macroscopic in-plane strains ε_1 and ε_2, as well as the total through-thickness elongation given by

$$\varepsilon_3 = \phi_{ply}\,\varepsilon_3^{ply} + \phi_{il}\,\varepsilon_3^{il} \tag{4.16}$$

4.4 Identification of each layer thermo-chemical properties and mechanical behavior at the meso-scale

With the aim of evaluating the plausibility of the proposed chemo-thermo-elastic model considering the presence of resin interlayers within the prepreg plies, the resolution of the developed equation system given by 4.15, requires the knowledge of the behavior of each layer during the cure, meaning mechanical, expansion and shrinkage behavior.

4.4.1 Estimation of the volume fraction of each layer

The volume fraction of each layer is obtained by image analyses of optical micrographs of cured laminate samples microstructure. As it can be seen from figure 4.2, we can define and measure each layer area denoted as (A_k) by analyzing the captured micrographs by means of the ImageJ software. Knowing the length (L) of the studied image, the estimation of each layer thickness can be deduced as

$$t_k = \frac{A_k}{L} \tag{4.17}$$

In order to obtain a precise and representative average value of each layer thickness, large areas along the sample's thickness were studied. To do so, several images with a magnification equal to 20x were captured on each sample (24 for each measurement) and combined to produce mosaics with approximately 4000×3000 μm^2 of area. The average value of each layer thickness is therefore calculated with ImageJ software and fixed equal to t_{ply} = **145±5** μ**m** for the prepreg layer and t_{il} = **40±5** μ**m** for the resin interlayer.

4.4.2 The resin inter-layer cure dependent behavior

Within the literature, no complete characterization of the M21 based resin interlayers formulation has previously been performed. Thereby, accurate data about the composition of the solid thermoplastic particles, their volume ratio within the interleaf layer or their shape are not available. As mentioned in chapter 2, the toughening particles may include a blend of high and low melting thermoplastic particles principally made of polyamide [64] and are considered as non reactants for a curing temperature $\leq$ 180°C. Consequently, and regarding the lack of information on the microstructure of the interleaf layer at the micro-scale, the latter will be assumed as a homogeneous medium at the meso-scale. The mechanical behavior of the resin inter-layer is considered as isotropic linear elastic that can be defined by the following compliance matrix $[S]^{il}$ as

$$[S]^{il} = \begin{bmatrix} \frac{1}{E^{il}} & -\frac{\nu^{il}}{E^{il}} & -\frac{\nu^{il}}{E^{il}} \\ -\frac{\nu^{il}}{E^{il}} & \frac{1}{E^{il}} & -\frac{\nu^{il}}{E^{il}} \\ -\frac{\nu^{il}}{E^{il}} & -\frac{\nu^{il}}{E^{il}} & \frac{1}{E^{il}} \end{bmatrix} \tag{4.18}$$

where E^{il} denotes the elastic modulus of the M21 resin inter-layer and ν^{il} is the Poisson's ratio whose values are detailed in next paragraphs.

4.4.2.1 Elastic modulus and Poisson's ratio

Brief literature review

The resin mechanical properties change throughout the cure process with polymerization and temperature. Various constitutive models have been proposed in the literature to capture such complex behavior for the estimations of the residual stresses and final properties of

composites. Elastic and viscoelastic models are generally most employed to describe the resin behavior [201]. Despite the fact that viscoelastic models are more realistic in describing time-dependent properties, as they take into consideration the stress relaxation occurring in the resin rubbery state [97–99], elastic models have been largely applied to avoid the complexity of such models which are more difficult to develop and furthermore lead to long computational time. Some authors [6, 15, 41, 46, 90] have reported more elaborate and descriptive representations between the elastic modulus and the conversion degree by also considering the influence of the glass transition temperature and the variation of the elastic properties with temperature. This is the case for example, of the CHILE model proposed by Johnston *et al.* [202] (for Cure Hardening Instantaneously Linear Elastic), which has been widely employed to describe epoxy resins' elastic behavior with cure and the hardening of the latter due to rubbery-glassy transitions (vitrification). In this constitutive model, the resin elastic modulus increases monotonically with cure and is generally related with the variable T^* equal to the difference between the cure temperature and the instantaneous resin glass transition temperature. This model was later modified by Curiel and Fernlund [41] to further capture the modulus development during cure. A typical variation of the Young's modulus of an epoxy film adhesive during a simple one-hold cure cycle as function of T^* is given in figure 4.3 [41].

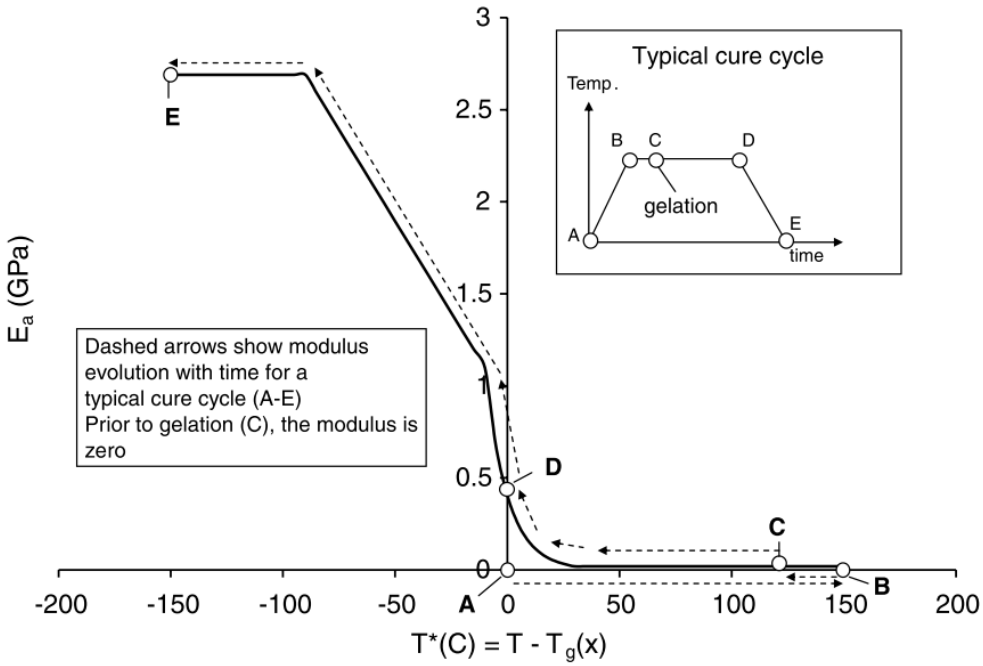

Figure 4.3: The evolution of an Epoxy resin modulus during a typical cure described by CHILE model as a function of T^*= T-Tg [41].

The material described by this model is assumed to be elastic with a constant modulus at any given instant that only changes with temperature and cross-linking effect. Prior to gelation the modulus is taken equal to zero and remains low until vitrification. Once (T<Tg), it evolves from the rubbery to the glassy state and increases sharply reaching almost 3000 MPa. This model was lately adopted by Moretti *et al.* [15] to describe similar based-epoxy

system M21E behavior during the cure. However, no precise information were available about the model fitting constants (which are of number of ten), so such model cannot be adopted to describe the cure dependent elastic behavior of the studied resin M21 that constitutes the interleaf layers. Despite the fact that several models were developed to predict this hardening of the resin, a large number of authors assumed a linear correlation between the resin modulus and the degree of cure [195, 203] while other [196] employed the well-known percolation theory [204].

To the best of our knowledge, no conclusive experimental information and theoretical approaches have appeared in the literature that clearly describe the development of the Poisson's ratio of thermoset resins as function of the state of cure. It is still considered time independent for simplicity. Under this assumption, the Poisson's ratio is commonly used as a constant value generally related to the measured coefficient at room temperature of fully cured samples which is in the expected range of 0.35 in the case of the cured M21 epoxy resins [81]. Bogetti and Gillespie [195] found that the changes in the Poisson's ratio of the resin with cure do not play a significant role on the macroscopic properties of the composite, nor on the process induced strains or residual stresses. O'Brien *et al.* [205, 206] concluded that the variation of the Poisson's ratio has no real influence with relatively minor effect on the shear modulus and they did not observe any effect of the curing state on the Poisson's ratio. On the other hand, Levitsky and Shaffer [207] assumed that the bulk modulus remains constant so that the Poisson's ratio and the elastic modulus vary as the material cures which is however in direct contractions to the observations of O'Brien *et al.*. By the same token, in a recent study conducted by Saseendran *et al.* [42], it was found that the Poisson's ratio of an investigated epoxy resin was affected by temperature and the curing state. The latter was ascertained to decrease over cure as given by figure 4.4 assuming that below the gelation point that corresponds to a cure state of 64%, the resin is in the liquid state with a Poisson's ratio of 0.5.

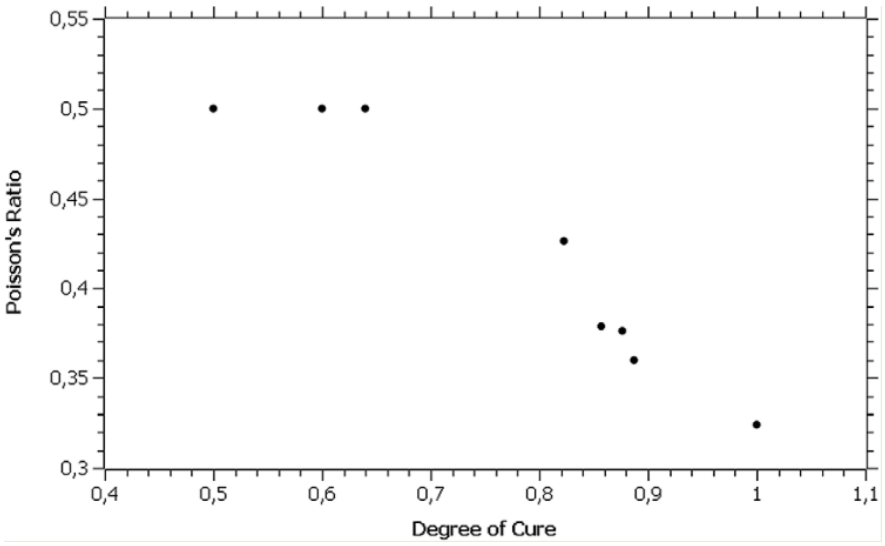

Figure 4.4: The evolution of the Poisson's ratio with the degree of cure of an epoxy resin [42].

Chosen parameters

In this work, and for the sake of simplicity in view of the limited available data about the M21 resin, the elastic modulus of the interleaf layer is assumed to follow a simple rule of mixtures relationship with the degree of cure excluding a direct temperature dependence. $E^{il}(\alpha)$ can be expressed as follows

$$E^{il}(\alpha) \quad = \quad (1-\alpha)\, E^{il-uncured} \quad + \quad \alpha\, E^{il-cured} \tag{4.19}$$

where $E^{il-uncured}$ and $E^{il-cured}$ represent the uncured and fully cured moduli of the resin interlayer respectively and α is the cure degree. In the uncured state, the epoxy resin is considered as a perfectly incompressible isotropic fluid with a negligible elastic modulus. On the basis of the rheological characterization detailed in chapter 2 (see section 2.5), an approximation of the Young's modulus $E^{il-uncured}$ value in the uncured state is calculated with the following equation according to the standard isotropic material relation

$$E^{il-uncured} \quad = \quad 2\,(1+\nu^{il})\,G \tag{4.20}$$

where G is the resin shear modulus measured with rheological tests and taken in the uncured state at $\alpha = 0$. For simplicity, ν^{il} is assumed to remain constant during cure and independent of temperature and the cure degree. The latter was fixed equal to 0.5 which is valid at least during the first stages of curing that correspond to the liquid state of the matrix including the before gelation phase. In the cured state, the Young's modulus of the fully cured resin can be defined according to the reported behavior of the M21 resin under tension tests conducted by Msallem *et al.* [46] on partially cured samples. The fully cured modulus is usually taken representative of typical room temperature values or related to the resin behavior at the end of cure after vitrification. It should be noted that, according to the defined cure cycle 2 in chapter 3 (see figure 3.8), no vitrification takes place during the curing of the studied material. Reported results in [46] showed that $E^{il-cured}$ remains very low in the rubbery state at the end of the isothermal cure (before vitrification) with values below to 500 MPa. This can explain the chosen $E^{il-cured}$ attributed to the M21 resin assumed in more accordance with the cure cycle 2. All mechanical properties of the resin are assumed constant once cure is complete. Given below in table 4.1, are gathered the interlayer mechanical properties values fixed for this investigation.

Table 4.1: Values of the resin interlayer mechanical and thermo-chemical properties.

Properties	Symbol	Value	Unit
Young's modulus in the Uncured state	$E^{il-uncured}$	$4.5\ 10^{-5}$	MPa
Young's modulus in the Cured state	$E^{il-cured}$	300	MPa
Poisson's ratio	ν^{il}	0.5	/
Linear CTE in the Uncured state	$\text{CTE}^{il-uncured}$	179	$10^{-6}K^{-1}$
Linear CTE in the Cured state	$\text{CTE}^{il-cured}$	62.7	$10^{-6}K^{-1}$
Linear CCS	CCS^{il}	-3.06	%

4.4.2.2 Linear coefficients of thermal expansion and chemical shrinkage

The linear coefficients of thermal expansion CTE_i^{il} and chemical shrinkage CCS_i^{il} of the resin interlayer are estimated from the measurements of the volumetric CTE_V and CCS_V carried out on the M21 resin presented in chapter 2 (see table 2.4). Since the interlayer is assumed isotropic, it is thereby defined by only one linear coefficient of cure shrinkage that will be denoted as CCS^{il} and two linear coefficients of thermal expansion denoted as $CTE^{il-uncured}$ for the liquid uncured state and $CTE^{il-cured}$ for the totally cured state. The coefficient of thermal expansion of the thermoset resin experiences various evolutions during the curing. The dependency on the conversion degree (α) of the interlayer linear CTE during the curing process can be described by a linear correlation using the mixture rule between $CTE^{il-uncured}$ and $CTE^{il-cured}$ as follows

$$CTE^{il}(\alpha) \quad = \quad (1-\alpha)\, CTE^{il-uncured} \quad + \quad \alpha\, CTE^{il-cured} \tag{4.21}$$

The resin interlayer thermo-chemical properties used for the estimation of its cure dependent behavior are depicted in table 4.1.

4.4.3 The prepreg layer cure dependent behavior

The prepreg lamina is a unidirectional reinforced ply with continuous IMA carbon fibers. Knowing the properties of the ply constituents, *i.e.* matrix (will be denoted by "m") and fibers (will be denoted by "f"), micro-mechanic analytical relations can be used to determine the elastic moduli and coefficients of thermal expansion and chemical shrinkage of the UD layer. The prepreg ply is thereby considered as a homogeneous medium at the meso-scale with a transversely isotropic behavior that can be described by the following elastic compliance matrix $[S]^{ply}$ written in the principal coordinate axes as illustrated in figure 4.2

$$[S]^{ply} = \begin{bmatrix} \frac{1}{E_1^{ply}} & -\frac{\nu_{12}^{ply}}{E_1^{ply}} & -\frac{\nu_{12}^{ply}}{E_1^{ply}} \\ -\frac{\nu_{12}^{ply}}{E_1^{ply}} & \frac{1}{E_2^{ply}} & -\frac{\nu_{23}^{ply}}{E_2^{ply}} \\ -\frac{\nu_{12}^{ply}}{E_1^{ply}} & -\frac{\nu_{23}^{ply}}{E_2^{ply}} & \frac{1}{E_2^{ply}} \end{bmatrix} \tag{4.22}$$

where $\nu_{12}^{ply} = \nu_{13}^{ply}$ and ν_{23}^{ply} represent the Poisson's ratios of the prepreg ply. E_1^{ply} is the longitudinal Young modulus and $E_2^{ply} = E_3^{ply}$ are the transverse Young moduli. The determination of the elastic properties expressions and values are detailed in next paragraphs as well as for the thermo-chemical properties.

4.4.3.1 Mechanical elastic properties

As it can be noticed from figure 4.2 (see also figure 1.5b for more clarity of the morphology along the longitudinal direction of the ply), at the micro-scale, the prepreg lamina consists of IMA fibers surrounded by the epoxy resin. As evident from this figure, the resin impregnating the fibers in the prepreg ply does not incorporate thermoplastic particles. It would be more

accurate to determine and employ the neat resin properties without accounting the presence of the thermoplastic particles while estimating the effective properties of the prepreg layer at the meso-scale. Nevertheless, since no exact data about the embedded thermoplastic particles are available in the literature, please note that, we suppose that the resin properties within the prepreg ply (without particles) and the resin interlayer properties (with particles) are alike. Besides, we assume that the volume fraction of fibers in the prepreg layer at the meso-scale is higher than the fiber volume ratio determined by the manufacturer for the studied IMA/M21 material ($V_f = 59.2\%$) which rather refers to the complete laminate including the resin interleaves within the prepreg plies. Therefore, we define the fiber volume fraction referred to the prepreg ply only denoted by V_f^{ply} using the following equation

$$V_f^{ply} = V_f \ (1 + \tfrac{t_{il}}{t_{ply}}) \tag{4.23}$$

In the case of a unidirectional lamina, good results are commonly provided by the classical rule of mixtures for the estimation of the longitudinal modulus and the related Poisson's ratio. Since we aim to compare the material properties (CTE and CCS) with experimental measurements in the uncured and cured states, the estimated ply properties are assumed cure degree dependent.

The Young's modulus $E_1^{ply}(\alpha)$ through the longitudinal direction and the Poisson's ratios ν_{12}^{ply} and ν_{13}^{ply} of the prepreg layer are estimated by using the rule of mixtures at the micro-scale according to the following relationships

$$E_1^{ply}(\alpha) = (1 - V_f^{ply})\, E^m(\alpha) + V_f^{ply}\, E_1^f \tag{4.24}$$

and

$$\nu_{12}^{ply} = \nu_{13}^{ply} = (1 - V_f^{ply})\, \nu^m + V_f^{ply}\, \nu^f \tag{4.25}$$

where

$$\begin{cases} E^m(\alpha) = E^{il}(\alpha) \\ \nu^m = \nu^{il} \end{cases} \tag{4.26}$$

$E^{il}(\alpha)$ is the interlayer modulus given by equation 4.19 assumed equal to the resin modulus $E^m(\alpha)$ present in the prepreg ply and ν^m is the Poisson's ratio related to the matrix present in the prepreg ply. The latter is considered constant during the cure and equal to the Poisson's ratio ν^{il}. E_1^f and ν^f are the Young's modulus and the Poisson's ratio of the IMA carbon fibers respectively.

Contrary to the resin, fibers do not react during the cure so their properties are independent of cross-linking. However, no precise data about IMA fibers mechanical properties were available. We assume that such high performance carbon reinforcements are rarely isotropic and can be adequately modeled as transversely isotropic. Note that, $\nu_{12}^f = \nu_{13}^f = \nu^f$ chosen arbitrarily and E_1^f value is taken equal to the reported data by the supplier [45]. These properties are gathered in table 4.2.

With the classical rule of mixtures, predicted values of the longitudinal modulus and the related Poisson's ratio agree well with the experimental data. However, the values obtained for the transverse modulus are generally less realistic and lower than the experimental data as it can be seen from figure 4.5a. The latter proposes a comparison between the proposed formulae by Jacquet *et al.* [43] and the rule of mixtures in predicting the transverse modulus for a unidirectional composite by assessing the influence of the relative volume of fibers. It can be noticed that the rule of mixtures provides much lower results whilst more coherence between the other methods can be observed. Jacquet *et al.* [43] carried out an additional comparison between the proposed simple formulae named as horizontal and vertical models with finite-element calculations (see figure 4.5b). The results are valid whatever the values of the relative reinforcement volume. Since the rule of mixtures becomes less accurate with high volume fraction of fibers (employed V_f^{ply} in our case is equal to 75.5%), the elastic modulus $E_2^{ply}(\alpha)$ in the transverse direction to the fiber axis is therefore calculated according to the analytical horizontal model proposed by Jacquet *et al.* [43] that can be expressed as

$$\frac{1}{E_2^{ply}(\alpha)} = \frac{\sqrt{V_f^{ply}}}{\sqrt{V_f^{ply}}E_2^f + (1-\sqrt{V_f^{ply}})E^m(\alpha)} + \frac{1-\sqrt{V_f^{ply}}}{E^m(\alpha)} \tag{4.27}$$

where E_2^f is the Young's modulus of IMA fibers in the transversal direction taken arbitrarily smaller than E_1^f (see table 4.2 for parameters values).

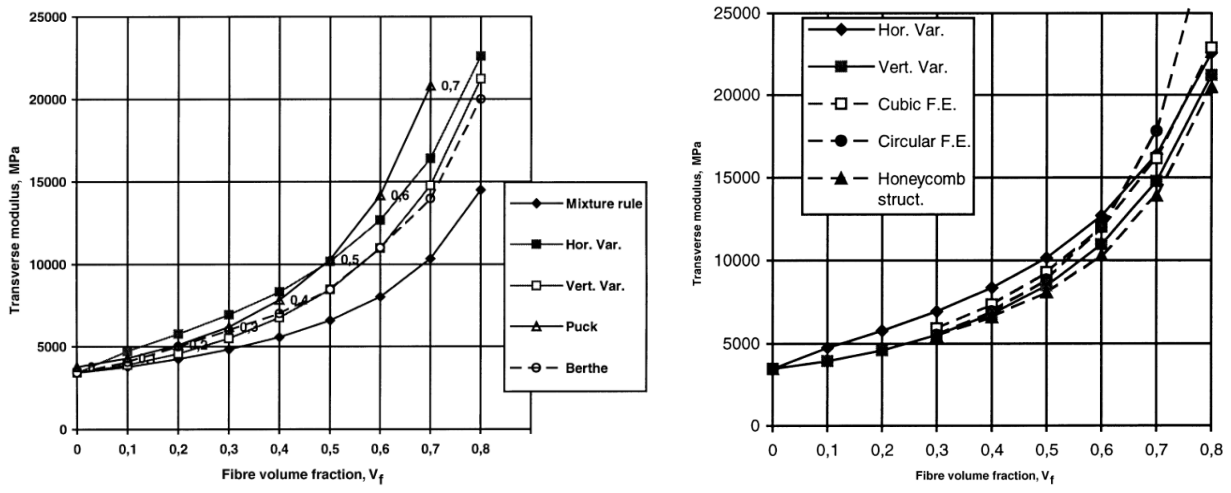

(a) (b)

Figure 4.5: (a) Comparison of predicted values of the transverse Young's modulus with fiber volume fraction for various theoretical methods. (b) Comparison between the proposed analytical models by Jacquet *et al.* [43] with numerical calculations.

Table 4.2: Values of the prepreg layer mechanical properties.

Properties	Symbol	Value	Unit
Young's modulus in longitudinal direction of the fiber	E_1^f	297	GPa
Young's modulus in transversal direction of the fiber	E_2^f	20	GPa
Poisson's ratio of fibers	ν^f	0.2	/
Fiber volume ratio of the laminate	V_f	59.2	%
Fiber volume ratio of the prepreg ply	V_f^{ply}	75.5	%
Poisson's ratio of the prepreg ply	ν_{12}^{ply}	0.23	/
Poisson's ratio of the prepreg ply	ν_{23}^{ply}	0.5	/

4.4.3.2 Coefficients of thermal expansion and cure shrinkage

Linear CTEs of the prepreg layer

Several analytical and semi-empirical homogenization techniques were developed to predict the effective transverse thermal expansion coefficient for unidirectional fiber reinforced composites [208–210]. Data about the CTEs of IMA fibers are scarce but one can assume that their expansion is negligible compared to the one of the matrix. Under the assumption of transversely isotropic prepreg plies with a negligible expansion along fibers, one can propose the following law based on the simple rule of mixture to estimate the cure dependent transversal CTE of the prepreg layer:

$$CTE_2^{ply}(\alpha) = CTE_3^{ply}(\alpha) = \frac{(1 - V_f^{ply}) \times \overbrace{3 \times CTE^m(\alpha)}^{CTE_V^m(\alpha)}}{2} \tag{4.28}$$

with

$$CTE^m(\alpha) \;=\; CTE^{il}(\alpha) \tag{4.29}$$

where $CTE^{il}(\alpha)$ can be calculated according to equation 4.21. The value of longitudinal CTE_1^{ply} of the prepreg layer is taken arbitrarily small and constant ($CTE_1^{ply} = 2{\times}10^{-8}K^{-1}$) in approximation with reported data in literature [186].

Linear CCSs of the prepreg layer

The effect of the chemical shrinkage is commonly assumed similar to the thermal behavior during the cure and could be similarly described by equation 4.28 to determine the effective coefficient of cure shrinkage of the lamina as function of the matrix CCS.

To do so, we can estimate the volumetric CCS_V^{ply} of the prepreg ply given by equations 4.30 and 4.31 by means of rule of mixtures assuming that fibers do not lock any shrinkage.

$$CCS_V^{ply} = (1 - V_{f,ply}) \times \underbrace{3 \times CCS^m}_{CCS_V^m} \tag{4.30}$$

with

$$CCS^m = CCS^{il} \tag{4.31}$$

The CCS_V^m is the volumetric coefficient of chemical shrinkage of the matrix assumed equal to the $CCS_V^{il} = 3 \times CCS^{il}$ of the interlayer. The latter is estimated experimentally from the M21 resin volumetric characterization behavior using the PvT-α mold in chapter 2 (see subsection 2.4.2).

Assuming that shrinkage occurs only along the transverse directions of the UD layer considered as transversely isotropic, the value of CCS_1^{ply} along fibers is considered negligible. Hence, one can deduce the linear transverse CCS of the prepreg layer as

$$CCS_2^{ply} = CCS_3^{ply} = CCS_V^{ply}/2 = -1.15\% \tag{4.32}$$

4.5 Comparison with experimental results and discussions

4.5.1 Calculation procedure

The procedure to obtain the laminate macroscopic coefficients of thermal expansion or chemical shrinkage consists in solving the equation system described by 4.15 for a given temperature variation or a degree of cure. In order to predict the thermo-chemical response for a whole thermal cure cycle, one can compute the macroscopic strains over each time increment and then the laminate strains development during the cure cycle can be obtained by adding the total strains of the consecutive steps. Strain variation of the laminate at a given time increment is calculated using the instantaneous elastic stiffness and the thermo-chemical properties of each lamina. As described in previous section, the latter are only changing as a result of the polymerization reaction. At each step of calculation, these properties are thereby assumed to have no viscoelastic character and the consequent internal state of the composite is frozen for a given cure degree which allowed the employment of the incremental calculation in this case.

The macroscopic strain solution at the end of a given time step is simply the total of the incremental solutions of the equation system 4.15 from all previous steps. The macroscopic strain $\{\varepsilon\}$ at the end of step n can be described by

$$\{\varepsilon\} = \begin{bmatrix} \varepsilon_1 \\ \varepsilon_2 \\ \varepsilon_3 \end{bmatrix} = \sum_{p=1}^{p=n} \{\Delta\varepsilon_i\}_p \tag{4.33}$$

where $\{\Delta\varepsilon_i\}_p$ is the change in strain during step p along the three principal directions of the laminate.

Prior to elastic constants and thermo-chemical properties calculations for a single step increment, the degree of cure is estimated thanks to Bailleul's cure kinetics model, whose parameters are detailed in chapter 2 (see equation 2.10), on the basis of the thermal cycle 2 (see figure 3.8b) that will be used in this analysis. Step-by-step resolution of the equation system 4.15 requires at first that the instantaneous stiffness matrix of each layer k, $[C_{ij}]_p^k$, to be computed for a given cure degree using the stated relations in previous section (equations 4.19, 4.24, 4.25 and 4.27).

Incremental thermal expansion strains, $\{\Delta\varepsilon^{t,k}\}_p$, for each layer k are computed over each time step p, to which corresponds a specific degree of cure α_p as follows

$$\{\Delta\varepsilon^{t,k}\}_p = \begin{bmatrix}\Delta\varepsilon_1^{t,k}\\ \Delta\varepsilon_2^{t,k}\\ \Delta\varepsilon_3^{t,k}\end{bmatrix}_p = \{CTE_i^k(\alpha_p)\}_p \times \Delta T_p \tag{4.34}$$

where ΔT_p is the temperature variation between two consecutive time increments and $\{CTE_i^k(\alpha_p)\}_p$ are the instantaneous thermal expansion coefficients related to the layer k at a constant degree of cure α_p determined according to equations 4.21 and 4.28 for the resin interlayer and the prepreg ply respectively.

Chemical shrinkage strain increments, $\{\Delta\varepsilon^{c,k}\}_p$, are also calculated for each time increment p according to

$$\{\Delta\varepsilon^{c,k}\}_p = \begin{bmatrix}\Delta\varepsilon_1^{c,k}\\ \Delta\varepsilon_2^{c,k}\\ \Delta\varepsilon_3^{c,k}\end{bmatrix}_p = \{CCS_i^k\}_p \times \Delta\alpha_p \tag{4.35}$$

where $\Delta\alpha_p$ is the cure degree increment variation between two consecutive time increments and $\{CCS_i^k\}_p$ is the instantaneous constant chemical shrinkage coefficients related to each layer k given in tables 4.1 for the resin interlayer and 4.5 for the prepreg ply.

Once the incremental thermally and chemically induced strains are computed for each layer, the changes in the stress during each step p in each lamina (given by equation 4.36) due to the temperature and the degree of cure variations can be calculated using $[C_{ij}]_p^k$, and therefore the equation system 4.15 can be solved.

$$\{\Delta\sigma^{tc,k}\}_p = \begin{bmatrix}\Delta\sigma_1^{tc,k}\\ \Delta\sigma_2^{tc,k}\\ \Delta\sigma_3^{tc,k}\end{bmatrix}_p \tag{4.36}$$

The macroscopic CTEs of the laminate are directly linked to the temperature increment ΔT and can be therefore estimated from the computed strains (equation 4.33) according to equation 4.37. During the isothermal cure, strains evolution are mainly due to chemical

shrinkage of the matrix that occurs during crosslinking. During this stage, CCSs of the laminate are directly linked to the cure degree increment $\Delta\alpha$ and can thereby be calculated from the computed macroscopic strains (equation 4.33) as follows

$$\begin{cases} CTE_i = \dfrac{\Delta\varepsilon_i}{\Delta T} \quad \text{with} \quad i = 2,3 \\ CCS_i = \dfrac{\Delta\varepsilon_i}{\Delta\alpha} \quad \text{with} \quad i = 2,3 \end{cases} \tag{4.37}$$

It has to be noted that the axial strain along the fibers direction remain negligible and will not be presented in the following for simplicity.

4.5.2 Results and discussions

Macroscopic strains are computed according to the thermal cure cycle 2. ε_2 and ε_3, for the in-plane and the thickness directions strains respectively, are given in figure 4.6. Investigated IMA/M21 sample 2 is taken as an example here, in order to compare experimental and estimated data. Measured deformations along both transverse directions are also plotted in these figures with the imposed thermal cycle 2. Please note that, since the material compaction behavior is not taken into account in the model, we do not focus here on stage 1 (the four stages are defined in figure 3.12), and the cure behavior is only analyzed beyond the 70°C pre-conditioning isothermal step. Plotted strains are zeroed at the beginning of the isothermal cure at 160°C for the sake of clarity for the following discussions.

Coefficients of Thermal Expansion

The predicted CTEs along both transverse directions to fibers with the proposed model are gathered in table 4.3. It has to be noted that the CTE of the uncured material is estimated from strains variation during the heating stage while $\alpha = 0\%$ which corresponds to the temperature range from 70°C to 130°C. After almost 140°C, strains evolution as function of temperature is no longer linear since the cure shrinkage starts to take place due to the polymerization reaction advancement. The CTEs related to the cured glassy state are calculated from strains variation during the cool down step.

Based on calculated values of the CTEs in table 4.3, we can firstly notice that the orthotropic thermal expansion behavior of the UD laminate is well captured even if some differences between measured and computed strains during the heating/cooling steps appear. The predicted CTE in the uncured state is significantly overestimated along the in-plane direction with error equal to 16.75% but stills in satisfactory agreement with the experimental value equal to 100 $10^{-6}K^{-1}$ with a standard variation equal to $\pm$ 11 $10^{-6}K^{-1}$. Conversely, the uncured CTE along the through thickness direction is relatively underestimated with the model but it is in excellent agreement with the experimental value of CTE equal to 178$\pm$9 $10^{-6}K^{-1}$. In the cured state, significant over-prediction of the CTEs along both directions can be noticed with errors equal to almost 5% and 10% through the in-plane and thickness directions respectively, but remain in accordance with experimental results.

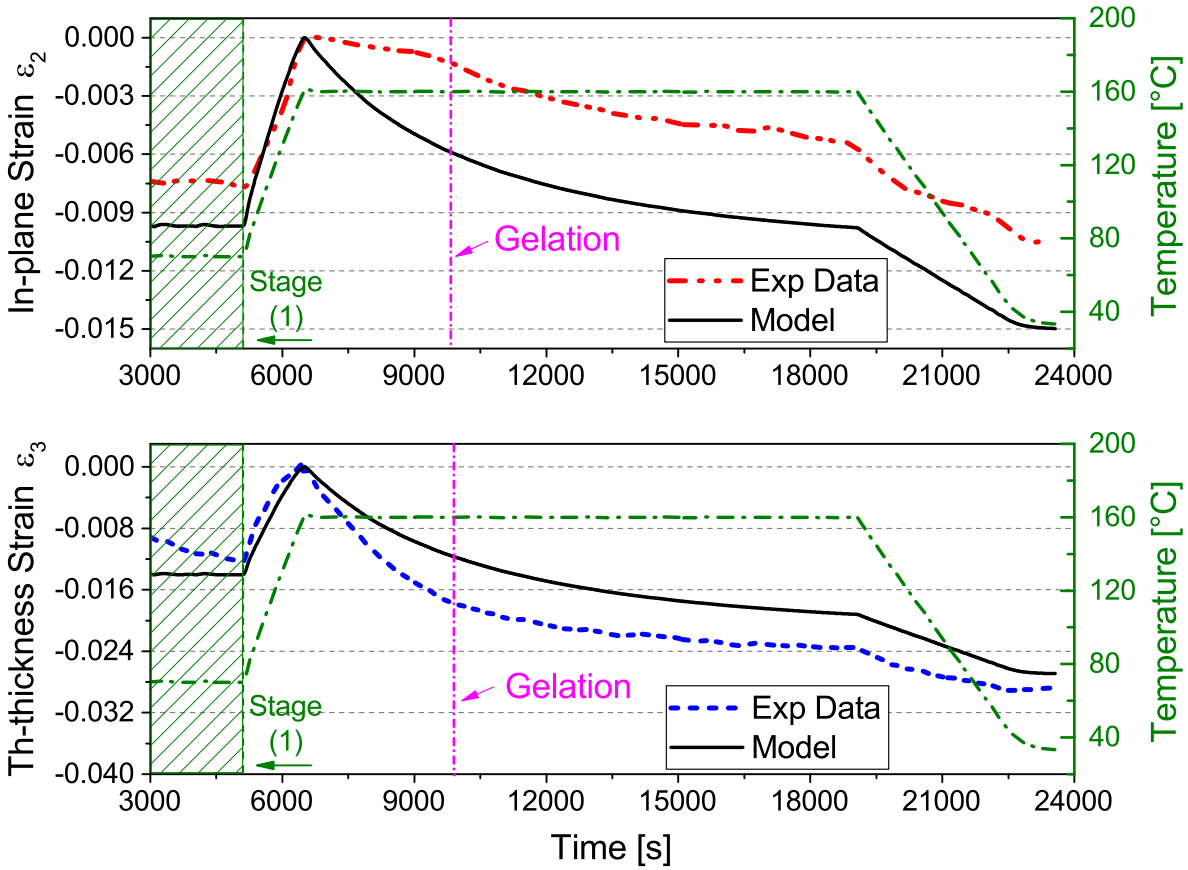

Figure 4.6: Comparison between measured and estimated deformations along both transverse directions of the UD IMA/M21 laminate. (Sample 2 is taken as example for the experimental data).

Table 4.3: Estimated values of the laminate macroscopic CTE by the multi-layer model. Comparison with experimental results gathered in table 3.5.

Material state / Direction	Property	Value	Unit	Error compared to Exp. Results
Uncured / In-plane	$CTE_2^{uncured}$	116.75	$10^{-6}K^{-1}$	16.75 %
Uncured / Through-thickness	$CTE_3^{uncured}$	172.78	$10^{-6}K^{-1}$	-2.93 %
Cured / In-plane	CTE_2^{cured}	40.94	$10^{-6}K^{-1}$	4.97 %
Cured / Through-thickness	CTE_3^{cured}	60.86	$10^{-6}K^{-1}$	10.67 %

Coefficients of Chemical Shrinkage

The predicted macroscopic CCSs with the proposed model through the in-plane and through the thickness directions of the laminate are given in table 4.4.

Table 4.4: Computed values of the laminate macroscopic CCS by the multi-layer model. (See table 3.7 for comparison with experimental results.)

Direction	Property	Value	Unit
In-plane	CCS_2	-1.28	%
Through-thickness	CCS_3	-2.52	%

According to the obtained results in figure 4.6 and table 4.4 we can clearly notice high differences between computed strains and the material experimental response during the isothermal cure. These variations are more significant especially before the matrix gelation. A sharp drop can be observed in the in-plane computed strains before gel point. The calculated CCS is equal to -1.28% which is more than four times higher than the experimentally measured coefficient in this stage estimated equal to -0.27±0.04%. Conversely, the through-thickness strains are rather under-estimated during the isothermal cure mainly before the matrix gelation with much lower computed CCS_3 than the experimental one. After gelation tendency of the computed strains during the isothermal hold are likely more in accordance with the experimental behavior. Indeed, the calculated CCS along both directions are in better agreement with the experimental values measured after the gel point of the matrix. Based on the proposed approaches in sub-subsection 4.4.3.2 and obtained results, one can deduce that the slope change of the chemical shrinkage at the macroscopic scale with the matrix gelation cannot be only explained by the resin interleaves presence in the laminate structure.

In order to translate the observed experimental transverse shrinkage behavior in regards with the material state (before/after gelation), we make these additional assumptions at the prepreg ply scale:

- Before gelation, the prepreg layer is supposed to shrink entirely along the through-thickness direction only. Thus, the through-thickness CCS_3^{ply} can be considered equal to the volumetric CCS of the prepreg lamina, whereas the in-plane CCS is assumed negligible.
- After gelation, we suppose that the UD prepreg layer shrinks in a similar way through both transverse directions resulting in a same linear transverse CCS.

Consequently, the linear coefficients of chemical shrinkage of the prepreg layer can now be defined as

$$\begin{cases} \text{if} \quad \alpha < \alpha_{gel} \quad CCS_3^{ply} = CCS_V^{ply} \quad \text{and} \quad CCS_2^{ply} \approx 0 \\ \text{if} \quad \alpha \geq \alpha_{gel} \quad CCS_3^{ply} = CCS_2^{ply} = CCS_V^{ply}/2 \end{cases} \tag{4.38}$$

The values of the calculated coefficients are gathered in table 4.5.

Table 4.5: Adjusted values of CCS of the prepreg ply.

Material state	Properties	Symbol	Value	Unit
$\alpha < \alpha_{gel}$	In-plane CCS	CCS_2^{ply}	-0.0001	%
	Through-thickness CCS	CCS_3^{ply}	-2.29	%
$\alpha \geq \alpha_{gel}$	Transverse CCS	$CCS_2^{ply} = CCS_3^{ply}$	-1.15	%

Along each transverse direction, before and after gelation new macroscopic CCSs are now calculated for the multilayered laminate and compared with experimental results. The computed values are given in table 4.6.

Table 4.6: New calculated values of the laminate macroscopic CCS by the multi-layer model. (See table 3.7 for comparison with experimental results.)

Material state / Direction	Property	Value	Unit	Error compared to Exp. Results
Before gel / In-plane	CCS_2^{BG}	-0.22	%	-19.7 %
Before gel / Through-thickness	CCS_3^{BG}	-3.62	%	-5.45 %
Post gel / In-plane	CCS_2^{PG}	-1.28	%	-8.32 %
Post gel / Through-thickness	CCS_3^{PG}	-2.52	%	21.91 %

Please note that, the same values of the macroscopic CTEs are obtained with the model since the proposed new assumptions are only related to the prepreg ply chemical shrinkage behavior.

Macroscopic strains; ε_2 and ε_3, are now computed by taking into account the new adjusted shrinkage behavior of the prepreg ply. Sample 2 is again taken as an example here, in order to compare experimental and new estimated data according to the cure cycle 2 as presented by figure 4.7. Plotted strains are again zeroed at the beginning of the isothermal cure at 160°C for better clarity.

Discussions

As it can be remarked from the plots given in figure 4.7, a better agreement is found now between estimated deformations with the multi-layer model and sample 2 experimental response. We can even better notice from these results that the orthotropic behavior of the UD laminate is well captured with the model. All the predicted properties given in tables 4.3 for the CTEs and 4.6 for the CCSs result in relative errors less or almost equal to 22% with reference to the average experimental values.

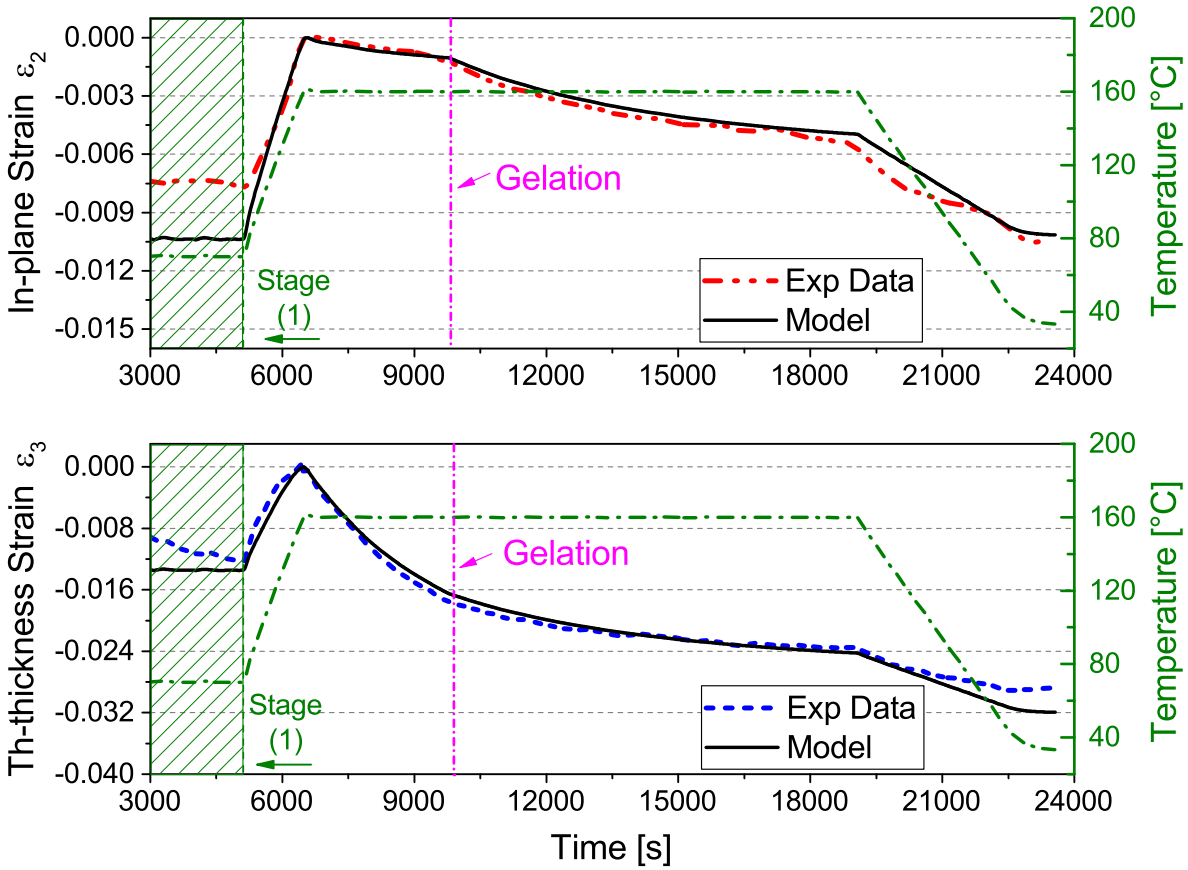

Figure 4.7: Comparison between measured and estimated deformations along both transverse directions of the UD IMA/M21 laminate after shrinkage behavior adjustment at the prepreg ply scale. (Sample 2 is taken as example for the experimental data).

Measured CTE obtained from sample 2 testing in the uncured state through the in-plane direction was estimated equal to 89 $10^{-6}K^{-1}$ which explains the high disparities between computed strain with the model and measured one during the heating ramp in figure 4.7. Through-thickness strains are, in contrary, in excellent agreement during the heating of the uncured material. During stage 4, which depicts the behavior during the cool-down step, clear comparison between the model response with experimental results can be now made. Indeed, it shows more variances between experimental and computed strains. In fact, the experimental in-plane cured CTE for sample 2 was estimated by linear regression during this stage equal to 38 $10^{-6}K^{-1}$ in comparison with the numerical value of CTE_2^{cured} equal to 40.94 $10^{-6}K^{-1}$. Despite of the slight difference between both values, the apparent deviation between experimental and computed strains can be mainly attributed to the alteration that appears between T = 118°C and T = 63°C in experimental ε_2 evolution when the material is cooled. On the other hand, through-thickness experimental cured CTE of sample 2 was estimated equal to 53 $10^{-6}K^{-1}$, which clearly explains the difference between both strains evolution since the computed one is rather over-predicted based on a numerical effective $CTE_3^{cured} = 60.86\ 10^{-6}K^{-1}$.

Good agreement between sample 2 experimental response and computed strains along both directions can be noticed from figure 4.7 during the isothermal cure step. Note that the reported experimental values of CCSs in table 3.7 are based on estimations from all tested samples including sample 1 cured according to cycle 1. Reported errors in table 4.6 are calculated on the basis of the experimental average CCSs from table 3.7.

Before gelation, estimated parameters with the model along both directions reveal excellent accordance with the experimental ones. The high relative error equal to almost 20% through the in-plane direction could be explained by the small absolute values of the CCS along this direction before gelation. In fact, the absolute difference between the predicted and the measured CCS is rather small and equal to 0.05%. The through-thickness coefficient presents a relative error of -5.45% compared to the average experimental value (equal to -3.83%) but it remains in good agreement with the material response along this direction. In fact, the experimental CCS_3^{BG} already revealed some disparities with relatively high standard deviation of $\pm 0.3\%$. After gel point, it was supposed that cure shrinkage acts in a similar way along both transverse directions at the UD prepreg layers scale. The predicted macroscopic CCSs of the laminate reported in table 4.6 are in good match with the experimental values approving the significant influence of the interleaf layers presence on the induced anisotropy of the UD laminate behavior through the transverse directions.

It is important to point out that even if the physics behind the complex changing trends at the gel point of the cure shrinkage still not totally understood and may need more experimental investigations, the fact that the UD prepreg layers do not shrink in an isotropic way in the (2-3) plane before gel is clearly evident. Indeed, the obtained results can validate that it is mainly due to the prepreg layers behavior that the macroscopic shrinkage of the laminate takes place along the thickness only before gelation. Such behavior might be related to the laminate stacking sequence or the fiber bed behavior. At the pre-gelation stage, the viscosity of the resin is much lower compared to the post gelation region during which the matrix modulus is assumed to be built. We can suppose that the chemical shrinkage could be correlated to the viscosity of the resin in relation with the fibers in-plane distribution that can lead to such an asymmetric tensile versus compressive behavior as long as the resin is in the uncured state. Hence at the pregelation stage, the resin ability to move the fiber bed is likely to be more difficult along the in-plane direction. After gelation, the resin could easily pull the fibers in the in-plane direction which therefore may explain the increase of the chemical shrinkage rate (CCS post gel) in this region.

4.6 Partial conclusion and perspectives

A thermo-mechanical modeling of the cure behavior based on the classical laminate theory (CLT) approach was proposed in this chapter by accounting the interleaf layers of resin in the laminate structure. The effective thermal expansion coefficients were predicted in the uncured and cured states of the material and good agreements with the experimental results was shown. The macroscopic coefficients of chemical shrinkage were also estimated by the model before and after gelation and a good match with the experimental values was ascertained. With these preliminarily results, it was possible to validate that the studied laminate behav-

ior is rather fully orthotropic due to the presence of the extra interleaf layers. This explains well the difference between the obtained laminate properties along both transverse directions of a typical UD structure. Nevertheless, the observed tendency of the chemical shrinkage distribution around the gelation point through the in-plane and thickness directions cannot be clearly explained by the resin interlayers presence in the laminate structure. Regarding the proposed assumptions about the prepreg layers tendency to shrink before/after gelation and given the obtained results, it would be more plausible to suppose that the macroscopic shrinkage behavior of the laminate is rather influenced by the prepreg plies behavior. The model requires a purely phenomenological modeling of the pre-gelation anisotropic shrinkage, accessible only by direct measurements such as the PvT-HADDOC. A deeper study at the micro-scale is now necessary to assess the assumption of the role of anisotropic fiber packing on the shrinkage evolution before gelation. In sum, observed differences between the computed and the measured coefficients can be attributed to the several simplifications used to estimate the material properties with the model. It is important to reiterate that the results gathered in tables 4.6 and 4.3 are based on a set of parameters identified for each layer in section 4.4. In this example, the fixed parameters and chosen approaches that describe the behavior of the constituents at each layer scale could induce relative changes in the estimated macroscopic behavior. The current model requires a more thorough analysis and comparisons between the different theories based on a sensitivity analysis that would help in view of the high numbers of parameters especially at micro-scale. It is worth noting that the particular anisotropic shrinkage of plies was only observed in the liquid state and has to be correlated to the observed anisotropic compaction behavior. The role of fibers arrangement should be questioned.

CHAPTER 5

CHARACTERIZATION AND MODELING OF THE COMPOSITE RHEOLOGICAL BEHAVIOR DURING THE CURE

Contents

5.1 Introduction **147**

5.2 Experimental procedure **147**

5.2.1 Sample preparation 147

5.2.2 Methodology of characterization tests 148

5.2.2.1 Curing cycle 149

5.2.2.2 Loading mode definition 150

5.2.3 Mechanical strains calculation strategy 154

5.3 Experimental results analysis **157**

5.3.1 General aspect of the mechanical behavior 157

5.3.2 Limitations due to the experimental setup compliance 160

5.3.3 Influence of the sample initial section 161

5.3.4 Influence of the degree of cure 162

5.4 Modeling results and discussions **169**

5.4.1 Theoretical background: Brief reminders on creep behavior of viscoelastic materials 169

5.4.2 Curve fitting and estimation of creep parameters of Burgers model during the cure 172

5.4.3 Sensitivity analysis of Burgers model parameters to a creep-recovery loading path 179

5.4.4 Parameters' evolution with cure and identification of the rheo-kinetic Burgers model . . . 183
5.4.4.1 Behavior before the gel point . . . 183
5.4.4.2 Behavior beyond the gel point . . . 186
5.4.4.3 Rheo-kinetic Burgers model . . . 187
5.5 Verification of the rheo-kinetic Burgers model predictions . . . **188**
5.5.1 Creep-recovery test . . . 189
5.5.2 Loading-unloading test, denoted as test I . . . 189
5.5.3 Loading-unloading test, denoted as test II . . . 192
5.5.4 Axial strain responses in comparison with the three tests . . . 194
5.6 Partial conclusion . . . **197**

5.1 Introduction

Identifying the mechanical behavior of thermosetting composites and understanding the evolution of the mechanical properties during the cure process is of crucial importance to predict the initial residual stresses state and to optimize the composite processing parameters and defect mitigation. The main objective of this chapter is to present a simplified experimental methodology with associated analytical model to identify the rheological properties of a unidirectional interlayer toughened aerospace prepreg during curing. The first part of this chapter (section 5.2) is dedicated to the presentation of the developed experimental methodology performed with the intention to elucidate the mechanical behavior during the cure. Samples' preparation protocol and the definition of the appropriate mechanical testing with the suitable curing cycle are therefore discussed. A detailed strategy of experimental data analysis which allows to estimate the measured mechanical properties is also described in this first part. In a second step, the obtained experimental results related to the mechanical behavior evolution with cure are discussed in section 5.3. Section 5.4 of this chapter is devoted to the experimental identification of the employed model parameters. Finally, rheological model predictability during the curing of the studied composite is therefore assessed and further discussed in section 5.5.

5.2 Experimental procedure

5.2.1 Sample preparation

The same processing route described in chapter 3 and employed to prepare the IMA/M21 prepreg samples for the measurement of the anisotropic thermo-chemical strains was also applied for the mechanical testing. Only unidirectional configurations are used in order to characterize the rheological behavior of the material using the same experimental set-up, the PvT-HADDOC thanks to the Instron press which allows dynamic and static testing.

The mechanical tests were performed on specimens made of 30 plies with in-plane sections of $[S_0 = 105 \times 30\ \text{mm}^2]$ and $[2S_0 = 105 \times 60\ \text{mm}^2]$. For each specimen, 30 rectangular plies of approximately $105 \times 30\ \text{mm}^2$ or $105 \times 60\ \text{mm}^2$ are firstly cut from the prepreg and stored in sealed bag at -18°C. Before the test, the 30 plies are removed from the freezer and kept at room temperature for 6 hours so that the material gets completely reheated before opening the storage bag to prevent condensation. Afterward, the laminate sample is stacked by hand lay-up and debulked at room temperature for two hours as outlined in chapter 3. The average initial height h_0 of all studied samples is 5.91 ± 0.05 mm before testing. An example of IMA/M21 sample is shown in figure 5.1a where axis 1 is aligned with the direction of fibers, axis 2 defines the in-plane transverse direction and axis 3 is referred to the through-thickness transverse direction. L_0 represents the initial length and l_0 is the initial width. Each sample is produced 14 hours before the mechanical testing in order to provide the same resting time for all specimens so that to annihilate any possible mechanical loading history related to the manufacturing step. The uncured sample is stored in sealed bag at room temperature for 14 hours so as to prevent any moisture regain before the test. This procedure allows us to assume that all tested prepreg samples have nearly the

same initial conditions. Sample installation inside the cavity relies on same detailed steps in section 3.2. The same level of pre-compressive stress of 2 KPa is applied on each specimen for this mechanical characterization.

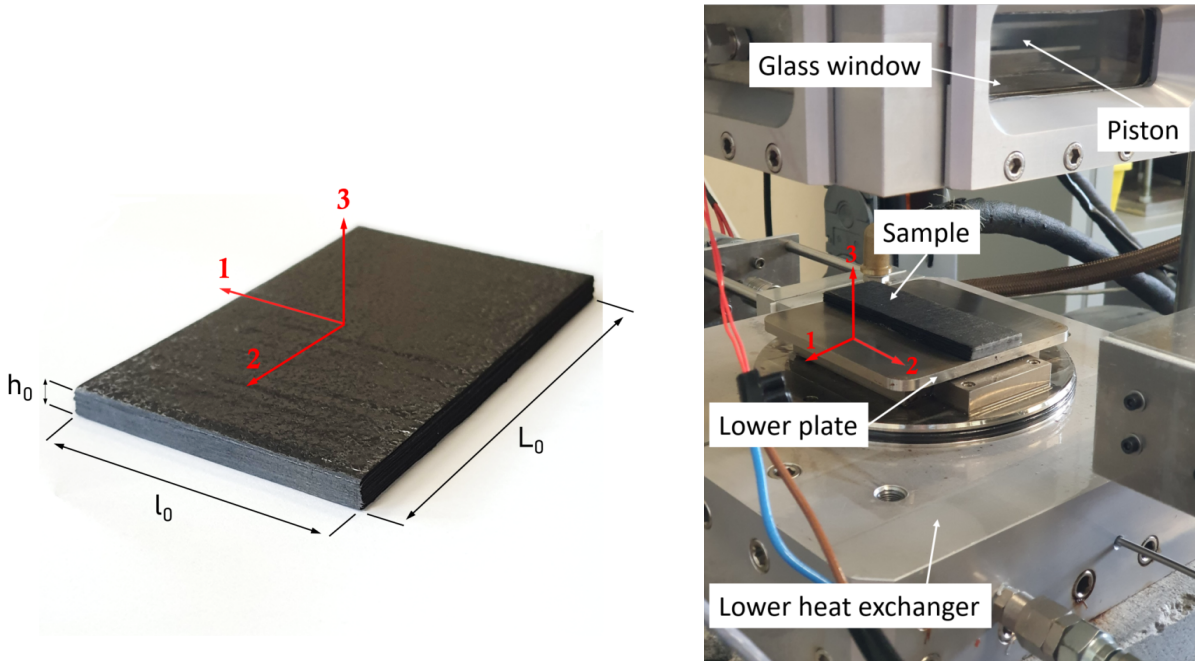

(a) (b)

Figure 5.1: (a) Coordinate system and initial dimensions' notations for a unidirectional IMA/M21 prepreg sample. (b) Specimen placed in the PvT-Haddoc setup for the mechanical testing (before mold cavity closure).

5.2.2 Methodology of characterization tests

The main purpose is to develop a methodology that allows a characterization procedure of the mechanical behavior simultaneously during the cure of the studied material. On the basis of the discussed results in chapter 3 and considering the compaction behavior of the IMA/M21 system, the new adjusted thermal cycles (see figure 3.8) which consist in adding an isothermal dwell at 70°C, are chosen to be applied during the characterization process of the mechanical behavior. Regarding the complexity of the curing behavior of thermoset prepregs, notably the studied case of the IMA/M21 system, the mechanical tests are assigned to be performed simultaneously as the material is submitted to the compressive hydrostatic stress of applied level ≥ 0.5 MPa, throughout the whole thermal cycle. In this setting, voids compaction could occur during the preconditioning step while the material is still in the uncured state. This leads to elaborating an experimental procedure that allows to assess the rheological behavior under applied stress only. This is because the application of the compressive hydrostatic pressure throughout the cycle is only possible when the sample is simultaneously submitted to the compressive force applied by the piston along its thickness combined to the lateral oil pressure as described in chapter 2.

To do this, we need to respond to the following questions:

- Which thermal cycle to apply?
- Which loading mode to perform?

5.2.2.1 Curing cycle

In order to respond to the first question, we need at the beginning to elucidate the approach adopted here to characterize the rheological behavior throughout the cure of the studied thermoset prepreg. Since the material undergoes several multi-physical phenomena during all stages of cure, *i.e.*, thermal expansion/ contraction, compaction related to the consolidation at the uncured state, chemical shrinkage and the development of the mechanical properties, it is crucial to simplify the experimental procedure given the complexity that exists especially in the pre-gelation region. Therefore, the mechanical testing will only be performed during the second isothermal hold, *i.e.*, at 160°C or 180°C based on the defined new cycles in chapter 3. This simplified strategy suggests, as a first step, the decoupling of physics in order to properly understand and identify the rheological behavior during the cure. Consequently, the preconditioning step of the material could not alter the characterization process of the mechanical behavior.

Now how to choose the appropriate temperature of the isothermal cure stage?

As the characterization procedure needs to be carried out throughout the material transformation, the latter should be slow enough so one can assume that the degree of cure is almost constant during each time-span of the applied mechanical testing. Such methodology provides more accurate measurements of the rheological properties as function of the degree of cure of the reacting material.

Data in figure 5.2 suggest a prediction of the polymerization rate's evolution according to Bailleul's model [46,211] adopted for our M21 resin system. In this figure we propose a comparison between the estimated reaction kinetics for both adjusted thermal cycles as function of time. As we can see from this figure, the maximum rate appears shortly at the start of the isotherm with a polymerization speed almost twice as high at 180°C cure temperature compared to 160°C. The higher the curing temperature, the faster is the kinetics, in accordance with the reaction's exothermic behavior activated and amplified by the temperature. Therefore, the adjusted cycle 2 was chosen for the mechanical testing because of the low speed of the reaction kinetics, besides, almost the total curing of the material developed during the isothermal hold with a cure degree that ranges from around 0.06 until 0.72. As illustrated by figure 5.3a and according to what has been discussed in subsection 3.3.3, the material will be submitted to a hydrostatic pressure of 0.5 MPa along the whole cure cycle, which implies a compensation compressive force of 350 N. The rheological measurements will be carried out during the isothermal stage only.

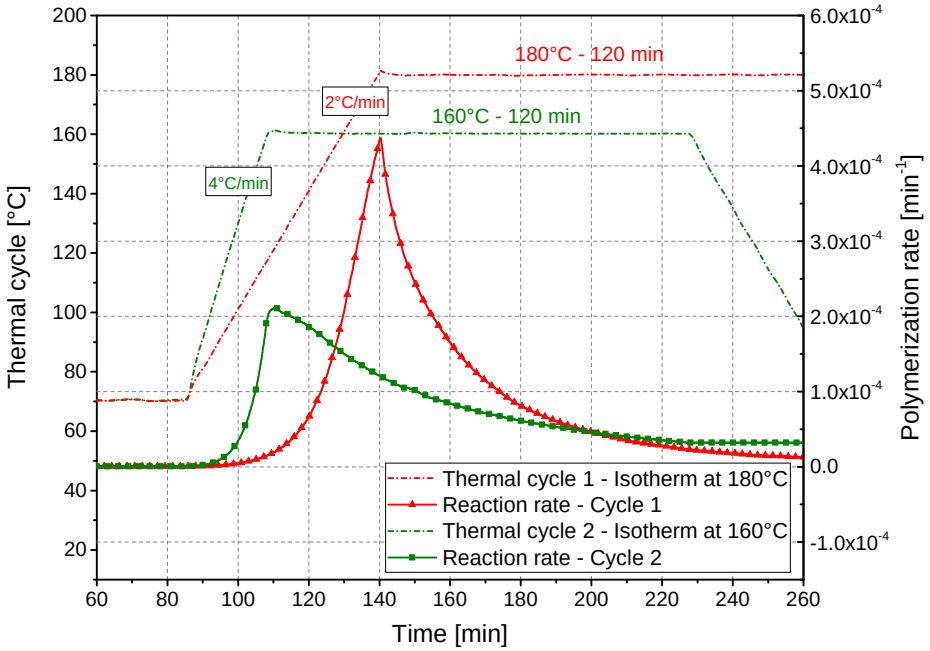

Figure 5.2: Predicted polymerization rates according to both adjusted thermal cycles.

5.2.2.2 Loading mode definition

5.2.2.2.1 Preliminary tests

The establishment of the appropriate mechanical testing to characterize the studied composite behavior from its uncured liquid state to its fully cured solid state was based on following the approach suggested by Msallem *et al.* [29] (see the sub-subsection 1.5.2.1) with a focus on yield stress fluids theory. Otherwise, since the procedure developed by Cardinaud [30] based on oscillatory measurements proved better efficiency in capturing the resin gelation process, it was rather considered here.

In our case, several techniques were tried to get the appropriate testing strategy. A preliminary oscillatory loading mode test was firstly developed as illustrated by the scheme in figure 5.3b. A sinusoidal compressive stress through the sample thickness, denoted as σ_3, was performed during the isotherm at 160°C with a frequency of 0.5 Hz. The oscillatory stress was held for 10 seconds (called by cycle in figure 5.3b), a period during which we can assume that the crosslinking reaction is almost constant regarding the polymerization rate at 160°C. After 10s of applied sinusoidal stress the material was held for 100s without stress application. Each stress amplitude, denoted as σ_a, was repeated four times after every 100s of hold. After such sequence (400s), the stress amplitude value increased and the procedure was repeated again until the end of the isothermal hold. One should precise that the average value of the sinusoidal stress was equal to the hydrostatic applied pressure. However, the major difficulty faced with this oscillatory mode under controlled stress was the inability to maintain contact with the piston and the upper surface of the sample once the performed σ_a exceeded the initial pre-compressive stress value. In that case, during the unloading stages, the material

was no longer submitted to a compressive stress, and as the piston moved upward, it became separated from the sample's surface. Due to the set-up configuration, the applied force cannot drop to zero because of the presence of the compressed silicon oil inside the cavity, which made it more complicated to assess the onset of the non-contact state between the sample and the piston. Obtained experimental results were therefore not reliable. Consequently, the oscillatory tests were not undertaken in our methodology as the initial pre-compressive stress value should be low enough to prevent the uncured material flow. To account for these limitations, only static compressive loading conditions under controlled stress were assigned for the rheological measurements.

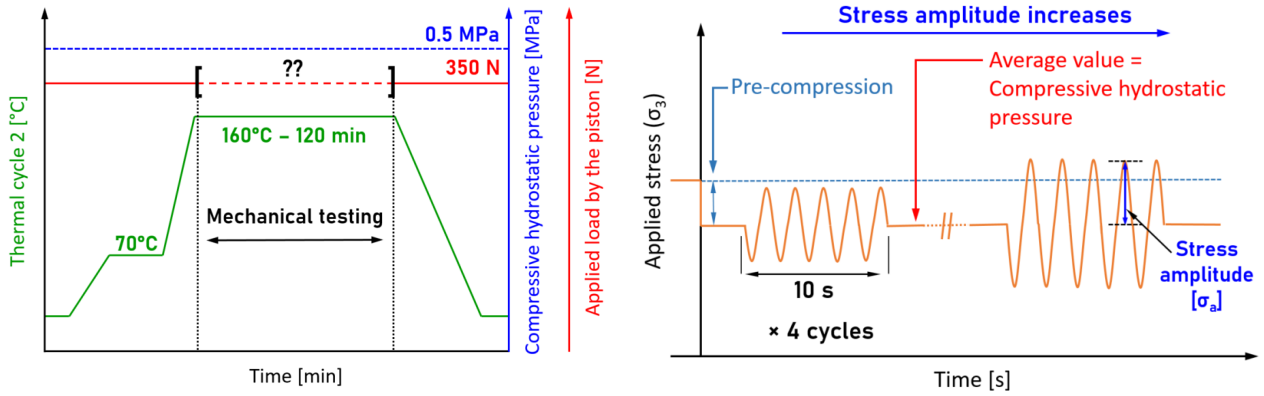

Figure 5.3: (a) Experimental procedure for the mechanical testing. (b) Preliminary oscillatory mode loading test.

5.2.2.2.2 The adopted strategy

Based on the conducted preliminary tests, it was not possible to apply the proposed procedure by Cardinaud [30] to probe the presence of yield stress evolution during curing as a way to investigate the composite material gelation process. For this reason, the adopted methodology was adjusted and three new mechanical testing were therefore defined. Figure 5.4a schematically illustrates the compressive loading-unloading test protocol defined as test I.

This kind of testing consists in loading the sample through its thickness with a compressive constant stress rate $\dot{\sigma_3}$ up to a defined level of stress amplitude, then the sample is unloaded until zero stress at $[-\dot{\sigma_3}]$. As a remark, when zero stress is applied through the axial direction, the material is always submitted to a compressive hydrostatic state. The loading stress is applied during 5s then the material is unloaded in 5s. The applied stress is then removed for 100s as a recovery step (denoted as $\Delta t_{recovery}$). Each applied σ_a is repeated four times and then the applied stress increased again.

The principal difficulty was the selection of loading conditions including especially the value of the stress amplitude to perform and the increment in load to choose. In fact, five experiments were first carried out in order to define the appropriate evolution of σ_a as the material state

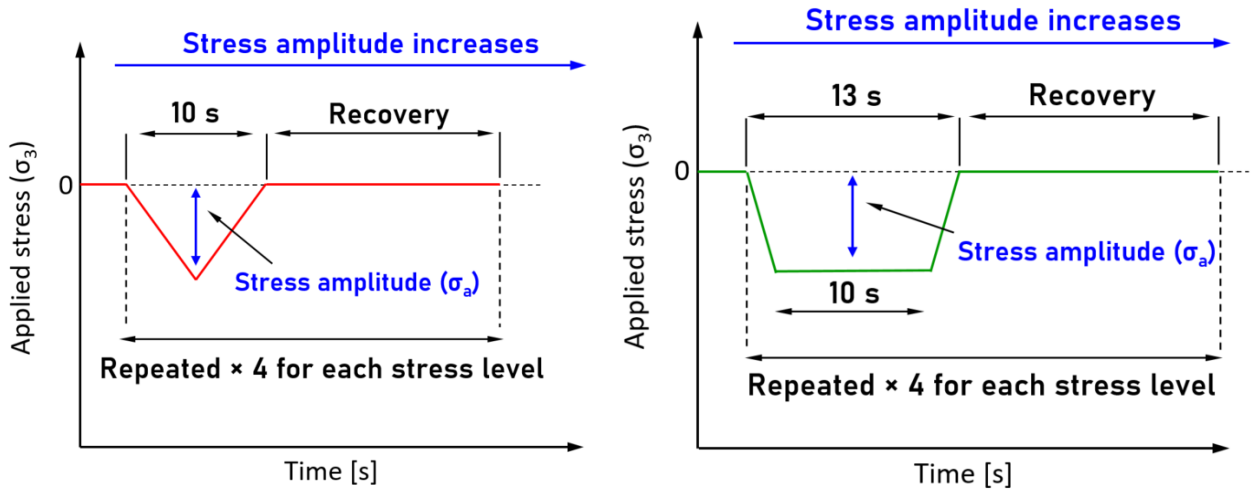

(a) (b)

Figure 5.4: Loading path diagrams: (a) Compressive loading-unloading test procedure (denoted as test I). (b) Creep-recovery test procedure (denoted as test III).

changes during polymerization. During the early stages of cure, the applied stress value should remain low enough to avoid the material flow at low resin viscosity. The selected stress levels correspond to less than 0.1% of axial deformation so that strains remain small and thus the "irreversible" accumulated induced creep flow remains negligible compared to other dimension variations. Conversely, under small stress conditions (for example $\sigma_a \leq 4$ 10^{-3}MPa) the machine sensitivity was very low and the signal outputs were very noisy. To have better accuracy, the applied stresses increased slightly as the degree of cure evolves. It started from $\sigma_a = 4.6$ 10^{-3}MPa and increased until 350 10^{-3}MPa. Ten levels of σ_a were finally chosen (see table 5.1). Fifty-two load cycles were therefore carried out on each sample during the testing.

Table 5.1: Defined σ_a levels for tests I, II and III with degree of cure variation values.

σ_a [$\times 10^{-3}$ MPa]	Degree of cure [%]
4.6 ($\times$4)	[11 - 18]
8 ($\times$4)	[20 - 26]
11 ($\times$4)	[27 - 32]
15.8 ($\times$4)	[34 - 38]
30 ($\times$4)	[39 - 43]
45.5 ($\times$4)	[44 - 47]
65 ($\times$4)	[48 - 51]
150 ($\times$4)	[52 - 54.5]
200 ($\times$4)	[55 - 57.5]
350 ($\times$16)	[58 - 66.3]

In figure 5.5 we represent the evolution of the defined σ_a during the isothermal hold for the mechanical testing procedure. Test I protocol (see figure 5.4a) was undertaken on four samples in order to evaluate the reproducibility of results where three samples had the same initial section $[S_0]$. Sample 4 with initial section of $[2S_0]$ was employed in order to assess whether there is an influence of sample's dimensions on the mechanical behavior. Details regarding the tested samples and mechanical experiments are gathered in table 5.2.

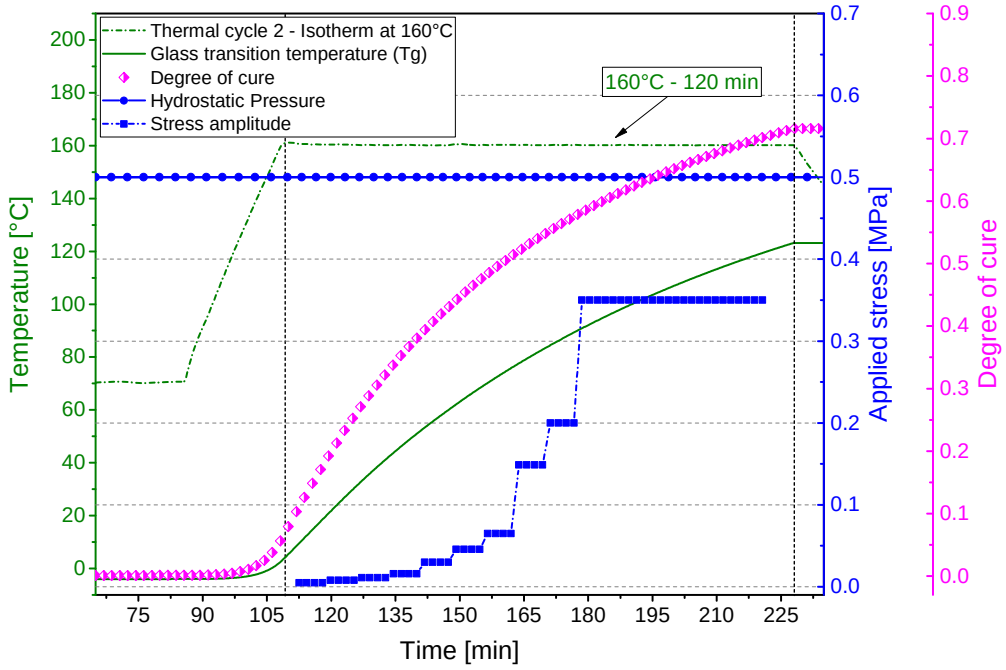

Figure 5.5: Experimental protocol of the mechanical testing procedure under controlled stress using the Pvt-HADDOC setup (focus on the isothermal hold).

Following the same loading form as test I, a second mechanical testing denoted as test II was defined by changing the loading cycle duration into 3s in order to investigate the effect of the stress rate. The third testing type, denoted as test III consists in a creep-recovery test described in figure 5.4b. It involves also a stress ramp of 1.5s, a 10s creep at the maximum stress value (σ_a) followed by a decreasing stress ramp of 1.5s. The material was hence submitted to the same stress rate $\dot{\sigma}_3$ in tests II and III. The same sequence is repeated four times every 100s for each stress amplitude.

Note that, for the three mechanical testing types performed in this study, the applied stress amplitudes are the same for each test which are gathered in table 5.1. A prediction of the degree of cure evolution is given in figure 5.5. The thermal cycle is used to achieve the same degree of cure (almost 72%) for all samples. The glass transition temperature is also shown in figure 5.5. During the mechanical testing procedure the latter remains below the cure temperature which means the material is only characterized in the rubbery state.

Table 5.2: Mechanical testing details and specimens used for each test.

		Testing type		
		Triangular	Load-unload	Creep-recovery
Test notation		I	II	III
Loading cycle duration Δt_{cycle}		10 s	3 s	24 s
Sample's number	Used section			
1, 2 and 3	S_0	×		
4	$2 \times S_0$	×		
5	S_0		×	
6	S_0			×

5.2.3 Mechanical strains calculation strategy

In this subsection we detail the employed procedure to analyze the rheological behavior of the studied IMA/M21 prepreg during the cure. It is important to point out that only transverse mechanical behavior through-the-thickness direction of the studied unidirectional prepreg was analyzed. The obtained data from the laser profilometer were not usable to investigate simultaneously the transverse in-plane mechanical response. Some improvements are needed to enhance the sampling frequency of the sensor and data acquisition process in order to capture the evolution of the mechanical behavior during the applied loading cycles. In order to estimate the mechanical axial strain ε_3^{mech}, a detailed strategy of experimental data analysis was developed and applied for every test. The analysis relies on the following steps.

Thermal baseline subtraction

The displacement of the piston was recorded by the press during the whole cure cycle. As detailed in chapter 3, one needs to subtract the baseline displacement in order to obtain the variation of sample thickness only. It is true that the mechanical tests were chosen to be carried out during the isothermal hold which means there is no coupling effects between thermal and mechanical properties assuming that no thermal gradients take place. Nevertheless, on the basis of the main out-comes of chapter 3, this step is crucial to examine the compaction behavior of the material and therefore to estimate the reference state after compaction.

Reference state after consolidation

As discussed in chapter 3, the consolidation stage correlated to thickness reduction seen through the curing process of the studied laminate represents a very important pre-conditioning step in the material state. In figure 5.6, we represent the measured displacements through the thickness direction of the tested samples together with the imposed thermal cycle after the thermal baseline subtraction. The focus here is given to the early stages of the curing behavior before reaching the isothermal hold at 160°C. The observed behavior reveals almost the same material response as reported in section 3.1. The measured displacements started to drop since the first steps of heating indicating the compaction process. Only sample 4 has an initial section of $[2S_0]$. The displacements evolution since approximately 42°C up to the end

of the isothermal dwell at 70°C exhibits a high scattering results. Accordingly, an assumption could be made that the sample initial section dimensions might have finally irrelevant effects on the compaction limits' values reached by each sample. Moreover, as evident from this figure, the material consolidation process started again during the second heating ramp. At 105°C the samples' thickness decreased and the displacements continued to drop until almost 140°C. This trend of behavior was not captured when performing the investigation of the thermo-chemical behavior of the material (see subsection 3.4.3). However, it is crucial to mention that for the mechanical behavior investigation the testings were carried out few weeks after the Shelf Life limit of the material. This could be a reason behind the occurrence of the second step compaction during heating up after 70°C. There has indeed been a certain evolution of the compaction behavior that makes our initial hold at 70°C too short for reaching a perfect densification. The examination of the compaction behavior during the pre-cure consolidation of this prepreg led us, therefore, to define a new reference state of the material thickness. The latter is taken at the beginning of the isothermal dwell, as shown in figure 5.6. Hence, according to each sample compaction behavior, a reference level was defined (illustrated by red arrow on figure 5.6) which allowed to obtain a reference thickness denoted as $h_{reference}$ to be taken into consideration for the mechanical strains calculation. $h_{reference}$ can be estimated according to equation 5.1 where h_0 is the initial thickness of each sample.

$$h_{reference} = h_0 - \mid \text{reference level} \mid \tag{5.1}$$

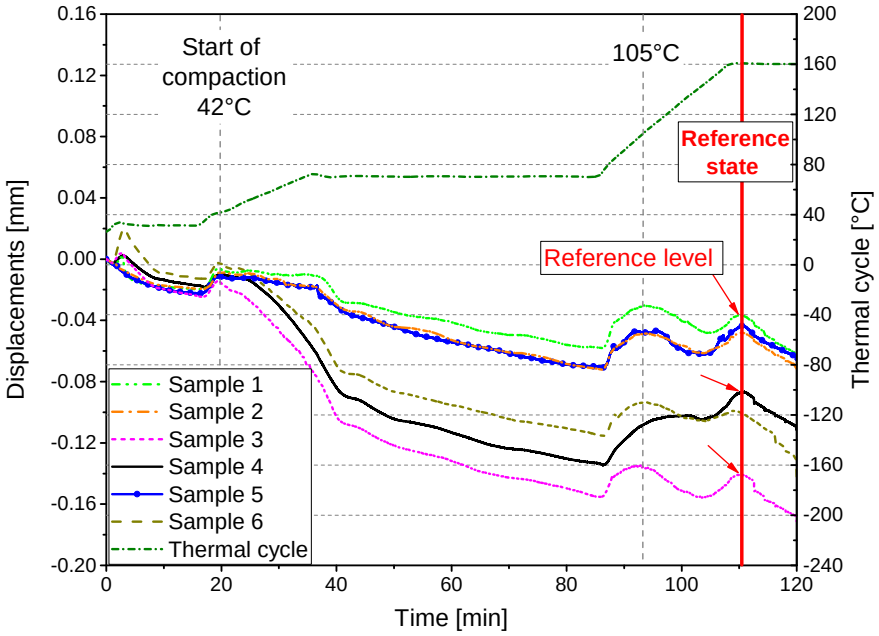

Figure 5.6: Through-thickness compaction behavior and reference state definition.

Compliance correction of the experimental bench

Raw displacements results are sourced from an optical encoder attached to the motor at the crosshead and not by means of an extensometer. Measured displacements represent in fact the sum of total system deformation including the specimen. A standard correction

step was carried out to eliminate the stiffness of the machine. The test consists in applying a compressive load without specimen to obtain the complete uni-axial force-displacement curve related the elastic deformation of the experimental bench. The stiffness of the machine was deduced from the slope of linear force-displacement curve denoted as K_{device} which was found equal to 50 KN/mm. The behavior of the experimental bench is assumed to remain elastic and linear. The applied load F and the elastic displacement of the machine (denoted as Δl_3^{device}) follow therefore equation 5.2:

$$F = K_{device} \times \Delta l_3^{device} \tag{5.2}$$

This yields a correction formula (equation 5.3) that allows to estimate only the induced material axial displacements indicated by $\Delta l_3^{material}$ at any given load, through the subtraction of Δl_3^{device} in addition to the thermal baseline denoted as $\Delta l_3^{baseline}$ from the total raw measured axial displacements described by Δl_3^{total} as follows

$$\Delta l_3^{material} = \Delta l_3^{total} - \Delta l_3^{baseline} - \Delta l_3^{device} \tag{5.3}$$

One should mention that no corrections were required due to the presence of metal bellows which were inserted in the experimental setup in order to provide frictionless coupling between the piston and the mold cavity (see section 2.2). The axial stiffness of the latter is 10 N/mm and it was only pressed in the range of 4 10^{-2} millimeters during the mechanical testing.

Chemical shrinkage subtraction

The analysis of the mechanical behavior during the isothermal hold is based on extracting each loading cycle to investigate the corresponding response for a given degree of cure which means studying the mechanical behavior evolution for the fifty-two applied cycles for each test. In order to extract the sample purely ε_3^{mech}, the instantaneous chemical shrinkage contribution, defined by ε_3^{chem}, has to be removed from the sample's total axial strains, denoted as $\varepsilon_3^{material}$ and defined by equation 5.4 "during the isothermal dwell"

$$\varepsilon_3^{material} = \varepsilon_3^{chem} + \varepsilon_3^{mech} \tag{5.4}$$

The chemical strain ε_3^{chem} can be estimated by

$$\varepsilon_3^{chem}(t) = \int_0^t CCS_3 \frac{\partial \alpha}{\partial t} \, \mathrm{d}t \tag{5.5}$$

considering a linear relation between the degree of cure and the chemical shrinkage. The coefficients of chemical shrinkage CCSs are taken as the average experimental values determined before and after gelation in chapter 3 with a gel point corresponding to 52% of degree of cure by

$$CCS_3 = \begin{cases} CCS_3 = -3.83\% & \text{if } \alpha < \alpha_{gel} \\ CCS_3 = -2.07\% & \text{if } \alpha \geq \alpha_{gel} \end{cases} \tag{5.6}$$

Thereby, after applying all the stated steps and assuming no thermal deformations could be induced during the isothermal dwell, the sample's total axial strains, can be also defined as

$$\varepsilon_3^{material} = \frac{\Delta l_3^{material}}{h_{reference}} \tag{5.7}$$

Therefore, on the basis on equations 5.4 and 5.7, the axial mechanical strains ε_3^{mech} can be obtained. The applied nominal stress is estimated as $\sigma_3 = \frac{F}{S}$ where F is the applied load and S is the measured in-plane initial section of the corresponding sample.

5.3 Experimental results analysis

5.3.1 General aspect of the mechanical behavior

Figure 5.7 depicts typical evolution of the estimated degree of cure, thermal cycle and the through-thickness total strain $\varepsilon_3^{material}$ before chemical shrinkage subtraction and purely ε_3^{mech} as a way of comparison. Reported strain curves have been obtained with the mechanical testing I carried out using sample 4 taken as an example. Strains are zeroed at the starting of the isotherm hold at 160°C considered as the material state reference for the mechanical behavior investigation as described previously.

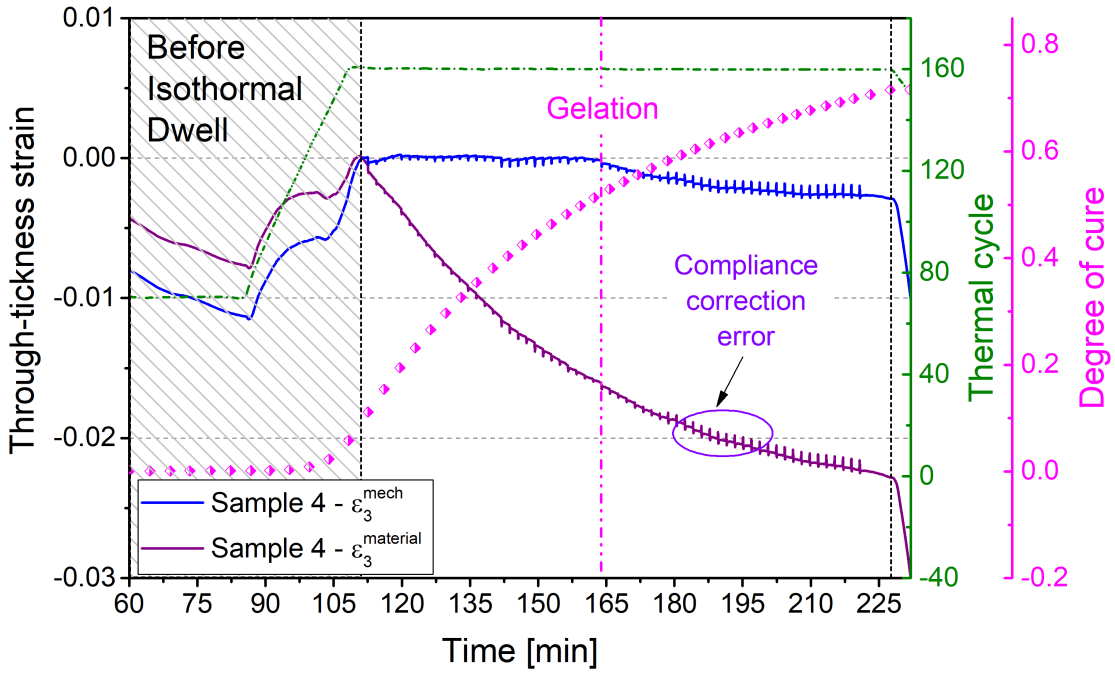

Figure 5.7: Through-thickness strain measurements resulting from the mechanical testing of sample 4.

Figure 5.8 represents the corresponding overall applied stress of test I illustrating the employed methodology. The focus here is made on the isothermal dwell during which the characterization testing was performed. In this example, the material was submitted to triangular compressive loading-unloading stress cycles of 10s duration each. Figure 5.8 also

shows the stress amplitude that evolves throughout the entire isothermal hold as given in table 5.2. A zoom has been made in this figure to highlight the repeated applied stress four times each 100 seconds.

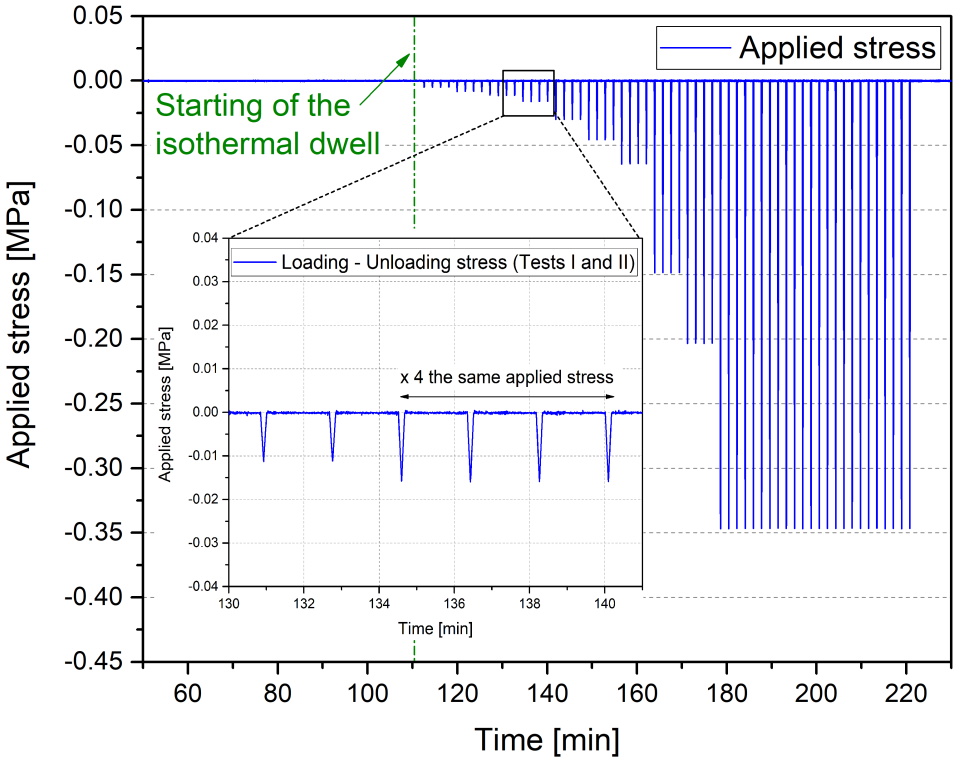

Figure 5.8: Applied loading-unloading stress evolution with time during the isothermal hold at 160°C. Illustration of mechanical test I.

As can be seen from the global overview of the strains evolution given in figure 5.7, the typical drop in $\varepsilon_3^{material}$ is due to the cure shrinkage through the thickness as reported in chapter 3. If we compare the latter with the total pure ε_3^{mech} before the gelation stage we could notice that ε_3^{mech} trend's evolution as function of time remained almost in the range of 0.1% or less. The steady evolution of the latter that remained close to zero during the pre-gelation stage could reveal the uncoupling effects between mechanical properties evolution and chemical shrinkage, which could justify the accuracy of the employed value of the CCS identified experimentally in chapter 3. On the contrary, during the post-gelation stage, we can clearly notice that the overall ε_3^{mech} starts to decrease since t = 164 min to reach nearly 0.28% by the end of the isothermal dwell. This drop seen in the mechanical strains is not due to the applied stress increase, but to curing and the resulting chemical shrinkage. This trend shows that the employed experimental post-gelation CCS value is slightly lower than the exact value of the CCS related to sample 4, which could be evidently discerned from the difference between both strains rate evolution. It should also be noted that possible source of error can be attributed to the chosen value of gel point. The latter actually ranges from 50% and 55% for M21 system. Nevertheless, such induced errors are fairly unavoidable since the CCS values were experimentally obtained using prepreg material that itself exhibits a slight

behavior variation. A striking illustration of this variation can be seen in figure 5.9 through the mechanical strains evolution as function of cure degree obtained from the mechanical testing of samples 1, 3, 4 and 6 taken as examples. As detailed in table 5.2, samples 1 and 3 have the same initial sections and were submitted to the same test I as well as sample 4 which has doubled initial section. Quite contrarily, specimen 6 was submitted to creep-recovery test with the same initial section as samples 1 and 3. The same stress amplitudes were applied to all samples as clear from table 5.1. Inspection of strains evolution of samples 1, 3 and 4, reveal a large variability. What we can draw up here as assumptions, is that the main decrease in the total mechanical strain during the isotherm, which reaches about 0.5% or more in the case of sample 6, could only be correlated to coupled effects with cure. Indeed, the estimation of chemical strains depends on the employed experimental CCS values which might vary by ±0.3% in the pre-gelation stage as identified in chapter 3. The latter is only function of cure degree regardless samples' dimensions. Such variability is often inherent in the manufacture of composites and a large number of potential sources of variability can be identified when dealing with reinforced systems.

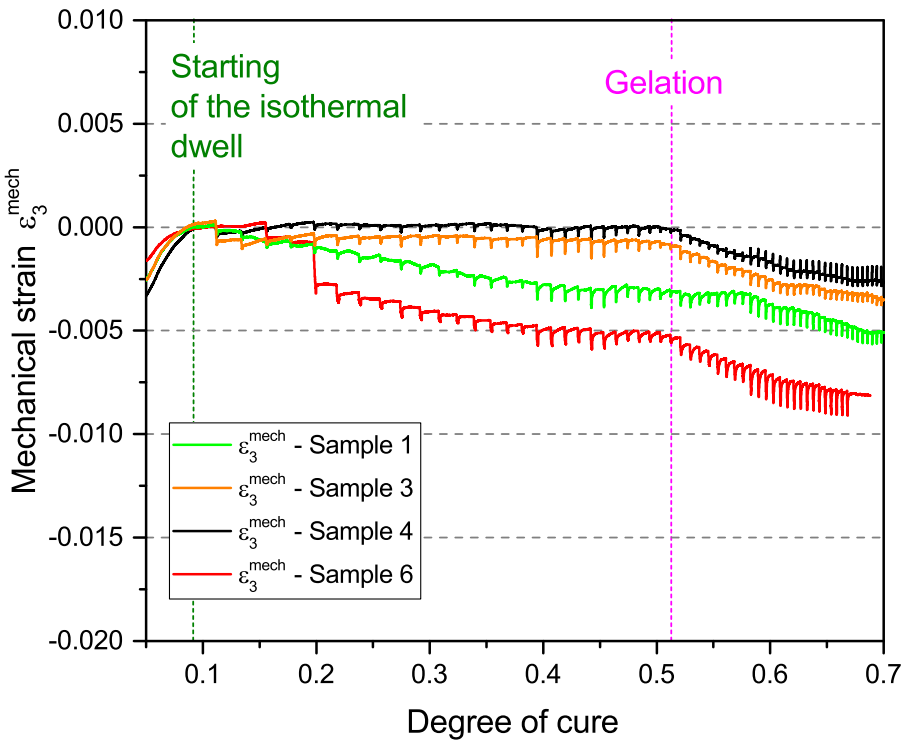

Figure 5.9: Mechanical strains evolution with degree of cure obtained from testing of samples 1, 3, 4 and 6 as examples.

In the case of sample 6, other than the whole decrease in strains due to coupled effects with cure shrinkage alike other samples, we can notice a slight difference in strains increase during each applied compressive cycle. At $\alpha = 20\%$, we can discern a drastic drop in strain that rise sharply although the applied stress amplitude was the same for four samples which might be correlated in this case to the material response to creep testing.

In the following sections will be detailed the analysis of the prepreg mechanical behavior methodology which relies on studying each loading cycle in order to gain more insight of the material mechanical properties development during the cure. However, it should be noted that despite the slight mismatch in predicting the chemical shrinkage, the degree of cure variation during one loading cycle remains very low in the range of 5 10^{-3} or less. Such variation has no significant consequence. The analysis of the stress strain response of the material during a given load cycle can therefore be associated to a precise value of α. Notice that, hereinafter in this chapter, the axial mechanical strain denoted as ε_3^{mech} will be referred to us by the axial strain ε_3, since only the purely mechanical strain will be analyzed in the upcoming parts.

5.3.2 Limitations due to the experimental setup compliance

Figure 5.10 provides an example of measured axial displacements obtained from creep-recovery test carried out on sample 6. Displacements are extracted from one loading cycle performed at 31% of degree of cure under applied load of 35 N. This figure contains the raw displacements and the applied load data collected from the Instron machine. Device displacements were estimated on the basis of the measured stiffness mentioned earlier (see equation 5.2). After adopting the detailed strategy described in subsection 5.2.3, the corresponding rectified material displacements are also gathered in figure 5.10. Whatever the considered curve, three stages can be observed, the quasi-instantaneous response during the first compressive loading ramp of 1.5s, then a creep response for 10s followed by the quasi-instantaneous unloading step and the material recovery stage when the load is removed.

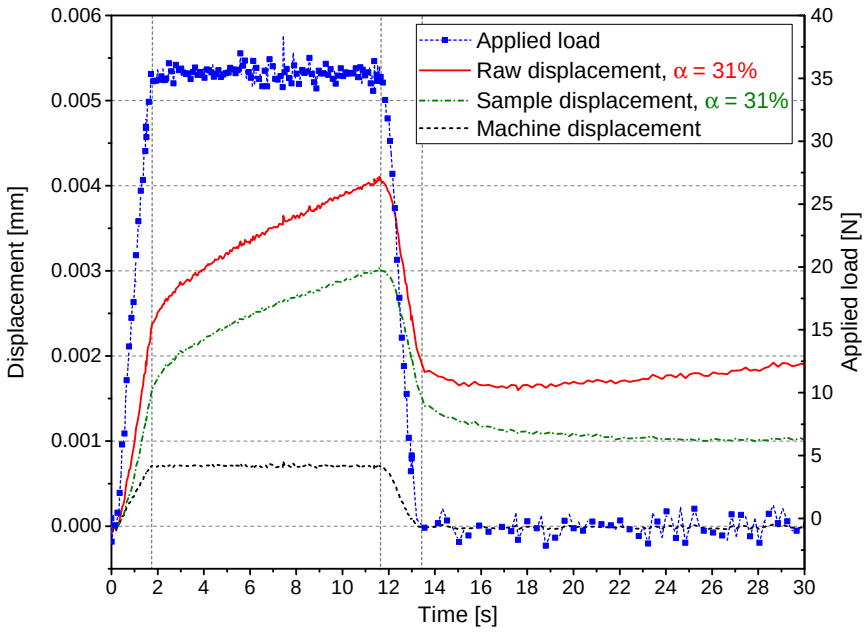

Figure 5.10: Measured transverse axial displacements obtained from creep-recovery test of sample 6 at α=31% together with the device displacements and the corresponding applied load.

Data in figure 5.11 gather the material response after gelation illustrated by the induced displacements extracted from two loading cycles for $\alpha = 58\%$ and $\alpha = 67\%$ under applied load of 1130 N. As visible from this figure, during the loading and unloading steps raw displacements are approximately of same magnitude as the machine elastic response. Indeed, as the material rigidity increases with the crosslinking reaction progress, the induced displacements are getting smaller so of the same order as our device deformation. Induced errors are thereby obtained during both loading and unloading ramps reported in figure 5.11 by compliance correction error. The same sort of effects was observed in case of testing I and II with triangular compressive loading form near to gelation region. These artifacts are also visible in figure 5.7. After gelation, the generated errors of strain calculation induced some sort of tensile aspect in the mechanical global response of sample 4 which is not possible regrading the applied compressive loading during the whole testing. The device low stiffness regarding the prepreg response after gelation was somewhat problematic in capturing the material behavior after gel point and slightly disappointing toward the main objectives of investigating the whole material transition behavior during the cure. Nevertheless, notwithstanding the compliance limitations consequences, the rheological behavior of the studied prepreg will be mainly analyzed during the pre-gelation stage for the three mechanical testing types.

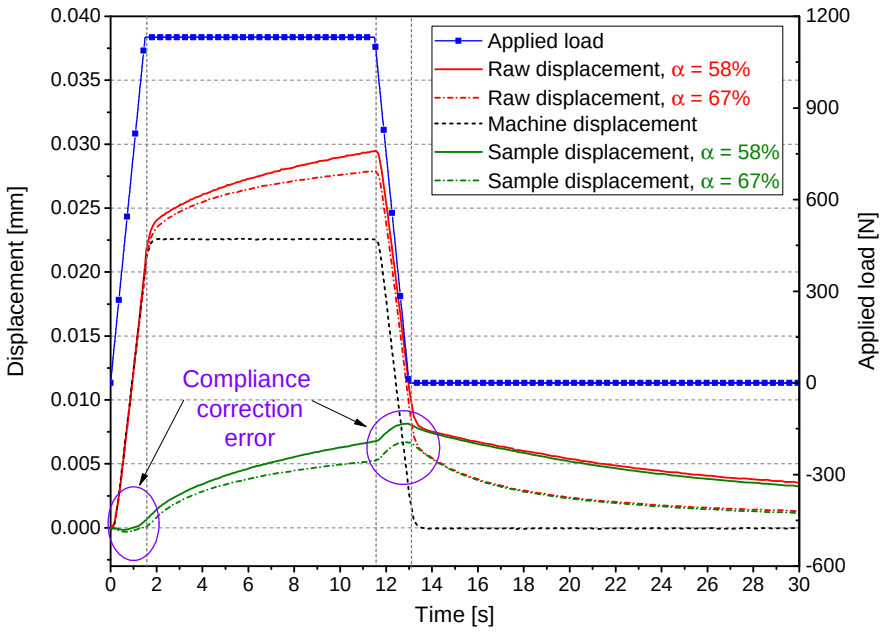

Figure 5.11: Measured transverse axial displacements obtained from creep-recovery test of sample 6 at α=58% and α=67% together with the device displacements and the corresponding applied load. Illustration of compliance device limitations after gelation.

5.3.3 Influence of the sample initial section

As it was detailed in section 5.2, sample 4 was tested under compressive triangular loading stress with an initial section of $[2\times S_0]$ that represents a doubled section comparing to the rest of tested specimens. Figure 5.12 provides an illustration of the material response to a

compressive loading-unloading cycle according to test I for an applied maximum stress of 15.5 10^{-3}MPa. The corresponding degree of cure of this cycle is 38%. The mean axial nominal strain represents an average curve obtained from samples 1, 2 and 3 submitted to the same testing conditions with the same initial section $[S_0]$.

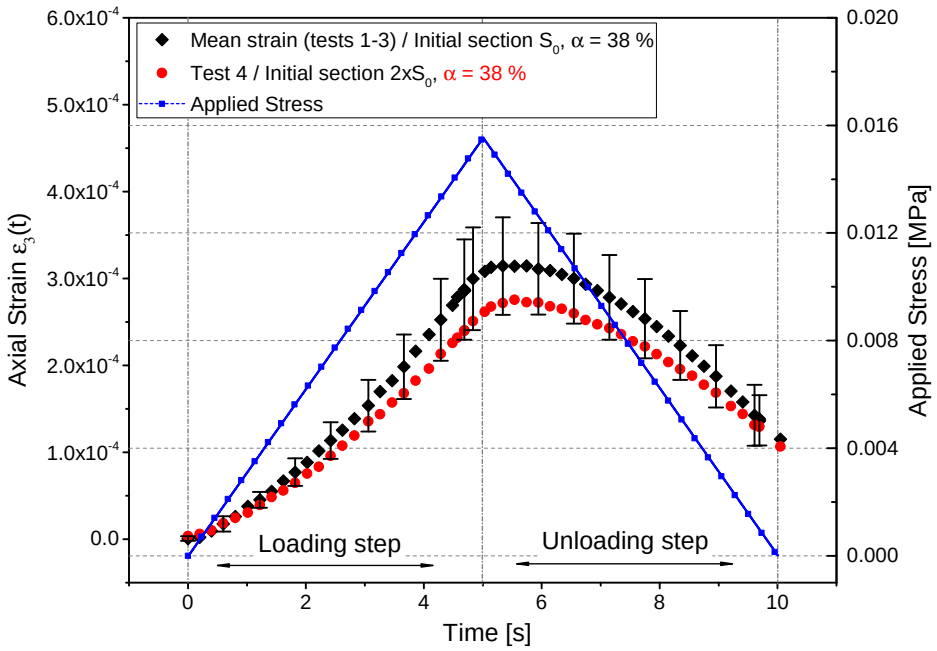

Figure 5.12: Axial mechanical strain evolution with time during a loading-unloading cycle at α=38%. Illustration of sample's initial section influence on the behavior.

The scattering of strain measurements is given by standard deviation error bars that remain below ± 5 10^{-3}% during the loading cycle for a maximum average strain level of almost 3 10^{-2}%. As it can be seen from this figure, sample 4 clearly has the same mechanical response which lies inside the error bars of samples [1 - 3]. Consequently, it was assumed that there is no effect of frictions on the mechanical behavior response and only material variability could be responsible of such behavior scattering.

Notice that, in the following sections, the mechanical response of samples [1 - 3] and 4 will be represented by an average curve obtained from the four samples strain measurements that were submitted to the same mechanical testing conditions.

5.3.4 Influence of the degree of cure

Now that the total mechanical strain induced during the isothermal hold of each sample was calculated, the analysis of the rheological behavior as function of cure degree relies on investigating each applied loading cycle separately in order to evaluate the mechanical properties. Some simplifying assumptions are therefore needed to be draw up:

- The degree of cure α is assumed constant during each loading cycle duration Δt_{cycle} (see table 5.2) and so is the mechanical state of the material.

- To estimate the strain resulting from an applied stress denoted as σ_3^{i+1}, introduced at time t_{i+1} corresponding to a given degree of cure α^{i+1}, where t_{i+1} can be defined by

$$t_{i+1} = t_i + [\Delta t_{cycle} + \Delta t_{recovery}] \tag{5.8}$$

with t_i the time increment at which σ_3^i was introduced corresponding to a given α^i and $\Delta t_{recovery}$ is the recovery step duration of 100s for all tests, it is supposed that the incremental strain response of the material to this second stress σ_3^{i+1} is independent of the one previously introduced at instant t_i. Thus, each performed loading cycle is assumed relating to a new material state ($\alpha^i \neq \alpha^{i+1}$) and the induced strain is assumed independent from the history of strain responses.

Creep-recovery test

The creep-recovery test is taken as an example to illustrate the mechanical behavior variation as function of the degree of cure. In figure 5.13 we present a compilation of the creep-recovery curves resulting from test III. In order to obtain a broader overview of the cure degree's influence on the material behavior disregarding the applied stress effect in interpreting the mechanical responses, a normalized axial creep strain, denoted as ε_3^*, and based on the applied stress amplitude σ_a is rather calculated for a given degree of cure according to equation 5.9. Thus, load dependence can be ruled out which allows to provide a mean to quantify the capacity of the material to flow in response to a constant applied stress. $\varepsilon_3^*(t)$ is also, commonly called as a material's creep compliance J(t).

$$\varepsilon_3^*(t) = \frac{\varepsilon_3(t)}{\sigma_a} \tag{5.9}$$

For reasons of clarity, only 7 creep-recovery responses are taken as examples and displayed in figure 5.13. For a given degree of cure, each applied σ_a is gathered in table 5.3.

Table 5.3: Applied stress amplitudes for each degree of cure (α).

α(%)	18	24	29	34	42
σ_a (10^{-3}MPa)	4.6	8	11	15.8	30
α (%)	43	46	47	48	49
σ_a (10^{-3}MPa)	30	45.5	45.5	65	65

As evident, only the evolution of the material pre-gelation state is presented here. It can be seen from the plots of $\varepsilon_3^*(t)$, whatever the considered behavior, it seems that the material displays elastic, viscous and possibly plastic properties. $\varepsilon_3^*(t)$ evolution during the loading steps, reveals an elastic instantaneous response which decreases with the degree of cure growth. Indeed, the induced normalized strain roughly falls from almost 4% at $\alpha = 18\%$ to approximately 0.23% for $\alpha = 48\%$. The material stiffness is clearly increased during the cure. When constant stress is applied, its response shows an increasing creep strain over time. It should be noted here that the normalized strain variation is directly ruled by the degree of cure increase and non dependency on stress can be deduced as the material presents a new state for each cure degree.

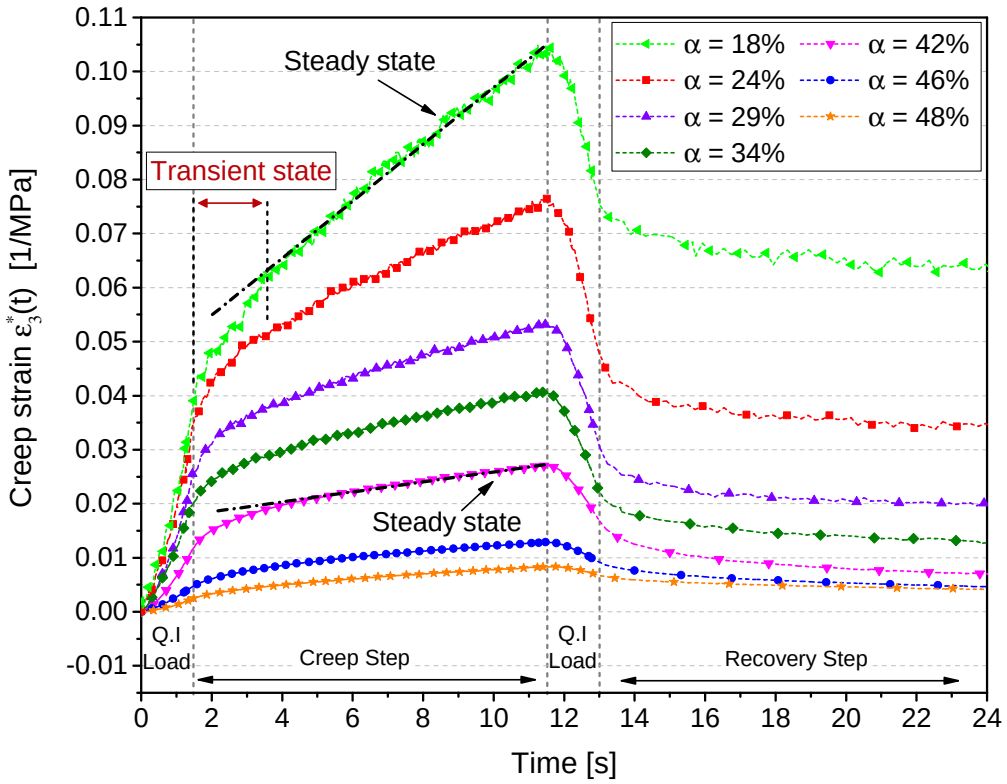

Figure 5.13: Experimental creep normalized strain ε_3^* evolution with time during creep-recovery test as functions of cure degree.

As illustrated by figure 5.13, the material normalized strain at $\alpha = 18\%$ is taken as an example to highlight the most important features of the creep-recovery response. It is clearly shown that the material behavior presenting a transient state ruled by the viscoelastic components from t = 1.5 s until approximately t = 3.5 s. This delayed deformation is then followed by a decreasing creep rate, afterwards the material eventually enters rapidly into a constant steady state illustrated by linear regression. With the increase of the degree of cure, we can see that the ability of the material to resist creep deformation gradually increases by inspecting the difference between both linear regression slopes illustrated at $\alpha = 18\%$ and 42%. We can also notice that even the steady state is reached later in time with the cure degree growth. If we compare the material responses at $\alpha = 18\%$ and 42%, we can observe that the steady state is reached at t = 4.5 s for 42% of cure degree. When unloaded during the "quasi-instantaneous" loading step, we can detect an elastic recovery–strain recovered over time. When the stress is totally removed, a permanent deformation is left in the material for all cure degrees with an ever decreasing amount along the pre-gelation stage by getting closer to gel point. The normalized creep permanent strain dropped from 65% to almost 0.5% near gelation. However, it is difficult to assess the origin of irrecoverable deformations only by creep-recovery tests. These induced permanent strains in the material could be on the one hand, related to the viscous flow under constant applied load, or, on the other hand,

it could represent permanent distortions that likely occurred once the material was subjected to stresses that exceeded its elastic yield strength. Thus, an investigation of the rheological behavior with other mechanical testing types other than creep testing was required.

Compressive loading-unloading tests

Another illustration of the degree of cure effect on the mechanical behavior can be obtained by exploring the material mechanical response to the applied compressive loading-unloading tests. Figure 5.14 contains stress-strain curves of sample 1 response to the mechanical testing I taken as example. In order to make more legible the influence of degree of cure on the rheological behavior, the performed stress and the resulted strain are normalized by the applied stress amplitude according to equations 5.10 and 5.9, respectively. The corresponding values of stress amplitudes are given in table 5.3 for four chosen levels of cure degree.

$$\sigma_3^*(t) = \frac{\sigma_3(t)}{\sigma_a} \tag{5.10}$$

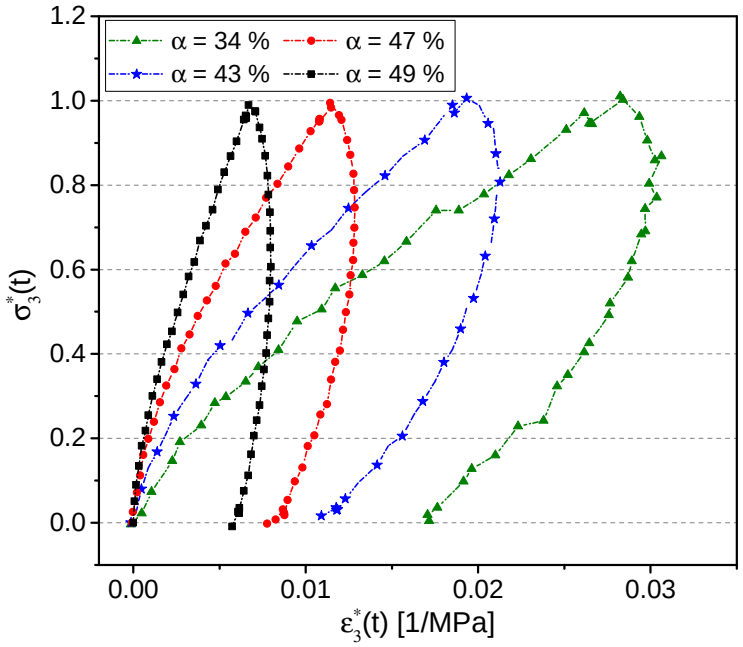

Figure 5.14: Mechanical response of sample 1 obtained with loading-unloading applied stress according to test I at four levels of cure degree. Resulted stress and strain are normalized by the corresponding stress amplitude for more legibility.

As visible from figure 5.14, the loading and unloading curves do not coincide for every cure degree and hysteresis loops appear upon complete unloading. Moreover, another important feature can be found in this figure, with the increasing level of cure degree, the mechanical behavior, as expected, becomes more rigid when approaching the gelation point. If we suppose that the material exhibits an instantaneous elastic response at the beginning of each loading step, we can definitely distinguish a significant growth in the material stiffness. The

hysteresis loops are clearly larger during the first stages of cure as shown by the example of $\alpha = 34\%$ compared to 49%. Strain levels displayed at the end of each unloading step are different from zero but become significantly lower with the increase of α. When it comes to viscoelastic materials behavior or viscoplastic mechanical response, the stress-strain curves obtained from loading-unloading tests can look very similar to the ones obtained here. This adds further difficulties in identifying the appropriate rheological behavior. Indeed, once the load is removed, a plastic material will usually not return to its original shape and permanent strains are likely to be left in the material. Conversely, a viscoelastic material has a time-dependent mechanical response which may exhibit recoverable viscoelasticity when left for a sufficient time after the unloading stage. Thus, the investigation of the resulting mechanical response under loading-unloading applied stress is yet limited. A close examination of loading-unloading-recovery tests is rather needed to broaden the inspection of the mechanical behavior in order to probe the origin sources of the obtained permanent strains and therefore to identify the appropriate rheological model to employ.

As detailed in section 5.2, loading-unloading mechanical tests were performed in an increasing stress amplitude with α during the whole isothermal hold while after each applied σ_a the material was held under zero stress for a $\Delta t_{recovery} = 100$ s for all tests. Sample 1 mechanical response already presented in figure 5.14 is now displayed as true stress - strain curves in figures 5.15a and 5.15c related to both degrees of cure 34% and 49%, respectively. In these figures, strains are plotted even after the stress reached zero in order to follow the evolution of strain with time. Additionally, in figures 5.15b and 5.15d are depicted the resulting strain evolution as function of time in both cases. Sample 3 stress-strain and strain-time evolutions are superimposed to ones of sample 1. We remind here that it was tested exactly in the same conditions.

The insight gained into the material behavior through these measurements can be summarized as follows:

- The complete recovery in time of strain level after the end of each unloading stage for both degrees of cure, implies that the material clearly presents a viscoelastic behavior. Indeed, plastic behavior would rather be accompanied by irreversible deformation that cannot recover over time. It is crucial to point out that for both states, the material was not submitted to the same stress level. The maximum applied stress at $\alpha = 49\%$ is 65 10^{-3}MPa whereas it was 15.8 10^{-3}MPa at $\alpha = 34\%$.
- The mechanical response of sample 3 is, in fact, presented to mention that some exceptions could be found within the material response. As it can be seen from figures 5.15a and 5.15b, the strain level did not reach zero after a complete recovery stage and permanent deformation of 10^{-4} is detected although the same level of stress was applied for both samples 1 and 3. Aside of the material behavior variability, previously discussed in subsection 5.3.1, we assume that during the recovery stage, the prediction of strains evolution on large scale of time longer than Δt_{cycle}, could include some erroneous. Inevitable coupled effects of chemo-rheological phenomena could take place regarding the induced errors in estimating the chemical shrinkage. A variation of almost $\Delta\alpha = 3\ 10^{-3}$ or less during Δt_{cycle} is presumed negligible since, barely no coupled

chemical shrinkage with mechanical properties evolution could be induced. However, during more than 50s, $\Delta\alpha$ could reach 2 10^{-2} depending on the polymerization rate. Thus, the calculation of true mechanical strains on larger scale than Δt_{cycle} could be inaccurate. Consequently, the origin of these permanents strains cannot be strictly attributed to plastic behavior.

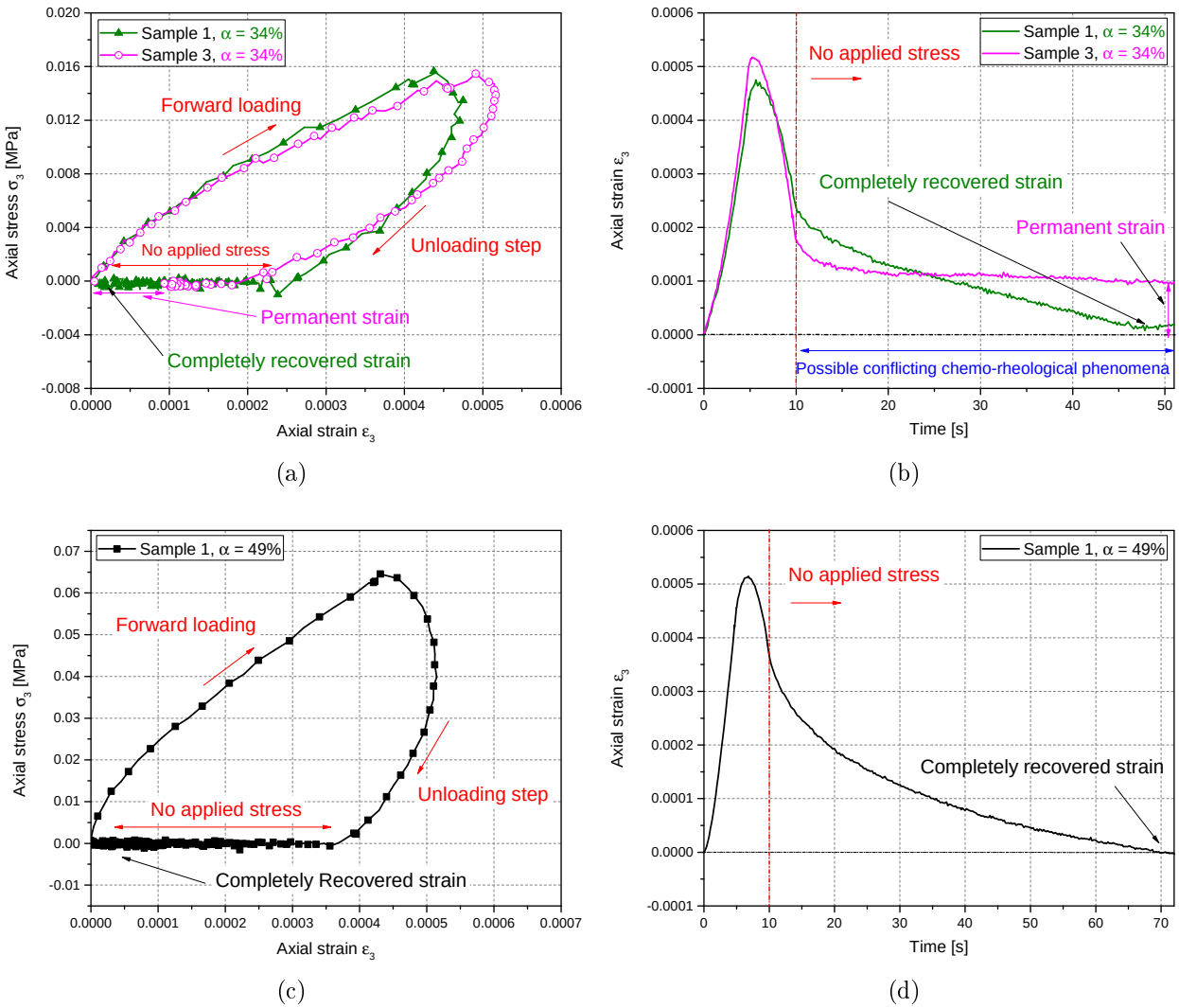

Figure 5.15: Experimental results of loading-unloading-recovery tests of samples 1 and 3. (a) Stress-strain curves at $\alpha = 34\%$ of samples 1 and 3. (b) Corresponding strain evolution with time at $\alpha = 34\%$. (c) Stress - strain curve at $\alpha = 49\%$ of sample 1. (d) Strain evolution with time of sample 1 at $\alpha = 49\%$.

In what follows, for triangular loading-unloading tests, the mechanical behavior will be only analyzed during load - applied stages and no recovery behavior will be further investigated.

Another aspect of the studied prepreg mechanical behavior can be revealed, the stress rate influence. Measurements according to test II were performed on sample 5 in order to assess the effect of $\dot{\sigma_3}$ while applying exactly the σ_a as other samples (see table 5.2). In figure 5.16 are gathered sample 5 stress-strain curve resulting from testing II at $\alpha = 34\%$ together with sample 1 mechanical response. Both samples were submitted to 15.8 10^{-3}MPa compressive stress. $\dot{\sigma_3}$ performed in the case of sample 5 equal to 10.53 10^{-3}MPa.s^{-1}, is almost more than three times higher than the one applied to sample 1 ($\dot{\sigma_3} = 3.16\ 10^{-3}$MPa.s^{-1}). It can be noticed from this figure that there is a dependence on the rate of loading. The faster the stress rate, the lower the stretching of the viscoelastic material is. The hysteresis loop area becomes smaller when the material is loaded faster meaning that less energy was dissipated in this case. Less viscous effects are indeed obtained once the loading duration become lower. We can additionally remark a decrease in permanent flow strain levels after unloading. Those tests, once again, clearly highlight the viscoelastic nature of the prepreg all along the curing cycle before gelation.

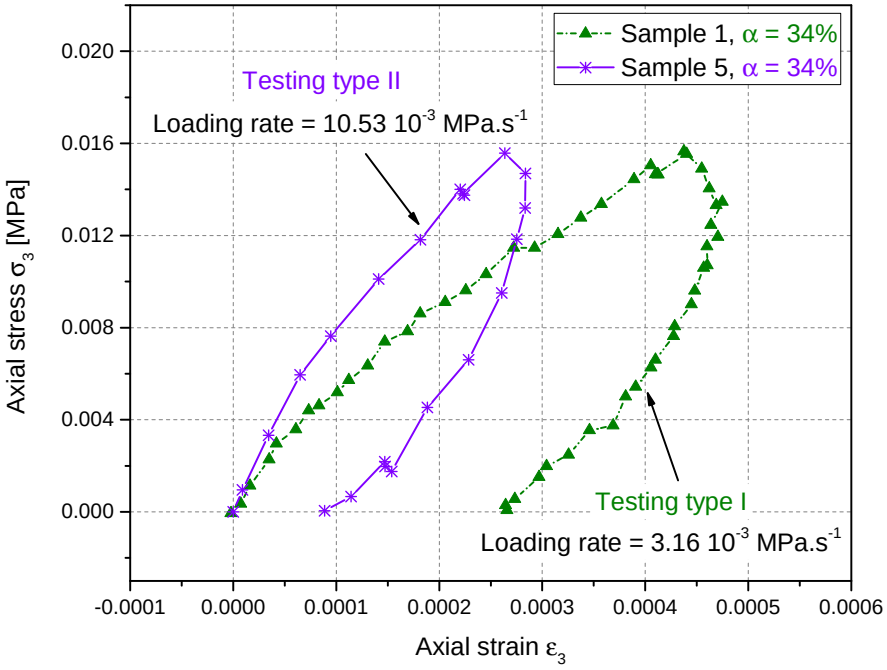

Figure 5.16: Response of the studied prepreg material to the compressive loading-unloading test with different rates of stress loading at $\alpha = 34\%$.

This qualitative analysis of loading-unloading curves and creep-recovery mechanical response of the material with degree of cure are however not sufficient to identify the rheological properties of the studied composite during the cure. It is therefore required to compare these interpretations with numerical data. Regarding the obtained experimental results, the rheological behavior of the material can be presumed as viscoelastic during the pregelation stage. The validity of this assumption is thereby investigated in next sections.

5.4 Modeling results and discussions

To exploit and further analyze the obtained experimental results, a rheological model for viscoelastic materials should be used to visualize the stress-strain relationship of the IMA/M21 studied prepreg. Creep-recovery tests were employed in order to identify the most suitable model to predict the material mechanical behavior and therefore to estimate the parameters of the appropriate rheological model and their evolution with cure.

5.4.1 Theoretical background: Brief reminders on creep behavior of viscoelastic materials

In this section, a number of one-dimensional linear viscoelastic models are presented. Viscoelastic materials have both viscous and elastic features, a bit like a fluid and a bit like a solid [212]. Mechanical models of viscoelastic behavior can be divided into appropriate models that describe rather viscoelastic solid behavior and polymeric viscoelastic fluid models. Creep behaviors of viscoelastic solids and fluids will be briefly reminded in next paragraphs, further details can be found in [212, 213].

Creep of a Solid Kelvin-Voigt Model

The kelvin-Voigt model consists of in parallel combination of spring that represents the linear elastic Hookean behavior with E_1 representing the elastic modulus of Kelvin–Voigt and dash-pot for the linear viscous behavior with a coefficient of viscosity η_1 as illustrated in figure 5.17-a. Given the parallel arrangement, strain experienced by the spring is the same as strain experienced by the dash-pot that can be denoted by $\varepsilon(t)$ leading to a constitutive law that can be expressed as a linear first - order differential equation by

$$\frac{d\varepsilon(t)}{dt} = \frac{\sigma(t) - E_1\varepsilon(t)}{\eta_1} \tag{5.11}$$

where $\sigma(t)$ is the total applied stress that represents the sum of stresses experienced in the spring and the dash-pot. The creep-recovery response of such model is given also in figure 5.17-a which shows that such model describes a material that undergoes viscoelastic reversible strain. Indeed, once stress is applied, a Kelvin - Voigt solid exhibits anelastic deformation due to the presence of spring whose elastic instantaneous stretching is rather held back by the presence of the dash-pot. After releasing the applied stress, the strain displays a delayed recovery. Thus, the entire deformation is recoverable with a Kelvin - Voigt system. The solution of the differential equation for an instantaneous stress step, of this model reads

$$\varepsilon(t) = \frac{\sigma(t)}{E_1}\left(1 - \exp(\frac{-E_1}{\eta_1}\ t)\right) \tag{5.12}$$

Creep of a Maxwell Model

The Maxwell model is usually used to describe viscoelastic fluid behavior and is obtained by adding a Newtonian dash-pot η_0 as Maxwell's coefficient of dynamic viscosity in series to linear spring represented by E_0 as Maxwell's elastic modulus. An illustration of Maxwell's model is depicted in figure 5.17-c together with the mechanical response to a creep-recovery

behavior predicted by this model. Once the material is loaded, an instantaneous extension takes place from the spring element E_0. During creeping, the mechanical response is ruled by an indefinite deformation from the dash-pot over time. When stress is removed, an elastic deformation is instantaneously recovered due to spring E_0 followed by a permanent strain resulting from viscous creep. Total strain during a creep loading is the sum of deformations of each element resulting in the following differentiating equation

$$\frac{d\varepsilon(t)}{dt} = \frac{1}{E_0}\,\frac{d\sigma(t)}{dt} + \frac{\sigma(t)}{\eta_0} \tag{5.13}$$

The creep behavior of Maxwell model can be then obtained as follows, for an instantaneous stress step:

$$\varepsilon(t) = \sigma(t)\left(\frac{1}{E_0} + \frac{t}{\eta_0}\right) \tag{5.14}$$

Creep of Standard Linear Solid or Zener Model

The standard linear solid (SLS), also known as the Zener model comprises a series arrangement of the Kelvin-Voigt model and a second Hookean spring defined as E_0 for the elastic modulus. A schematic representation of this model is illustrated in figure 5.17-b. As can be seen from this figure, solid viscoelastic behavior described by Zener model represents a material that undergoes an elastic and viscoelastic reversible strain. Instantaneous elastic deformation occurs once load is applied ruled by the linear spring E_0. At constant load, a delayed elasticity of the Kelvin unit takes place and strain will creep over time until the parallel spring E_1 carries all the applied stress. When the stress is suddenly removed, instantaneous strain recovery takes place due to the presence of linear spring E_0, then anelastic recovery occurs but no permanent strain remains in the material. The constitutive law of Zener model can be defined as a first - order linear differential equation by

$$\frac{d\varepsilon(t)}{dt} = -\frac{E_1}{\eta_1}\,\varepsilon(t) + \frac{1}{E_0}\,\frac{d\sigma(t)}{dt} + \frac{\sigma(t)}{\eta_1}\left(\frac{E_0 + E_1}{E_0}\right) \tag{5.15}$$

and the mechanical response to creep test can be described by the differential equation's solution defined by

$$\varepsilon(t) = \sigma(t)\left(\frac{1}{E_0} + \frac{1}{E_1}\left(1 - \exp(\frac{-E_1}{\eta_1}\,t)\right)\right) \tag{5.16}$$

Creep of a Burgers Model

Burgers model, presented in figure 5.17-d, is the most common and general creep model that describes in a better way the creep behavior of viscoelastic fluids. This model is a combination in series of a branch constituted by the Kelvin-Voigt model with the Maxwell unit. The total extension of a material submitted to a creep test is a sum of the Maxwell strain response and Kelvin-Voigt deformation. It is therefore a four-parameters model. The constitutive law can be then obtained by the differentiating equation as

$$\frac{d\varepsilon(t)}{dt} = \frac{1}{E_0}\,\frac{d\sigma(t)}{dt} + \frac{\sigma(t) - E_1\varepsilon(t)}{\eta_1} + \frac{\sigma(t)}{\eta_0} \tag{5.17}$$

where E_0 is the elastic modulus of Maxwell's element spring, η_0 is the viscosity of dash-pot element of Maxwell representing the residual viscosity, E_1 is the elasticity of spring element of Kelvin-Voigt and η_1 is the dash-pot element viscosity of Kelvin-Voigt. For a material subjected to a constant creep stress, the solution of this equation for an instantaneous stress step yields:

$$\varepsilon(t) = \underbrace{\frac{\sigma(t)}{E_0}}_{\text{Elastic}} + \underbrace{\frac{\sigma(t)}{E_1}\left(1 - \exp(\frac{-E_1}{\eta_1}\ t)\right)}_{\text{Viscoelastic behavior}} + \underbrace{\frac{\sigma(t)\ t}{\eta_0}}_{\text{Viscous flow}} \tag{5.18}$$

where $\varepsilon(t)$ is clearly the sum of a Maxwell model creep response and of a Kelvin-Voigt model. The parameter $\tau = \frac{\eta_1}{E_1}$ can be defined as the retardation time of the material. The total deformation is a combination of an instantaneous elastic stretching, a time-dependent recoverable deformation and irreversible flow. An illustration of the strain response of a viscoelastic Burgers material to a creep-recovery loading is given in figure 5.17-d. It clearly shows the main components of the mechanical behavior. Once the load is applied, a Burgers material exhibits an instantaneous elastic deformation which is then followed by a retarded elastic region with decreasing rate of strain as the Kelvin-Voigt component is extended. The third stage of the behavior evolution is a steady state of creep ruled by the Newtonian viscous deformation which continues to grow as long as the stress is applied. When the stress is removed, the Hookean elastic strain is instantaneously recovered. This stage is followed by the negative exponential recovery of the Kelvin-Voigt branch which controls the rate of strain recovery. The Newtonian deformation cannot be recovered indeed which explains the occurrence of permanent strain.

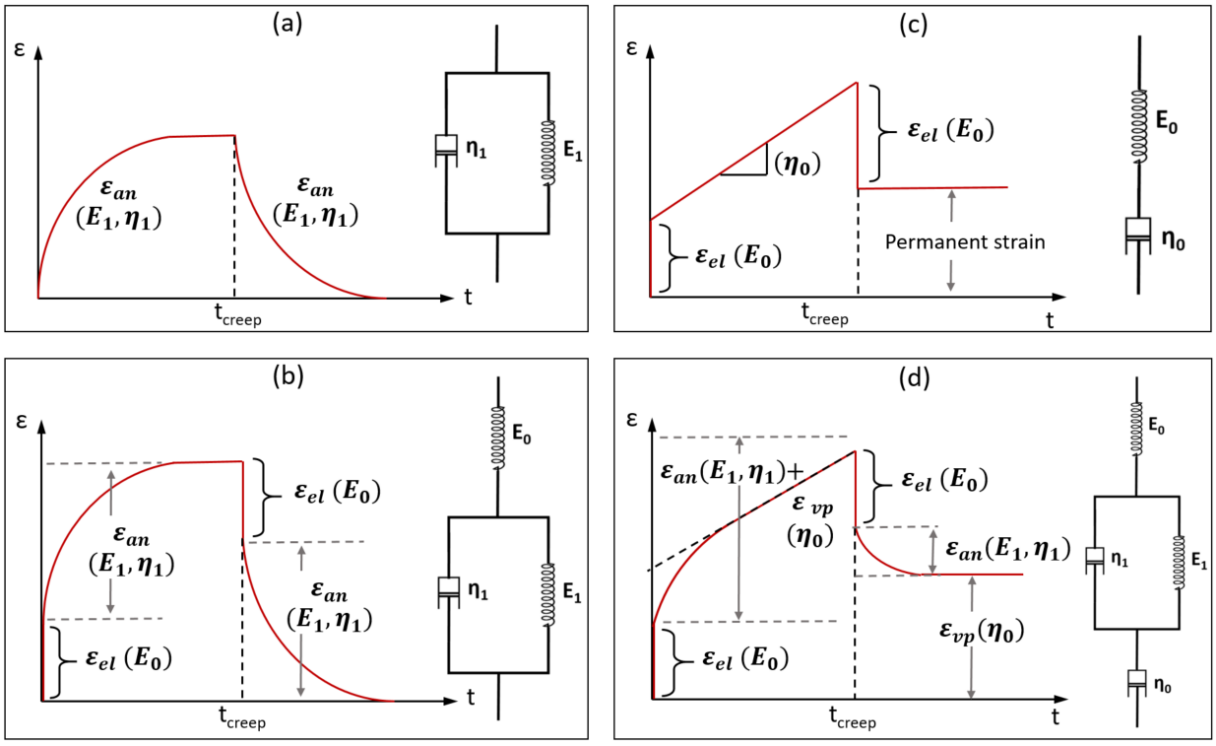

Figure 5.17: Viscoelastic models' responses to creep-recovery testing.

Based on the presented viscoelastic models in this subsection, and regarding the experimental measurements conducted on the studied IMA/M21 prepreg, it is evident that the behavior of the tested material given in figure 5.13 is in fact similar to the one described in figure 5.17-d. Therefore, the Burgers model seemed to be suitable to better predict the mechanical phenomena of the material response during the creep-recovery testing. An attempt to further understand the material rheological behavior during curing will be thereby carried out based on the analysis of the experimental results in comparison with the Burgers model commonly used for viscoelastic fluids.

5.4.2 Curve fitting and estimation of creep parameters of Burgers model during the cure

In order to predict the material behavior in terms of the degree of cure, the adopted strategy relies on identifying the rheological parameters of the Burgers model firstly by fitting the creep-recovery numerical response to experimental data for each degree of cure. The estimation of the model constants was carried out for all the applied creep-recovery cycles during the mechanical testing of sample 6. For each α, numerical fitting of experimental data was made using the Nonlinear Programming solver provided in MATLAB®'s Optimization Toolbox *"fmincon"* in order to identify the optimum four parameters. The material response was computed by solving the differential equation 5.17 for each creep-recovery loading cycle using the ODE15s solver in MATLAB with relative and absolute error tolerances of 10^{-8}. The distance function $\phi(E_0, \eta_0, E_1, \eta_1)$ was then calculated using a least square approximation as

$$\phi(E_0, \eta_0, E_1, \eta_1) = \frac{1}{N}\sqrt{\sum_{i=1}^{N}\left[\varepsilon^i_{num} - \varepsilon^i_{exp}\right]^2} \qquad \text{with } \varepsilon^i_{num} = \varepsilon^i_{num}(t_i, E_0, \eta_0, E_1, \eta_1) \tag{5.19}$$

The minimization of the defined residual between the experimental values (ε_{exp}) and the corresponding theoretical ones (ε_{num}) using Matlab minimization routine yields the estimation of optimized Burgers model constants for each degree of cure.

It should be noted that model parameters could be identified experimentally through the characteristic stages of creep detailed previously. Indeed, the instantaneous elastic strain ε_{el} occurred during the initial moment of loading could lead to the estimation of the experimental elastic modulus E_0 of Maxwell branch resulting from the Hook's law as illustrated in figure 5.17-d, in this case E_0 is given by

$$E_0 = \frac{\sigma}{\varepsilon_{el}} \tag{5.20}$$

In our case of testing conditions, during the loading step of 1.5s, there was rather an instantaneous resulting elastic strain coupled to the material viscous response. This could be explained by the retardation time related to the studied material which it appeared to be smaller or of a same scale as the loading application duration. Thus, it was difficult to accurately estimate the experimental pure instantaneous elastic deformation. Therefore,

the obtained strain during the first loading step will be hereinafter referred to us as "quasi-instantaneous" deformation. With the purpose of accelerating the fitting procedure, the initial guess of E_0 for each α was chosen as given by equation 5.20.

Moreover, the experimental value of Maxwell's coefficient of dynamic viscosity η_0 is inversely proportional to the slope of linear regression of the steady-state viscous flow, ε_{vp}, as

$$\eta_0 = \frac{\sigma}{\varepsilon_{vp}} \tag{5.21}$$

Thus, the initial guess of η_0 was estimated this way for the identification procedure for each α. The whole parameters that were estimated are brought in table 5.4 for further discussions.

An example of a comparison between the fitted data with Burger model and experimental results is given in figure 5.18.

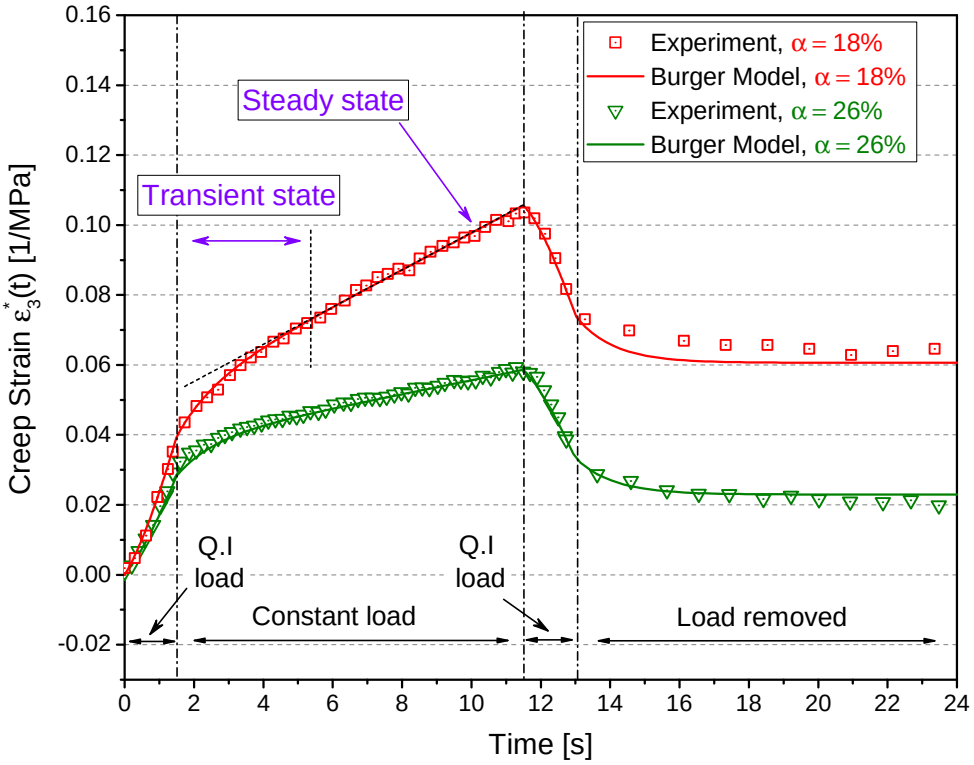

Figure 5.18: Comparison of experimental response to creep-recovery test with modeling results predicted by Burgers model at $\alpha = 18\%$ and $\alpha = 26\%$.

As the main objective is to mention the influence of cure degree on the mechanical behavior, the representative experimental curves of creep strains with time of sample 6 are normalized by the applied stress amplitudes (see equation 5.9) which are 4.6 10^{-3}MPa for $\alpha = 18\%$ and 8 10^{-3}MPa for $\alpha = 26\%$ gathered in table 5.4. The predicted curves by using Burgers model are drawn in solid lines. On the basis of a visual evaluation of the plots, a very good agreement between the prediction of Burgers model and the experimental data for each degree

of cure can be noticed. A very good consistency of simulated response with experimental one can be observed over both range of creep, primary and secondary ranges. The ˝quasi-instantaneous˝ deformation of the material is well predicted during the first step of loading. It can be seen that with α increase, the normalized strain is slightly reduced. The identified instantaneous Maxwell's Young modulus E_0 shows already a significant rise during the cure evolution from 42 MPa to 55 MPa which is in line with the elastic strain decrease. The prediction of the viscous-retarded elastic strain during the transient-state, as illustrated by figure 5.18 at $\alpha = 18\%$ shows also good agreement with experimental data. When the load is removed, further recovery takes place. The transient-state during recovery seemed to be well predicted by Burgers model at $\alpha = 26\%$ and a very slight discrepancy can be observed at $\alpha = 18\%$. The viscous response during the steady-state is well predicted by Burgers model and the identified values of Maxwell coefficients of dynamic viscosity show a significant rise with cure. At $\alpha = 18\%$ the estimated η_0 is almost 193 MPa.s whereas at 26% it reaches nearly 503 MPa.s. Such evolution is in fact coherent with the observed tendency in creep evolution with cure. The advancement of the crosslinking reaction during the isothermal hold at 160°C induces the increase of the material viscosity with cure which explains the decrease in the viscous flow during creeping with degree of cure. The resulting permanent strains are therefore decreased with the viscosity increase. As a conclusion from those two examples, Burgers' Model seems to provide an excellent agreement with our experimental results. This motivates a further global fitting of the material parameters evolution with α.

As previously mentioned, the identification procedure of Burgers model parameters was performed for every applied creep-recovery loading cycle. Since the investigation was limited to the pregelation stage of the material, the identification of model constants and therefore fitted data were compared to experimental results on the basis of 25 creep-recovery cycles of sample 6 response. In figures 5.19 - 5.23 are presented the overall fitted creep strains ε_3 with time under different stress levels. All applied stress values are gathered in table 5.4. Notice that, the mechanical strains for all applied stress levels never went beyond 0.1%, which confirms the small strains approach adopted in this study.

Visual evaluation of all curves presented in figures 5.19 - 5.23 first confirm that Burgers model is perfectly suitable for predicting the studied prepreg rheological behavior. Indeed, below 50% of cure degree, for every applied stress level, a very good consistency of computational characteristics with experimental data was achieved, notably for the first three stages of creep behavior, *i.e.*, ˝quasi-instantaneous˝ response, transient-state and pure viscous flow. The model predicted very well the ˝quasi-instantaneous˝ deformation to stress being applied. Once the applied stress is constant, fitted curves showed good agreement with experimental data for every stress level, and thus, for every α. During the transient-state, the predicted delayed elastic response also shows a very good consistence of viscoelastic retardation. Once the steady-creep state is reached, it can be observed that Burgers model simulations are well correlated to experimental data during the pregelation of material. As presented by the illustration in figure 5.17-d of Burgers model's fluid response, pure viscous deformation and permanent strain levels reached during recovery step are directly dependent on the Maxwell viscosity element.

When the load is removed, the recoverable elastic deformations are well estimated for all $\alpha \leq 49\%$, which is in line with the good prediction of the loading step both ruled by the linear spring E_0 and viscoelastic constants of Kelvin - Voigt branch E_1 and η_1. Through the recovery stage, we can notice some discrepancies between simulated and experimental data. In most cases, *i.e.*, most degrees of cure, the model seemed to well estimate the irrecoverable viscous deformation level reached at first instances when the applied stress is equal to zero. However, we can clearly find out that from $\alpha \geq 32\%$, experimental recovery is slower with a decreasing exponential type, and it seemed to never tend towards asymptotic values even on extended interval of time. It is true that the focus in these figures is rather made on creep responses for the sake of legibility, but the recovery stages were checked for longer scale of time beyond 50 seconds. It was noticed that, conversely to what previously discussed in subsection 5.3.4, strain rate never reached nil values during the whole interval of 100s. This can be attributed to the correction procedure of mechanical strains calculation. Chemical shrinkage subtraction, as discussed before, presents however possible source of error in the estimation of true strains evolution on larger scale of time. For this reason, more attention is rather given to the rheological behavior evolution during the creep stage which seemed well predicted by Burgers model. Moreover, during 11.5s, the assumption of constant degree of cure during loading remains valid since cure degree variation during this small amount of time is less then 3 10^{-3}. In practice, more weight was attributed to the early creep-recovery stage in the distance function $\phi(E_0, \eta_0, E_1, \eta_1)$ given by equation 5.19 as follows

$$\phi = \frac{1}{N}\sqrt{\sum_{i=1}^{N}\left[\varepsilon_{num}(t_i) - \varepsilon_{exp}(t_i)\right]^2 \cdot w(t_i)} \qquad (5.22)$$
$$\text{with } w(t_i) = 0.7 \cdot (t_i < \Delta t_{cycle}) + 0.3 \cdot (t_i \geq \Delta t_{cycle})$$

In view of the identified model parameters (see table 5.4) through the pregelation region, it is crucial to point out that the studied unidirectional prepreg clearly shows higher values of elastic modulus through the thickness direction compared to the neat matrix. Likewise, identified values of viscosity through the early stages of cure are far from being of the same order of magnitude of what is usually reported for neat resin which can be mainly explained by the presence of fiber in the material.

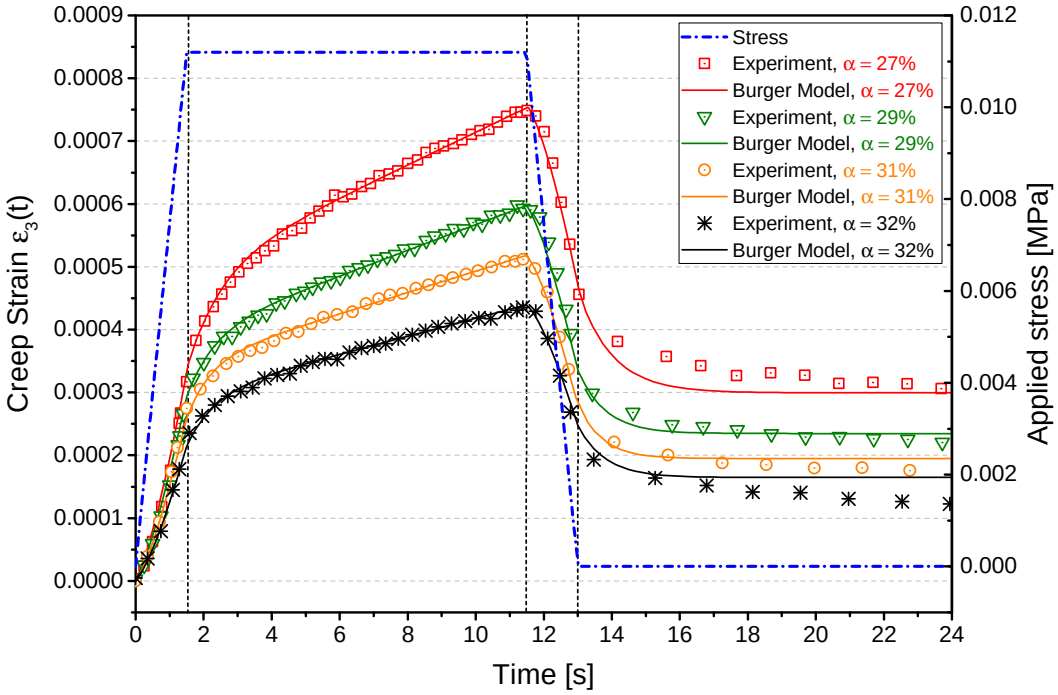

Figure 5.19: Comparison between creep-recovery experimental and fitted data predicted by Burgers model for an applied stress of 11 10^{-3}MPa at different α.

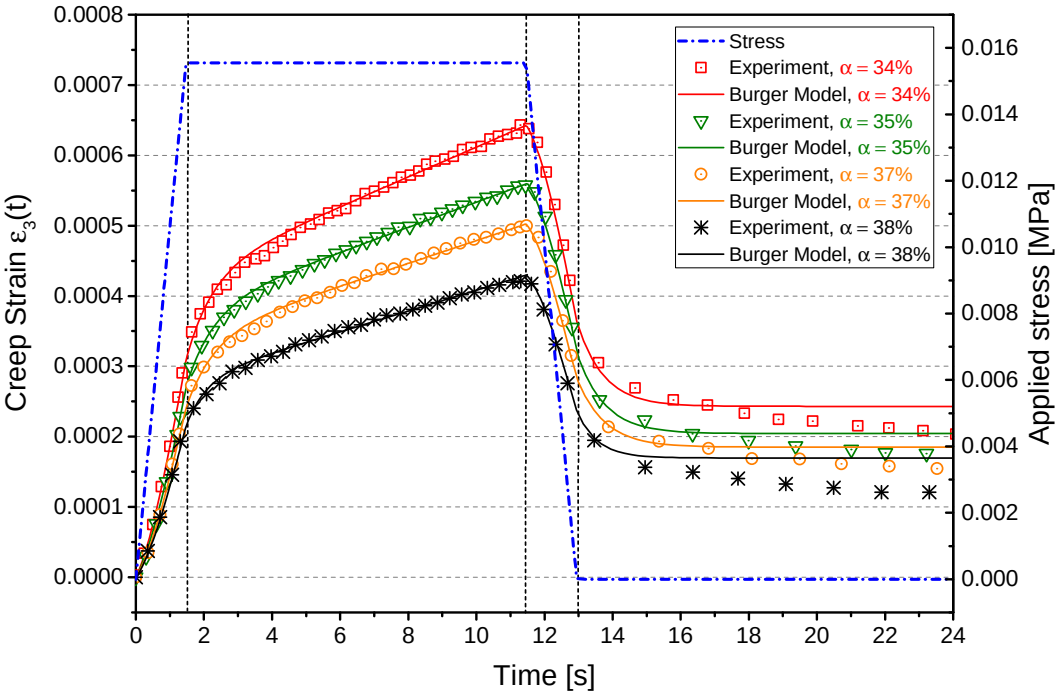

Figure 5.20: Comparison between creep-recovery experimental and fitted data predicted by Burgers model for an applied stress of 15.8 10^{-3}MPa at different α.

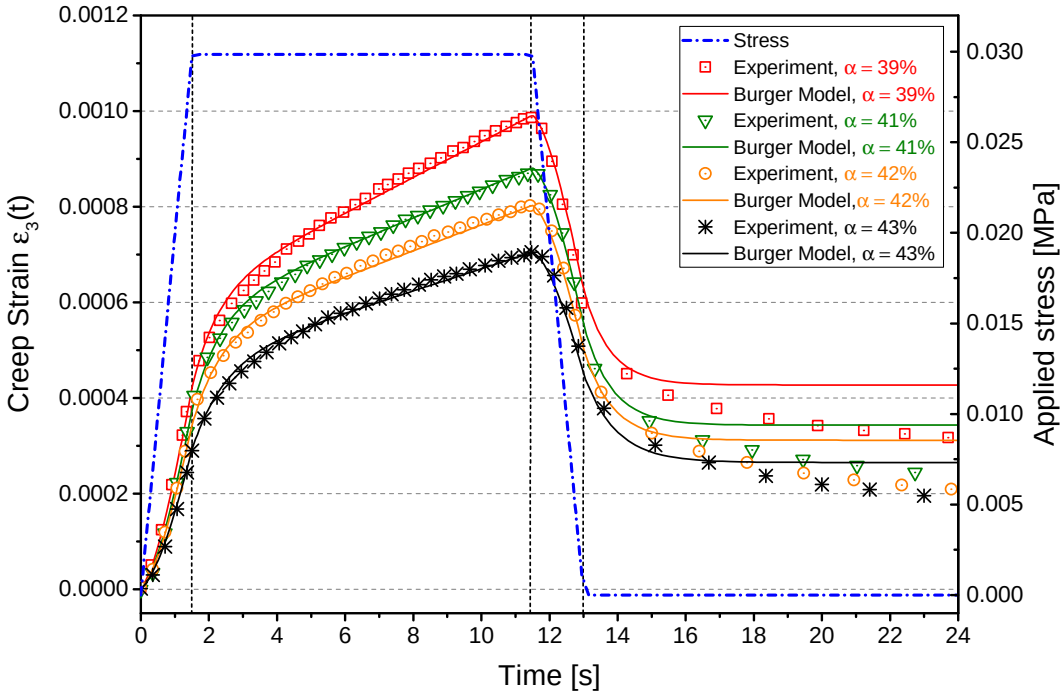

Figure 5.21: Comparison between creep-recovery experimental and fitted data predicted by Burgers model for an applied stress of 30 10^{-3}MPa at different α.

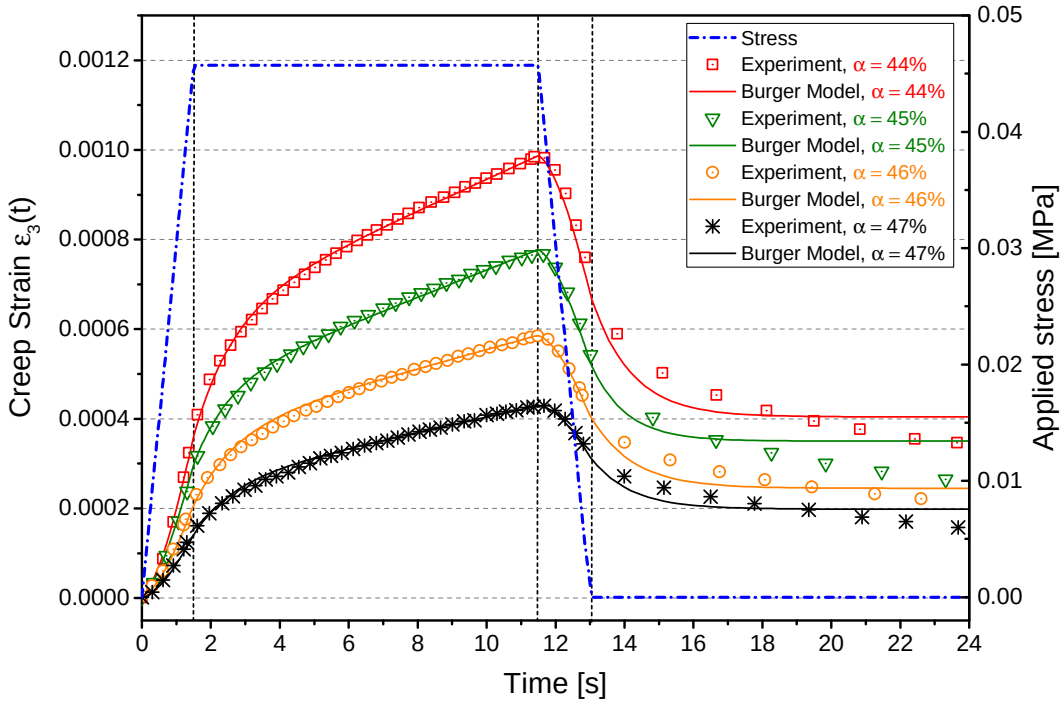

Figure 5.22: Comparison between creep-recovery experimental and fitted data predicted by Burgers model for an applied stress of 45.5 10^{-3}MPa at different α.

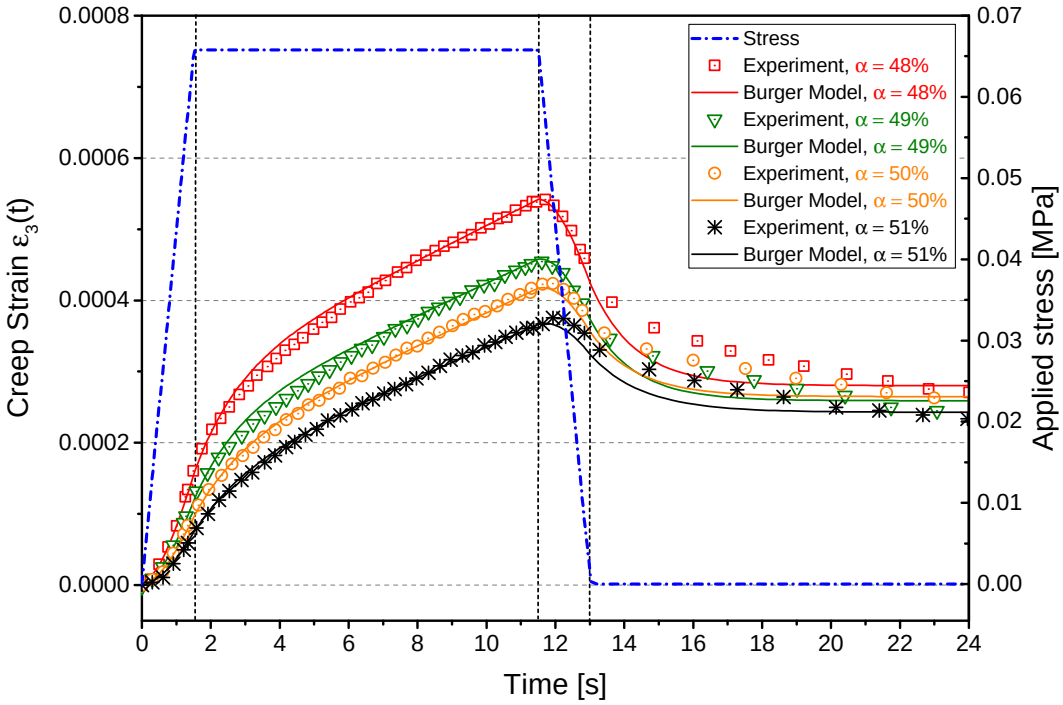

Figure 5.23: Comparison between creep-recovery experimental and fitted data predicted by Burgers model for an applied stress of 65 10^{-3}MPa at different α.

Figure 5.23 depicts the material mechanical response to creep-recovery when approaching gel point. The predicted plots of Burgers model show important disparities compared to experimental measurements. This mismatch is observed slightly in the model ability to predict the viscous-retarded elastic deformation when constant-load is applied. The model seems to relatively over-predict the material retarded strains but significantly during the recovery stage when stress is removed. Even an increase in experimental creep strains can be noticed during unloading step at α=51% leading to higher discrepancies compared to fitted data. This, unfortunately, is due to the induced errors resulted from low stiffness of the device piston when calculating the mechanical strains, as discussed in the previous subsection 5.2.3.

Table 5.4: Parameters of the Burgers model identified by curve fitting on the basis of creep-recovery test for each loading cycle during the cure.

σ_a $\times 10^{-3}$ [MPa]	α [%]	Burgers model parameters			
		E_0 [MPa]	η_0 [MPa.s]	E_1 [MPa]	η_1 [MPa.s]
4.6	16	37.3	80.2	24.2	28.7
4.6	18	42	192.5	40.8	43.9
8	20	46.6	45	18.9	27.1
8	24	48	315.4	47.6	41
8	26	55	502.7	53.1	58.3
11	27	64	443.5	39	39
11	29	72.5	548.4	50	40
11	31	100	650	49	34
11	32	109	781.3	61.2	49
15.8	34	109	734	57	44
15.8	35	122.7	891.2	66.2	52.8
15.8	37	145	951.8	69.1	55.5
15.8	38	171	1050	86.3	52
30	39	211.1	803.4	66.3	50.9
30	41	295	1000	65	53
30	42	290	1100.6	73.1	61.2
30	43	328.7	1301.3	82	76.6
45.5	44	389.8	1299.8	93	107
45.5	45	410	1500	135	135
45.5	46	701.1	2112.8	154	185
45.5	47	1286.4	2650	218.8	250
65	48	1680	2701	272.8	351
65	49	3000	2900	336.5	431.4
65	50	3500	2836.3	432.4	590.3
65	51	5776.6	3100	510	770.5

5.4.3 Sensitivity analysis of Burgers model parameters to a creep-recovery loading path

Now that model parameters are estimated during the pregelation stage of the material, the influence of creep parameters on the creep-recovery deformation is discussed in this subsection. Each parameter among the four parameters of Burgers model is studied individually for a better physical understanding of its impact on the creep behavior. The identified creep parameters for 31% of cure degree presented in table 5.4 are taken as a reference to compare the model response to each modification made to one parameter at a time. Therefore the parameter values are varied as per a "one-at-a-time" (OAT) sensitivity analysis to determine the incremental effect of each employed parameter. Doing so, each model parameter was var-

ied by ±20% and ±40% compared to the basic value identified at $\alpha = 31\%$. In figure 5.24 are depicted the "elementary effects" of each parameter on curve shape during a creep-recovery applied load.

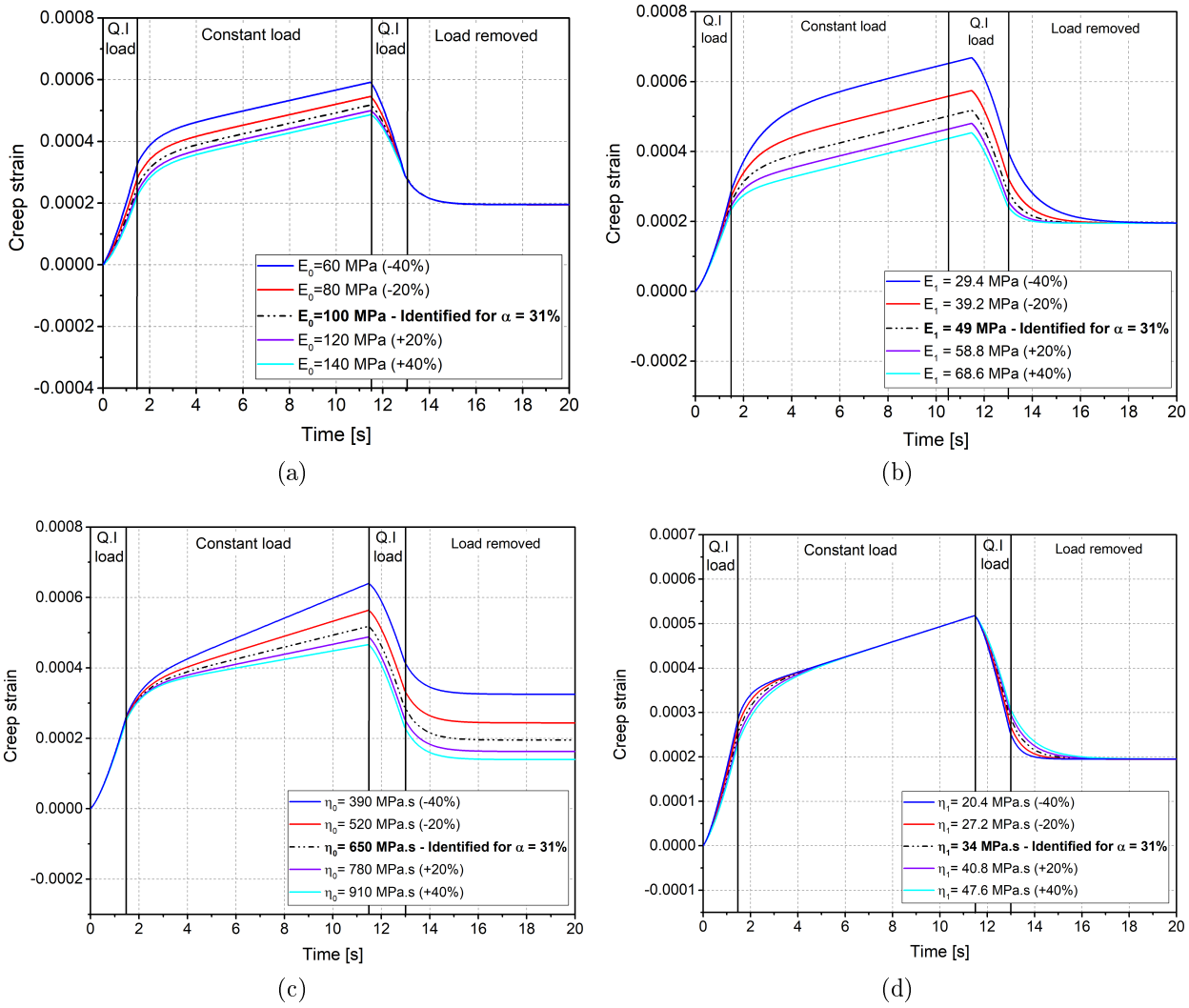

Figure 5.24: Sensitivity analysis of Burgers model parameters on creep-recovery response. (a) The influence of E_0. (b) The influence of E_1. (c) The influence of η_0. The influence of η_1.

Figure 5.24a illustrates the calculated curves resulted from the variation of the elastic modulus of Maxwell E_0 while keeping other parameters constants. It can be seen that E_0 mainly influences the instantaneous deformation during the "quasi-instantaneous" loading and unloading steps. Shape of curves are the same but with different instantaneous stretching. The lower is E_0, for example with a value of 60 MPa at -40% compared to the basic value of 100 MPa, the greater is the instantaneous strain during loading as well as for the recoverable elastic deformation.

Figure 5.24b shows the impact of the kelvin-Voigt elastic modulus E_1 on the creep-recovery response. When E_1 decreases, the instantaneous deformation remains the same. However, the greater impact can be seen on the final creep deformation amount. The smaller E_1, the highest is the level reached by creep strains. It can also be evident from this figure that the variation of E_1 values strongly affects the time during which the creep deformation rate stabilizes and the steady viscous state is reached. That is to say, since the viscoelastic deformation is ruled by the Kelvin-Voigt branch, E_1 has a significant impact on the retardation time of a material response and thus the delayed elastic deformation. The smaller the E_1, the longer it takes to creep deformation to stabilize.

Data in figure 5.24c suggest an illustration of the dynamic viscosity η_0 of Maxwell's branch influence on the creep-recovery strain response. During the ¨quasi-instantaneous¨ loading step, the mechanical behavior shows absolutely no visible variation due to the change in η_0 values. Once the applied load is constant, we can clearly notice how creep strain increases when η_0 gets smaller. This, is in fact, very predictable since Maxwell's viscosity constant is directly correlated to the pure viscous deformation part among the creep response. The slope of the steady viscous response mainly depends on η_0 values. It can be also noted from this figure, when the material is unloaded, that viscous deformations are not recoverable and permanent strain level reached at the end of the recovery step is dominated by Maxwell's viscosity parameter. The smaller the η_0, the higher are irreversible strains that remain in the material.

Figure 5.24d contains the calculated curves resulted from η_1 parameter variation. As it can be seen, the kelvin-Voigt viscosity constant seemed to have the minor effect on creep-recovery response. The induced influence of η_1 variation mainly affects the viscoelastic deformation part. It slightly influences the time when the creep strain rate stabilizes. The smaller η_1, the quicker it takes for the deformation to reach constant creep rate.

The sensitivity analysis could be performed in a more quantitative way in order to accurately assess the exact impact of each parameter on the model output. Applying the same sensitivity analysis strategy, the parameter values of each Burgers model constant are changed as per a ¨one-at-a-time¨ (OAT), by +10% from their nominal value that corresponds to the same identified creep parameters for 31% of cure degree. Thus, the values of other parameters remain the same each time the parameter in question is changed. Doing so, a sensitivity coefficient S^* is therefore calculated as follows

$$S^* = p_{nom} \frac{\partial \varepsilon}{\partial p} \tag{5.23}$$

where ε is the calculated strain as the model output, p is the parameter in question to be varied by +10% with respect to p_{nom} which is the input nominal value of Burgers parameter identified for a $\alpha = 31\%$.

Figure 5.25 depicts the evolution of the calculated sensitivity coefficients S^* which correspond to each Burgers model parameter. The induced influence of each parameter is presented as function of time during the whole applied stress of creep-recovery test. During the ¨quasi-

instantaneous" loading step, we can see from this figure that the elastic modulus of Maxwell's elements seemed to have the most significant impact on the "quasi-instantaneous" induced deformation. Strains are reduced by 10^{-4} for an increase of 10% of E_0. It appears that η_0 has the minor effect on strain response during this stage of loading whilst E_1 and η_1 have, additionally to E_0, a considerable impact on strain decrease during this step. When load becomes constant, sensitivity coefficient related to E_1 steeply drops to higher values inducing 2 10^{-4} of strain decrease through the first stages of creep before reaching a steady evolution along last instances of creep. Conversely, η_0 reveals a more significant effect on creep strains reduction during this stage. η_1, on the one hand, fairly contributes to strain decrease by impacting, mainly, the viscoelastic part of deformation through the first stages of creep. E_0, on the other hand, has barely no effect on strains evolution regarding the constant value of S^* while the applied stress is constant. During the removal of load, it can be noticed that the sensitivity coefficient related to η_0 no longer varies but has the most important impact on reached levels of permanent strain during recovery. E_1 appears to have particularly a great effect on the shape of the recovery curve since it controls the strain rate of the recoverable viscoelastic deformation as well as η_1 parameter.

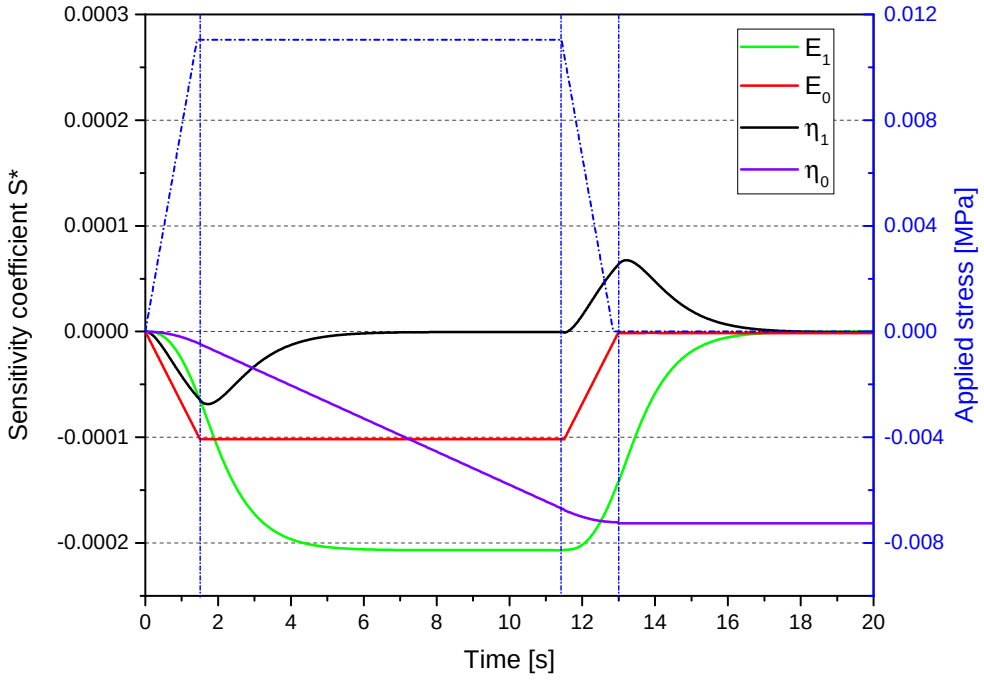

Figure 5.25: Sensitivity analysis of Burgers model parameters on creep-recovery response through sensitivity coefficient S^* evolution during an applied loading cycle. Each parameter was varied at a time by +10% from the nominal value identified for a $\alpha = 31\%$.

5.4.4 Parameters' evolution with cure and identification of the rheo-kinetic Burgers model

5.4.4.1 Behavior before the gel point

Up to this point, each identified set of parameters $[E_0,\ \eta_0,\ E_1,\ \eta_1]_{\alpha_i}$ of Burgers model, considered as constant coefficients, represent the best values to predict the behavior of the studied IMA/M21 prepreg during creep for a given degree of cure α_i at the time instant "i". However, to elaborate a model that allows to predict the rheological behavior during the pregelation stage, it is necessary to take into account the effect of the degree of cure in the physical model. For this purpose, an idea of searching functional dependencies for Burgers model parameters as a function of the polymerization degree has been proposed. Therefore, in figure 5.26, are displayed the identified values of parameter η_0 corresponding to each cure degree utilizing the results compiled in table 5.4. Moreover, the applied stress levels during the pregelation phase are also given in this figure to illustrate the evolution of load amplitude with the degree of cure. It can be noticed that η_0 increases with the polymerization reaction progress until the gelation of the material. An exponential regression was proposed to find the best fit of the set of values of η_0 as depicted in figure 5.26 and marked by dashed line.

Results are globally satisfactory with a R-squared (R^2) variance of 95.2%. It can be observed in this figure that $\eta_0(\alpha)$ presents a particular evolution trend with respect to the applied stress amplitude. As it can be seen, with every enhancement in the stress level, a steep drop in the viscosity value occurred. The illustrated blue arrows are introduced in order to indicate the increment of stress performed each time. The increase of η_0 with the degree of cure is clearly evident when the applied stress is unvaried. As an example, under a performed stress level of 11 10^{-3}MPa from $\alpha = 27\%$ to 32%, η_0 increases from 443.5 MPa.s to 781.3 MPa.s. Nevertheless, once the stress amplitude evolved to 15.8 10^{-3}MPa, despite of the continuous increase in the degree of cure, the dynamic viscosity η_0 declined to 734 MPa.s. Nearly the same phenomenon is repeated at every increment of stress amplitude. However, from a degree of cure of 44%, when the material state gets closer to the gelation, it can be noticed that the viscosity growth accelerates rapidly and the identified values of η_0 before and after each increment of stress amplitude denoted as σ_a^6 and σ_a^7 remain fairly unvaried. It could be assumed that the dynamic viscosity of Burgers model revealed a strong dependency to the applied stress level which cannot be further examined in this study nor taken into account in the physical model of the studied prepreg. Besides, such effect of applied stress level on the viscosity could explain the observed discrepancies of the identified numerical values compared to the proposed exponential regression. A more complex model might indeed be necessary.

Figure 5.27 plots the identified moduli of elasticity E_1 and E_0 with the degree of cure. It can be seen that both moduli growth begins slowly through the first stages of curing and then accelerates sharply when the gelation region of the material comes closer. Exponential regressions were thereby employed to predict the evolution of both parameters in terms of α. As a way of comparison with the dynamic viscosity parameter η_0, we can observe an important similarity in the variation of E_1 with the applied stress level below 40% of cure degree. Conversely, the elastic modulus E_0 evolution does not reveal any further correlation with stress levels.

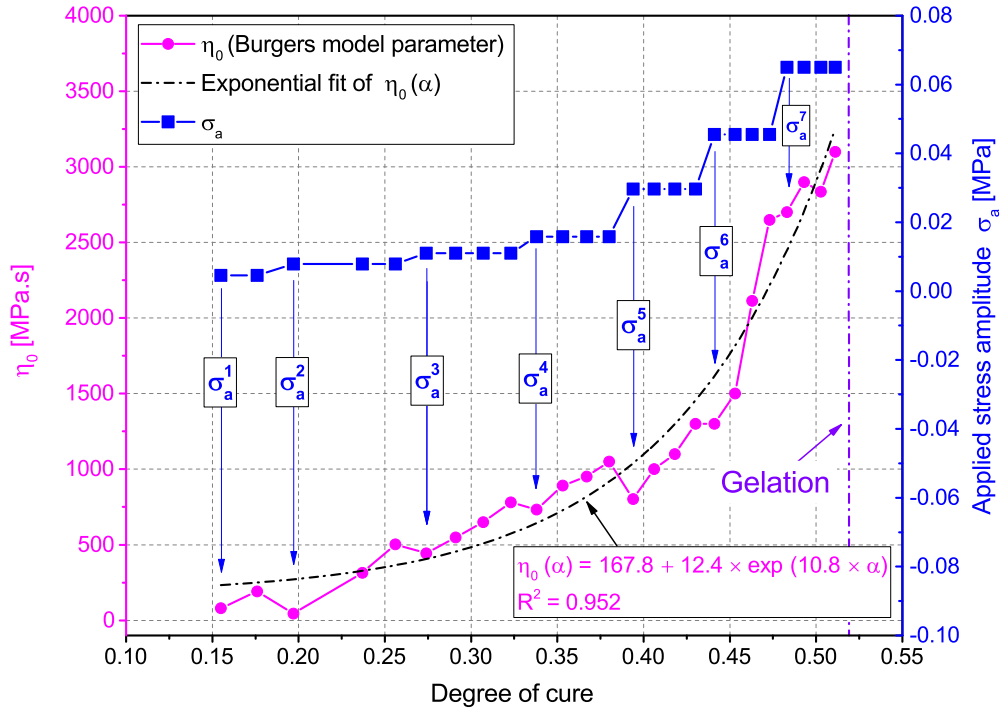

Figure 5.26: Plot of a proposed regression dependency for dynamic viscosity $\eta_0(\alpha)$ of Maxwell branch for the Burgers model as an exponential function of degree of cure.

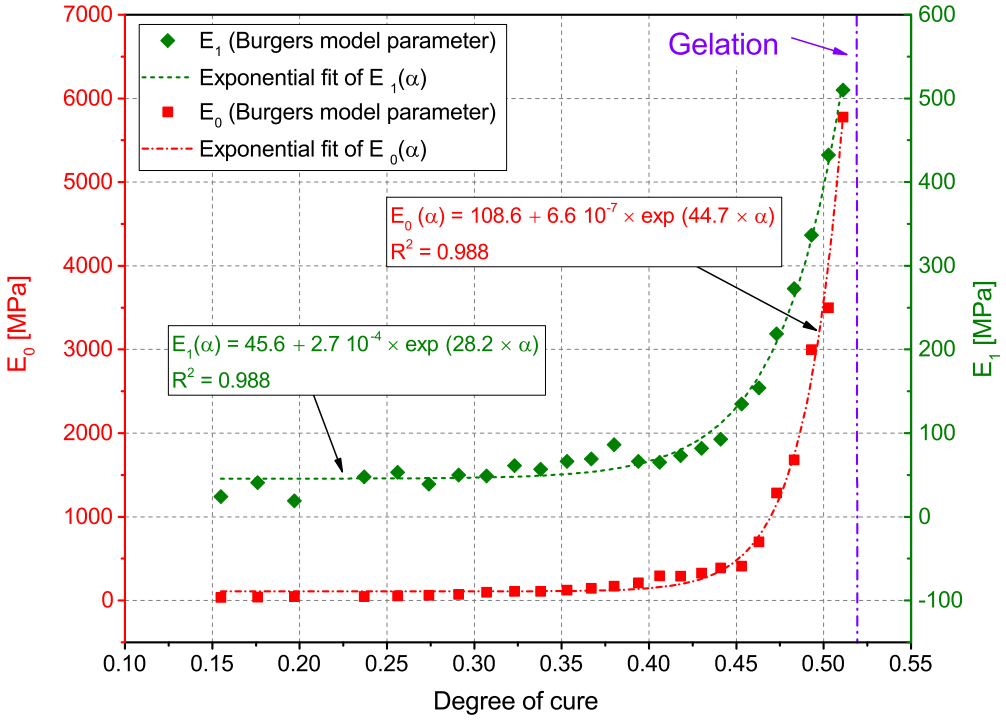

Figure 5.27: Plots of proposed regression dependencies for modulus of elasticity of Maxwell branch $E_0(\alpha)$ and relaxing response $E_1(\alpha)$ for the Burgers model as exponential functions of cure degree.

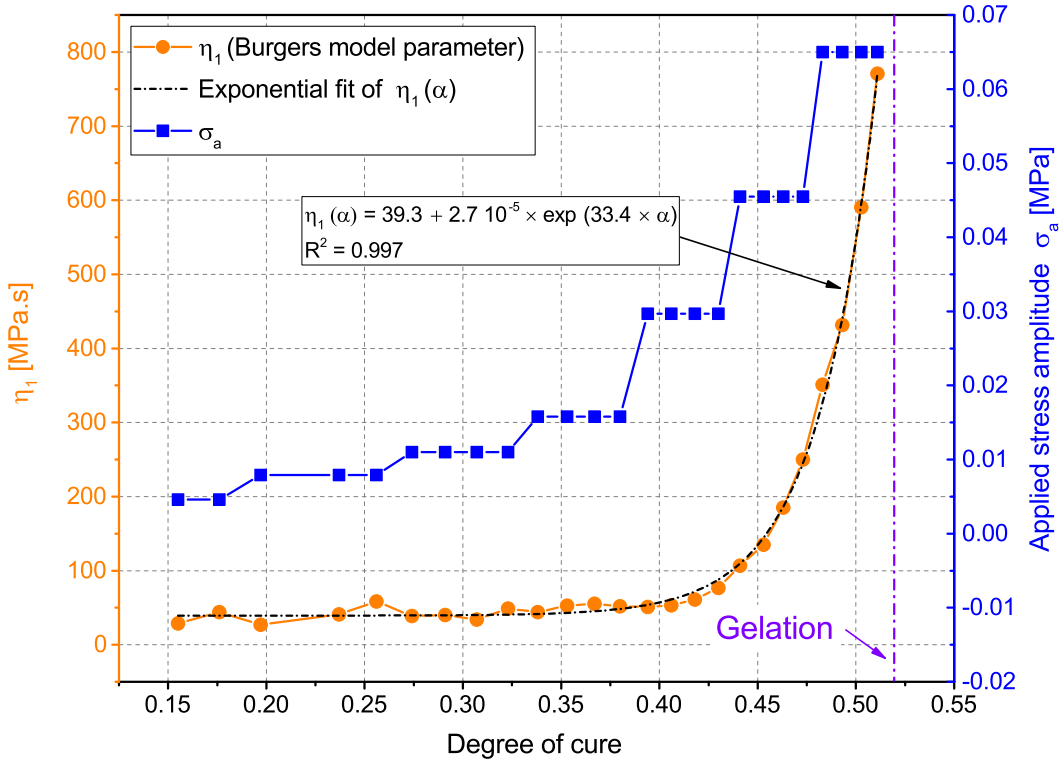

Figure 5.28: Plot of a proposed regression dependency for dynamic viscosity $\eta_1(\alpha)$ of Kelvin-Voigt branch for the Burgers model as an exponential function of degree of cure.

The identified values of the dynamic viscosity η_1 related to Kelvin-Voigt dash-pot are represented as function of cure degree in figure 5.28 altogether with the applied stress amplitudes (σ_a^i). The same evolution trend with cure was observed for η_1 which remains below 100 MPa.s before gelation. A sharp increase can be noticed from $\alpha = 45\%$ and the value of η_1 becomes approximately eight time higher at the gelation of the material. An exponential function was identified to fit η_1 evolution with cure degree. Again, stress level effect on the values of η_1 is questioned. However, the inspection of this figure cannot strictly reveal whether the dynamic viscosity η_1 exhibits a stress dependency. Indeed, during the first stages of cure a slight similarity in the variation of η_1 can be visible much the same as E_1 and η_0. Once the cure degree exceeds 40%, it becomes quite difficult to evaluate the influence of applied stress on η_1 evolution with cure.

Assuming a level of stress as an independent variable, the proposed regression dependencies on the degree of cure of Burgers' four parameters are given by equation 5.24 where the coefficients of each exponential regression are gathered in table 5.5.

$$\begin{cases} \eta_0(\alpha) &= a_{01} &+ a_{02}\exp\left(a_{03}\times\alpha\right) \\ E_0(\alpha) &= b_{01} &+ b_{02}\exp\left(b_{03}\times\alpha\right) \\ \eta_1(\alpha) &= a_{11} &+ a_{12}\exp\left(a_{13}\times\alpha\right) \\ E_1(\alpha) &= b_{11} &+ b_{12}\exp\left(b_{13}\times\alpha\right) \end{cases} \tag{5.24}$$

Table 5.5: Coefficient values of the exponential regressions given by equation 5.24.

Coefficients of exponential regression	a_{01}	a_{02}	a_{03}	R^2
Values	167.8	12.4	10.8	0.952
Coefficients of exponential regression	b_{01}	b_{02}	b_{03}	R^2
Values	108.6	$6.6\ 10^{-7}$	44.7	0.988
Coefficients of exponential regression	a_{11}	a_{12}	a_{13}	R^2
Values	39.3	$2.7\ 10^{-5}$	33.4	0.997
Coefficients of exponential regression	b_{11}	b_{12}	b_{13}	R^2
Values	45.6	$2.7\ 10^{-4}$	28.2	0.988

5.4.4.2 Behavior beyond the gel point

Since the investigation of the mechanical behavior of the studied composite was limited to the pregelation region, an attempt to explore the experimental measurements after gelation was made. In fact, figure 5.29 represents a zoomed portion of plots that was already depicted in figure 5.11 in order to give greater focus to the induced errors on the mechanical response after gelation.

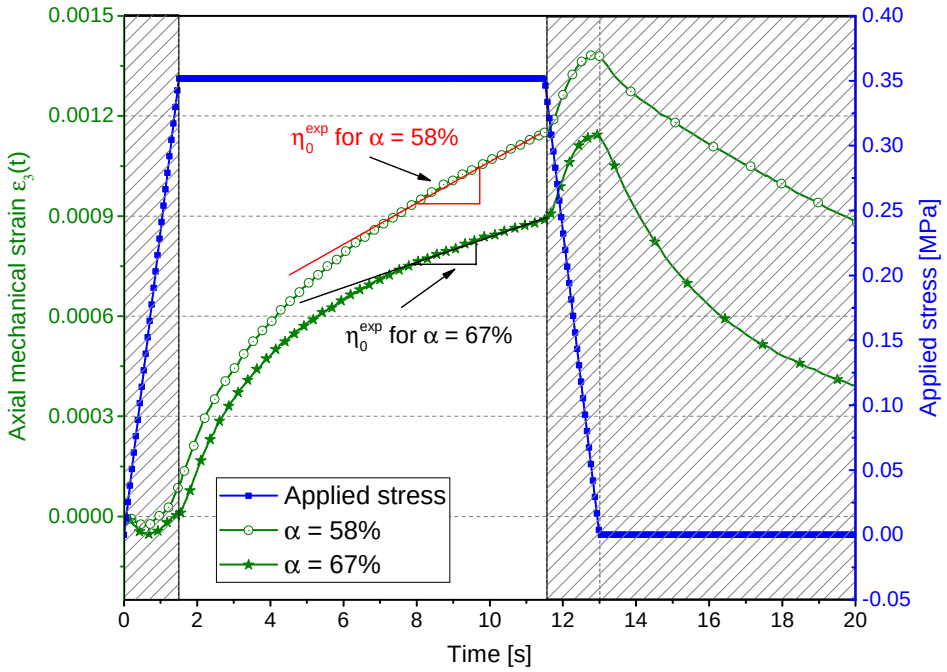

Figure 5.29: Measured axial strains of sample 6 after gelation.

Axial mechanical strains are presented in this figure and were calculated on the basis of sample 6 measured displacements for a $\alpha = 58\%$ and a $\alpha = 67\%$. It can be seen that during both "quasi-instantaneous" loading steps the material mechanical response is no longer exploitable, neither is it during the recovery stage. Nevertheless, the creep deformation illustrated by the non hatched area was analyzed since no possible errors can be included related to the machine displacements because of the constant applied load. Doing so, the experimental viscosity values denoted as η_0^{exp} after gelation were calculated on the basis of the linear regression's

slope of the steady state of creep (according to equation 5.21) as illustrated by this figure. Consequently, it was possible to have a broaden overview of η_0 evolution through the entire curing. Since the studied material remains in the rubbery state during the whole testing, the assumption of having a viscoelastic fluid behavior after gelation is still valid. The measured values of η_0^{exp} are reported in figure 5.30. The identified numerical constants of η_0 denoted here as η_0^{num} together with the proposed exponential fit of $\eta_0(\alpha)$ (referred here by $\eta_0^{num}(\alpha)$) marked by solid line are also presented along the total isothermal hold at 160°C. The results from extrapolation of obtained regression dependency of $\eta_0^{num}(\alpha)$ are marked by broken line.

Before gelation, calculated values of η_0^{exp} are very similar to η_0^{num} identified with Burgers model. These experimental values were employed as initial guesses in the identification process of the model parameters as mentioned in subsection 5.4.2. After gelation, it can be observed that η_0^{exp} growth accelerates rapidly with cure advancement. Notice that, blue arrows are introduced to indicate the stress amplitude increments performed each time. It is clear that η_0^{exp} shows the same dependency to stress as η_0^{num} before gel point. Once the material reached gelation, the effect of applied stress on η_0^{exp} is omitted and becomes more obvious with the extended evolution with cure in this region to confirm the observations already made on the basis of η_0^{num}. Indeed, as an example, the applied σ_a^8 is almost more than two times higher (equal to 150 10^{-3}MPa) than the applied σ_a^7 (equal to 65 10^{-3}MPa) which clearly does not induces any further effect on the material behavior. η_0^{exp} maintains the same growth trend to reach 10^4 MPa.s at the end of the isothermal dwell which is almost more than three times higher than the estimated values before gelation. We can observe that the extrapolated fit under-predicts the viscosity evolution with cure after $\alpha = 58\%$.

Indeed, stress independent behavior revealed by the evolution of η_0^{exp} beyond gel point on the contrary of the observed trend before gelation, suggests once again the need to investigate the applied stress impact on the rheological behavior of such composite along the whole cure cycle. Further investigations are still needed to elucidate the potential non-linear rheological behavior of this material. For now, only regression dependence on cure will be considered in this study as presented by equation 5.24 by assuming applied stress level as an independent variable.

5.4.4.3 Rheo-kinetic Burgers model

On the basis of the identified equations of the four parameters evolution with cure a coupled rheo-kinetic Burgers model was developed to include the degree of cure effect on the rheological behavior. In order to do so, the following differential equation was solved again in a MATLAB routine

$$\frac{d\varepsilon(t,\alpha)}{dt} = \frac{1}{E_0(\alpha)}\frac{d\sigma(t)}{dt} + \frac{\sigma(t) - E_1(\alpha)\varepsilon(t)}{\eta_1(\alpha)} + \frac{\sigma(t)}{\eta_0(\alpha)} \tag{5.25}$$

together with corresponding kinetic equation 2. (in chapter 2). Please notice that thanks to the different characteristic times, their solving can be largely uncoupled for the duration of a single mechanical test.

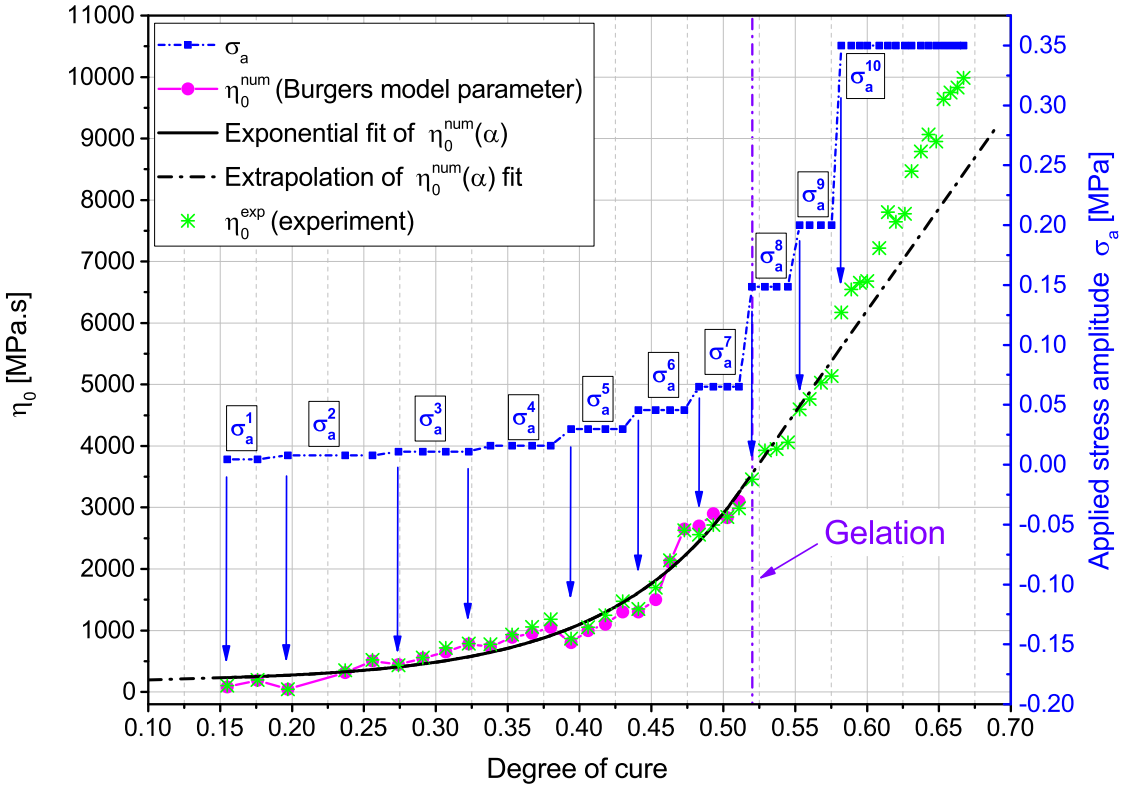

Figure 5.30: Plots of the exponential regression of the numerical viscosity $\eta_0^{num}(\alpha)$ together with calculated experimental values η_0^{exp} as function of cure degree along the whole isothermal curing.

Therefore, the mechanical response of a material subjected to a constant creep stress for a given degree of cure can be estimated by, as it will be termed for the following section, the "rheo-kinetic Burgers model" equation given by

$$\varepsilon(t,\alpha) = \frac{\sigma(t)}{E_0(\alpha)} + \frac{\sigma(t)}{E_1(\alpha)}\left(1 - \exp(\frac{-E_1(\alpha)}{\eta_1(\alpha)}\ t)\right) + \frac{\sigma(t)}{\eta_0(\alpha)}\ t \tag{5.26}$$

where $E_0(\alpha)$, $E_1(\alpha)$, $\eta_0(\alpha)$ and $\eta_1(\alpha)$ are estimated according to equation 5.24 and table 5.5.

5.5 Verification of the rheo-kinetic Burgers model predictions

It is now crucial to validate the applicability of the "rheo-kinetic Burgers model" given by equation 5.26, by comparing the theoretical predictions of the model with the experimental results.

5.5.1 Creep-recovery test

The creep-recovery test is firstly taken as example for comparison. Data in figure 5.31 illustrate the evolution of experimental calculated creep strain with time for four degree of cure : 29%, 39%, 43% and 46%. Axial creep strains were normalized by the applied stress amplitudes which can be found in table 5.4. Predicted data with the model are presented with solid lines. On the basis of a visual evaluation of plots, it can be noticed that the obtained simulated curves show a very good fit to the experimental data. For more legibility, the analysis of the obtained creep curves will be performed by probing each creep region response separately in order to examine the predictability of the model with cure degree. During the first step of loading, the inspection of experimental and numerical ¨quasi-instantaneous¨ deformations reveals a good fitting for the four levels of cure degree. $E_0(\alpha)$ is indeed a good estimate. The retarded elastic region related with Kelvin-Voigt unit are well predicted by the rheo-kinetic model except some discrepancies that appear for $\alpha = 29\%$ and $\alpha = 39\%$. The overestimation of the viscous-retarded elastic deformation could be explained by the under-prediction of the retardant elasticity E_1 by the model that presents a relative error of -4.6% with regard to the identified value in this case. During the steady-state viscous flow region, it can be observed that modeling curves show a satisfactory agreement with experimental data. Indeed, the estimation of the parameter η_0 by the rheo-kinetic model could represent significant errors since it revealed very sensitive to the applied stress. The example illustrated for $\alpha = 43\%$ shows an important variance in the estimation of the creep strain and it can be evident from this curve that the viscosity was however over-predicted by the rheo-kinetic model. Such disparity is nevertheless inevitable since the model does not take into account the applied stress effect on the viscosity evolution which was not explored in this study. Model simulations of the recovery response of the material are globally well correlated to the experimental data.

5.5.2 Loading-unloading test, denoted as test I

The rheo-kinetic Burgers model has also to be tested under other kinds of paths. Thus, it was additionally employed to predict the material behavior when submitted to other mechanical testing as an applied quasi-static compressive loading-unloading test. Therefore, experimental results obtained according to test I are illustrated in figure 5.32 as an average curve calculated on the basis of the mechanical response of four tested samples 1 - 4. As to mention the influence of degree of cure on the material behavior, strains were normalized by the applied stress. Two levels of degree of polymerization were chosen, 29% and 43%, in order to examine the mechanical response as function of cure. The simulation of the mechanical behavior with the rheo-kinetic Burgers model was performed by estimating parameters values according to equations 5.24 for a given degree of cure assumed constant during the testing duration of a given loading cycle. The constitutive law obtained by the differential equation 5.25 is therefore solved for the obtained set of parameters. The resulting model curves for each cure degree are plotted with dashed lines in this figure. It is evident that the investigated material indicates a large variability resulting in such scattered behavior. The influence of cure degree is fairly clear on the mechanical behavior. At higher cure degree, it can be observed that induced strains levels are quite lower with the enhancement of the material stiffness. When unloaded stress reached to zero, the material irrecoverable strain level

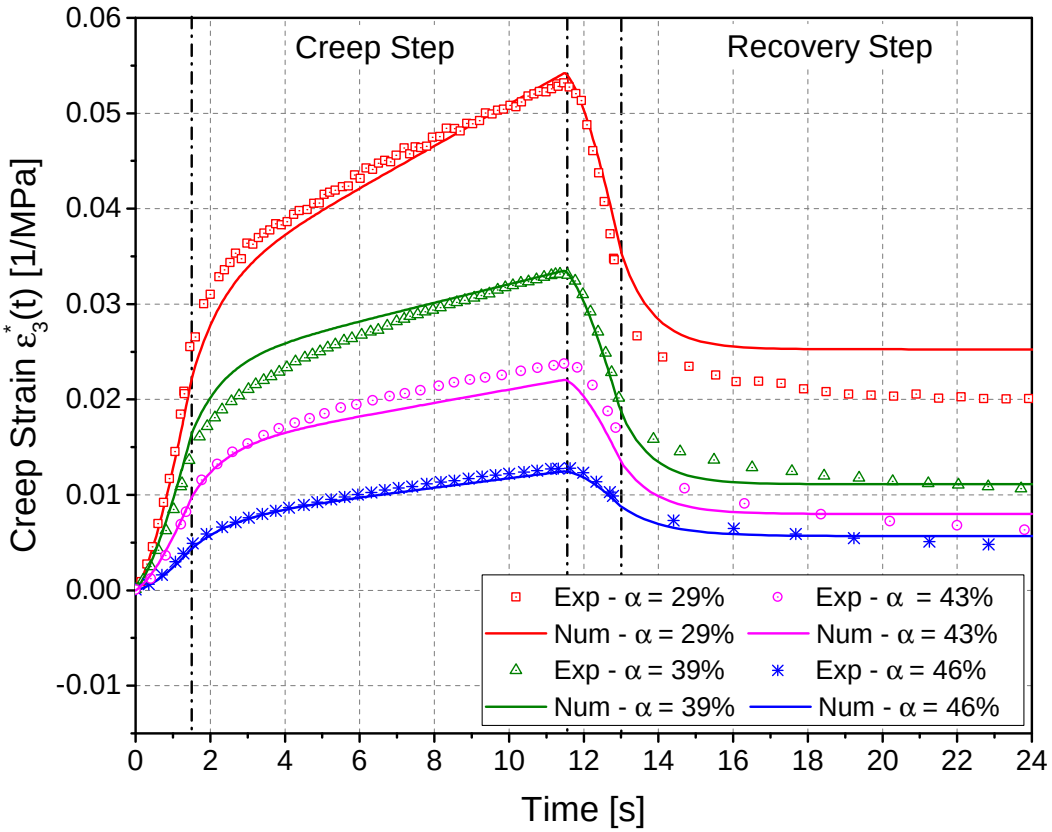

Figure 5.31: Comparison between the experimentally determined creep-recovery behavior with those calculated according to rheo-kinetic Burgers model for different degrees of cure. Experimental results were obtained from sample 6 testing according to test III.

became smaller with cure degree advancement. The model shows a good consistency with the average calculated strains for both degrees of cure. Although the material variability, it can be noticed that the calculated error bars overlap the model fit along the whole mechanical test. During the loading step, the material viscoelastic deformation is well predicted. Through the unloading step, the model showed a satisfactory agreement in predicting strain levels displayed at the end of each applied stress cycle.

In order to gain more insights into the material behavior submitted to the described loading path above, the influence of model parameters on the resulting strains are shortly discussed. To do so, the sensitivity coefficient S^* was calculated according to equation 5.23 by employing the same analysis strategy based on (OAT) method. The predicted parameters by rheo-kinetic Burgers model for $\alpha = 29\%$: $E_0(\alpha = 0.29)$, $E_1(\alpha = 0.29)$, $\eta_0(\alpha = 0.29)$ and $\eta_1(\alpha = 0.29)$ were assumed as nominal values. The parameter in question was varied by $+10\%$. The same simulated strains at $\alpha = 29\%$ as in figure 5.32 can be found in figure 5.37 with rather axial strain ε_3 evolution with time.

In figure 5.33 is depicted the evolution of the calculated sensitivity coefficients with time for each parameter during an applied cycle of loading-unloading stress of type I. It can be seen from this figure, when compressive stress is applied forward, the material strain response is

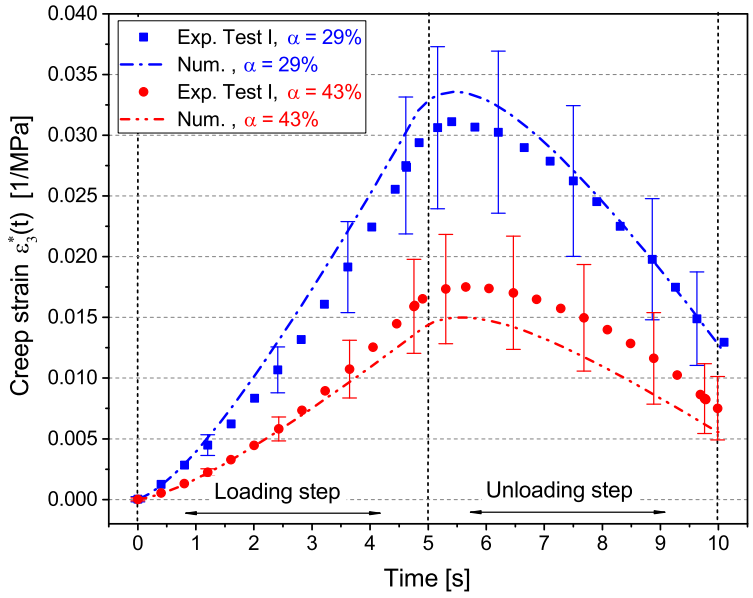

Figure 5.32: Axial average normalized strains ε_3^* for a loading-unloading applied stress performed on samples [1 - 4] according to test I. Superimposition of the response of the rheo-kinetic Burgers model for two levels of cure degree with experimental data.

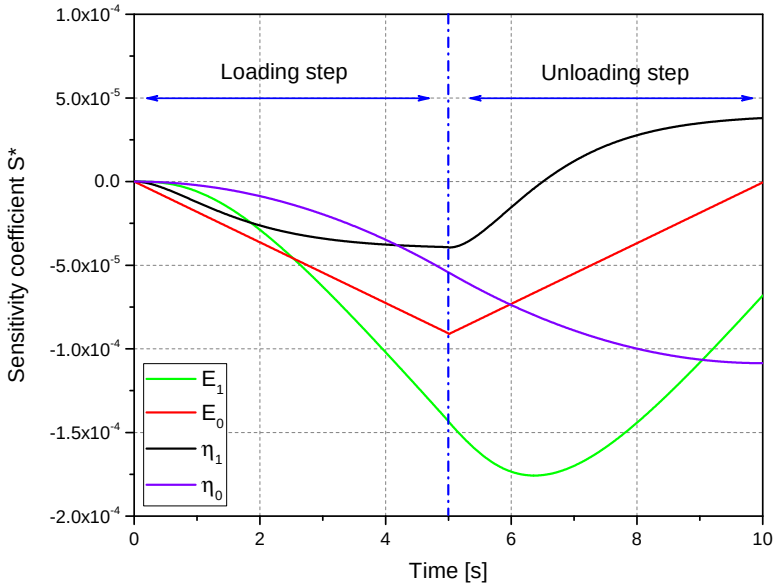

Figure 5.33: Sensitivity analysis of rheo-kinetic Burgers model parameters on loading-unloading response through sensitivity coefficient S^* evolution during an applied loading cycle at $\alpha = 29\%$ according to test I.

initially controlled by E_0 until almost t = 2.6s with a sensitivity coefficient of approximately -5 10^{-5}. Afterwards, more viscously retarded elastic deformation appears and the impact of E_1 becomes more dominant on the resulting strain. When the material is unloaded, strain response in mainly influenced by both elastic moduli E_0 and E_1 with a sensitivity close to 10^{-4}. Irrecoverable strains are reached when stress is nil and are significantly controlled by the

Young modulus E_1 and, with lesser impact, induced by viscosity related parameters η_1 and η_0. As it can be seen from figures 5.26, 5.27 and 5.28, the scattering between identified parameters and proposed exponential regressions with cure is rather very weak at $\alpha = 29\%$. This example could ascribe the origin of presented inconsistency between experimental data and fitted curves mainly to the material variability. At $\alpha = 43\%$, exponential regressions reveal some disparities with model parameters, especially for E_1 and η_0 which could induce more possible sources of error between experimental strains measurements and modeled response of testing I at 43% of cure degree.

5.5.3 Loading-unloading test, denoted as test II

Results obtained from testing II performed on sample 5 to investigate the effect of loading rate on the mechanical behavior are also employed in this section to probe the predictability of the rheo-kinetic model. Mechanical strain response of sample 5 obtained under the same applied σ_a for samples [1-4] testing at the same degrees of cure 29% and 43%, are presented in figure 5.34 as a way of comparison with figure 5.32. Strains are normalized by the applied stress levels (see table 5.1). The predicted response of a material subjected to the compressive loading-unloading stress is given by the numerical strains evolution with time as illustrated in figure 5.34. As evident from this figure, the viscoelastic rheo-kinetic model permits to correctly predict the mechanical response of the IMA/M21 prepreg with cure for different applied stress rates. The loading region is well reproduced by the model except some slight disparities that appear at 43% of cure degree. Numerical strain levels reached during the forward loading indicate a very good fitting with experimental measured strain. During unloading, model prediction reveals minor deficit in estimating strains evolution with time. At 29% of cure degree, the model seems to over-predict the viscoelastic unrecoverable strains. Anyways, this new test reveals here again the very good predictability of our model for several loading types and all over the curing process, at least below gelation.

The sensitivity analysis of the rheo-kinetic Burgers model was performed to assess in more reliable way the influence of each parameters on the model response to the mechanical testing II. As described previously, the sensitivity coefficient S^* was calculated according to equation 5.23 by employing the (OAT) method and considering $E_0(\alpha = 0.29)$, $E_1(\alpha = 0.29)$, $\eta_0(\alpha = 0.29)$ and $\eta_1(\alpha = 0.29)$ as nominal values. The simulated strains at $\alpha = 29\%$ according to test II can be found in figure 5.37 as axial strains evolution with time.

Data in figure 5.35 illustrate the evolution of sensitivity coefficients S^* with time related to each parameters. One should notice, applied stress rates according to test II are likely three times higher than the ones employed in case of test I. From this figure, it can be observed that during the loading step, the mechanical behavior is mainly controlled by E_0 of Maxwell's unit. In fact, more elastic response is revealed when the material is rapidly loaded and viscous effects are almost diminished. It appears that viscosity parameter η_1 and elastic modulus E_1 of kelvin unit have considerably less impact on strains evolution with lower sensitivity of approximately 6 10^{-5} and 5 10^{-5}, respectively.

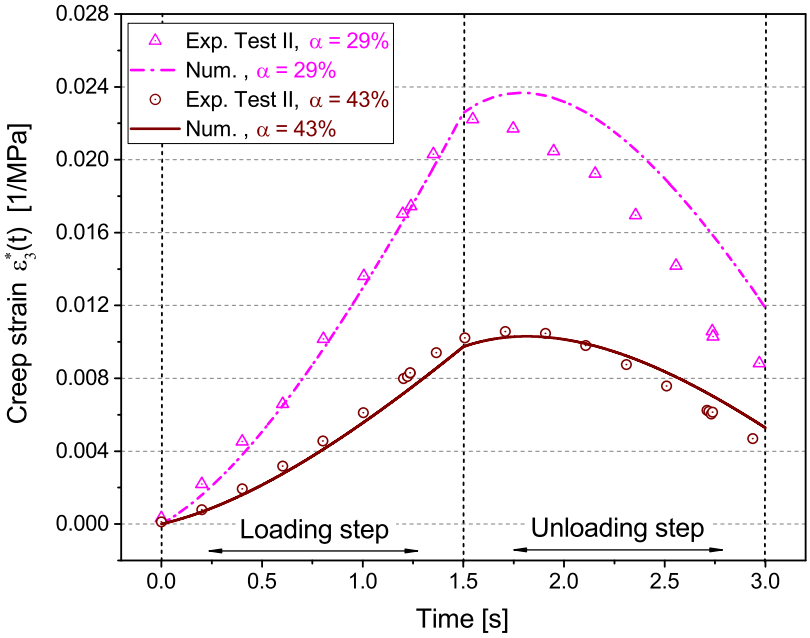

Figure 5.34: Axial normalized strains ε_3^* for a loading-unloading applied stress performed on sample 5 according to test II. Superimposition of the response of the rheo-kinetic Burgers model for two levels of cure degree with experimental data.

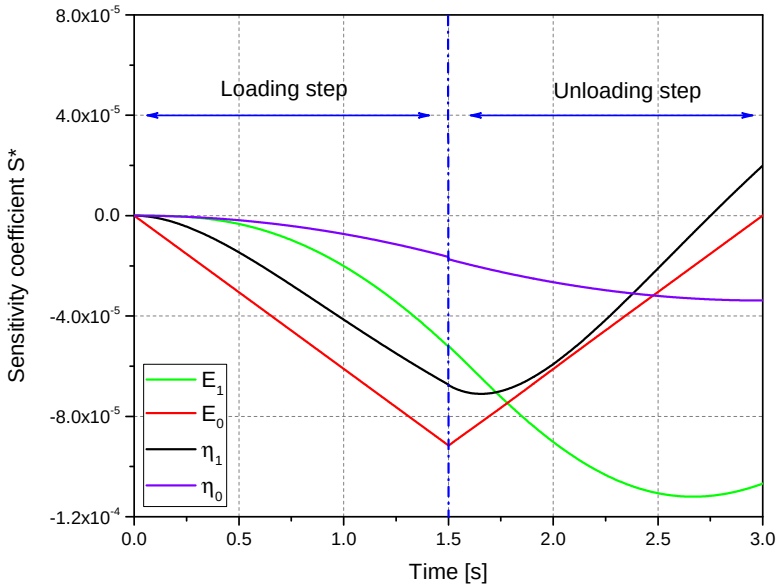

Figure 5.35: Sensitivity analysis of rheo-kinetic Burgers model parameters on loading-unloading response through sensitivity coefficient S^* evolution during an applied loading cycle at $\alpha = 29\%$ according to test II.

Viscosity η_0 related to Maxwell dash-pot exhibits on the contrary, roughly no influence on the viscoelastic behavior. When stress is unloaded, E_0 remains the parameter with most important impact on the mechanical behavior which controls the material recoverable elastic

deformation. E_1 seems to be most responsible of irrecoverable viscoelastic strains levels reached during this step of unloading. It is evident from sensitivity coefficient curve correlated to the viscosity η_0 that this parameter did not influence much the mechanical behavior in this case of loading path with an impact on the material strain response that does not exceed -3 10^{-5} considering this analysis example.

These interpretations could further explain the good prediction of the loading region as presented in figure 5.34 since the material response during loading step is mainly controlled by the elastic component related to E_0 whose proposed exponential regression showed good fitting with a R^2 variance of 98%. Disparities are mostly revealed through the unloading region. In view with the performed sensitivity analysis, these discrepancies could rather be explained by the material behavior variability.

5.5.4 Axial strain responses in comparison with the three tests

In figure 5.36, the superimposition of the viscoelastic rheo-kinetic model strain responses with experimental results of loading-unloading tests and creep-recovery test are displayed as function of time.

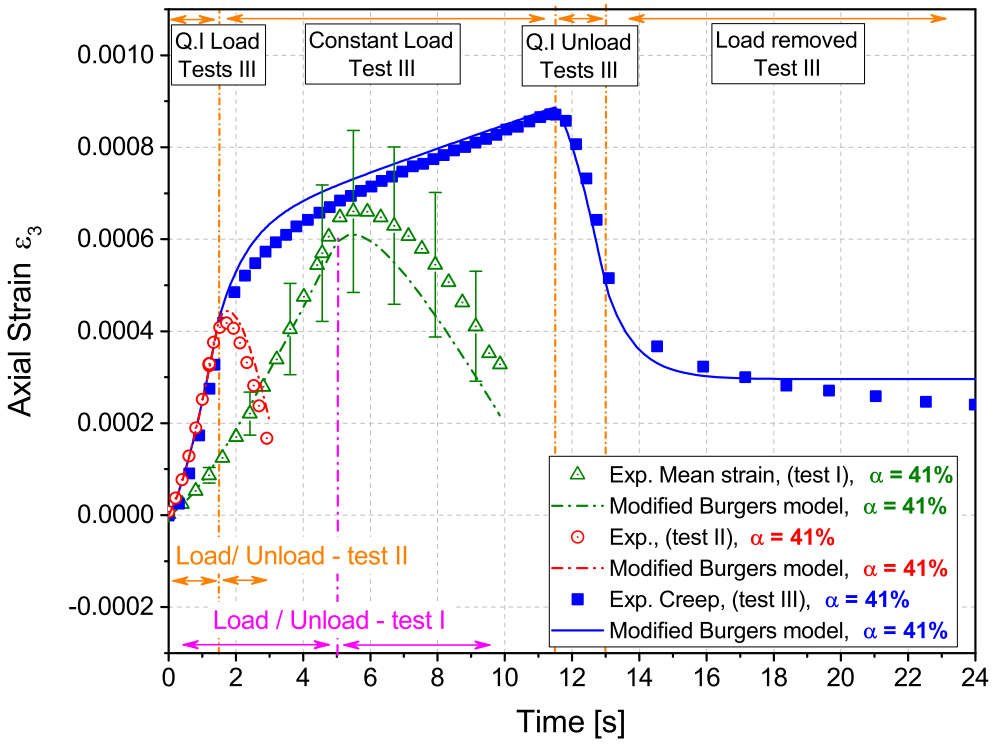

Figure 5.36: Axial strain responses for loading-unloading stress according to tests I and II on samples [1 - 4] and 5, respectively, with obtained axial creep strain according to creep-recovery test III carried out on sample 6. Superimposition of the response of the rheo-kinetic Burgers model to each loading path at 41% of cure degree.

The presented examples are taken for a degree of cure at 41% and all samples were submitted to the same $\sigma_a = 30\ 10^{-3}$MPa under different loading paths. Samples [1 - 4] were submitted to testing I with a stress rate $\dot{\sigma_3} = \pm 6\ 10^{-3}$MPa.$s^{-1}$ during loading/unloading steps. Sample 5 was loaded under $\dot{\sigma_3} = \pm 2\ 10^{-2}$ MPa.s^{-1}. Sample 6 was submitted to the creep-recovery test. It was loaded with the same $\dot{\sigma_3}$ as sample 5 during the "quasi-instantaneous" loading steps with a stress hold at $\sigma_a = 30\ 10^{-3}$MPa during 10 seconds.

The rheo-kinetic Burgers model predictions for those tests show that the elaborated model is able to predict the rheological behavior for different loading paths. It can be seen from this figure, samples 5 and 6 experimental responses during the first loading step along 1.5s show a very good repeatability of behavior under the same applied $\dot{\sigma_3}$. Model prediction during the compressive loading of both samples proves a good consistency in reproducing strain-time curves. Such good predictability under high stress rate could be ascribed to the model sensitivity which remains significantly low below 10^{-4} to mainly E_0 and η_1 whose evolution with cure revealed already a good fitting. Through the loading region of test I, the average strain obtained from the response of samples [1 - 4] appears to be correctly predicted by the model. The simulated creep strain response of sample 6 shows a satisfactory agreement with the experimental data. The appeared disparities could be produced due to the overestimation of the material viscosity η_0 and the under-prediction of E_0 but mainly related to the model high sensitivity to E_1. This sort of inconsistency could be considered as reasonable results since the establishment of the rheo-kinetic model is based on only one sample's response. Moreover, applied stress dependency on the mechanical response should further be investigated and likely included to ensure more accurate prediction and avoid such errors.

During the unloading steps of all samples response, the model shows a satisfactory fit to the measured strains according to the three types of testing. A high variability of the material response can be noticed through the scattering of the average strain measurements which reach $\pm 1.75\ 10^{-3}$. This large variability is indeed revealed more conspicuous when the material is unloaded. Model prediction of sample 5 response through testing II unload step reveals a very good consistence with experimental data. Even if this test was conducted on only one sample, it is very prominent that discrepancies between the simulated characteristics and experimental ones are substantially much smaller in this case of loading conditions. The predicted retardation time with the model at $\alpha = 41\%$ of sample 5 is $\tau = 0.9$s which is very close to the loading/unloading duration of each step equals to 1.5s. This clearly proves again the more elastic response exhibited by the viscoelastic material when submitted to higher stress rate and therefore, the good agreement between model results with the experimental data. The measured strain during the recovery of sample 6 submitted to test III, does not seem to reach an asymptotic value when load is removed. As previously discussed in subsection 5.4.2, the recovery behavior is difficult to assess in these testing conditions which might require more adjusted identification of induced shrinkage with cure to accurately estimate the irrecoverable deformations. Meanwhile, model simulated response proves very satisfactory agreement with experimental data during the first instants of recovery despite the variance between predicted and measured permanent strains levels.

Figure 5.37 gathers the material strain responses when submitted to three testing types for a degree of cure equal to 29%. These curves were previously plotted as normalized strains ε_3^* with time in order to examine the degree of cure effect on behavior. For further understanding of the viscoelastic properties evolution, here is an other example of the material behavior at early stage of curing when loaded differently. The maximum σ_a applied to all samples in this example is 11 10^{-3}MPa. Samples [1 - 4] are submitted to $\dot{\sigma_3} = \pm 22\ 10^{-4}$ MPa.s^{-1} whereas sample 5 and 6 are loaded under $\dot{\sigma_3} = \pm 74\ 10^{-4}$ MPa.s^{-1}.

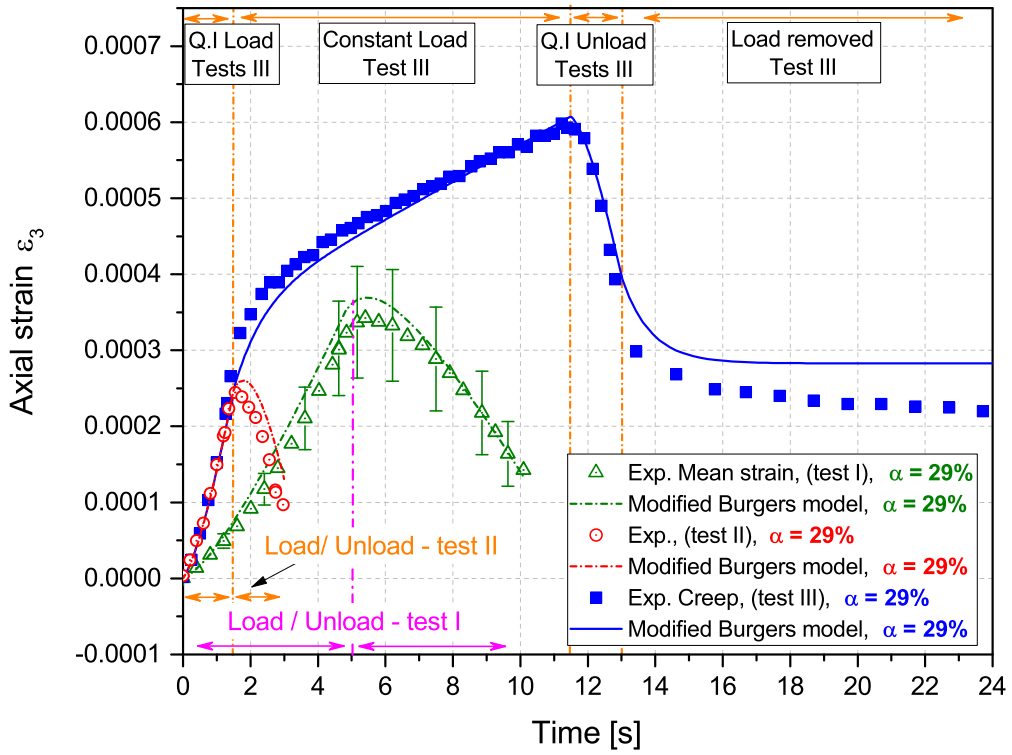

Figure 5.37: Axial strains response for loading-unloading applied stress performed according to tests I and II on samples [1 - 4] and 5, respectively, with obtained axial creep strain according to creep-recovery test III carried out on sample 6. Superimposition of the response of the rheo-kinetic Burgers model to each loading path at 29% of cure degree.

As evident from this figure, the model can give a great simulation of the studied material behavior at pregelation state. The repeatability of the mechanical response when the material is loaded at higher stress rate is also provided for this cure degree which can be noticed from sample 5 and 6 measured strains during loading step. The rheo-kinetic Burgers model permits to correctly predict it. Moreover, we can see that the model tends to give satisfactory predictions of strain levels attained under same applied stress but with different stress rate. Sample 5 response reveals higher stiffness and tends to favor the elastic properties of the material. On the contrary, tested specimens according to test I show more viscous effects that result in higher levels of deformation when the material is loaded forward. Modeling curve of creep strain presents an overall good correlation between model estimation and experimental data.

The obtained results from the comparison between model prediction and measured properties of the material tend to prove that the rubber-like phase behavior of the studied IMA/M21 prepreg can be modeled during the pregelation stage from a Burgers model by taking into consideration the effect of cure degree.

5.6 Partial conclusion

In this chapter, a new experimental methodology was developed with the purpose of investigating the mechanical behavior of an interlayer toughened Carbon fiber/Epoxy unidirectional composite during the curing process. The challenging issue was to provide an appropriate method that permits to continuously identify the mechanical behavior of a reacting material using the experimental device PvT-HADDOC. Preliminary tests were firstly carried out in order to assess technical limitations related to the experimental bench which allowed us to adjust and establish the appropriate procedure that allows to realize the objectives of this study.

The employed experimental approach was simplified given the complexity of the studied material behavior which undergoes several multi-physical phenomena during the cure cycle, as detailed in chapter 3, including thermal expansion/contraction, the through-thickness compaction correlated to the initial pre-consolidation, chemical shrinkage and the mechanical properties development. Thus, the adopted strategy consists in performing a total thermo-mechanical cure cycle under applied high compressive hydrostatic pressure in order to ensure the preconditioning of the material state during the first stages of cure. Afterwards, once the isothermal curing dwell was reached, convincing mechanical tests were performed aiming at characterizing properly the behavior of the studied prepreg as the polymerization reaction progresses.

Testing conditions were constrained by the experimental setup configuration which enables to perform only compressive loading conditions under controlled stress. Three types of loading paths were defined for the rheological measurements. Test I and test II, consisted in loading the sample with a constant stress rate up to a certain stress amplitude, then reversal loading was performed until zero stress. The applied stress amplitude was chosen to increase with the degree of cure in order to produce significant mechanical strain and prevent from an excessive flowing. In both types of tests, the applied stress amplitude was the same for each degree of cure. Test II loading rates for each stress amplitude was nearly three times higher than for test I. Testing III was defined as a compressive creep-recovery test under applied stress whose amplitude values were equals to the employed stress levels according to test I and II with the stress rates of test II. The whole system [sample-experimental bench] was mounted on a standard testing machine. The contribution of the assumed elastic behavior of the setup within the mechanical response of the studied material was taken into account in the estimation strategy of the mechanical strains of the material. However, the device stiffness appeared to be lower than the sample when the latter reached the gel point. This limited the investigation methodology to the pregelation region only, that is to say, the com-

posite material was only characterized at the liquid state before gelation. Only unidirectional laminate samples were employed for this investigation. Therefore, the mechanical behavior was characterized through the axial transverse direction along the sample thickness.

The material response was analyzed and modeled thanks to a Burgers viscoelastic model which consists of a series associations of Maxwell unit with Kelvin-Voigt branch. The model was analytically fitted to the experimental results obtained from the creep-recovery testing. This allowed to identify the relative material properties, *i.e.* the viscosity η_0 and Young's modulus E_0 related to Maxwell's unit, and the viscosity η_1 and Young's modulus E_1 that comprise the kelvin-Voigt unit. An idea of searching functional dependencies for Burger model parameters as function of degree of cure has been proposed. Exponential regressions were identified for each parameter and integrated into the classic Burgers model to develop, as termed in this chapter, the modified "rheo-kinetic Burgers model". This one accounts for the influence of the crosslinking reaction on the development of the material rheological properties. The predictability of the modified model was verified by comparing the model prediction with the experimental results under different kinds of loading paths, *i.e.* test I, II and III, for various level of cure degree. The obtained results showed good agreements between model simulations and experimental response which proved that the rubbery sate of the studied IMA/M21 prepreg can be accurately modeled during the pregelation stage by a viscoelastic Burgers model related to fluid-like behavior by taking into consideration the effect of cure degree.

Therefore, the developed methodology allowed to identify the mechanical behavior of a unidirectional thermosetting composite along the transverse direction, considered in the liquid state through the pregelation region using the PvT-HADDOC experimental device. As a consequence, the developed model represents a good alternative of a non-accurate purely elastic approach. In spite of the fact that this method relies on several simplifying assumptions, the obtained simulated results are consistent with experimental behavior evolution with cure, which proves the ability of the modified model to describe the viscoelastic behavior of the IMA/M21 prepreg during cure. Modeling of creep behavior during the pregelation stage of a thermosetting composite may yield a further understanding of the development of creep mechanisms with the crosslinking process and may allow predictions of the creep behavior, which is of major importance when dealing with designing of composite structural components.

The proposed rheo-kinetic Burgers model may present satisfactory estimation of the material behavior with cure. However, it appeared that model parameters might be also dependent to the applied stress level. Nevertheless, it was quite difficult with the already performed tests to quantitatively assess the impact of applied stress amplitude on the observed non linear behavior before gelation. It was also not possible to justify whether the material behavior presented a yielding threshold that would increase with cure upon which the material might exhibit stress dependent behavior and might flow (on the basis of the yield stress fluids theory). Thus, in order to probe these assumptions, further mechanical testing at lower temperature of isothermal cure are required so that the chemical shrinkage effects can be

accurately omitted. These mechanical testing would be probably more complex and time consuming due to the irreversible crosslinking reaction but are still needed to perform in order to further develop this rheological characterization.

GENERAL CONCLUSION AND PERSPECTIVES

The growing use of advanced thermosetting composites in various sectors, notably in the aerospace industry, has drawn a lot of attention to process-induced residual stresses. Considerable effort has gone into understanding their significance, reasons behind their occurrence and their quantities. If these stresses are not precisely determined, they may result in material failures and dimensions instabilities. Process-induced strains have a crucial role on the development of these stresses and final dimensions variations of composite parts. The work presented in this thesis has focused, through the employment of new experimental strategies, on studying the curing deformations of thermosetting composites in addition to the development of their mechanical properties during the cure. These objectives have been set with the aim of contributing to a better understanding of the complex behavior of these materials. The entire research work was performed on a specific aerospace-grade epoxy based prepreg named as IMA/M21. The contributions of this work are summarized as follows.

The literature review, presented in chapter 1, proved the need to fully understand how process-induced strains develop in composite materials as being a key issue to ensure more reliable predicting tools of parts deformations. Their prediction requires, indeed, to be accompanied by an important work of characterization including the identification and modeling of the material mechanical behavior. As a consequence, it appeared as crucial to accurately quantify these deformations, which is possible through the estimation of the coefficients of thermal expansion and of chemical shrinkage. The commonly employed experimental methods allowing the measurements of these properties in thermoset composites have been presented. Most of them remain very limited to partially or totally cured composite samples while other only provide information on cure shrinkage after the matrix gelation. Almost the majority of available methods are only limited to non representative conditions of currently employed manufacturing processes. Besides, they mainly lack from directional measurements. A brief description of the physics that drive the consolidation of thermoset composites in the uncured state was given in this literature review, since the compaction behavior of these materials has also a very significant impact on the final shape of parts and their dimensions variation. Finally, as with the anisotropic shrinkage in composite materials, the measurement

methods of rheological properties during the entire curing are really scarce in the literature and showed significant limitations. Employed techniques to investigate the mechanical behavior through the before gelation stage, are almost non-existent. Most of the developed mechanical constitutive models are based on tests rather performed on fully or partially cured specimens. Modeling approaches of rheological properties during the cure are consequently, whether purely elastic-based-approaches, or, are difficult to implement since they are based on viscoelastic and/or viscoplastic behavior descriptions that require complicated experimental characterization and intensive calculations for parameters identification. Hence, this allowed us to raise several issues of the measurement of the mechanical properties of thermoset composites, particularly before gelation, during which the behavior is commonly, either approximated, or considered negligible.

Chapter 2, firstly introduced the studied thermosetting prepreg material. The neat epoxy resin used in the impregnation of the supplied prepreg was also provided by the supplier. The measurements of its thermo-chemical properties during the cure according to the manufacturer's recommended thermal cycle have been the subject of the first part of this second chapter. The PvT-α device, dedicated to the characterization of thermosetting resins and associated composites was employed and allowed to determine the resin volumetric coefficients of thermal expansion and cure shrinkage. The device enabled to obtain the experimental degree of cure advancement which allowed to validate the Bailleul's cure kinetics model modified by Msallem as the appropriate one to be used in this work for describing the matrix polymerization advancement during curing. The second part of this chapter was devoted to the presentation of the PVT-HADDOC experimental set-up used in this work with the aim of characterizing the process-induced strains and the rheological behavior throughout the cure of the studied composite. This device allows the simultaneous measurement of the cure deformations of a composite sample along two directions: one through the thickness of the sample and the other along its plane. In addition, it enables to obtain other physical quantities such as the cure reaction progress, the temperature of the sample surfaces and the applied pressure during the test. In this chapter, the global working principle of this device was described. A special interest was given to detailing the measuring principle of the curing strains along both directions under a precised cure cycle which was the main objective of the following chapter.

Only UD configurations were characterized in this study. The analysis of the performed preliminary multi-axial measurements of cure deformations in chapter 3 revealed a complex behavior which required some adjustment in the applied cure cycle. Firstly, thanks to the new defined curing cycles, it was possible to divide the entire cure behavior of the material into 4 stages with a further breakdown of the pre-gelation stage. The induced strains were therefore analyzed depending on the evolution of the material state, in line with, the thermal cycle and physical phenomena that drive the cure behavior during the entire cycle. The compaction of the laminate occurred in the viscous uncured state is proved to be anisotropic. Indeed, the material was only compacted along the thickness direction. Observed disparities between cure deformations along the whole cure cycle through the three measured directions proved that the material behavior is fully orthotropic than transversely isotropic unlike to what a UD stacking may suggest. The measured CTE (uncured/cured glassy state) and CCS

(before/after gelation) along the thickness direction were proved to be higher than the in-plane transverse direction. Good agreement has been found between obtained values of cured glassy CTEs with the PvT-HADDOC device and the ones obtained with linear dilatometer. The measured chemical shrinkage of the IMA/M21 prepreg revealed the importance of such original in-situ multi-axial characterization. In fact, it was demonstrated that the studied UD laminate does not shrink likewise before and after gelation along both transverse directions in the contrary to what has been commonly assumed. The linear dependency of the chemical shrinkage on the degree of cure exhibits a change of slope around the gel point. The shrinkage behavior showed an independence on the curing temperature.

A thermo-mechanical modeling of the cure behavior, based on the classical laminate theory (CLT) approach, was proposed in chapter 4, by accounting the resin interleaf layers in the laminate structure. The objective of this chapter was to discuss whether the presence of these interlayers is behind the obtained disparities between cure deformations measured along both transverse direction of the UD laminate. To do so, the macroscopic thermal expansion coefficients were calculated in the uncured and cured states and good agreements with the experimental results was shown. The macroscopic coefficients of chemical shrinkage were also estimated by the model before and after gelation. The comparison with the experimental values showed satisfying agreement. The first outlined conclusion of this chapter was the validation of the orthotropic behavior of the studied material to be due to the presence of the extra interleaf layers. Moreover, the captured tendency of the chemical shrinkage development around the gelation point was assumed to be influenced by the prepreg plies behavior and the anisotropic fiber packing effect. The observed differences between the computed and the measured coefficients can be attributed to the several simplifications used to estimate the material properties with the model which requires much improvements.

Finally, chapter 5 was devoted to present the new experimental methodology, developed using the PvT-HADDOC device with the purpose of investigating the mechanical behavior of the studied prepreg during the curing. The adopted strategy consisted in performing the mechanical tests during the isothermal curing dwell only, in order to allow a decoupling of physics as a first step. Three types of particular compressive loading cycles were defined for the rheological measurements. They were applied under controlled stress with an increasing stress amplitude as function of the cure degree so as to follow the material stiffness growth with the advancement of the polymerization reaction. It was proved that the composite material exhibited a fluid viscoelastic behavior in the fluid state during the early stages of cure. The evolution of rheological behavior with the increase of the degree of cure was well captured until the matrix gelation point. The material response was modeled thanks to a Burgers viscoelastic model which was analytically fitted to the experimental results obtained from the creep-recovery testing. This allowed to identify a cure dependent viscoelastic model that accounts for the influence of the crosslinking reaction on the development of the material rheological properties. Obtained results proved the ability of such original method with complex testing protocol to allow a fine characterization of composite thermo-mechanical behavior by employing representative sample dimensions while preventing porosity development issues due to the high applied pressure.

Perspectives

Several perspectives can be proposed as results of this thesis work. The observed findings about the consolidation phenomenon highlighted the need for a deeper understanding of the compaction behavior that occurs in the uncured state which is barely studied. In the short-term, it will be interesting to look in more details into the influence of processing conditions on the compaction kinetics. Dimensions changes induced by this phenomenon in such anisotropic, but mostly, new toughened prepreg generation, require fine multi-axial measurement to further understand the parameters that control their thickness variability. It will be also interesting to investigate the size effects like thicker composite samples and different configurations of laminate stacking impact on the compaction behavior. Thorough understanding of this phenomenon would highly provide better prediction of defect formation for manufacture of prepreg based structures.

The findings about the CTE and CCS revealed the importance of the present experimental device to provide such fine measurements of these parameters. As future short-term objectives, it would be interesting to study different stacking sequences of laminates in order to further understand the development of the cured-induced deformation in such anisotropic materials. Additional investigations can be also carried out in order to determine the evolution of the CTE of thermoset composites throughout the full curing. Concrete knowledge about such parameter dependency on the degree of cure is fundamental for model implementation required for shape deformations prediction of composite parts like the so-called spring-in phenomenon. Improvements of the proposed model in chapter 4 can be considered as further short-term goals of this work. The latter can be developed for different type of prepreg stacking sequences to estimate the macroscopic CTE and CCS.

Improvements should be integrated to the present experimental device for the mid-term future in order to enhance the set-up stiffness. This would enable the whole rheological behavior characterization for next works. Moreover, local deformation measurement method along the thickness direction should be incorporated in the device. This would allow to reduce the corrections steps conducted for strains calculation, by removing thermal baseline subtraction step and compliance correction. More information about the composite rheological behavior during the cure is still required in the composite industry in order to better elucidate the pre-gelation behavior under processing conditions. The already developed methodology allowed to identify the mechanical behavior as fluid viscoelastic through the pre-gelation region. Over the long-term, the developed model can represent a good alternative of purely elastic approaches largely employed to describe composites behavior in residual stress prediction models. The improvement of the present device, would also enable further studies on the mechanical behavior to be conducted so as to assess the assumptions related to yield stress fluid approaches. Multi-scale model can therefore be developed by taking into account the matrix behavior assimilated to a fluid with yield stress which may allow better prediction of residual stresses developments in thermoset composites.

RÉSUMÉ ÉTENDU EN FRANÇAIS

Objectifs de la thèse et verrous scientifiques

Les travaux présentés dans ce manuscrit ont été réalisés au Laboratoire de Thermique et Énergie de Nantes (LTEN) et financés par Nantes Université. L'objectif principal de cette thèse est d'approfondir la compréhension des mécanismes de déformation induits par le procédé de mise en œuvre des composites thermodurcissables et les couplages multi-physiques qui se produisent durant leur cuisson.

Au vu de l'utilisation croissante des composites thermodurcissables dans divers secteurs, notamment dans l'industrie aéronautique, de nombreuses études s'intéressaient aux contraintes résiduelles induites par le procédé de mise en œuvre. Des efforts considérables ont été déployés pour comprendre les mécanismes et les raisons de leur formation. Si ces contraintes ne sont pas déterminées avec précision, elles peuvent être la cause de phénomènes désastreux et entraîner parfois des défaillances des matériaux et des instabilités dimensionnelles. Les déformations induites par le procédé tel que le retrait chimique et la contraction thermique ont un rôle crucial sur le développement de ces contraintes et les variations dimensionnelles finales des pièces composites. En raison de leur hétérogénéité et de leur forte anisotropie, les matériaux composites thermodurcissables sont compliqués à mettre en œuvre et l'interaction entre les différents phénomènes multi-physiques complexes pendant la cuisson de ces matériaux joue un rôle majeur dans la génération de ces contraintes résiduelles. Une modélisation fine du comportement du matériau est donc nécessaire pour prédire la forme finale des pièces et leurs propriétés. Afin d'alimenter ces modèles et évaluer leur précision, des mesures directes et fiables des propriétés des composites pendant leur cuisson sont nécessaires, bien qu'elles représentent encore de réelles difficultés expérimentales. Au vu de ces verrous scientifiques, la recherche bibliographique a été orientée principalement suivant trois axes. Les principaux mécanismes responsables de l'apparition des contraintes résiduelles ont été présenté en premier lieu. En conséquence, il est apparu crucial de quantifier précisément ces déformations de cuisson, ce qui est possible par l'estimation des coefficients de dilatation thermique et de retrait chimique. Les méthodes expérimentales couramment employées permettant de

mesurer ces propriétés dans les composites thermodurcissables ont été présentées. La plupart d'entre elles restent très limitées aux échantillons de composites partiellement ou totalement polymérisés tandis que d'autres ne fournissent des informations sur l'évolution du retrait chimique qu'après la gélification de la matrice. Presque la majorité des méthodes disponibles sont limitées à des conditions non représentatives des procédés de fabrication actuellement utilisés. De plus, elles manquent principalement de mesures directionnelles. Une brève description de la physique qui conduit la consolidation des composites thermodurcissables à l'état cru a été donnée dans cette revue de la littérature, puisque le comportement de compactage de ces matériaux a également un impact très significatif sur la forme finale des pièces et leur variation dimensionnelle. Enfin, comme pour le retrait anisotrope dans les matériaux composites, les méthodes de mesure des propriétés rhéologiques pendant la totalité de la polymérisation sont rares dans la littérature et ont montré des limites importantes. Les techniques employées pour étudier le comportement mécanique avant la gélification sont presque inexistantes. La plupart des modèles mécaniques constitutifs développés sont basés sur des tests plutôt réalisés sur des spécimens entièrement ou partiellement polymérisés. Les approches de modélisation des propriétés rhéologiques pendant la polymérisation sont donc soit purement élastiques, soit difficiles à mettre en œuvre car elles sont basées sur des descriptions de comportements viscoélastiques et/ou viscoplastiques qui nécessitent une caractérisation expérimentale compliquée et des calculs intensifs pour l'identification des paramètres. Ceci nous a permis de soulever plusieurs questions relatives à la mesure des propriétés mécaniques des composites thermodurcissables, en particulier avant la gélification, pendant laquelle le comportement est généralement, soit approximatif, soit considéré comme négligeable.

Dans ce but, le travail présenté dans cette thèse s'est concentré sur la caractérisation des déformations induites en cours de cuisson ainsi que le comportement rhéologique d'un pré-imprégné thermodurcissable en utilisant un dispositif expérimental nommé PvT-HADDOC développé au laboratoire LTEN.

Matériau d'étude et méthodes expérimentales

Le matériau étudié est présenté dans la première section du chapitre 2. Il s'agit d'un pré-imprégné thermodurcissable renforcé par fibres de carbone type IMA à base de résine époxyde de type M21 qui a été également fournie séparément par Hexcel Composite France en plus du pré-imprégné. La résine M21 est une matrice thermodurcissable époxy chargée de nodules thermoplastiques qui permettent d'améliorer la ténacité du matériau. Le pré-imprégné obtenu est donc formé par des couches de résine renforcées par des particules thermoplastiques qui constituent une sorte des inter-plis entre les plis de pré-imprégné constitués des fibres et de la matrice. Les mesures des propriétés thermochimiques de la résine seule pendant la cuisson selon le cycle thermique recommandé par le fabricant ont fait l'objet de la première partie du deuxième chapitre. L'appareil PvT-α, dédié à la caractérisation des résines thermodurcissables et des composites associés a été employé et a permis de déterminer les coefficients volumétriques de dilatation thermique et de retrait chimique de la résine. L'appareil a permis d'obtenir le degré expérimental d'avancement de la polymérisation, ce qui a permis de valider le modèle cinétique de polymérisation de Bailleul modifié par Msallem comme étant

le modèle approprié à utiliser dans ce travail pour décrire l'avancement de la polymérisation de la matrice pendant la cuisson. La deuxième partie de ce chapitre a été consacrée à la présentation du dispositif expérimental PvT-HADDOC (voir section 2.6) utilisé dans ce travail dans l'objectif de caractériser les déformations induites par le procédé et le comportement rhéologique tout au long de la polymérisation du composite étudié. Ce dispositif permet la mesure simultanée des déformations de cuisson d'un échantillon composite selon deux directions : l'une à travers l'épaisseur de l'échantillon et la deuxième; le long de son plan. De plus, il permet d'obtenir d'autres grandeurs physiques telles que l'évolution de la réaction de polymérisation, la température des surfaces de l'échantillon et la pression appliquée pendant l'essai.

Mesures des déformations thermochimiques anisotropes du pré-imprégné M21/IMA pendant la cuisson

Seuls des empilements unidirectionnels ont été caractérisés dans cette étude. L'analyse préliminaire des déformations de cuisson effectuée dans le chapitre 3 a révélé un comportement complexe de ce type de pré-imprégné dit de 3ème génération. Une première compagne d'essai a montré la nécessité d'un ajustement du cycle de cuisson classique appliqué selon les recommandation du fournisseur. Grâce aux nouveaux cycles de cuisson définis, il a été possible de découpler au mieux les mécanismes observés préalablement et diviser l'ensemble du comportement du matériau en 4 phases avec une décomposition supplémentaire de l'étape de pré-gélification (voir figure 3.12). Les déformations induites ont été mesurées à travers les trois directions principales du stratifié unidirectionnel et ont donc été analysées en fonction de l'évolution de l'état du matériau, par rapport au cycle thermique et les phénomènes physiques qui régissent le comportement de cuisson pendant la totalité du cycle. Il est à noter que pendant la cuisson, le composite étudié a été soumis à un état de compression hydrostatique de l'ordre de 5 à 7 bars.

Un phénomène de compactage a été identifié par la réduction de l'épaisseur des échantillons dans les premiers stades de la phase de chauffage. Ce phénomène est directement lié à la consolidation du matériau à l'état cru et s'est avéré être anisotrope. En effet, le composite étudié ne se compacte qu'à travers son épaisseur. Les différences observées entre les déformations mesurées à travers les deux directions transverses aux fibres tout au long du cycle de cuisson ont prouvé que le comportement du matériau est entièrement orthotrope et non pas isotrope transverse, contrairement à ce qu'un empilement UD pourrait suggérer. En effet, les CTE mesurés aux états cru et cuit vitreux du matériau ainsi que les CCS qui correspondent à la phase avant et après gélification, à travers l'épaisseur, se sont avérés être plus élevés que ceux mesurés dans la direction transverse aux fibres dans le plan. Un bon accord a été trouvé entre les valeurs obtenues des CTE qui correspondent à l'état cuit vitreux avec le dispositif PvT-HADDOC et celles obtenues avec un dilatomètre linéaire usuel. Le retrait chimique mesuré du pré-imprégné a révélé l'importance de la caractérisation multi-axiale originale in-situ réalisé dans le cadre de ces travaux. En effet, il a été démontré que le stratifié étudié ayant un empilement UD ne se contracte pas de la même manière avant et après la gélification dans les deux directions transversales hors-plan et dans le plan, contrairement à ce

qui était communément admis. La dépendance linéaire du retrait chimique en fonction du degré de polymérisation présente un changement de pente autour du point de gélification. L'évolution du retrait chimique a montré une indépendance par rapport à la température de polymérisation employée (160°C et 180°C dans notre cas).

Modèle multicouche considérant la présence des inter-plis de résine

Dans le quatrième chapitre (chapitre 4) on propose une modélisation des phénomènes observés dans le chapitre 3, notamment au-delà de la phase de la consolidation de la matière à l'état cru. Une nouvelle approche de modélisation thermo-mécanique est proposée qui tient compte de l'architecture orthotrope du pré-imprégné étudié par la prise en considération de la présence des couches d'inter-plis de résine avec les plis du pré imprégné constitués par fibres et matrice dans le calcul des coefficients macroscopiques de dilatation thermique et de retrait chimique du stratifié. Le modèle thermo-mécanique multicouche est basé sur la théorie classique des stratifiés (CLT). Les coefficients d'expansion thermique effectifs ont été prédits dans les états non polymérisé et polymérisé du matériau et de bons accords avec les résultats expérimentaux ont été montrés. Les coefficients macroscopiques de retrait chimique ont également été estimés par le modèle avant et après gélification et une bonne correspondance avec les valeurs expérimentales a été constatée. Avec les résultats préliminaires obtenus dans ce chapitre, il a été possible de valider que le comportement du stratifié étudié est totalement orthotrope en raison de la présence des inter-couches supplémentaires de résine. Cela explique bien la différence entre les propriétés du stratifié obtenues dans les deux directions transversales d'une structure UD typique. Néanmoins, la tendance observée de la distribution du retrait chimique autour du point de gélification dans le plan et à travers l'épaisseur ne peut pas être clairement expliquée par la présence des inter-plis de résine dans la structure du stratifié. Il serait plus plausible de supposer que le comportement de contraction chimique macroscopique du stratifié est plutôt influencé par le comportement des couches de pré-imprégnés (constitués par fibres et matrice). Ce modèle nécessite une modélisation purement phénoménologique du retrait anisotrope avant la gélification, accessible uniquement par des mesures directes telles que celles effectuées par le PvT-HADDOC. Une étude plus approfondie à l'échelle micro est maintenant nécessaire pour évaluer l'hypothèse du rôle de la distribution anisotrope des fibres sur l'évolution du retrait avant la gélification. En résumé, les différences observées entre les coefficients calculés et mesurés peuvent être attribuées aux nombreuses simplifications utilisées pour estimer les propriétés du matériau avec le modèle. Dans cet exemple proposé, les paramètres fixés et les approches choisies qui décrivent le comportement des constituants à l'échelle de chaque couche pourraient induire des changements relatifs dans le comportement macroscopique estimé. Le modèle actuel nécessite une analyse plus approfondie et des comparaisons entre les différentes théories basées sur une analyse de sensibilité qui serait utile compte tenu du nombre élevé de paramètres, en particulier à l'échelle micro. Il convient de noter que le retrait anisotrope particulier des plis n'a été observé qu'à l'état liquide et doit être corrélé au comportement anisotrope observé de la compaction. Le rôle de la distribution des fibres doit être remis en question.

Caractérisation et modélisation du comportement rhéologique du composite pendant la cuisson

Le cinquième chapitre avait pour but de fournir une caractérisation et une modélisation de la rhéologie des pré-imprégnés en cours de cuisson. Le dispositif PVT-HADDOC a été employé dans cette phase d'étude. Le chapitre 5 est divisé en deux parties principales. La première partie de ce chapitre décrie la méthodologique expérimentale développée pour caractériser le comportement rhéologique pendant la cuisson du pré-imprégné étudié. L'approche expérimentale employée a été simplifiée étant donné la complexité du comportement du matériau étudié qui subit plusieurs phénomènes multi-physiques pendant le cycle de cuisson, comme détaillé dans le chapitre 3, y compris la dilatation/contraction thermique, la compaction à travers l'épaisseur corrélée à la consolidation initiale, le retrait chimique et le développement des propriétés mécaniques.

Ainsi, la stratégie adoptée consiste à étudier le comportement rhéologique du matériau pendant l'isotherme de cuisson et sous pression hydrostatique appliquée afin d'éviter le développement des porosités et d'assurer le préconditionnement de l'état du matériau pendant les premières étapes de la cuisson. Pour cela, des séquences rhéométriques ont été plutôt appliquées pour des niveaux de degré d'avancement considéré constant au fur et à mesure que la réaction de polymérisation avance (voir section 5.2). Les conditions d'essai ont été limitées par la configuration du dispositif expérimental qui permet de réaliser uniquement des conditions de chargement en compression sous contrainte contrôlée. Trois types de chargement ont été définis pour les mesures rhéologiques. Les essais I et II consistaient à charger l'échantillon avec un taux de contrainte constant jusqu'à une certaine amplitude de contrainte, puis on décharge jusqu'à une contrainte nulle. L'amplitude de la contrainte appliquée a été choisie de manière qu'elle augmente progressivement avec le degré de polymérisation afin de produire une déformation mécanique significative et d'éviter un écoulement excessif à l'état cru. Dans les deux types d'essais, l'amplitude de la contrainte appliquée était la même pour chaque degré de polymérisation. Les taux de charge de l'essai II pour chaque amplitude de contrainte étaient presque trois fois plus élevés que ceux de l'essai I. L'essai III a été défini comme un essai de fluage-recouvrance en compression sous contrainte appliquée dont les valeurs d'amplitude étaient égales aux niveaux de contrainte employés selon les essais I et II. Cependant, la rigidité du dispositif s'est avérée inférieure à celle de l'échantillon lorsque ce dernier atteint le point de gel. Cela a limité la méthodologie de caractérisation qu'à la région de pré-gélification. Le comportement mécanique a été caractérisé dans la direction transversale hors-plan (à travers l'épaisseur de l'échantillon).

Un modèle analytique a été proposé dans la deuxième partie de ce chapitre afin d'analyser la réponse du matériau. Le modèle choisi est un modèle viscoélastique de Burgers qui consiste en une série d'associations du modèle de Maxwell avec une branche Kelvin-Voigt. Le modèle a été ajusté analytiquement aux résultats expérimentaux obtenus lors des essais de fluage-recouvrance. Cela a permis d'identifier les propriétés rhéologiques du matériau, à savoir la viscosité η_0 et le module de Young E_0 liés à l'unité de Maxwell, et la viscosité η_1 et le module de Young E_1 qui correspond à l'unité de Kelvin-Voigt. Des régressions exponentielles ont été identifiées pour chaque paramètre pour décrire son évolution avec le degré d'avancement

de la réaction et intégrées au modèle classique de Burgers pour développer, ce on l'appelait dans ce chapitre, le modèle rhéocinétique de Burgers modifié ". Celui-ci tient compte de l'influence de la réaction de réticulation sur le développement des propriétés rhéologiques du matériau. La prédictibilité du modèle modifié a été vérifiée en comparant la réponse du modèle avec les résultats expérimentaux sous différents types de chargement, *i.e.* test I, II et III, pour différents degrés de réticulation. Les résultats obtenus ont montré de bons accords entre les simulations du modèle et la réponse expérimentale, ce qui prouve que l'état caoutchouteux du pré-imprégné IMA/M21 étudié peut être modélisé avec précision pendant la phase de pré-gélification par un modèle viscoélastique de Burgers lié à un comportement de type fluide en prenant en compte l'effet du degré de polymérisation. En conséquence, le modèle développé représente une bonne alternative à une approche purement élastique. Malgré le fait que cette méthode repose sur plusieurs hypothèses simplificatrices, les résultats simulés obtenus sont cohérents avec l'évolution du comportement expérimental pendant la cuisson, ce qui prouve la capacité du modèle modifié à décrire le comportement viscoélastique du pré-imprégné pendant la cuisson. Cependant, il est apparu que les paramètres du modèle pouvaient également dépendre du niveau de contrainte appliquée. Néanmoins, il a été assez difficile avec les tests déjà réalisés d'évaluer quantitativement l'impact de l'amplitude de la contrainte appliquée sur le comportement non linéaire observé avant la gélification. Il n'a pas non plus été possible de justifier si le comportement du matériau présentait un seuil d'écoulement qui augmenterait avec la réticulation et à partir duquel le matériau pourrait présenter un comportement dépendant de la contrainte et pourrait s'écouler (sur la base de la théorie des fluides à seul). Ainsi, afin de vérifier ces hypothèses, d'autres essais mécaniques à des températures plus basses de cuisson isotherme sont nécessaires afin que les effets de retrait chimique puissent être omis avec précision. Ces essais mécaniques seraient probablement plus complexes et plus longs, mais ils sont néanmoins nécessaires pour développer davantage cette caractérisation rhéologique.

Perspectives

Plusieurs perspectives peuvent être proposées comme résultats de ce travail de thèse. Les résultats observés sur le phénomène de consolidation ont mis en évidence la nécessité d'approfondir la compréhension du comportement de compactage qui se produit à l'état cru et qui est peu étudié. A court terme, il sera intéressant d'étudier plus en détail l'influence des conditions du procédé de mise en œuvre sur la cinétique du compactage. Les changements de dimensions induits par ce phénomène dans une telle génération de prépregs anisotropes renforcés par des inter-plis de résine, nécessitent des mesures multi-axiales fines pour mieux comprendre les paramètres qui contrôlent la variabilité de leur épaisseur. Il sera également intéressant d'étudier différentes configurations d'empilement des stratifiés sur le comportement de compactage. Une compréhension approfondie de ce phénomène permettrait de mieux prédire la formation de défauts pour la fabrication de structures à base de pré-imprégnés.

Les résultats concernant le CTE et le CCS ont révélé l'importance du dispositif expérimental actuel pour fournir des mesures aussi fines de ces paramètres. Comme futurs objectifs à court terme, il serait intéressant d'étudier différentes séquences d'empilement de laminés afin de

mieux comprendre le développement de la déformation induite durant la cuisson dans ces matériaux anisotropes. Des investigations supplémentaires peuvent également être menées afin de déterminer l'évolution du CTE des composites thermodurcissables tout au long de la polymérisation. La connaissance concrète de la dépendance de ces paramètres au degré de polymérisation est fondamentale pour la mise en œuvre des modèles précis étant nécessaire à la prédiction des distorsions de forme des pièces composites. Les améliorations du modèle proposé dans le chapitre 4 peuvent être considérées comme des objectifs à court terme de ce travail. Ce dernier peut être développé pour différents types de séquences d'empilement de pré-imprégnés afin d'estimer le CTE macroscopique et le CCS.

Des améliorations devraient être intégrées au dispositif expérimental actuel à moyen terme afin d'augmenter la rigidité du banc. Cela permettrait de caractériser l'ensemble du comportement rhéologique pour les prochains travaux. De plus, une méthode de mesure des déformations locales hors-plan devrait être intégrée au dispositif. Cela permettrait de réduire les étapes de corrections effectuées pour le calcul des déformations mesurées à travers l'épaisseur. L'industrie des composites a toujours besoin de plus d'informations sur le comportement rhéologique des composites pendant la cuisson afin de mieux comprendre le comportement de la pré-gélification dans les conditions de mise en œuvre. La méthodologie déjà développée a permis d'identifier le comportement mécanique comme viscoélastique fluide dans la région de pré-gélification. A long terme, le modèle développé peut représenter une bonne alternative aux approches purement élastiques largement utilisées pour décrire le comportement des composites dans les modèles de prédiction des contraintes résiduelles. L'amélioration du présent dispositif, permettrait également de mener des études complémentaires sur le comportement mécanique afin d'évaluer les hypothèses liées aux approches des fluides à seuil. Un modèle multi-échelle pourrait également être développé en prenant en compte le comportement de la matrice assimilée à un fluide à seuil d'écoulement, ce qui permettrait une meilleure prédiction des développements des contraintes résiduelles dans les composites thermodurcissables.

BIBLIOGRAPHY

[1] Hexcel, "Hexcel ready to fly on the A350 XWB," *Reinforced Plastics*, vol. 57, pp. 25–26, may 2013.

[2] Sibin Saseendran, *Effect of Degree of Cure on Viscoelastic Behavior of Polymers and their Composites*. PhD thesis, Luleå University of Technology, 2016.

[3] Olimy, "Carbon fiber prepreg, available online." `https://olimy.com/service/carbon-fiber-prepreg.html`.

[4] N. Nash, T. Young, P. McGrail, and W. Stanley, "Inclusion of a thermoplastic phase to improve impact and post-impact performances of carbon fibre reinforced thermosetting composites — A review," *Materials & Design*, vol. 85, pp. 582–597, nov 2015.

[5] P. Hubert, G. Fernlund, and A. Poursartip, *Autoclave processing for composites*. Woodhead Publishing Limited, 2012.

[6] L. Khoun, "Process-Induced Stresses and Deformations in Woven Composites Manufactured by Resin Transfer Moulding," *A thesis*, pp. 12–14, 2009.

[7] N. Zobeiry and A. Poursartip, "The origins of residual stress and its evaluation in composite materials," in *Structural Integrity and Durability of Advanced Composites*, pp. 43–72, Elsevier, 2015.

[8] M. M. Shokrieh, *Residual Stresses in Composite Materials*. 2014.

[9] I. Baran, K. Cinar, N. Ersoy, R. Akkerman, and J. H. Hattel, "A Review on the Mechanical Modeling of Composite Manufacturing Processes," *Archives of Computational Methods in Engineering*, vol. 24, no. 2, pp. 365–395, 2017.

[10] M. Thor, M. G. Sause, and R. M. Hinterhölzl, "Mechanisms of origin and classification of out-of-plane fiber waviness in composite materials — A review," *Journal of Composites Science*, vol. 4, no. 3, 2020.

[11] H. Bedayat, M. Roy, A. Forghani, C. Hickmott, F. Palmieri, B. Grimsley, B. Coxon, G. Fernlund, and A. Poursartip, "An efficient modelling approach for prediction of porosity severity in composite structures," *International SAMPE Technical Conference*, pp. 1880–1888, 2017.

[12] Y. Nawab, X. Tardif, N. Boyard, V. Sobotka, P. Casari, and F. Jacquemin, "Determination and modelling of the cure shrinkage of epoxy vinylester resin and associated composites by considering thermal gradients," *Composites Science and Technology*, vol. 73, no. 1, pp. 81–87, 2012.

[13] N. Ersoy and M. Tugutlu, "Cure kinetics modeling and cure shrinkage behavior of a thermosetting composite," *Polymer Engineering & Science*, vol. 50, pp. 84–92, jan 2010.

[14] T. Garstka, N. Ersoy, K. Potter, and M. Wisnom, "In situ measurements of through-the-thickness strains during processing of AS4/8552 composite," *Composites Part A: Applied Science and Manufacturing*, vol. 38, no. 12, pp. 2517–2526, 2007.

[15] L. Moretti, B. Castanié, G. Bernhart, and P. Olivier, "Characterization and modelling of cure-dependent properties and strains during composites manufacturing," *Journal of Composite Materials*, 2020.

[16] H. Hu, S. Li, J. Wang, L. Zu, D. Cao, and Y. Zhong, "Monitoring the gelation and effective chemical shrinkage of composite curing process with a novel FBG approach," *Composite Structures*, vol. 176, pp. 187–194, sep 2017.

[17] J. Chen, J. Wang, X. Li, L. Sun, S. Li, and A. Ding, "Monitoring of temperature and cure-induced strain gradient in laminated composite plate with FBG sensors," *Composite Structures*, vol. 242, no. January, p. 112168, 2020.

[18] S. Minakuchi, S. Niwa, K. Takagaki, and N. Takeda, "Composite cure simulation scheme fully integrating internal strain measurement," *Composites Part A: Applied Science and Manufacturing*, vol. 84, pp. 53–63, 2016.

[19] S. Motagi, S. Namilae, T. Freeman, and S. Boetcher, "In-situ Measurement of Resin Shrinkage with Respect to Degree of Cure," in *AIAA Scitech 2020 Forum*, vol. 1 PartF, (Reston, Virginia), pp. 1–10, American Institute of Aeronautics and Astronautics, jan 2020.

[20] C. Duffner, *Experimental Study of the Pre-gelation Behaviour of Composite Prepreg*. PhD thesis, University of British Columbia, 2019.

[21] J. P. Belnoue, O. J. Nixon-Pearson, D. Ivanov, and S. R. Hallett, "A novel hyper-viscoelastic model for consolidation of toughened prepregs under processing conditions," *Mechanics of Materials*, vol. 97, pp. 118–134, 2016.

[22] T. Centea, L. Grunenfelder, and S. Nutt, "A review of out-of-autoclave prepregs – Material properties, process phenomena, and manufacturing considerations," *Composites Part A: Applied Science and Manufacturing*, vol. 70, pp. 132–154, mar 2015.

[23] C. Duffner, N. Zobeiry, and A. Poursartip, "Examination of pre-gelation behaviour in AS4/8552 prepreg composites," *33rd Technical Conference of the American Society for Composites 2018*, vol. 2, pp. 880–892, 2018.

[24] P. I. Karkanas and I. K. Partridge, "Cure modeling and monitoring of epoxy/amine resin systems. II. Network formation and chemoviscosity modeling," *Journal of Applied Polymer Science*, vol. 77, no. 10, pp. 2178–2188, 2000.

[25] C.-y. M. Tung and P. J. Dynes, "Relationship between Viscoelastic Properties and Gelation in Thermosetting Systems," *Journal of Applied Polymer Science*, vol. 27, no. I, pp. 569–574, 1982.

[26] M. R. Martínez-Miranda, V. García-Martínez, and M. R. Gude, "Gel point determination of a thermoset prepreg by means of rheology," *Polymer Testing*, vol. 78, no. June, p. 105950, 2019.

[27] M. Libor, "Rheology of epoxy networks near the gel point," *Polymer Bulletin*, vol. 116, pp. 109–116, 1991.

[28] M. Hayaty, M. H. Beheshty, and M. Esfandeh, "A new approach for determination of gel time of a glass/epoxy prepreg," *Journal of Applied Polymer Science*, vol. 120, pp. 1483–1489, may 2011.

[29] Y. A. Msallem, F. Jacquemin, and A. Poitou, "Residual stresses formation during the manufacturing process of epoxy matrix composites: Resin yield stress and anisotropic chemical shrinkage," *International Journal of Material Forming*, vol. 3, no. SUPPL. 2, pp. 1363–1372, 2010.

[30] R. Cardinaud, *Couplages thermo - cinétique et mécanique lors de la mise en forme par compression de SMC hautes performances*. PhD thesis, University of Nantes, 2017.

[31] M. Xie, Z. Zhang, Y. Gu, M. Li, and Y. Su, "A new method to characterize the cure state of epoxy prepreg by dynamic mechanical analysis," *Thermochimica Acta*, vol. 487, pp. 8–17, apr 2009.

[32] G. Kister and E. Dossi, "Cure monitoring of CFRP composites by dynamic mechanical analyser," *Polymer Testing*, vol. 47, pp. 71–78, 2015.

[33] J. Jakobsen, M. Jensen, and J. H. Andreasen, "Thermo-mechanical characterisation of in-plane properties for CSM E-glass epoxy polymer composite materials - Part 2: Young's modulus," *Polymer Testing*, vol. 32, no. 8, pp. 1417–1422, 2013.

[34] N. Ersoy, T. Garstka, K. Potter, M. R. Wisnom, D. Porter, M. Clegg, and G. Stringer, "Development of the properties of a carbon fibre reinforced thermosetting composite through cure," *Composites Part A: Applied Science and Manufacturing*, vol. 41, pp. 401–409, mar 2010.

[35] M. Ivankovic, L. Incarnato, J. M. Kenny, and L. Nicolais, "Curing kinetics and chemorheology of epoxy/anhydride system," *Journal of Applied Polymer Science*, vol. 90, no. 11, pp. 3012–3019, 2003.

[36] R. Geissberger, J. Maldonado, N. Bahamonde, A. Keller, C. Dransfeld, and K. Masania, "Rheological modelling of thermoset composite processing," *Composites Part B: Engineering*, vol. 124, pp. 182–189, 2017.

[37] G. Nikolic, S. Zlatkovic, M. Cakic, S. Cakic, C. Lacnjevac, and Z. Rajic, "Fast fourier transform IR characterization of epoxy GY systems crosslinked with aliphatic and cycloaliphatic EH polyamine adducts," *Sensors*, vol. 10, no. 1, pp. 684–696, 2010.

[38] M. Peron, *Mesure et modélisation des phénomènes de retraits anisotropes dans les matériaux composites durant leur mise en forme.* PhD thesis, University of Nantes, 2016.

[39] H. Corporation, "HexPly ® M21," pp. 1–6, 2015.

[40] P. Zhang, W. Yao, X. Hu, and T. Q. Bui, "3D micromechanical progressive failure simulation for fiber-reinforced composites," *Composite Structures*, vol. 249, no. June, 2020.

[41] T. Curiel and G. Fernlund, "Deformation and stress build-up in bi-material beam specimens with a curing FM300 adhesive interlayer," *Composites Part A: Applied Science and Manufacturing*, vol. 39, no. 2, pp. 252–261, 2008.

[42] S. Saseendran, M. Wysocki, and J. Varna, "Cure-state dependent viscoelastic Poisson's ratio of LY5052 epoxy resin," *Advanced Manufacturing: Polymer and Composites Science*, vol. 3, no. 3, pp. 92–100, 2017.

[43] E. Jacquet, F. Trivaudey, and D. Varchon, "Calculation of the transverse modulus of a unidirectional composite material and of the modulus of an aggregate. Application of the rule of mixtures," *Composites Science and Technology*, vol. 60, no. 3, pp. 345–350, 2000.

[44] J. Cinquin, "Les composites en Aerospatial," *Technique de l'ingénieur*, vol. AM5, no. 645, pp. 1–14, 2002.

[45] D. Sheet, "HexTow IMA Carbon Fiber Product Data Sheet," vol. 000, pp. 1–2, 2016.

[46] Y. Abou Msallem, F. Jacquemin, N. Boyard, A. Poitou, D. Delaunay, and S. Chatel, "Material characterization and residual stresses simulation during the manufacturing process of epoxy matrix composites," *Composites Part A: Applied Science and Manufacturing*, vol. 41, no. 1, pp. 108–115, 2010.

[47] B. Piquet and L. Blumendeld, "A350XWB Special Edition," *Airbus Technical Magazine*, no. June, p. 25, 2013.

[48] D. Zhang, Q. Zhang, X. Fan, and S. Zhao, "Review on Joining Process of Carbon Fiber-Reinforced Polymer and Metal: Methods and Joining Process," *Xiyou Jinshu Cailiao Yu Gongcheng/Rare Metal Materials and Engineering*, vol. 47, no. 12, pp. 3686–3696, 2018.

[49] Total Foundations, "Fuels in Aviation and Shipping," pp. 1–5, 2019.

[50] I. Hamerton and L. Mooring, "The use of thermosets in aerospace applications," in *Thermosets*, ch. 7, pp. 189–227, Elsevier, 2012.

[51] F. Campbell, *Structural Composite Materials*. ASM International, 2010.

[52] D. Ratna, "Handbook of Thermoset Resins," Smithers Rapra technology, United Kingdom, 2009.

[53] M. Asim, M. Jawaid, N. Saba, Ramengmawii, M. Nasir, and M. T. H. Sultan, "Processing of hybrid polymer composites—a review," in *Hybrid Polymer Composite Materials*, pp. 1–22, Elsevier, 2017.

[54] D. Ratna, "Epoxy Composites: Impact Resistance and Flame Retardancy," Tech. Rep. 5, 2005.

[55] C. B. Bucknall, *Toughened Plastics*, vol. 18. Dordrecht: Springer Netherlands, oct 1977.

[56] S. Mortimer and J. Cawse, "THERMOPLASTIC TOUGHENING MATERIAL AND RELATED METHOD," 2011.

[57] G. Di Pasquale, O. Motta, A. Recca, J. T. Carter, P. T. McGrail, and D. Acierno, "New high-performance thermoplastic toughened epoxy thermosets," *Polymer*, vol. 38, no. 17, pp. 4345–4348, 1997.

[58] C. Girodet, E. Espuche, H. Sautereau, B. Chabert, R. Ganga, and E. Valot, "Influence of the addition of thermoplastic preformed particles on the properties of an epoxy/anhydride network," *Journal of Materials Science*, vol. 31, no. 11, pp. 2997–3002, 1996.

[59] A. J. Kinloch, M. L. Yuen, and S. D. Jenkins, "Thermoplastic-toughened epoxy polymers," *Journal of Materials Science*, vol. 29, no. 14, pp. 3781–3790, 1994.

[60] M. Jabbar and A. Nasreen, "Composite fabrication and joining," in *Composite Solutions for Ballistics*, pp. 177–197, Elsevier, 2021.

[61] N. Sela and O. Ishai, "Interlaminar fracture toughness and toughening of laminated composite materials: a review," *Composites*, vol. 20, no. 5, pp. 423–435, 1989.

[62] C. Hunt, J. Kratz, and I. K. Partridge, "Cure path dependency of mode i fracture toughness in thermoplastic particle interleaf toughened prepreg laminates," *Composites Part A: Applied Science and Manufacturing*, vol. 87, pp. 109–114, 2016.

[63] M. Yasaee, I. Bond, R. Trask, and E. Greenhalgh, "Mode I interfacial toughening through discontinuous interleaves for damage suppression and control," *Composites Part A: Applied Science and Manufacturing*, vol. 43, pp. 198–207, jan 2012.

[64] D. Tilbrook, D. Blair, M. Boyle, and P. MacKenzie, "Composite materials with blend of thermoplastic particles," 2010.

[65] T. Tanimoto, "Improving the fatigue resistance of carbon/epoxy laminates with dispersed-particle interlayers," *Acta Materialia*, vol. 46, no. 7, pp. 2455–2460, 1998.

[66] M. Artun, S. L. Peake, and S. S. Kaminski, "Advance composites with thermoplastic particles at the interface between layers," 1990.

[67] D. BROSIUS, "Boeing 787 Update, available online," *Composite World magazine*, 2009.

[68] "HexPly® Technology Prepreg,"

[69] P. Hubert, T. Centea, L. Grunefelder, S. Nutt, J. Kratz, and A. Levy, "Out-of-Autoclave Prepreg Processing," in *Comprehensive Composite Materials II*, pp. 63–94, Elsevier, 2018.

[70] M. Djabourov, "Gelation-A Review," *Polymer International*, vol. 25, pp. 135–143, 1991.

[71] H. H. Winter and F. Chambon, "Analysis of Linear Viscoelasticity of a Crosslinking Polymer at the Gel Point," *Journal of Rheology*, vol. 30, pp. 367–382, apr 1986.

[72] P. J. Halley and M. E. Mackay, "Chemorheology of thermosets - An overview," *Polymer Engineering & Science*, vol. 36, pp. 593–609, mar 1996.

[73] J. B. Enns and J. K. Gillham, "Time-Temperature-Transformation (TTT) Cure Diagram : Modeling the Cure Behavior of Thermosets," *Journal of Applied Polymer Science*, vol. 28, pp. 2567–2591, 1983.

[74] J. P. Pascault and R. J. J. Williams, "Glass transition temperature versus conversion relationships for thermosetting polymers," *Journal of Polymer Science Part B: Polymer Physics*, vol. 28, pp. 85–95, jan 1990.

[75] A. Hale, C. W. Macosko, and H. E. Bair, "Glass Transition Temperature as a Function of Conversion in Thermosetting Polymers," *Macromolecules*, vol. 24, no. 9, pp. 2610–2621, 1991.

[76] K. D. Potter, "Understanding the origins of defects and variability in composites manufacture," *ICCM International Conferences on Composite Materials*, 2009.

[77] P. P. Parlevliet, H. E. Bersee, and A. Beukers, "Residual stresses in thermoplastic composites – a study of the literature. Part III: Effects of thermal residual stresses," *Composites Part A: Applied Science and Manufacturing*, vol. 38, pp. 1581–1596, jun 2007.

[78] M. R. Wisnom, M. Gigliotti, N. Ersoy, M. Campbell, and K. D. Potter, "Mechanisms generating residual stresses and distortion during manufacture of polymer-matrix composite structures," *Composites Part A: Applied Science and Manufacturing*, vol. 37, no. 4, pp. 522–529, 2006.

[79] E. Kappel, "Forced-interaction and spring-in - Relevant initiators of process-induced distortions in composite manufacturing," *Composite Structures*, vol. 140, pp. 217–229, 2016.

[80] Y. Abou Msallem, N. Boyard, F. Jaquemin, A. Poitou, D. Delaunay, and S. Chatel, "Identification of thermal and rheological properties of an aeronautic epoxy resin-simulation of residual stresses," *International Journal of Material Forming*, vol. 1, pp. 579–582, apr 2008.

[81] Y. Abou Msallem, *Caractérisation thermique et mécanique d'un matériau composite aéronautique pendant le procédé d'élaboration - Contribution à l'estimation des contraintes résiduelles.* PhD thesis, Université de nantes, 2008.

[82] R. Kulkarni and O. Ochoa, "Transverse and longitudinal CTE measurements of carbon fibers and their impact on interfacial residual stresses in composites," *Journal of Composite Materials*, vol. 40, no. 8, pp. 733–754, 2006.

[83] C. Pradere and C. Sauder, "Transverse and longitudinal coefficient of thermal expansion of carbon fibers at high temperatures (300-2500 K)," *Carbon*, vol. 46, no. 14, pp. 1874–1884, 2008.

[84] M. Huson, "High-performance pitch-based carbon fibers," in *Structure and Properties of High-Performance Fibers*, pp. 31–78, Elsevier, 2017.

[85] R. H. Nelson and D. S. Cairns, "Prediction of dimensional changes in composite laminates during cure," 1989.

[86] D. W. Radford and T. S. Rennick, "Separating Sources of Manufacturing Distortion in Laminated Composites," *Journal of Reinforced Plastics and Composites*, vol. 19, pp. 621–641, may 2000.

[87] N. Ersoy, K. Potter, M. R. Wisnom, and M. J. Clegg, "Development of spring-in angle during cure of a thermosetting composite," *Composites Part A: Applied Science and Manufacturing*, vol. 36, pp. 1700–1706, dec 2005.

[88] C. Albert and G. Fernlund, "Spring-in and warpage of angled composite laminates," *Composites Science and Technology*, vol. 62, no. 14, pp. 1895–1912, 2002.

[89] M. R. Wisnom, K. D. Potter, and N. Ersoy, "Shear-lag analysis of the effect of thickness on spring-in of curved composites," *Journal of Composite Materials*, vol. 41, no. 11, pp. 1311–1324, 2007.

[90] O. G. Kravchenko, S. G. Kravchenko, and R. B. Pipes, "Cure history dependence of residual deformation in a thermosetting laminate," *Composites Part A: Applied Science and Manufacturing*, vol. 99, pp. 186–197, 2017.

[91] M. Engineering and A. Austin, "Identification of the Most Significant Processing Parameters on the Development of Fiber Waviness in Thin Laminates," vol. 36, no. 12, 2002.

[92] P. Hubert, *Aspects of flow and compaction of laminated composite shapes during cure.* PhD thesis, 1996.

[93] P. Hubert and A. Poursartip, "A Review of Flow and Compaction Modelling Relevant to Thermoset Matrix Laminate Processing," *Journal of Reinforced Plastics and Composites*, vol. 17, pp. 286–318, mar 1998.

[94] H. Hahn and N. Pagano, "Curing Stresses in Composite Laminates," *Journal of Composite Materials*, vol. 9, pp. 91–106, jan 1975.

[95] W. A. Schulz, D. G. Myers, T. N. Singer, P. G. Ifju, and R. T. Haftka, "Determination of residual stress and thermal history for IM7/977-2 composite laminates," *Composites Science and Technology*, vol. 65, pp. 2014–2024, oct 2005.

[96] N. Zobeiry, "Viscoelastic constitutive models for evaluation of residual stresses in thermoset composites during cure," no. July, 2006.

[97] T. M. Wang, I. M. Daniel, and J. T. Gotro, "Thermoviscoelastic Analysis of Residual Stresses and Warpage in Composite Laminates," *Journal of Composite Materials*, vol. 26, no. 6, pp. 883–899, 1992.

[98] B. D. Harper and Y. Weitsman, "On the effects of environmental conditioning on residual stresses in composite laminates," *International Journal of Solids and Structures*, vol. 21, no. 8, pp. 907–926, 1985.

[99] M. M. Shokrieh and S. M. Kamali Shahri, "Modeling residual stresses in composite materials," in *Residual Stresses in Composite Materials*, pp. 193–213, Elsevier, 2 ed., 2021.

[100] H. W. Wiersma, L. J. Peeters, and R. Akkerman, "Prediction of springforward in continuous-fibre/polymer L-shaped parts," *Composites Part A: Applied Science and Manufacturing*, vol. 29, no. 11, pp. 1333–1342, 1998.

[101] Q. Zhu, P. H. Geubelle, M. Li, and C. L. Tucker, "Dimensional accuracy of thermoset composites: Simulation of process-induced residual stresses," *Journal of Composite Materials*, vol. 35, no. 24, pp. 2171–2205, 2001.

[102] Y. Nawab, S. Shahid, N. Boyard, and F. Jacquemin, "Chemical shrinkage characterization techniques for thermoset resins and associated composites," *Journal of Materials Science*, vol. 48, no. 16, pp. 5387–5409, 2013.

[103] Y. Nawab, N. Boyard, and F. Jaquemin, "Effect of pressure and reinforcement type on the volume chemical shrinkage in thermoset resin and composite," *Journal of Composite Materials*, vol. 48, no. 26, pp. 3191–3199, 2014.

[104] P. A. Olivier, "A note upon the development of residual curing strains in carbon/epoxy laminates. Study by thermomechanical analysis," *Composites Part A: Applied Science and Manufacturing*, vol. 37, no. 4, pp. 602–616, 2006.

[105] J. Jakobsen, M. Jensen, and J. H. Andreasen, "Thermo-mechanical characterisation of in-plane properties for CSM E-glass epoxy polymer composite materials - Part 1: Thermal and chemical strain," *Polymer Testing*, vol. 32, no. 8, pp. 1350–1357, 2013.

[106] J. Parameswaranpillai, A. George, J. Pionteck, and S. Thomas, " Investigation of Cure Reaction, Rheology, Volume Shrinkage and Thermomechanical Properties of Nano-TiO 2 Filled Epoxy/DDS Composites ," *Journal of Polymers*, vol. 2013, pp. 1–17, 2013.

[107] J. T. Tsai, J. S. Dustin, and J. A. Mansson, "Cure strain monitoring in composite laminates with distributed optical sensor," *Composites Part A: Applied Science and Manufacturing*, vol. 125, no. June, p. 105503, 2019.

[108] M. Mulle, F. Collombet, P. Olivier, R. Zitoune, C. Huchette, F. Laurin, and Y. H. Grunevald, "Assessment of cure-residual strains through the thickness of carbon-epoxy laminates using FBGs Part II: Technological specimen," *Composites Part A: Applied Science and Manufacturing*, vol. 40, no. 10, pp. 1534–1544, 2009.

[109] H. Hu, D. Cao, M. Pavier, Y. Zhong, L. Zu, L. Liu, and S. Li, "Investigation of non-uniform gelation effects on residual stresses of thick laminates based on tailed FBG sensor," *Composite Structures*, vol. 202, no. April, pp. 1361–1372, 2018.

[110] S. Minakuchi, "In situ characterization of direction-dependent cure-induced shrinkage in thermoset composite laminates with fiber-optic sensors embedded in through-thickness and in-plane directions," *Journal of Composite Materials*, vol. 49, no. 9, pp. 1021–1034, 2015.

[111] T. C. Chu, W. F. Ranson, and M. A. Sutton, "Applications of digital-image-correlation techniques to experimental mechanics," *Experimental Mechanics*, vol. 25, no. 3, pp. 232–244, 1985.

[112] G. Singer, G. Sinn, H. C. Lichtenegger, S. Veigel, M. Zecchini, and R. Wan-Wendner, "Evaluation of in-situ shrinkage and expansion properties of polymer composite materials for adhesive anchor systems by a novel approach based on digital image correlation," *Polymer Testing*, vol. 79, no. July, p. 106035, 2019.

[113] K. R. Knowles, J. Tu, and J. S. Wiggins, "Thermal and volumetric property analysis of polymer networks and composites using elevated temperature digital image correlation," *Polymer Testing*, vol. 58, pp. 48–53, 2017.

[114] S. Heinz, J. Tu, M. Jackson, and J. Wiggins, "Digital image correlation analysis of strain recovery in glassy polymer network isomers," *Polymer*, vol. 82, pp. 87–92, 2016.

[115] V. A. Costa and A. C. Sousa, "Modeling of flow and thermo-kinetics during the cure of thick laminated composites," *International Journal of Thermal Sciences*, vol. 42, no. 1, pp. 15–22, 2003.

[116] W.-b. Young, "Consolidation and Cure Simulations for Laminated Composites," *Polymer Composites*, vol. 17, no. 1, 1996.

[117] M. Li, Y. Gu, Z. Zhang, and Z. Sun, "A simple method for the measurement of compaction and corresponding transverse permeability of composite prepregs," *Polymer Composites*, vol. 28, pp. 61–70, feb 2007.

[118] P. Hubert and A. Poursartip, "Aspects of the compaction of composite angle laminates: an experimental investigation," *Journal of Composite Materials*, vol. 35, no. 1, pp. 2–26, 2001.

[119] T. G. Gutowski, Z. Cai, S. Bauer, D. Boucher, J. Kingery, and S. Wineman, "Consolidation Experiments for Laminate Composites," *Journal of Composite Materials*, vol. 21, no. 7, pp. 650–669, 1987.

[120] O. Nixon-Pearson, J.-H. Belnoue, D. Ivanov, K. Potter, and S. Hallett, "An experimental investigation of the consolidation behaviour of uncured prepregs under processing conditions," *Journal of Composite Materials*, vol. 51, pp. 1911–1924, jun 2017.

[121] S. R. Hallett, S. G. Advani, G. Sorba, C. Binetruy, E. Syerko, and A. Leygue, "Multi-scale modelling of non-uniform consolidation of uncured toughened unidirectional prepregs," vol. 020032, 2018.

[122] S. Thomas and S. R. Nutt, "Temperature dependence of tesin flow in a Resin Film Infusion (RFI) process by ultrasound imaging," *Applied Composite Materials*, vol. 16, no. 3, pp. 183–196, 2009.

[123] T. A. Cender, P. Simacek, and S. G. Advani, "Resin film impregnation in fabric prepregs with dual length scale permeability," *Composites Part A: Applied Science and Manufacturing*, vol. 53, pp. 118–128, 2013.

[124] T. A. Cender, J. J. Gangloff, P. Simacek, and S. G. Advani, "Void reduction during out-of-autoclave thermoset prepreg composite processing," *International SAMPE Technical Conference*, no. May 2015, 2014.

[125] R. Harshe, "A review on advanced out-of-autoclave composites processing," *Journal of the Indian Institute of Science*, vol. 95, no. 3, pp. 207–220, 2015.

[126] M. Mehdikhani, L. Gorbatikh, I. Verpoest, and S. V. Lomov, "Voids in fiber-reinforced polymer composites: A review on their formation, characteristics, and effects on mechanical performance," *Journal of Composite Materials*, vol. 53, no. 12, pp. 1579–1669, 2019.

[127] L. Grunenfelder and S. Nutt, "Void formation in composite prepregs – Effect of dissolved moisture," *Composites Science and Technology*, vol. 70, pp. 2304–2309, dec 2010.

[128] R. Helmus, T. Centea, P. Hubert, and R. Hinterhölzl, "Out-of-autoclave prepreg consolidation: Coupled air evacuation and prepreg impregnation modeling," *Journal of Composite Materials*, vol. 50, no. 10, pp. 1403–1413, 2016.

[129] J. M. Maguire, P. Simacek, S. G. Advani, and C. M. Ó Brádaigh, "Novel epoxy powder for manufacturing thick-section composite parts under vacuum-bag-only conditions. Part I: Through-thickness process modelling," *Composites Part A: Applied Science and Manufacturing*, vol. 136, no. May, p. 105969, 2020.

[130] P. R. Ciriscioli, Q. Wang, and G. S. Springer, "Autoclave Curing — Comparisons of Model and Test Results," *Journal of Composite Materials*, vol. 26, no. 1, pp. 90–102, 1992.

[131] T. E. Saliba, D. Hofmann, and P. Smolinski, "Development of an in situ Hall-effect sensor for on-line monitoring of thickness and compaction during composite curing," *Composites Science and Technology*, vol. 51, no. 1, pp. 1–9, 1994.

[132] M. M. Thomas, B. Joseph, and J. L. Kardos, "Experimental characterization of autoclave-cured glass-epoxy composite laminates: Cure cycle effects upon thickness, void content, and related phenomena," *Polymer Composites*, vol. 18, pp. 283–299, jun 1997.

[133] T. Centea and P. Hubert, "Measuring the impregnation of an out-of-autoclave prepreg by micro-CT," *Composites Science and Technology*, vol. 71, no. 5, pp. 593–599, 2011.

[134] T. Centea and P. Hubert, "Out-of-autoclave prepreg consolidation under deficient pressure conditions," *Journal of Composite Materials*, vol. 48, no. 16, pp. 2033–2045, 2014.

[135] S. Sassi, P. Marguerès, P. Olivier, and R. Le Begue, "Determination of anisotropic geometrical parameters for the electrical characterization of carbon/epoxy composite during oven curing," *Composites Part A: Applied Science and Manufacturing*, vol. 80, pp. 204–216, jan 2016.

[136] M. Yeager, W. R. Hwang, and S. G. Advani, "Prediction of capillary pressure for resin flow between fibers," *Composites Science and Technology*, vol. 126, pp. 130–138, 2016.

[137] M. Li, S. K. Wang, Y. Z. Gu, Y. X. Li, K. Potter, and Z. G. Zhang, "Evaluation of through-thickness permeability and the capillary effect in vacuum assisted liquid molding process," *Composites Science and Technology*, vol. 72, no. 8, pp. 873–878, 2012.

[138] F. LeBel, A. E. Fanaei, E. Ruiz, and F. Trochu, "Experimental characterization by fluorescence of capillary flows in dual-scale engineering fabrics," *Textile Research Journal*, vol. 83, pp. 1634–1659, sep 2013.

[139] N. Zobeiry and C. Duffner, "Measuring the negative pressure during processing of advanced composites," *Composite Structures*, vol. 203, no. June, pp. 11–17, 2018.

[140] Y. A. Tajima and D. Crozier, "Thermokinetic modeling of an epoxy resin I. Chemoviscosity," *Polymer Engineering and Science*, vol. 23, pp. 186–190, mar 1983.

[141] P. J. Halley, M. E. Mackay, and G. A. George, "Determining the gel point of an epoxy resin by various theological methods," *High Performance Polymers*, vol. 6, pp. 405–414, aug 1994.

[142] H. H. Winter and M. Mours, "Rheology of Polymers Near Liquid-Solid Transitions," in *Neutron Spin Echo Spectroscopy Viscoelasticity Rheology*, pp. 165–234, Berlin, Heidelberg: Springer Berlin Heidelberg, 1997.

[143] F. Chambon and H. H. Winter, "Linear Viscoelasticity at the Gel Point of a Crosslinking PDMS with Imbalanced Stoichiometry," *Journal of Rheology*, vol. 31, pp. 683–697, nov 1987.

[144] D. Lairez, J. R. Emery, D. Durand, and M. Adam, "Rheological Behavior of an Epoxy/Amine System near the Gel Point," *Macromolecules*, vol. 25, no. 1, pp. 286–289, 1992.

[145] K. Mphahlele, S. S. Ray, and A. Kolesnikov, "Cure kinetics, morphology development, and rheology of a high-performance carbon-fiber-reinforced epoxy composite," *Composites Part B: Engineering*, vol. 176, no. April 2018, p. 107300, 2019.

[146] M. Leali Costa, E. Cocchieri Botelho, and J. Maria Faulstich de Paiva, "Characterization of Cure of Carbon / Epoxy Prepreg Used in Aerospace Field," *Materials Research*, vol. 8, no. 3, pp. 317–322, 2005.

[147] J. C. Scanlan and H. H. Winter, "Composition dependence of the viscoelasticity of end-linked poly(dimethylsiloxane) at the gel point," *Macromolecules*, vol. 24, pp. 47–54, jan 1991.

[148] S. R. Raghavan, L. A. Chen, C. McDowell, S. A. Khan, R. Hwang, and S. White, "Rheological study of crosslinking and gelation in chlorobutyl elastomer systems," *Polymer*, vol. 37, pp. 5869–5875, jan 1996.

[149] A. Cadenato, J. M. Salla, X. Ramis, J. M. Morancho, L. M. Marroyo, and J. L. Martin, "Determination of gel and vitrification times of thermoset curing process by means of TMA, DMTA and DSC techniques: TTT diagram," *Journal of Thermal Analysis*, vol. 49, no. 1, pp. 269–279, 1997.

[150] B. Bilyeu, W. Brostow, and K. P. Menard, "Separation of gelation from vitrification in curing of a fiber-reinforced epoxy composite," *Polymer Composites*, vol. 23, pp. 1111–1119, dec 2002.

[151] X. Ramis, A. Cadenato, J. M. Morancho, and J. M. Salla, "Curing of a thermosetting powder coating by means of DMTA, TMA and DSC," *Polymer*, 2003.

[152] E. C. Bingham, "An investigation of the laws of plastic flow," in *Bulletin of the Bureau of Standards*, vol. 13, p. 309, aug 1916.

[153] M. Dinkgreve, J. Paredes, M. M. Denn, and D. Bonn, "On different ways of measuring "the" yield stress," *Journal of Non-Newtonian Fluid Mechanics*, vol. 238, pp. 233–241, dec 2016.

[154] P. Saramito, "A new constitutive equation for elastoviscoplastic fluid flows," *Journal of Non-Newtonian Fluid Mechanics*, vol. 145, pp. 1–14, aug 2007.

[155] R. A. Brockman, C. W. Lee, T. M. Storage, and B. L. Volk, "Omc processing simulation using an elastic-viscoplastic material model," *International SAMPE Technical Conference*, vol. 2015-Janua, 2015.

[156] K. Hyun, M. Wilhelm, C. O. Klein, K. Soo, J. Gun, K. Hyun, S. Jong, R. H. Ewoldt, and G. H. Mckinley, "A review of nonlinear oscillatory shear tests : Analysis and application of large amplitude oscillatory shear (LAOS)," *Progress in Polymer Science*, vol. 36, no. 12, pp. 1697–1753, 2011.

[157] W. Stark, M. Jaunich, and J. McHugh, "Cure state detection for pre-cured carbon-fibre epoxy prepreg (CFC) using Temperature-Modulated Differential Scanning Calorimetry (TMDSC)," *Polymer Testing*, 2013.

[158] W. Stark, M. Jaunich, and J. McHugh, "Dynamic Mechanical Analysis (DMA) of epoxy carbon-fibre prepregs partially cured in a discontinued autoclave analogue process," *Polymer Testing*, vol. 41, pp. 140–148, feb 2015.

[159] D. B. Shah, K. M. Patel, S. J. Joshi, B. A. Modi, A. I. Patel, and V. Pariyal, "Thermo-mechanical characterization of carbon fiber composites with different epoxy resin systems," *Thermochimica Acta*, vol. 676, pp. 39–46, jun 2019.

[160] J. Domínguez, "Rheology and curing process of thermosets," in *Thermosets*, pp. 115–146, Elsevier, 2018.

[161] G. Lelli, "Modelling of the Chemo–Rheological Behavior of Thermosetting Polymer Nanocomposites," *Polymers and Polymer Composites*, vol. 16, no. 2, pp. 101–113, 2008.

[162] C. Paris, *Etude et Modélisation de la Polymérisation Dynamique de Composites à Matrice Thermodurcissable*. PhD thesis, University of Toulouse, 2011.

[163] Y. LEDRU, *Etude de la porosité dans les matériaux composites stratifiés aeronautiques*. PhD thesis, University of Toulouse, 2009.

[164] I. T. Smith, "The mechanism of the crosslinking of epoxide resins by amines," *Polymer*, vol. 2, no. C, pp. 95–108, 1961.

[165] C. C. Riccardi and R. J. Williams, "A kinetic scheme for an amine-epoxy reaction with simultaneous etherification," *Journal of Applied Polymer Science*, vol. 32, no. 2, pp. 3445–3456, 1986.

[166] A. Yousefi, P. G. Lafleur, and R. Gauvin, "Kinetic studies of thermoset cure reactions: A review," *Polymer Composites*, vol. 18, no. 2, pp. 157–168, 1997.

[167] J. K. Stevenson, "Free radical polymerization models for simulating reactive processing," *Polymer Engineering & Science*, vol. 26, no. 11, pp. 746–759, 1986.

[168] D.-S. Lee and C. D. Han, "Effect of particulates and fiber reinforcements on the curing behavior of unsaturated polyester resin," *Journal of Applied Polymer Science*, vol. 33, pp. 419–429, feb 1987.

[169] R. B. Prime, "Differential scanning calorimetry of the epoxy cure reaction," *Polymer Engineering & Science*, vol. 13, no. 5, pp. 365–371, 1973.

[170] M. R. Kamal and S. Sourour, "Kinetics and thermal characterization of thermoset cure," *Polymer Engineering & Science*, vol. 13, no. 1, pp. 59–64, 1973.

[171] S. Sourour and M. R. Kamal, "Differential scanning calorimetry of epoxy cure: isothermal cure kinetics," *Thermochimica Acta*, vol. 14, no. 1-2, pp. 41–59, 1976.

[172] C. M. Lin, C. I. Weng, and C. T. Ho, "Kinetic parameters estimation for unsaturated polyester-styrene systems," *Polymer Engineering and Science*, vol. 40, no. 2, pp. 290–299, 2000.

[173] D. J. Michaud, A. N. Beris, and P. S. Dhurjati, "Curing Behavior of Thick-Sectioned RTM Composites," *Journal of Composite Materials*, vol. 32, pp. 1273–1296, jul 1998.

[174] C. L. Lee and K. H. Wei, "Curing kinetics and viscosity change of a two-part epoxy resin during mold filling in resin-transfer molding process," *Journal of Applied Polymer Science*, vol. 77, no. 10, pp. 2139–2148, 2000.

[175] B. De Parscau Du Plessix, F. Jacquemin, P. Lefébure, and S. Le Corre, "Characterization and modeling of the polymerization-dependent moisture absorption behavior of an epoxy-carbon fiber-reinforced composite material," *Journal of Composite Materials*, vol. 50, no. 18, pp. 2495–2505, 2016.

[176] Y. Ledru, G. Bernhart, R. Piquet, F. Schmidt, and L. Michel, "Coupled visco-mechanical and diffusion void growth modelling during composite curing," *Composites Science and Technology*, vol. 70, no. 15, pp. 2139–2145, 2010.

[177] J.-L. Bailleul, *Optimisation du cycle de cuisson de pièce épaisses en matériau composite. Application à un préimprégné résine époxyde / fibres de verre.* PhD thesis, University of Nantes, 1997.

[178] E. Ruiz and F. Trochu, "Numerical analysis of cure temperature and internal stresses in thin and thick RTM parts," *Composites Part A: Applied Science and Manufacturing*, vol. 36, no. 6, pp. 806–826, 2005.

[179] R. Hardis, J. L. P. Jessop, F. E. Peters, and M. R. Kessler, "Cure kinetics characterization and monitoring of an epoxy resin using DSC, Raman spectroscopy, and DEA," *Composites Part A: Applied Science and Manufacturing*, vol. 49, pp. 100–108, 2013.

[180] N. BOYARD, A. MILLISCHER, V. SOBOTKA, J. BAILLEUL, and D. DELAUNAY, "Behaviour of a moulded composite part: Modelling of dilatometric curve (constant pressure) or pressure (constant volume) with temperature and conversion degree gradients," *Composites Science and Technology*, vol. 67, pp. 943–954, may 2007.

[181] M. Péron, V. Sobotka, N. Boyard, and S. Le Corre, "Bulk modulus evolution of thermoset resins during crosslinking: Is a direct and accurate measurement possible?," *Journal of Composite Materials*, vol. 51, no. 4, pp. 463–477, 2017.

[182] C. Ip, "Calsil™ ip 50-1000 1.," no. May, pp. 1–2, 2013.

[183] M. Péron, R. Cardinaud, N. Lefèvre, J. Aubril, V. Sobotka, N. Boyard, and S. Le Corre, "PvT-HADDOC: A multi-axial strain analyzer and cure monitoring device for thermoset composites characterization during manufacturing," *Composites Part A: Applied Science and Manufacturing*, vol. 101, pp. 129–142, oct 2017.

[184] B. De Parscau du Plessix, P. Lefébure, N. Boyard, S. Le Corre, N. Lefèvre, F. Jacquemin, V. Sobotka, and S. Rolland du Roscoat, "In situ real-time 3D observation of porosity growth during composite part curing by ultra-fast synchrotron X-ray microtomography," *Journal of Composite Materials*, vol. 53, no. 28-30, pp. 4105–4116, 2019.

[185] L. Moretti, *Simulation des distorsions de cuisson de pièces composites élaborées par co-bonding en autoclave*. PhD thesis, Toulouse, 2019.

[186] T. Frerich, C. Brauner, J. Jendrny, and A. S. Hermann, "Modeling the influence of interleaf layers in composite materials on elastic properties, thermal expansion, and chemical shrinkage," *Journal of Composite Materials*, vol. 53, pp. 2415–2428, jul 2019.

[187] E. Kappel and R. Prussak, "On abnormal thermal-expansion properties of more orthotropic M21E/IMA carbon-fiber-epoxy laminates," *Composites Communications*, vol. 17, no. October 2019, pp. 129–133, 2020.

[188] C. Li, K. Potter, M. R. Wisnom, and G. Stringer, "In-situ measurement of chemical shrinkage of MY750 epoxy resin by a novel gravimetric method," *Composites Science and Technology*, vol. 64, no. 1, pp. 55–64, 2004.

[189] H. Yu, S. G. Mhaisalkar, and E. H. Wong, "Cure shrinkage measurement of nonconductive adhesives by means of a thermomechanical analyzer," *Journal of Electronic Materials*, vol. 34, no. 8, pp. 1177–1182, 2005.

[190] Y. Wang and Z. Huang, "Analytical Micromechanics Models for Elastoplastic Behavior of Long Fibrous Composites: A Critical Review and Comparative Study," *Materials*, vol. 11, p. 1919, oct 2018.

[191] P. Kanouté, D. P. Boso, J. L. Chaboche, and B. A. Schrefler, "Multiscale Methods for Composites: A Review," *Archives of Computational Methods in Engineering*, vol. 16, pp. 31–75, mar 2009.

[192] J. D. Eshelby, "The determination of the elastic field of an ellipsoidal inclusion, and related problems," *Proceedings of the Royal Society of London. Series A. Mathematical and Physical Sciences*, vol. 241, pp. 376–396, aug 1957.

[193] R. Hill, "A self-consistent mechanics of composite materials," *Journal of the Mechanics and Physics of Solids*, vol. 13, pp. 213–222, aug 1965.

[194] T. Mori and K. Tanaka, "Average stress in matrix and average elastic energy of materials with misfitting inclusions," *Acta Metallurgica*, vol. 21, pp. 571–574, may 1973.

[195] T. A. Bogetti and J. W. Gillespie, "Process-Induced Stress and Deformation in Thick-Section Thermoset Composite Laminates," *Journal of Composite Materials*, vol. 26, pp. 626–660, mar 1992.

[196] E. Lacoste, S. Fréour, and F. Jacquemin, "A Multi-Scale Study of Residual Stresses Created during the Cure Process of a Composite Tooling Material," *Materials Science Forum*, vol. 681, pp. 309–314, mar 2011.

[197] W. Voigt, "Ueber die Beziehung zwischen den beiden Elasticitätsconstanten isotroper Körper," *Annalen der Physik*, vol. 274, no. 12, pp. 573–587, 1889.

[198] A. Reuss, "Berechnung der Fließgrenze von Mischkristallen auf Grund der Plastizitätsbedingung für Einkristalle .," *ZAMM - Zeitschrift für Angewandte Mathematik und Mechanik*, vol. 9, no. 1, pp. 49–58, 1929.

[199] Z. Hashin and S. Shtrikman, "A variational approach to the theory of the elastic behaviour of multiphase materials," *Journal of the Mechanics and Physics of Solids*, vol. 11, no. 2, pp. 127–140, 1963.

[200] N. SRISUK, *A MICROMECHANICS MODEL OF THERMAL EXPANSION COEFFICIENT IN FIBER REINFORCED COMPOSITES*. PhD thesis, The University of Texas, 2010.

[201] N. Zobeiry, A. Forghani, C. Li, K. Gordnian, R. Thorpe, R. Vaziri, G. Fernlund, and A. Poursartip, "Multiscale characterization and representation of composite materials during processing," *Philosophical Transactions of the Royal Society A: Mathematical, Physical and Engineering Sciences*, vol. 374, no. 2071, 2016.

[202] A. Johnston, R. Vaziri, and A. Poursartip, "A plane strain model for process-induced deformation of laminated composite structures," *Journal of Composite Materials*, vol. 35, no. 16, pp. 1435–1469, 2001.

[203] X. Huang, J. W. Gillespie, and T. Bogetti, "Process induced stress for woven fabric thick section composite structures," *Composite Structures*, vol. 49, no. 3, pp. 303–312, 2000.

[204] D. Adolf and R. Chambers, "Verification of the capability for quantitative stress prediction during epoxy cure," *Polymer*, vol. 38, no. 21, pp. 5481–5490, 1997.

[205] D. J. O'Brien, P. T. Mather, and S. R. White, "Viscoelastic properties of an epoxy resin during cure," *Journal of Composite Materials*, vol. 35, no. 10, pp. 883–904, 2001.

[206] D. J. O'Brien, N. R. Sottos, and S. R. White, "Cure-dependent viscoelastic poisson's ratio of epoxy," *Experimental Mechanics*, vol. 47, no. 2, pp. 237–249, 2007.

[207] M. Levitsky and B. W. Shaffer, "Thermal Stresses in Chemically Hardening Elastic Media With Application to the Molding Process 1," no. September 1974, pp. 647–651, 2017.

[208] C. Karch, "Micromechanical Analysis of Thermal Expansion Coefficients," *Modeling and Numerical Simulation of Material Science*, vol. 04, no. 03, pp. 104–118, 2014.

[209] K. Dong, J. Zhang, M. Cao, M. Wang, B. Gu, and B. Sun, "A mesoscale study of thermal expansion behaviors of epoxy resin and carbon fiber/epoxy unidirectional composites based on periodic temperature and displacement boundary conditions," *Polymer Testing*, vol. 55, pp. 44–60, 2016.

[210] Z. Ran, Y. Yan, J. Li, Z. Qi, and L. Yang, "Determination of thermal expansion coefficients for unidirectional fiber-reinforced composites," *Chinese Journal of Aeronautics*, vol. 27, no. 5, pp. 1180–1187, 2014.

[211] J. Bailleul, G. Guyonvarch, B. Garnier, Y. Jarny, and D. Delaunay, "Identification des propriétés thermiques de composites fibres de verre/résines thermodurcissables Application à l'optimisation des procédés de moulage," *Revue Générale de Thermique*, vol. 35, no. 409, pp. 65–76, 1996.

[212] Kelly, "Solid Mechanics, Part I, Section 10.1, Viscoelasticity," pp. 283–342, 1830.

[213] N.-n. Flows, *Springer Handbook of Experimental Fluid Mechanics*. No. May 2014, 2007.

DOCTORAT BRETAGNE SCIENCES LOIRE POUR L'INGENIEUR

Nantes Université

Titre : Comportement des Composites Thermodurcissables Durant la Cuisson : Mesure des Déformations, Caractérisation et Modélisation du Comportement Rhéologique

Mots clés : Composite thermodurcissable, Retrait chimique, Dilatation/ Retrait thermique, Anisotropie, Comportement Rhéo-cinétique

Résumé : En raison de la nature anisotrope et hétérogène des composites thermodurcissables, l'interaction entre des phénomènes multi physiques complexes pendant la cuisson de ces matériaux joue un rôle majeur dans la génération de contraintes résiduelles. Ces dernières produisent plusieurs défauts comme la déformation des pièces et la réduction de la résistance mécanique des composants composites. Une modélisation fine du comportement du matériau est donc nécessaire pour prédire la forme finale des pièces et leurs propriétés. Afin d'alimenter ces modèles et évaluer leur précision, des mesures directes et fiables des propriétés des composites pendant leur cuisson sont nécessaires, bien qu'elles représentent encore de réelles verrous. Dans ce but, le travail présenté dans cette thèse s'est d'abord concentré sur la caractérisation des déformations induites en cours de cuisson d'un pré-imprégné thermodurcissable de type Epoxy/Carbone UD en utilisant un dispositif experimental nommé PvT-HADDOC. Le comportement du matériau UD a été prouvé orthotrope avec des CTE et CCS mesurés beaucoup plus élevés à travers l'épaisseur. Les CTE ont été estimés à l'état cru et cuit. Le retrait chimique a été mesuré dans les deux directions transversales. Il a été demontré que le matériau ne se rétracte pas de la même manière avant et après la gélification. Enfin, un modèle rhéocinétique analytique basé sur le modèle viscoélastique de Burgers a été développé. Il a été prouvé que pendant la phase de pré-gélification, le comportement du pré-imprégné étudié, supposé à l'état caoutchouteux, peut être décrit avec précision par un comportement de type fluide.

Title : Behavior of Thermoset Composites during the Cure: Measurement of Process-Induced Strains, Characterization and Modeling of the Rheological Behavior

Keywords : Thermoset composite, Chemical shrinkage, Thermal Expansion/Contraction, Anisotropy, Rheo-kinetic behavior

Abstract: Due to the anisotropic and heterogeneous nature of thermoset composites, interaction between complex multi-physical phenomena during the cure of these materials play a major role in generating residual stresses. The latter lead to several defects like part distortion and reduced mechanical strength of composite components. A fine modeling of the material behavior is therefore necessary to predict the final shape of parts and their properties. To feed the models and assess their accuracy, reliable direct measurements of the composite properties during the cure are crucial while they are still a considerable challenge. For this purpose, the work presented in this thesis has firstly focused on the characterization of the process-induced strains throughout the entire cure of a thermoset-interlayered carbon/epoxy UD prepreg using a laboratory bench named as PvT-HADDOC. Analyses of cure behavior revealed an orthotropic behavior of the studied UD material with measured CTE and CCS much higher through the thickness direction. CTE were estimated in the uncured and cured glassy states. Cure shrinkage was measured along both transverse directions and has proved that the material does not shrink likewise before and after gelation. Finally, an analytical rheo-kinetic model based on Burgers viscoelastic model was developed. It has been proven that during the pre-gelation stage, the studied prepreg behavior, assumed in the rubbery state, can be accurately described by a fluid-like behavior.